

**Structural, Mineralogical and Fluid Evolution of the
Shahumyan Intermediate Sulphidation Vein Deposit, Kapan
District Armenia**

by

Dharani Raja Yarra

B.Sc (Hons), Brock University, 2013

A THESIS SUBMITTED IN PARTIAL FULFILLMENT OF
THE REQUIREMENTS FOR THE DEGREE OF

MASTER OF SCIENCE

in

THE FACULTY OF GRADUATE AND POSTDOCTORAL STUDIES
(Geological Sciences)

THE UNIVERSITY OF BRITISH COLUMBIA

(Vancouver)

August 2017

© Dharani Raja Yarra, 2017

Abstract

The Kapan District located in the Syunik province of SE Armenia is part of the Lesser Caucasus. The district consists of multiple vein type deposits that were emplaced in the Middle-Upper Jurassic. The Shahumyan deposit is the only actively producing deposit within the district. Understanding vein geometry, and hydrothermal fluid evolution is fundamental in establishing the genesis and exploration significance within an epithermal vein district, providing both near mine and district scale targets.

Over 120 veins of varying thicknesses (20cm to 3 m) are identified at the Shahumyan deposit. The veins are sub-vertical, south-dipping and trend east to northeast. Veins comprise of small bends, extensional jogs, soft and hard linked step-overs, pinch and swell structures and cymoid loops. These features are observed along both strike and down-dip of individual veins and contain higher metal grades relative to the rest of the vein. Along strike and down-dip connectivity of these structural features define high-grade ore-shoots within mineralized veins.

Three main hydrothermal stages associated with mineralization are defined: Stage 1, pyrite, fine grained quartz \pm chlorite; Stage 2a & b, pyrite, chalcopyrite, sphalerite, galena, sulfosalts, Au-Ag tellurides, fine and coarse white quartz, \pm calcite; Stage 3; calcite, quartz, pyrite. Au-Ag-Pb tellurides are associated with localized brecciation. Tellurides are predominantly present in fractured sphalerite, pyrite, chalcopyrite and galena. Based on textures and fluid inclusion studies, Au-Ag-Pb tellurides are linked to boiling mechanisms.

The epithermal event at The Shahumyan deposit is characterised by punctuated periods of hydrothermal brecciation interspersed with more quiescent periods when coarsely banded vein material was precipitated. Localized brecciation provide increased fluid permeability and ideal fluid pathways for mineralizing fluids. Localized brecciation corresponds with continued propagation or re-opening of the fracture-vein system. Localized boiling is interpreted to be the primarily driver for Au-Ag telluride precipitation.

Lay Summary

The economic potential of a mineral deposit is determined by their metal content (gold, silver, copper, zinc and lead) and ratio's. Gold significantly increases the value of these deposits making them economic to mine. These metals are carried in hydrothermal solution and precipitate due to changing physical and chemical conditions, such as temperature, pressure and acidity. This project tries to identify the transport pathways within the earth's crust which, these hydrothermal solutions travelled through and constrains the physical and chemical conditions which caused these metals to precipitate. The results of this project would help the Shahumyan deposit to become more economic by helping local geologists to target areas for high precious metal (gold and silver) to base metal (copper, zinc, lead) ratios.

Preface

An introduction is presented in Chapter 1, where research concepts and objectives are outlined. A summary and discussion of the research results, implications and suggested future work is present in Chapter 5. Chapter 2 reviews the tectonic and regional geology of the Lesser Caucasus and the Kapan Volcanic Zone in addition to economic history of the Kapan District and its exploited metals. Chapters 3 and 4 include a presentation of quantitative and qualitative data collected to answer objectives outlined in Chapter 1 in addition to data interpretation.

The author is responsible for all of the structural measurements, descriptive data collected and for the selection of the following analytical samples: (1) shortwave infrared spectroscopy; (2) X-ray diffraction; (3) microprobe / SEM; (4) lithogeochemical; (5) fluid inclusion microthermometry; and (6) Ar/Ar and K/Ar geochronology. The author is responsible for the generation of all figures and tables, unless otherwise noted. Analytical methods 2-3 were undertaken at UBC by the author with assistance from Jenny Lai and Edith Czech. Methods 1 and 5 were undertaken at UBC with the assistance of Farhad Bouzari and Murray Allan. The preparation of lithogeochemical samples was performed by the author at the MDRU lab and analyzed at Acme Labs, Vancouver, Canada.

Samples for Ar/Ar geochronological analyses were partially prepared at UBC by the author and sent to the University of Geneva, Geneva Switzerland and analysed by Dr. Richard Alan Spikings. Samples for K/Ar geochronological analyses were partially prepared at UBC and sent to Institute for Nuclear Research, Hungarian Academy of Sciences, Debrecen, Hungary for K/Ar analyses and analysed by Drs. Zsolt Benkó and Zoltán Pécskay undertook K/Ar analyses.

Data analysis and modelling of analytical results, and structural measurements was carried by the author, using ioGAS®, ArcGIS®, Leapfrog®, OpenStereo™ and Geochemists Workbench® computer software.

Table of Contents

Abstract	ii
Lay Summary	iii
Preface	iv
Table of Contents.....	v
List of Tables.....	ix
List of Figures	x
Abbreviations.....	xii
Acknowledgements	xiii
1. Introduction	1
1.1 Introduction.....	1
1.1.1 Objectives	3
1.2 Conceptual Framework.....	7
1.2.1 Epithermal Deposits- Intermediate Sulphidation.....	7
1.2.2 Hydrothermal Alteration in Epithermal Deposits	9
2. Geology of the Lesser Caucasus and Kapan District	11
2.1 Tectonic and Geologic Setting, Lesser Caucasus	11
2.1.1 Geology of the Somkheto-Karabakh Volcanic Zone (SKVZ)	14
2.1.2 Structural Regimes, Caucasus	15
2.1.3 Metallogenic Overview, Lesser Caucasus	17
2.2 Geology of the Kapan District.....	21
2.2.1 Cenozoic-Paleogene Complex	22
2.2.2 Upper Jurassic to Lower Cretaceous Complex.....	22
2.2.3 Middle Jurassic Complex	23
2.3 Litho geochemistry of Middle Jurassic Volcanic rocks.....	25
2.4 Structural Trends, Kapan District.....	30
2.4.1 Folding and Bedding Trends	31
2.5 Mineralized Veins within the Kapan District.....	33
2.5.1 Centralni	33
2.5.2 Noreshenik	36
2.5.3 Arachadzor.....	36
2.5.4 Barabtoom and Gyangibut	37

3. Mineralization Paragenesis and Structural Evolution of the Vein System at Shahumyan	38
3.1 Introduction	38
3.2 Vein Mineralogy and Textures.....	39
3.2.1 Ore Minerals	39
3.2.2 Gangue Minerals and Textures	42
3.2.2.1 Major Gangue	42
3.2.2.2 Minor Gangue.....	44
3.3 Mineralization Paragenesis.....	44
3.3.1 Stage 1	46
3.3.2 Stage 2.....	47
3.3.3 Stage 3.....	49
3.4 Centralni and Noreshenik Vein Mineralogy	49
3.4.1 Centralni.....	49
3.4.2 Noreshenik	51
3.5 Vein Geometry, Shahumyan	52
3.5.1 South Zone (Vein 17 and 20).....	54
3.5.2 Middle Zone (Vein 34-33, 57).....	55
3.5.3 North Zone (Vein 35)	56
3.5.4 High Grade Ore Shoots	56
3.6 Discussion	58
3.6.1 Hydrothermal Stages	58
3.6.2 Vein Geometry	60
3.6.3 Vein and Oreshoot Formation	61
4. Fluid Characterization, Alteration and Fluid Inclusions	65
4.1 Introduction	65
4.2 Hydrothermal Alteration, Shahumyan	66
4.2.1 Least Altered Rocks, (Barabatom Volcanics).....	67
4.2.2 Distal Alteration Assemblage	67
4.2.3 Intermediate Alteration Assemblage	70
4.2.4 Proximal Alteration Assemblage	70
4.2.5 Lithocap Alteration	71
4.3 Mineral Compositions	71
4.3.1 White Mica Group	72

4.3.2 Chlorite Group.....	73
4.3.3 Kaolinite Group.....	73
4.4 Geochemistry of Alteration Assemblages	74
4.4.1 Mass Transfer Calculations.....	75
4.4.1.1 Major Elements Mass Transfer.....	77
4.3.1.2 Base and Precious Metal Mass Transfer	78
4.3.1.3 Trace Elements and REE Mass Transfer.....	78
4.4.2 Molar element ratio diagrams and alteration trends.....	79
4.4.3 Alteration Discussion	80
4.5 Fluid Inclusions	83
4.5.1 Fluid Inclusion Petrography	84
4.5.2 Fluid Inclusion Results	89
4.5.3 Fluid Characteristics- Fluid inclusions.....	91
4.6 Physiochemical Constraints	93
4.6.1 Fluid Chemistry, pH and Temperature	93
4.6.2 Constraints on Te and S Fugacities	98
5. Summary and Discussion.....	104
5.1 Vein Mineralogy, Alteration and Fluid Inclusions.....	104
5.2 Vein Geometry and Ore Shoots, Shahumyan.....	106
5.3 Discussion	107
5.4 Conclusions.....	113
5.5 District Scale Exploration Implications.....	114
5.6 Future Work:	118
References	120
Appendix 1: Lithogeochemistry	138
Appendix 2: Geochronology: Ar-Ar and K-Ar.....	147
Appendix 3: Alteration Analysis.....	153
Appendix 3a: Whole Rock Geochemistry for Alteration Analysis	154
Appendix 3b: Alteration Mass Balance.....	173
Appendix 3c: Shortwave Infrared	180
Appendix 3d: Illite-Sericite Microprobe Results.....	187
Appendix 3e: Chlorite Microprobe Results.....	202
Appendix 4: Fluid Inclusion Study.....	208

Appendix 4a: Fluid Inclusion Results	209
Appendix 4b: Fluid Inclusion Petrography.....	218
Appendix 5: Underground Vein Maps.....	221
Appendix 6: Ore Petrography	234

List of Tables

Table 1.1: Characteristics of Epithermal subtypes.....	5
Table 2.1: Known historical exploration and mining within the Kapan District.....	34
Table 3.1: Paragenetic table of hydrothermal stages and textures at Shahumyan.....	46
Table 3.2: Paragenetic table of hydrothermal stages at Centralni East.....	50
Table 3.3: Paragenetic table of hydrothermal stages at Noreshenik.....	50
Table 4.1: Summary of observed fluid inclusion assemblages.....	84
Table 4.2: Physiochemical parameters of mineralizing fluids.....	100

List of Figures

Figure 2.1: Location map of the Caucasus.....	12
Figure 2.2: The Meghri-Ordubad and Kapan ore districts.....	17
Figure 2.3: Metallogenic ages, Lesser Caucasus.....	18
Figure 2.4: A geologic map of the Kapan district.....	19
Figure 2.5: A simplified stratigraphic section of Kapan District.....	20
Figure 2.6 (A-B): Major and trace element diagram of Middle Jurassic volcanic units.....	27
Figure 2.7 (A-H): C1 chondrite-normalized REE plots-Middle Jurassic.....	28
Figure 2.8: Bedding and structural trends within the Kapan District.....	31
Figure 2.9: Orientation data of mineralized veins within the Kapan district.....	35
Figure 3.1: A plan view map of Shahumyan veins.....	43
Figure 3.2 (A-C): Vein samples from Shahumyan.....	45
Figure 3.3 (A-F): Photomicrographs and SEM imagery of vein samples.....	48
Figure 3.4: A cymoid vein structure in Vein 20.....	52
Figure 3.5 (A-D): Observed vein textures in Shahumyan veins.....	57
Figure 3.6: Vein 17 drift back map: mineralogy, texture, structure, assays.....	59
Figure 3.7: (A-E): Schematic of isolated fault model and examples.....	62
Figure 4.1: A schematic of alteration assemblages.....	66
Figure 4.2: (A-H): Photomicrographs and pictures of alteration at Shahumyan.....	69
Figure 4.3: (A-C): Characterizing alteration: SWIR and Geochemistry.....	73
Figure 4.4: (A-C): Mass balance graphs.....	77
Figure 4.5: Photomicrographs of FIA's.....	85
Figure 4.6: (A-D): Photomicrographs of FIA's. , continued.....	87

Figure 4.7: Petrography of FIA's.....	88
Figure 4.8: Homogenization temperature vs salinity graph for all measured FIA's.....	90
Figure 4.9: Activity diagram for principal phases in an MgO-Al ₂ O-SiO ₂ -H ₂ O system.....	95
Figure 4.10: Activity-pH diagram highlighting fluid pathways at Shahumyan	97
Figure 4.11: Sulfide and telluride equilibrium in f_{Te_2}/f_{S_2} space.....	101
Figure 5.1: A schematic model for boiling fluids induced by water table drop.....	112
Figure 5.2: Schematic diagram of fault block offset in the Kapan district.....	116

Abbreviations

Cy: Mica and/or Clay	FIA: Fluid Inclusion Assemblages
Py: Pyrite	wt% Weight percent
Cpy: Chalcopyrite	equiv. equivalent
Pg: Plagioclase	T: Temperature
Sph: Sphalerite	T _e : Eutectic Temperature
Tt-Tn(?): Tetrahedrite/ Tennantite	T _h : Temperature of Homogenization
Te (?): Telluride of unknown composition	T _m : Temperature of Final Melting
He: Hessite	log a: Log Activity
Ga: Galena	<i>f</i> : Fugacity
Au: Gold	Ma: Mega Annum
Ag: Silver	LS: Low Sulphidation
Cu: Copper	IS: Intermediate Sulphidation
Zn: Zinc	HS: High Sulphidation
Pb: Lead	REE: Rare Earth Elements
Qtz(1): Fine grained quartz	LREE: Light Rare Earth Elements
Qtz(2): Prismatic/euhedral quartz	HREE: Heavy Rare Earth Elements
Ca: Calcite	HFSE: High Fields Strength Elements
F: Fluorite	LILE: Light Ion Lithophile Elements
Hb: Hornblend	SWIR: Shortwave Infrared
Chl: Chlorite	XRD: X-ray Diffraction
-T: Transmitted light (postscript, e.g XPL-T)	SEM: Scanninc electron microscope
-RL: Reflected light (postscript, e.g XPL-RL)	SAB: South Armenia Block
XPL: Cross polarized light	SKVZ: Somkheto Karabakh Volcanic Arc
PPL: Plane Polarized light	SASZ: Sevan-Akera Suture zone
	IAES: Izmir-Ankara-Erzican suture zone
	KVZ: Kapan Volcanic Zone

Acknowledgements

The Author would like to thank the many Sponsors of the Western Tethyan Project, most especially Dundee Precious Metals. It was a genuine pleasure to work with the staff and contractors at Dundee Precious Metals. I would like to thank Dr. Aleksandar Mišković and Dr. Craig Hart for putting the project together and for their contributions and discussions for the duration of the project, as well as the opportunity to work on the project. Special thanks to committee members Dr. Murray Allan, Dr. Ken Hickey for their insights, discussions, and mentorship. Many thanks to Dr. Farhad Bouzari, Dr. Richard Tosdal for their contribution and in depth discussions during the project. A personal thanks to Sara Jenkins and Arne Toma for their never ending technical support and patience in helping with the necessary tools and software needed to conduct research.

My heartfelt thanks to my fellow colleagues and friends at the University of British Columbia and the Western Tethyan project: Kaleb Boucher, Graham Leroux, Paula Brunetti, Jelena Zivanovic, Fabien Rabayrol; Dragan Dragic, Erde Bilir, and many others at the Mineral Deposits Research Unit and the department of Earth Ocean and Atmospheric Sciences. I would not have made it this far without your continued support, friendship and our numerous inebriated insights. I am truly thankful to have met you and shared a large part of my life and time over the past several years. Finally, no amount of thanks would be sufficient in encompassing the gratitude and love I feel for my family, who have always supported me.

1. Introduction

1.1 Introduction

Shallow hydrothermal mineral deposits form in most metallogenic belts; however, only some have sufficient primary metal enrichments to be an economic ore body. In shallow hydrothermal environments, ore bodies are irregular in shape and are strongly influenced by zones of high permeability, which are either structurally or lithologically controlled (Brathwaite et al., 2001, Oliver et al., 2001 and Simmons et al., 2005). Epithermal veins are shallow hydrothermal ore bodies are a result of circulating hydrothermal fluids through interconnected fault and fracture systems (Cox, 2005, Simmons et al., 2005, Micklethwaite et al., 2010 and Micklethwaite et al., 2010). Therefore, epithermal veins provide insights into how hydrothermal fluid pathways, responsible for ore bodies are generated in shallow crustal levels.

Some epithermal veins develop in normal faults in extensional environments (Sillitoe and Hedenquist, 2003 and Christie et al., 2007). Hydrothermal fluid flow within these structures is governed by hydraulic gradients and interconnections between fluid pathways (Sibson, 1996 and Cox, 2005). The presence of irregularities, jogs and intersections within normal faults localise pathways for hydrothermal fluids to be focused and concentrated (Sibson, 1996, Rowland and Sibson, 2004, Cox, 2005 and Faulkner et al., 2010). The presence of highly permeable conduits combined with an efficient ore deposition mechanism is critical to forming economically viable ore shoots within epithermal veins (Simmons and Browne, 2000; Berger et al., 2003; Cox, 2005, Simmons and Brown, 2006 and Micklethwaite, 2009). Mechanical changes attributed to fault rupturing events (earthquakes) directly influence physical processes, and therefore physicochemical parameters such as: pressure, acidity and salinity that affect vein and alteration mineralogy. Identifying favourable structural pathways and

their effect on physicochemical parameters based on vein and alteration mineralogy is key to understanding epithermal vein's and ore shoot formation. Vein and ore-shoot geometry, mineral assemblages help constrain hydrothermal fluid characteristics, which are fundamental to exploration because they characterize an epithermal vein system.

The Kapan District is located in the Syunik province of SE Armenia is considered to have formed during a Mesozoic metallogenic event (Mederer et al, 2013). The district comprises multiple vein deposits that have been exploited since the 1800s with the production estimated at 370,000 tonnes of Cu since 1953. (Table 1.1). The Shahumyan deposit is the only actively producing locality in the Kapan district with an indicated and inferred resource of 15.87 Mt at cut off grades of 2.72 g/t Au, 48.5 g/t Ag, 0.5% Cu, 1.82% Zn and 0.1% Pb (White et al., 2015). The Shahumyan deposit is a strongly structurally controlled epithermal vein system hosted in an Early-Middle Jurassic volcanic rock suite, characterized by porphyritic andesites, dacites, volcanic flows and volcanoclastic rocks. Previous geological studies in the district were conducted by Soviet geologists from 1950-1990's and most recently by Mederer et al. (2013, 2014). The Shahumyan polymetallic vein deposit represents an ideal case in which to study local and district scale structures involved in localizing hydrothermal fluid flow and to study the relationships between mineralogical variations and structural features. Shahumyan has similar characteristics to the world class Creede, USA; Acupan, Phillipines; and Morococha, Peru, epithermal vein districts.

The current geologic datasets at the actively mined Shahumyan deposit sufficiently augments the data collected as part of this thesis in order to model structural and hydrothermal fluid evolution. A detailed structural and mineralogical analysis is used to constrain the physicochemical parameters of hydrothermal fluids at the Shahumyan deposit. Combined mineralogical, textural, structural, geochemical and

microthermometric data obtained from selected samples and field observations are used to propose a model for epithermal vein formation. Tectonic and fluid assisted fracturing (hydraulic) processes are examined, where earlier structures, reactivated and reopened in association with boiling processes, play a significant role in vein filling and ore deposition.

1.1.1 Objectives

The objectives of this thesis are to: (1) Establish an alteration and mineral paragenesis to characterize occurrences of Au-Ag rich ore zones within veins; (2) Identify key structural controls on fluid flow and mineralization at the deposit scale and develop a genetic evolution model of vein geometry at Shahumyan; (3) Define physiochemical parameters of hydrothermal fluids responsible for economic mineralization.

1) The Kapan district contains numerous vein deposits which are principally base metal rich; however, Shahumyan unique to other deposits in the district contains anomalously high Ag: Au ratios in addition to abundant base metals. The alteration assemblages at the Shahumyan deposit also slightly differ, indicating different fluid chemistry from other veins within the district. Vein mineralogy and alteration assemblages record the fluid evolution within hydrothermal deposits and are important aspects in identifying key hydrothermal stages responsible for high-grade mineralization. Alteration minerals formed as a function of hydrothermal fluid flow reflect the geochemical composition of ore-forming fluids.

Mineralization paragenesis was characterized by employing petrographic studies accompanied by scanning electron microscope (SEM) and microprobe analyses. Samples were taken from drill core and underground mapping sta-

tions. Thirty two polished thin sections were used in the petrographic study at Shahumyan. Additionally, five vein samples from the Noreshenik deposit and three vein samples from the Centralni deposit were used in a comparative study between the three deposits. From the forty one samples taken, ten representative samples were further described using the SEM and microprobe, to identify telluride and sulphosalt species.

Sixty rock samples comprising the Middle Jurassic suite were evaluated for petrography, rock classification, and alteration analyses from drill core and surface samples. These sixty samples were further supplemented by the Dundee Precious Metal sample database and data from Mederer et al. (2013). An alteration study was conducted on forty of the sixty samples comprising of the Barabatoom unit, which hosts the Shahumyan deposit. The alteration study consisted of petrographic analysis of alteration assemblages followed by Shortwave Infrared (SWIR) and X-ray diffraction (XRD) analyses to confirm observed minerals and or identify minerals indistinguishable through petrographic analyses. Furthermore, whole-rock analyses were used for mass balance calculations and determine elemental gains and losses between identified alteration assemblages and least altered host rock.

2) Epithermal mineralization is typically localized in fault-fracture systems and related zones of brecciation that are developed in the brittle portion of the crust. These fault fracture systems are regarded as fluid conduits for mineralizing fluids. These systems experience episodic fluid flow which is penecontemporaneous with fault propagation events (Sibson, 1981; Sibson, 1987; Fossen and Rotevatn, 2016) related to earthquake rupture processes. Mineralization in these systems concentrates at specific structural sites where local dilation has occurred within the fault systems. Deposit geometry and structural frame-

work of vein systems are therefore fundamental to understanding the deposit genesis and hydrothermal evolution, because changes in vein orientation, morphology and texture highlight vein opening events which constrain fluid flow

	High Sulphidation	Intermediate Sulphidation	Low Sulphidation
Tectonic setting	Extensional and compressive island arc	Extensional continental compressive island arc	Extensional continental island arc, back arc
Genetically related igneous rocks	Calc-alkaline, andesite-rhyodacite	Calc-alkaline, andesite-rhyodacite locally rhyolite	Calc-alkaline to alkaline, rhyolite-basalt, basalt trachyte
Major metals	Au-Ag, Cu, As-Sb	Ag-Au, Zn, Pb, Cu	Au± Ag
Minor metals	Zn, Pb, Bi, W, Mo, Sn, Hg	Mo, As, Sb	Zn, Pb, Cu, Mo, As, Sb, Hg
Ore minerals	Enargite, luzonite, famantinite, covellite, acanthite, stibnite	Sphalerite (low-Fe), galena, Ag-sulfosalts, acanthite, sulfosalts, chalcocopyrite, tellurides	Ag-sulfosalts, sphalerite (high Fe), galena, sulfosalts, chalcocopyrite, arsenopyrite, pyrrhotite, selenides, tellurides
Ore mineral abundance	10-90 vol. %	5-20 vol. %	<1-2 vol. % and up to 20 vol. %
Gangue minerals	Quartz-barite	Quartz, carbonates (Mn, Mg)	Chalcedony, quartz, carbonate
Mineral textures	Fine to massive, residual quartz	Crustiform, comb-quartz, fine-massive	Crustiform, carbonate replacement textures
Principal alteration	Quartz-alunite, quartz-pyrophyllite, dickite, kaolinite	Sericite/illite, adularia (uncommon)	Illite, smectite, adularia, roscoelite
Fluid temperatures	100° to >400°	200° to 300°	150° to 300°
Fluid salinities	<5wt% NaCl	0-23 wt% NaCl	<3.5 wt% NaCl
Fluid composition	Magmatic, acidic, oxidized	Magmatic ± meteoric, near-neutral, reduced	Meteoric ± magmatic, near-neutral, reduced-oxidized
Formation depth	Shallow 0 to >300m	Deep, 300-800m (> 1000m)	Shallow, <300m

Compiled from: Buchanan (1981), White and Hedenquist (1990), Cooke and Simmons (2000), Hedenquist et al. (2000), and Sillitoe and Hedenquist (2003)

Table 1.1: Characteristics of Epithermal subtypes: low sulphidation, intermediate sulphidation and high sulphidation deposits. Compiled from Buchanan (1981), White and Hedenquist (1990), Cooke and Simmons (2000), Hedenquist et al. (2000), Sillitoe and Hedenquist (2003).

and thus mineral precipitation. Identifying key structural controls on fluid flow and mineralization by establishing a structural framework and grade distribution within individual veins, provides mine geologists better tools to target highly economic ore shoots and model the vein system at the Shahumyan deposit. Integrating and comparing the structural framework of Shahumyan deposit veins with district wide veins (Centralni and Noreshenik deposits), will promote better exploration targets for the Kapan district.

This objective is accomplished by detailed underground drift mapping of Shahumyan veins. Shahumyan veins were studied by evaluating mine level maps, longitudinal sections, cross-sections, and geometry of interconnecting struc-

tures. This was followed by detailed mapping at accessible underground levels and stopes at 1:100 scales. Three zones (South, Middle, North) consisting of five veins were chosen for detailed mapping. These veins were selected due to mine accessibility of each vein at different depths and their spatial distribution within the mine. Within each vein the distribution of hydrothermal stages, textural and structural variability were examined and mapped. Longitudinal sections showing thickness and grade distribution were created from channel assay database, provided by Dundee Precious Metals.

3) Mineralization paragenesis and alteration mineral assemblages provide a basis for modelling and determining hydrothermal fluid conditions during mineralization. Changes in physicochemical conditions such as temperature, pressure, salinity, pH and eH are effective mechanisms for precious metal precipitation (Zhu et al., 2011, Cooke et al., 2001; Cooke et al., 1996; Spycher and Reed, 1989). These geochemical and physicochemical parameters help geologists determine the environment of formation and provides a genetic model for district and regional scale exploration program for similar deposits.

Hydrothermal fluid chemistry and temperature of mineralizing fluids at Shahumyan were constrained by a fluid inclusion analysis. Seven suitable samples were chosen from thirty two polished thin sections originally used for the mineralization paragenesis study. Homogenization temperatures and salinity data were collected in accordance to the hydrothermal stages outlined by the paragenetic study. Doubly polished thick sections (100µm thickness) were prepared for the chosen samples.

1.2 Conceptual Framework

1.2.1 Epithermal Deposits- Intermediate Sulphidation

Epithermal deposits are products of circulating magmatic or magmatic-meteoric fluids at 100-300°C and form in the upper portions of the crust (1-2 km). They were originally defined by Lidgren (1933), who classified such deposits largely by their mineralogy and textures, as well as interpreted a depth and temperature of formation. Understanding of epithermal systems has improved and are now further classified based on: fluid chemistry, alteration and gangue mineralogy and purely descriptive observations (Hayba et al., 1985; Heald et al., 1987; Berger and Henley, 1989). The current classification scheme is based on the stability of sulphur bearing minerals (i.e., sulphur and oxygen fugacity), which gives insights into the chemical state of hydrothermal fluids. Three subtypes of epithermal deposits are recognized based on the fluid characteristics: low-sulphidation (LS), intermediate-sulphidation (IS) and high-sulphidation (HS) (Table 1.1; Hedenquist et al., 2000; Einaudi et al., 2003; Sillitoe and Hedenquist, 2003; Gemmell, 2004; Sillitoe, 2008).

LS-epithermal deposits are products of near-neutral meteoric waters that formed distal to hypabyssal intrusions. HS epithermal deposits in contrast, are dominantly a product of magmatic fluids, and formed proximal to sub-volcanic intrusions and are related to porphyry deposits. Unlike the HS-epithermal and LS-epithermal schemes which existed in the original epithermal classification, the intermediate sulphidation scheme was recently recognized as a hybrid between the high- and low-sulphidation types (Hedenquist et al., 2000) and expanded on by Einaudi et al. (2003), Sillitoe and Hedenquist (2003) and Gemmel (2004). IS-epithermal deposits have a spatial and temporal association with both high-sulphidation and low-sulphidation deposits. According to Einaudi et al (2003) and Sillitoe and Hedenquist (2003), IS-epithermal de-

posits form from near-neutral (pH ~6), reduced, moderately saline (5-20 wt % NaCl), and moderate temperature (150-300°C) fluids. Intermediate sulphidation deposits typically contain characteristics of both HS and LS epithermal systems. IS-epithermal systems have fluid characteristics akin to both magmatic and meteoric fluids, with ore and alteration mineralogies reflective of both LS and HS epithermal systems.

IS-epithermal deposits are typically sulphide-rich and may contain hydrothermal phases characteristic of the high-sulphidation subtype, although lacking enargite. They are generally silver- and base metal-rich with high Ag:Au ratios (10:1 to >100:1). Sulphide assemblages in IS-deposits include Fe-poor sphalerite, galena, pyrite, chalcopyrite, and tetrahedrite-tennantite. Silver occurs as Ag-bearing sulphosalts (Einaudi et al., 2003), argentiferous galena or as Ag-tellurides (i.e. hessite and empressite) and gold may occur as electrum or Au-tellurides (i.e. petzite, sylvanite). Changes in the mole percent FeS of sphalerite coexisting with pyrite or pyrrhotite reflects the variability of the sulphidation state in a given system and as such provides useful information in classifying an epithermal deposit (Scott and Barnes, 1971; Czamanske, 1974; Einaudi et al., 2003). The mole percent FeS of sphalerite in IS-epithermal systems typically vary from <1 to 10, however, values up to 20 have been reported (e.g. Creede; Barton et al., 1977; Einaudi et al., 2003). These values are contrasted with mole percent FeS reported for HS-systems (0.05 to 1.0) and LS-systems (20 to 40) deposits (Scott and Barnes, 1971; Czamanske, 1974; Einaudi et al., 2003).

Mineral precipitation in hydrothermal deposits results from changes in physical and or chemical variables such as temperature, pressure, salinity, acidity and redox state, as well as ligand concentration (e.g. chloride, bisulphide; Cooke and McPhail, 2001). These variables can be directly affected by processes such as cooling, pressurization, boiling, fluid mixing and water-rock interaction (Cooke and McPhail, 2001; Reed and Plumlee, 1992; Seward, 1989; Spycher and Reed; 1989; Drummond and

Ohmoto, 1985; Reed and Spycher, 1985). These processes have been linked to tectonic events such as fracturing and faulting (Weatherley and Henley, 2013; Wilkinson and Johnson, 1996; Boullier and Robert, 1992; Sibson et al., 1988). Hydrothermal fluids tend to reuse transport pathways such as veins, thus recording hydrothermal evolution of the vein system.

1.2.2 Hydrothermal Alteration in Epithermal Deposits

Hydrothermal alteration is a result of fluid-rock interaction controlled by permeability, temperature, pressure, and fluid and rock composition. Permeability is an important factor for hydrothermal fluid transport and is as important for mineralization as it is for alteration. Permeability within a system is maintained by repeated hydraulic fracturing and tectonic ruptures or a combination of both. The temperature of hydrothermal fluids can be inferred from the presence of temperature-dependant hydrothermal clay minerals (Steiner, 1968; Browne, 1978). Illite-smectite is stable below $\sim 140^{\circ}\text{C}$, sericite/illite is stable above $\sim 220^{\circ}\text{C}$, and muscovite above $\sim 300^{\circ}\text{C}$; these stabilities also vary depending on the acidity (pH) of hydrothermal fluids. Pressure can directly affect the formation of hydrothermal minerals. Boiling and throttling are two physical mechanisms which are a direct result of pressure changes. Boiling zones can be recognized by the presence of bladed calcite and in some cases, increased quartz content and adularia are precipitated within veins (Brown and Ellis, 1970; Keith and Muffler, 1978; Keith et al., 1978). It is difficult to classify intermediate sulphidation deposits as they may have alteration assemblages and sulphidation states from both high and low sulphidation deposits as the system evolves.

HS-epithermal deposits are primarily characterized by quartz-alunite-kaolinite (advanced argillic) proximal to ore and sericitic alteration (argillic) surrounding the advanced argillic alteration (Heald et al 1987; Sillitoe and Hedenquist, 2003). Further-

more, argillic alteration can be mineralogically zoned, with kaolinite nearer to ore and smectite further away (Heald et al., 1987; Sillitoe and Hedenquist, 2003). Lithocaps consisting of quartz-alunite alteration require pH <2 to mobilize alumina (Stoffregen, 1987) and alunite forms at a pH of 2-3 (Sillitoe and Hedenquist, 2003). Propylitic alteration is the most distal assemblage and is characterized by the presence of chlorite, epidote and calcite which are indicative of alkaline fluid conditions.

LS-epithermal deposits are characterized by dominantly sericitic alteration that borders silicified zones near veins. In some instances the sericitic alteration grades into an argillic assemblage consisting of illite and/or illite/smectite. In other cases the sericitic assemblage grades into a propylitic assemblage (Heald et al., 1987). Additionally, proximal to veins fine grained adularia and/or chlorite are disseminated with the wall rock (Heald et al., 1987; Sillitoe and Hedenquist, 2003; Browne, 1978).

2. Geology of the Lesser Caucasus and Kapan District

2.1 Tectonic and Geologic Setting, Lesser Caucasus

The Caucasus region is in the central part of the Tethyan metallogenic belt and is composed several main tectonic units such as the Greater Caucasus, the Lesser Caucasus and an intermontane region called the Transcaucasus (Figure 2.1).

The Lesser Caucasus is oriented northwest and is composed of three main zones; from southwest to northeast, they are the South Armenia Block (SAB), the Sevan-Akera Suture zone (SASZ) and the Eurasian plate margin (Milanovsky, 1986, Sosson et al., 2010; Mederer et al., 2013). Paleomagnetic studies (Bazhenov et al., 1996 and Meijers et al., 2015) and paleogeographic reconstructions (Barrier and Vrielynck, 2008; Knipper and Khain, 1980; Monin and Zonenshain, 1987; Sengor et al., 1988) indicate the SAB to be a Gondwanian terrane. The SAB is composed of a metamorphic basement covered by Paleozoic sediments, Mesozoic volcanic and sedimentary formations, and Paleogene and Neogene detrital volcanogenic rocks (Sosson et al., 2010). There are two separate views of the geodynamics of the SAB; where, Barrier and Vrielynck (2008), Sosson et al. (2010), Hässig et al. (2013a, 2013b), and Hässig et al. (2015) group the SAB together with the Eastern Anatolian platform and interpret it as the northern portion of the Tauride microcontinent since the Jurassic. In contrast, Adamia et al. (1981), Golonka (2004), Alavi (1991) and Adamia et al. (2011) propose the SAB terrane to be part of the Sanandaj-Sirjan zone. Both views, however agree that the SAB is of Gondwanan origin.

The Lesser Caucasus is a segment of the Tethyan orogenic belt, and is the consequence of north-northeast to eastward-verging Jurassic-Cretaceous subduction of the Neotethys oceanic crust beneath the Eurasian plate (Kazmin et al., 1986 and Rol-

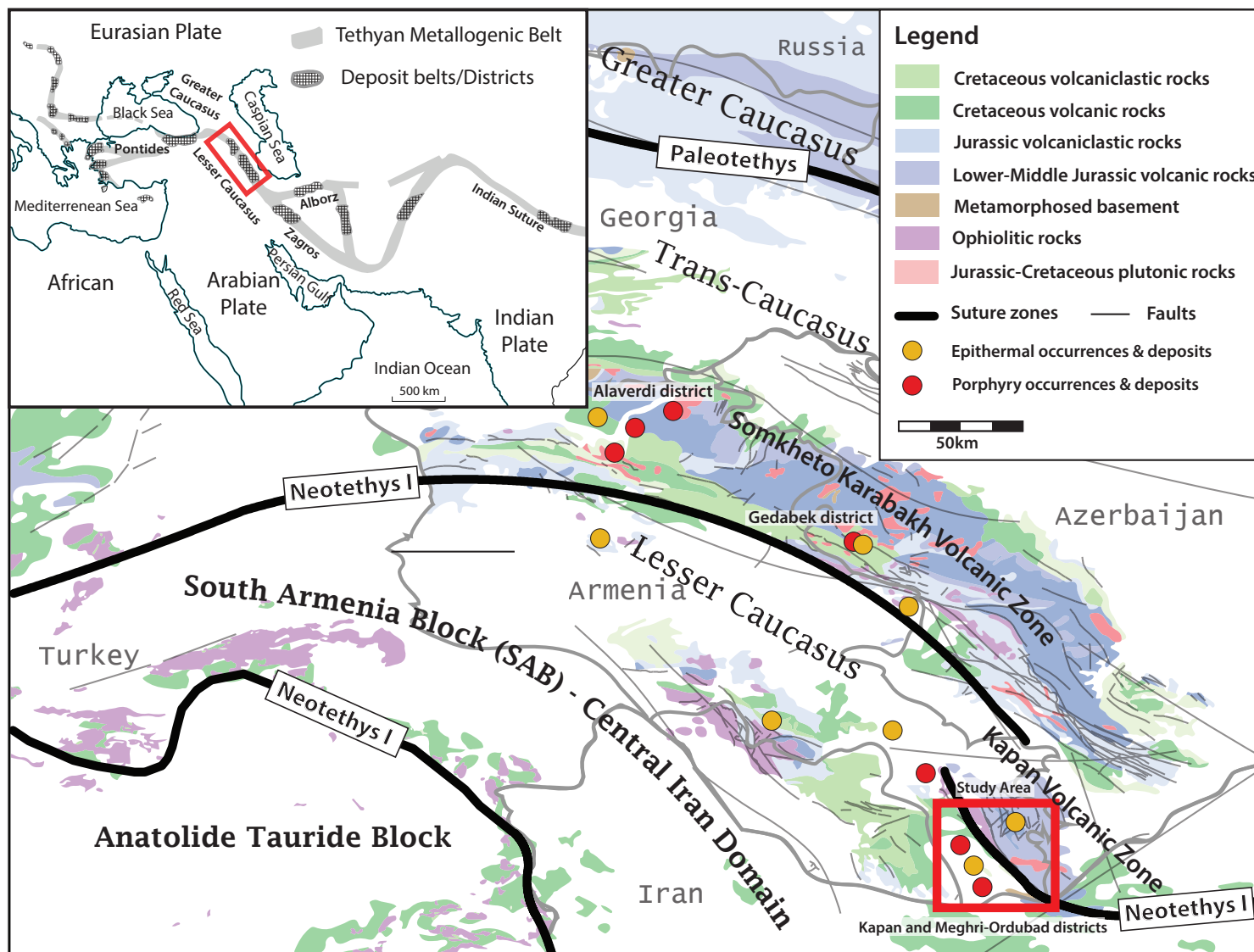


Figure 2.1: Location map of the Caucasus and major epithermal and porphyry ore deposits. Major tectonic sutures and Mesozoic volcanic units are also highlighted.

land et al., 2011). This subduction event resulted in increased volcanic activity during the Bajocian–Bathonian (170-166 Ma) to the Kimmeridgian (157-152 Ma) (Kazmin et al., 1986, Achikgiozyan et al., 1987, Lordkipanidze et al., 1989, and Mederer et al., 2013) followed by collisional deformation and magmatism (Mederer et al., 2013). The subduction of Neotethys oceanic crust was followed by Late Cretaceous collision with the Gondwana-derived SAB (Rolland et al., 2009a and Rolland et al., 2009b, Meijers et al., 2015a-b). The east-verging subduction of the Neotethys crust and the Cenozoic convergence which continued between the Eurasian and Arabian plates resulted in an Eocene magmatic climax followed by collisional deformation and magmatism from the Oligocene to the Pliocene (Khain, 1975, Gamkrelidze, 1986, Kazmin et al., 1986, Lordkipanidze et al., 1989 and Sosson et al., 2010).

The SASZ are tectonized ophiolitic complexes that separate the SAB from the Eurasian margin (Adamia et al., 1977; Maghakyan et al., 1985). The ophiolitic complexes were obducted onto the SAB between 88 and 83 Ma (Galoyan et al., 2007; Rolland et al., 2010; Sosson et al., 2010). The ophiolitic complexes overlay blueschist to amphibolite facies rocks (Rolland et al., 2009a; Sosson et al., 2010). The SASZ is correlated with the Izmir-Ankara-Erzican suture zone (IAES) of Northern Anatolia and with the unnamed ophiolites within the Iraninan Zagros range (Galoyan et al., 2009; Rolland et al., 2009a). The SASZ is absent or unidentified in southeast Armenia between the Kapan Volcanic Zone and the Meghri-Ordubad and Bargushat Plutons. The tectonic zone separating the composite plutons and the Kapan Zone is identified as the Ankhavan-Zangezur fault zone and locally as the Khustup-Giratakh fault zone (Moritz et al., 2015). It includes ultramafic rocks, gabbro, spilite, andesite and radiolarite of the Zangezur tectonic melange. This is imbricated with Late Precambrian to early Cambrian metamorphic rocks and Devonian and Permian limestones and terrigenous sedimentary rocks which are interpreted as the remains of an ophiolite (Khain, 1975; Knipper and Khain, 1980; Belov, 1981). Hassig et al. (2013a) correlate

the Zangezur ophiolites with the Sevan-Akera ophiolites, although direct relationships are hidden by Cenozoic molasse and volcanic rocks (Moritz et al., 2015).

The Eurasian plate margin of the Lesser Caucasus can be further sub-divided into the Somkheto-Karabakh and the Kapan volcanic zones (Gevorkyan and Aslanyan, 1997). Both developed during the northeast subduction of the Neotethys oceanic crust below the Eurasian margin and has similar geological and tectonic characteristics to one another and are interpreted as one single volcanic arc (Kazmin et al., 1986) displaced by northeast-trending strike-slip faults as described elsewhere in the region (Kazmin et al., 1986; Jackson, 1992; Kopp, 1997). It has also been proposed that the Eastern Pontides in Turkey and the Sanandaj-Sirjan Zone in Iran are western and southeastern extensions respectively, of the SKVZ and KVZ in the Lesser Caucasus (Adamia et al., 1981; Kazmin et al., 1986; Yilmaz et al., 2000; Golonka, 2004, Alavi, 2007 and Adamia et al., 2011).

2.1.1 Geology of the Somkheto-Karabakh Volcanic Zone (SKVZ)

The SKVZ is approximately 350 by 75 km and encompasses southern Georgia to northern Armenia, Nagarno-Karabakh, and ends in Azerbaijan. The SKVZ zone is composed of a Hercyninan basement of Lower Permian (293 ± 7 Ma: Bagdasaryan et al., 1978) covered by Jurassic shales, and clastic rocks (Nikishin et al., 2001). Thick volcanic sequences were deposited upon the sediments, starting in the Aalenian (Lower Jurassic) and reached its peak during the Bajocian-Bathonian (Kazmin et al., 1986; Mederer et al., 2013). Overlying the Middle Jurassic volcanic rocks are Upper Jurassic and Lower Cretaceous volcanic rocks alternating with calcareous sedimentary and volcanoclastic rocks (Kazmin et al., 1986). Locally the Upper Jurassic- Lower Cretaceous rocks unconformably overlie the Middle Jurassic volcanic rocks (Mederer, 2013). Upper Cretaceous and Paleogene volcanic rocks unconformably overlie the

Upper Jurassic-Lower Cretaceous rocks (Aslanyan, 1958; Bagdasaryan and Melkonyan, 1968).

2.1.2 Structural Regimes, Caucasus

Since the Late Cretaceous several tectonic regimes dominated, alternating between compression and extension, resulting in continuous reactivation along previously formed structural features. Paleostress investigations by Saintot and Angelier (2002), Avagyan et al. (2010) and McCann et al. (2010), reveal several main tectonic episodes within the Caucasus since the Mesozoic.

- During the Mesozoic to Paleocene, the Caucasus was under both compressional and extensional regimes. Compressional events were propagated by northward subduction of the Neotethys oceanic plate beneath the Eurasian margin. Extensional regimes dominated locally during compressional relaxation.
- During the Paleocene-Eocene, a transpressional event with an east to southeast trending σ_1 developed.
- Previously formed north-northeast to northeast-trending faults were inverted and correspond to the accretion of the Transcaucasian terranes during the transpressional event.
- During the Late Eocene a north-northeast to northeast oblique extension to trans-tensional event resulted in reactivation of existing faults.
- Towards the Late Eocene north-northeast to northeast trending compression characteristics are apparent.

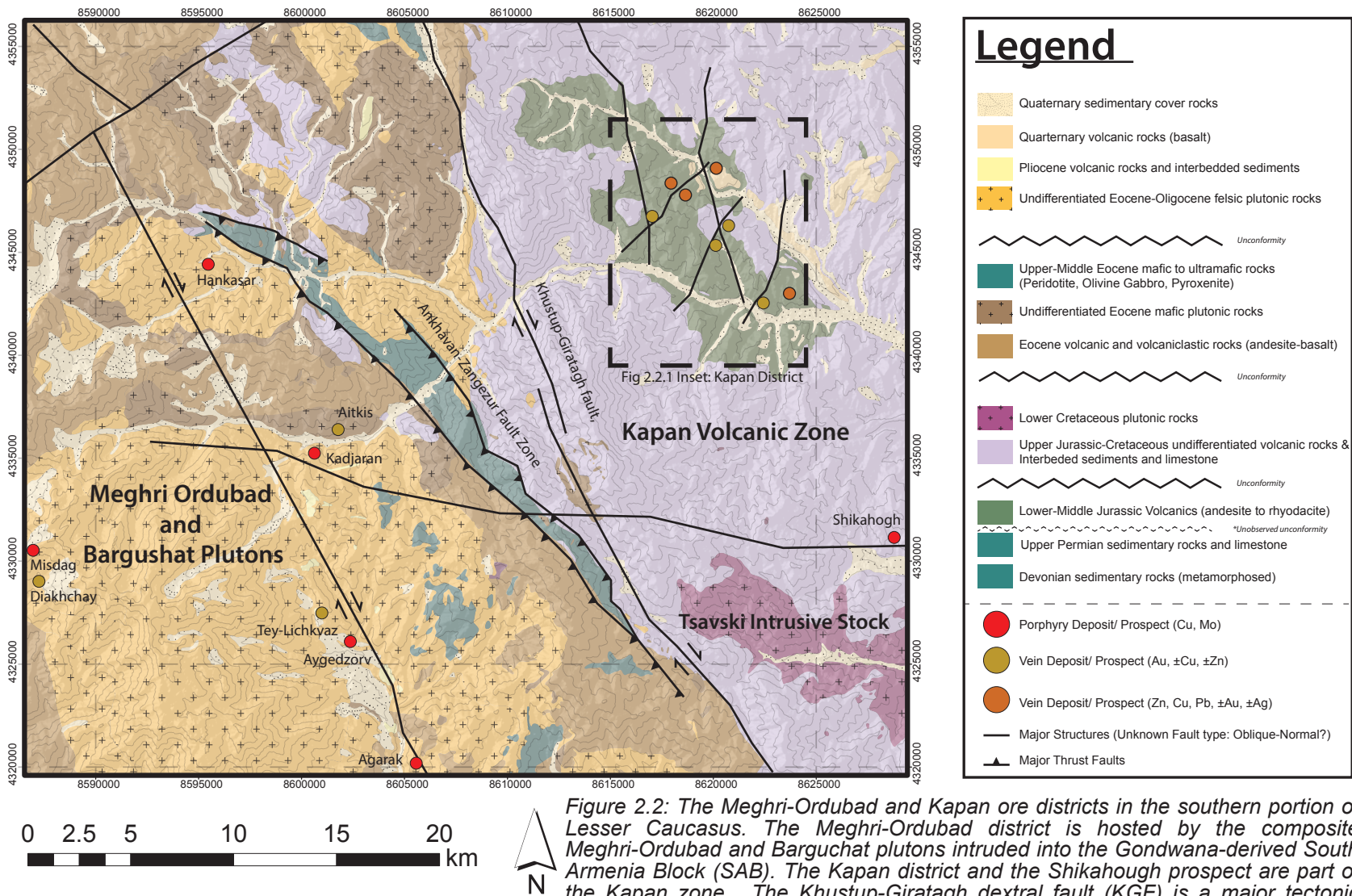


Figure 2.2: The Meghri-Ordubad and Kapan ore districts in the southern portion of Lesser Caucasus. The Meghri-Ordubad district is hosted by the composite Meghri-Ordubad and Barguchat plutons intruded into the Gondwana-derived South Armenia Block (SAB). The Kapan district and the Shikahough prospect are part of the Kapan zone. The Khustup-Giratagh dextral fault (KGF) is a major tectonic

break between the Kapan zone and the South Armenia Block. Proterozoic basement rocks, Devonian metasediments and Upper Permian sediments and carbonates are part of an ophiolitic sequence obducted on the SAB during the collision between the SAB with the Eurasian Margin. Adopted from: Bairamov et al., 2008, Bingöl, 1989, Emami et al., 1993, Gudjabidze, 2003, Kharzyan, 2005 and Lotfi et al., 1993.

- The youngest event is the compressional regime with south-south-east trending σ_1 that currently affects the northwestern Caucasus; under this oblique compression.

The Kapan Volcanic Zone (KVZ) in southeastern Armenia (Figure 2.2) is believed to be displaced from the SKVZ by a sinistral strike-slip fault (Kazmin et al., 1986; Hassig et al., 2013 and Moritz et al., 2015). The sinistral strike-slip fault coincides with the Vorotan River valley and will herein be referred to as the Vorotan fault. The Vorotan fault is a part of the Arrarat-Araks conjugate fault system, which dominates southeast Armenia (Mkrtchian, 1969). The dextral Arrarat and sinistral Araks faults constitute a major conjugate fault system within a pure-shear setting (Mkrtchian, 1969) consisting of multiple smaller conjugate faults such as the sinistral Vorotan fault propagating from the larger Arrarat and Araks faults. The KVZ is within a large north-trending anticlinorium with shallow (20°-40°) dipping limbs and slightly plunges to the southeast (Azaryan, 1978 Avanesyan et al., 1990; Tumanyan, 1992; Avanesyan et al., 1992).

2.1.3 Metallogenic Overview, Lesser Caucasus

The Lesser Caucasus hosts multiple mining districts that are present in Georgia, Armenia, Azerbaijan and Iran. Two main metallogenic epochs are identified based on geochronological data of mineral deposits (Kekelia et al. 2004; Melkonyan and Akopyan 2006; Babazadeh et al., 2007; Moon et al., 2001, Mortiz et al., 2012, Moritz et al., 2013) (Figure 2.3): 1) the Middle Jurassic to Lower Cretaceous epoch is related to the long-lasting Jurassic-Cretaceous subduction of the Neotethys oceanic crust beneath the Eurasian margin; and 2) the Oligocene to the Late Miocene event associated with accretion of the SAB with the Eurasian Margin. The Mesozoic mineralization can be sub-divided into: (i) Middle Jurassic Au-Cu porphyry deposits;

(ii) Middle to Upper Jurassic Cu, and barite-bearing polymetallic deposits; (iii) Upper Jurassic Fe skarn deposits; and (iv) Lower Cretaceous porphyry Cu deposits. The Cenozoic mineralization can be subdivided into: (i) Late Oligocene to Early Miocene Cu-Mo and Cu-Au porphyry deposits; and (ii) epithermal Cu-Au mineralization (Jamali and Mehrabi, 2014). Cenozoic mineralization resulted from Eocene back-arc magmatism in the Adjara-Trialeti belt and collision magmatism of the Zangezur-Ordubad region (Moritz et al., 2015).

Mesozoic deposits include; the Teghout Cu deposit within the Alaverdi deposit (Amiryan et al., 1987; Melkonyan and Akopyan, 2006); the Gedabek, Chovdar and Gosha epithermal and Cu-Au porphyry districts in Western Azerbaijan (Babazadeh

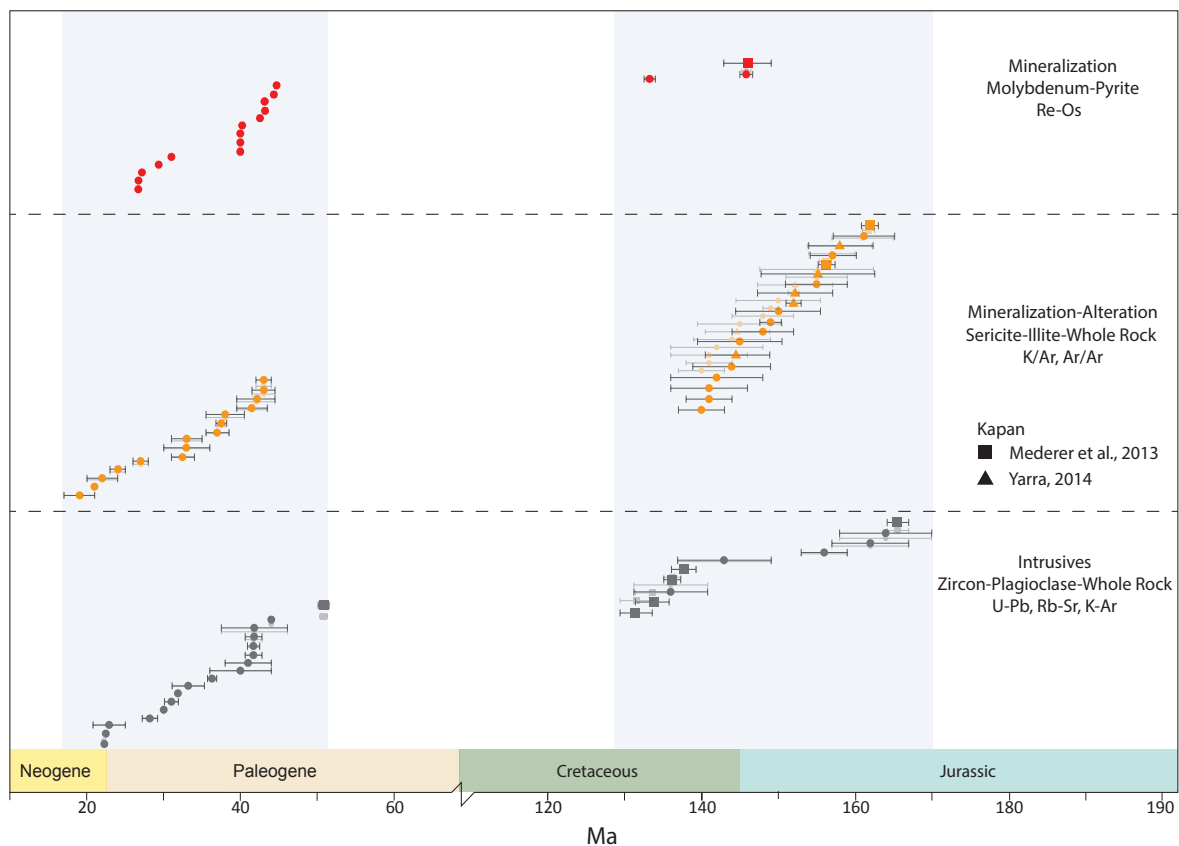


Figure 2.3: Magmatic, hydrothermal alteration and mineralization ages of the Lesser Caucasus. Two main metallogenic events are identified: one between 170-130mya and another between 50-18mya. Data from: Moritz et al., 2015; Melkonian et al., 2014; Mederer et al 2013; Hovakimyan and Tayan, 2008; Zohrabyan, 2005; Babazadeh et al., 1990; Karamyan, 1962; Karamyan, 1978; Pijyan, 1975; Mkrtchyan et al., 1969; Movsesyan and Isaenko, 1974; Karamyan, 1978; Amiryan, 1984; Achik-giozian et al., 1987.

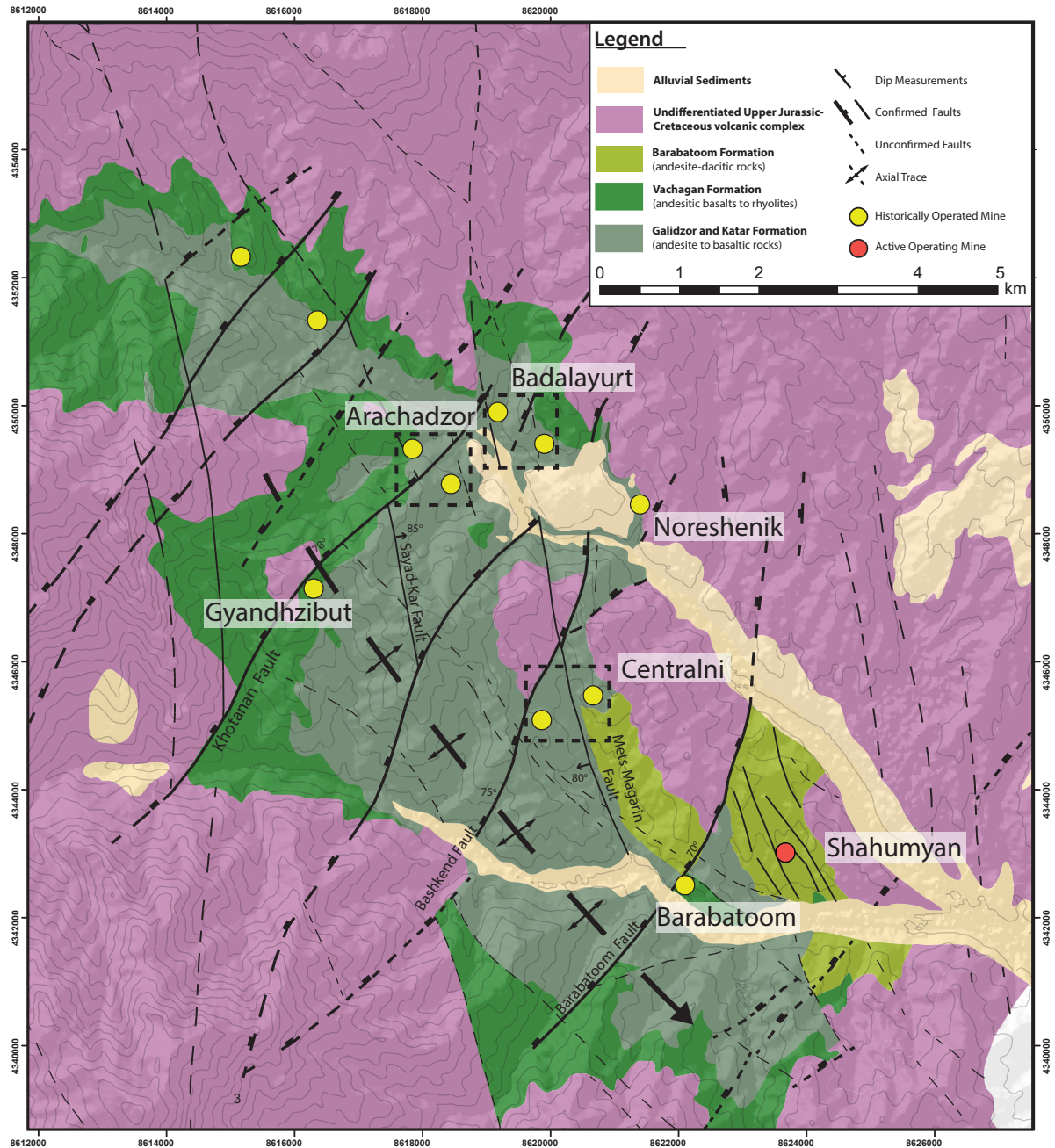


Figure 2.4: A geologic map of the Kapan district within the Kapan Volcanic Zone. Shahumyan is the only operating mine within the district. Centralni and Barabatoom have been previously exploited for Cu and polymetallic ore (Au, Cu, Zn, Pb), respectively. Arachadzor-Badalayurt and Noreshenik have been operated at a smaller scale with several producing and exploratory drifts. Gyandzhibut and Antarashat are long standing prospects, identified but never fully explored. The map is compiled from numerous soviet maps, and ground-truthed during present study. Compiled from: Schmidt et al., 1985; Achikigiozyan et al., 1987.

et al., 1990 and Hemon et al., 2012); the Shikahogh Cu-Au-Mo porphyry deposit, 20 km south of the Kapan district (Achikigiozyan et al., 1987); the Madneulli Au-Cu-

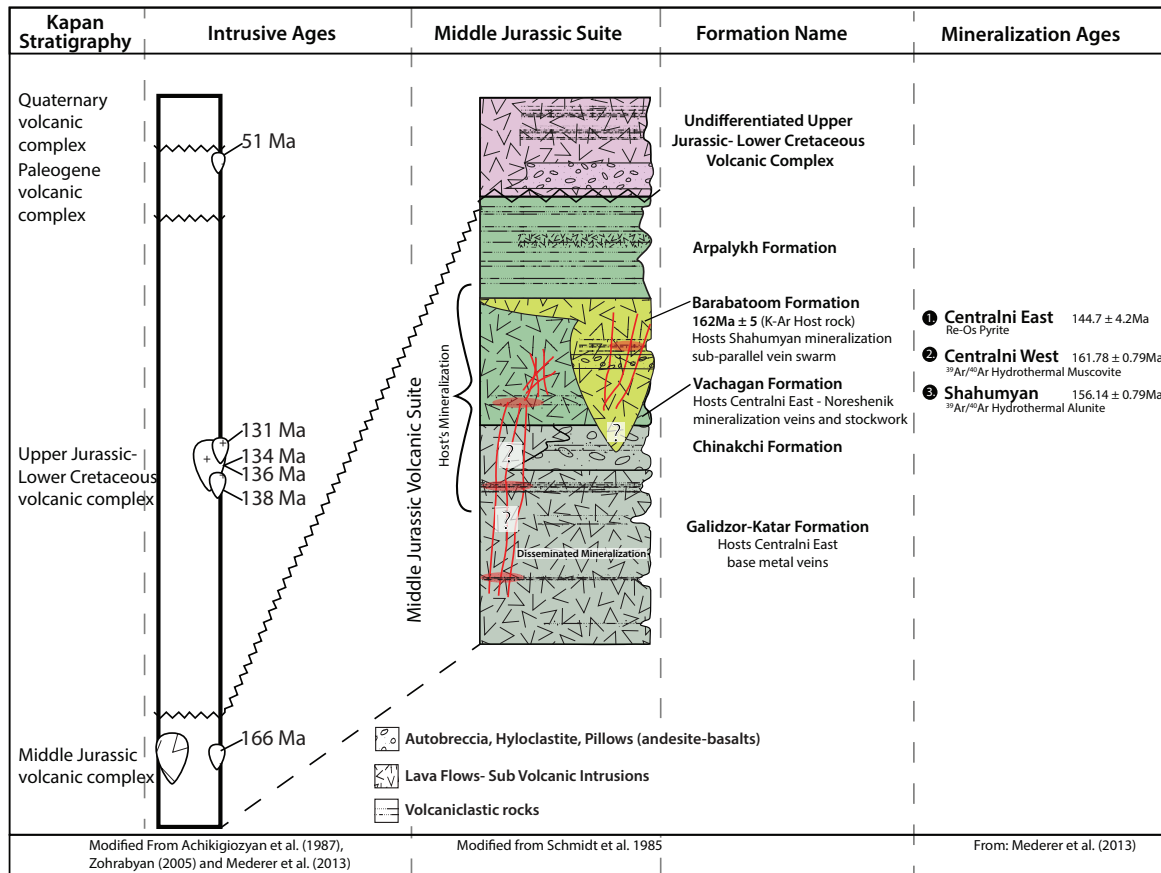


Figure 2.5: A simplified stratigraphic section based on the district geology map (Figure 2.4). Compiled from: Schmidt et al., 1985; Achikigiozyan et al., 1987; Zohrabyan, 2005, Mederer et al., 2013.

Zn-Pb VMS- epithermal-porphyry district in Georgia (Gialli et al., 2012; Mortiz et al., 2012); the Au-Cu-Zn-Pb Mehmana epithermal-porphyry district (Vardanyan, 2011; Vardanyan, 2008); polymetallic vein Toukhmanuk deposit and the high sulphidation and polymetallic intermediate-sulphidation deposits of the Kapan district (Mederer et al., 2013).

Eocene back-arc magmatism in the Adjara-Trialeti belt comprises epithermal deposits in the Zod district (Konstantinov et al., 2010; Kozerenko, 2004); the polymetallic Megradzor deposit (Amiryan and Karapetyan, 1965; Kovalenker et al., 1990); and the recently discovered high-sulphidation Amulsar deposit (www.lydianinternational.co.uk). A major ore-deposit cluster of the Zangezour-Ordubad region formed during

the Cenozoic following the collision of the SAB with Eurasia (Moritz et al., 2015). Cu-Mo porphyry prospects and deposits such as the Kadjaran and Agarak Cu-Mo-Au porphyry districts (Karamyan, 1978; Mkrtchian, 1969) are hosted by the Meghri and Bargushat plutons (Moritz et al., 2015). Associated epithermal deposits of lesser economic interest are hosted by volcanic and plutonic rocks (Amiryan, 1984; Babazadeh et al., 1990).

Moritz et al. (2015) identify the Cenozoic porphyry deposits of the Zangezur-Ordubad region to be significantly enriched in Mo with respect to the older Upper Jurassic-Lower Cretaceous porphyry deposits hosted within the SKVZ. Prior Re-Os molybdenite dating by Mortiz et al. (2013) reveal two main porphyry events within the Zangezur-Ordubad region; the first in the Eocene and the second in the Late Oligocene. The Zangezur-Ordubad porphyry cluster is believed to extend into the Alborz/Arasbaran and Urumieh-Dokhtar/Kerman belts which include epithermal prospects and related Cu-Mo porphyry deposits such as the Sungun deposit (Calagari, 2003 and Calagari 2004), Saunajil (Hosseinzadeh et al., 2008), Haftcheshmeh (Hassanpour et al., 2011) and Masjed-Daghi (Akbarpour, 2005) porphyry Cu-Au-Mo deposits (Jamali et al., 2010, Aghazadeh et al., 2015, Hassanpour et al., 2015 and Simmons and Moazzen, 2015; Moritz et al., 2015).

2.2 Geology of the Kapan District

The Kapan district is located in the Syunik province of southern Armenia (Figure 2.4). The district is 15 by 12 km and consists of multiple vein deposits mined intermittently since the 1800's by French expats and then the Soviet Union from the 1960's to 1990's and most recently by Armenian and Canadian companies. Geologically the Kapan district is within the KVZ and has similar geologic and structural characteristics. Stratigraphy of the KVZ (Figure 2.5) closely correlates to the SKVZ and can similarly be split similarly into the Middle Jurassic, Upper Jurassic-Lower Cretaceous and Pa-

leogene volcano-magmatic complexes which are overlain unconformably by Quaternary basenite flows (Mederer et al., 2013) .

2.2.1 Cenozoic-Paleogene Complex

The Paleogene magmatic complex dominates the western part of the Kapan district and unconformably overlays the Upper Jurassic-Lower Cretaceous complex. The Paleogene magmatic complex is composed of andesitic to rhyolitic lava flows and breccia flows in the lower portion and with volcanoclastics interlayered with dirty limestone lenses dominate the upper portion (Mederer et al., 2013) which unconformably overlay the Upper Jurassic-Lower Cretaceous rocks.

Intrusive rocks within Paleogene complex consist of green-gray gabbro and gabbro to diorite dikes. Green-gray gabbro is very fine grained with an ophitic porphyritic texture and is composed of plagioclase, pyroxene, hornblende and trace olivine. The gabbro dikes are highly magnetic and have chilled margins and occasionally contain millimeter-sized carbonate veins and calcite amygdules. Green-gray gabbro dikes are observed throughout the district. They are typically north to northeast-trending and reflect existing fault-vein architecture. Mederer et al. (2013) dated a pyroxene-hornblende gabbro intrusive stock from the Mt Khustup region, approximately 10 km southeast of Shahumyan to 50.82 ± 0.51 Ma, which may correlate with gabbro dikes within the Kapan district. Black-white diorite dikes have a peppered appearance and unlike the gabbroic dikes are not magnetic and are uncommon within the district. They have a fine to medium grained granular texture composed of plagioclase, pyroxene, quartz, and minor mica.

2.2.2 Upper Jurassic to Lower Cretaceous Complex

The Upper Jurassic to Lower Cretaceous complex comprises of Upper Oxford-

ian to Lower Aptian lava flows (~163-125Ma), and volcanoclastic layers of basaltic to andesitic composition which unconformably cover the Middle Jurassic rocks (Achikigiozian et al., 1987; Zohrabyan, 2005). Volcanic rocks within the complex are relatively fresh with little to no hydrothermal alteration, and are easy to differentiate from the Middle Jurassic rocks within the Kapan district (Figure 2.2.3A-B).

Upper Jurassic to Lower Cretaceous intrusive rocks are not observed within the Kapan district; however, the Tsavski intrusive stock outcrops in the southern part of the Kapan Volcanic Zone. Its multiple phases are dated to the Lower Cretaceous (138-131Ma) (Mederer et al., 2013). The Tsavski stock is characterized as a hornblende-biotite granodiorite and biotite-hornblende monzodiorite (Mederer et al., 2013), and is approximately 7-10km south of the Kapan district.

2.2.3 Middle Jurassic Complex

The Middle Jurassic complex is comprised of Bajocian to Bathonian lava flows, flow breccias, hyaloclastites, and volcanoclastics of basaltic to rhyolitic but dominantly andesitic in composition (Akopyan, 1962; Cholahyan et al., 1972; Mederer et al., 2013; Mederer et al., 2014). Interbedded fossil bearing calcareous sedimentary and volcanoclastic rocks confirm an early Bajocian to Callovian age (170.3 ± 1.4 to 163.5 ± 1.0) (Aslanian, 1958; Hakobyan 1962; Azaryan, 1978; Avanesyan et al., 1990; Avanesyan et al., 1992). Sub-volcanic and sub-aerial quartz-dacite units such as the Barabatom formation yield a 162 ± 5 Ma K-Ar age (Sarkisyan, 1970; Zhorbyan, 1975 and 2005). The Middle Jurassic complex is further sub-divided by Soviet geologists based on bulk composition into the: Galidzor-Katar, Chinakchi, Vachagan, and Barabatom formations. It is difficult to identify the contacts between these formations as they compositionally grade into one another (Figure 2.7 C-F).

The Galidzor-Katar formation is characterized by lava flows, lava breccias and

interlayered tuff members of basaltic composition. Coherent flows within the formation are characterized by subhedral plagioclase, hornblende phenocrysts and rounded quartz phenocrysts within an aphanitic matrix, consisting of plagioclase microliths, and microcrystalline quartz and hornblende. Rocks from this formation also contain minor disseminated sulphide alteration (pyrite). The Galidzor-Katar formation is the lowermost formation within the Middle Jurassic complex in the Kapan district with an approximate thickness of 600m (Achikgiozian et al., 1987: Soviet Mapping).

The Chinakchi formation is characterized by volcanoclastic deposits which include tuff and tuff breccias of rhyolitic to dacitic compositions. This formation has been described by Soviet geologists as quite discontinuous within the region with varying thickness 0-90m (Achikgiozian et al., 1987: Soviet Mapping).

The Vachagan formation is characterized by volcanic flows, lava breccias and interbedded volcanoclastics of basaltic-andesite composition. Coherent flows within the formation are characterized by anhedral plagioclase phenocrysts of varying amount (up to 10 vol%) have a glomeroporphyritic textures within an aphanitic matrix consisting of microliths of plagioclase and microcrystalline quartz and hornblende; anhedral hornblende phenocrysts are also present, but rare. The Vachagan formation is approximately 300m thick within the Kapan district (Achikgiozian et al., 1987: Soviet Mapping). Alteration minerals within these rocks primarily consist epidote and chlorite imparting the rocks a greenish hue. Argillic alteration is present locally and consists of white mica minerals replacing plagioclase.

The Barabatom formation is characterized by volcanic flows, sub-volcanic intrusions and interlayered volcanoclastics of quartz-rich andesites. The formation is largely interpreted as a sub-volcanic dome intruded into the Vachagan and Galidzor-Katar formations (Achikgiozian et al., 1987). However, subaerial volcanic flows are also observed at Shahumyan, south of the Centralni deposits and in the Gyan-

gibite exploration area. This formation is unique in that it contains large euhedral bipyramidal quartz phenocrysts ranging up to 15% by volume. In addition, the unit contains varying amounts sizes of plagioclase and hornblende phenocrysts. Crystal morphology of the bi-pyramidal quartz phenocrysts range from euhedral to rounded, suggesting resorption of crystals due to the quartz being in disequilibrium with the surrounding magma. Plagioclase and hornblende phenocryst abundance ratio varies, with some areas having a higher amount of hornblende whereas others, plagioclase. Plagioclase and hornblende phenocryst size varies between 0.50 - 2 cm, and are generally euhedral when not altered. Bi-pyramidal quartz phenocrysts indicate a source magma that formed at depth ~ 3 GPa where bi-pyramidal β -quartz is most stable. With magma ascent, β -quartz is unstable and will recrystallize to form α -quartz, but retain the β -quartz crystal form.

Intrusive rocks associated with the Middle Jurassic magmatic complex were not identified in the study area. However, Achikgiozryan et al. (1987) identified a gabbro-diorite intrusion during a drilling campaign south of the town of Kapan. Furthermore, recent fieldwork by Mederer et al. (2013) identified a sub-vertical polymict pebble dike containing rounded clasts of biotite bearing equigranular tonalite with a proposed average age of 165.6 ± 1.4 Ma ($n=11$). Mederer et al. (2013) suggests a tonalitic intrusive body to be present at depth, as a source to tonalite within the pebble dike.

2.3 Lithogeochemistry of Middle Jurassic Volcanic rocks

Sixty samples of drillcore and outcrop samples were analysed for whole rock geochemistry, of which nineteen were determined to be least altered and are used to classify the Middle Jurassic Complex geochemically. From the nineteen samples, eight samples are from the Barabatoom formation, seven samples from the Vachagan formation and four samples from the Galidzor-Katar formation. Samples from the

Chinakchi formation were too weathered/altered to justify for whole rock geochemistry analyses. Supplementary data of samples from the Middle Jurassic complex are used (e.g. Mederer et al., 2013 and Galoyan et al., 2009) for comparison. Major elements data were recalculated on an anhydrous basis, and plotted in Figure 2.3.1A. Using the volcanic TAS classification diagram of LeMaitre (1992), the Galidzor-Katar formation samples plot in the basaltic andesite, andesite and dacite fields, the Vachagan formation rocks plot in the dacites and rhyolites fields and the Barabatoom formation rocks are primarily classified as dacite with some samples falling within the andesite and rhyolite field. Fluid mobile elements such as large ion lithophile elements (LILE) may be redistributed and mobilized during hydrothermal alteration, our classifications and interpretations are largely based on high field strength elements (HFSE) and rare earth elements (REE), which are less affected by hydrothermal fluids (Rollinson, 1993). Pearce (1996) and Winchester and Floyd (1977) are used to successfully classify rocks more accurately.

The Pearce (1996) trace element classification diagram (Figure 2.6 B) is used to cross-check the classifications made using the LeMaitre (1989) TAS major element diagram of the Middle Jurassic Volcanic rocks. The Galidzor-Katar volcanics plot within the basalt field, the Vachagan volcanics plots in the andesite/basaltic-andesite to rhyolite-dacite fields and the Barabatoom volcanics plot in the basalt and andesite/basaltic-andesite fields. Both classification diagrams reveal similar trends; where the Galidzor-Katar formation is mafic, the Vachagan formation is felsic and the Barabatoom formation is of intermediate composition to the two other formations.

Trace element data is normalized and plotted on multi-element diagrams for petrogenetic interpretation. C1 chondrite-normalized rare earth multi-element plots of Middle Jurassic volcanic and intrusive rocks are shown in Figures 2.3.2 (A-D). All rocks within the Middle Jurassic volcanics have relatively flat REE patterns in the C1

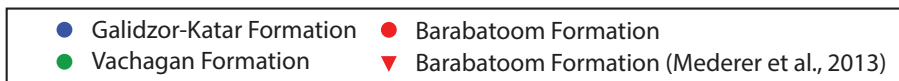
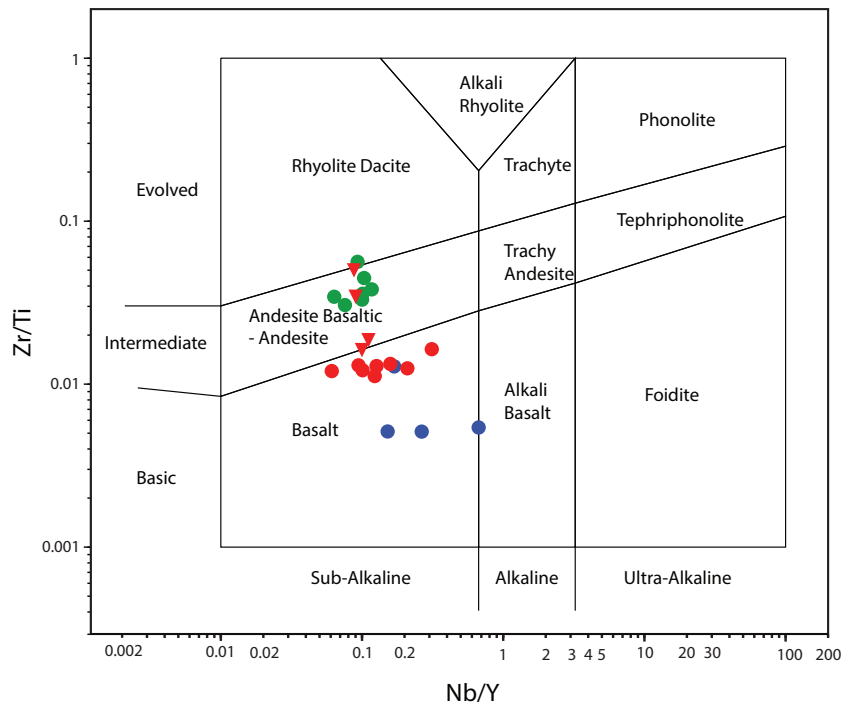
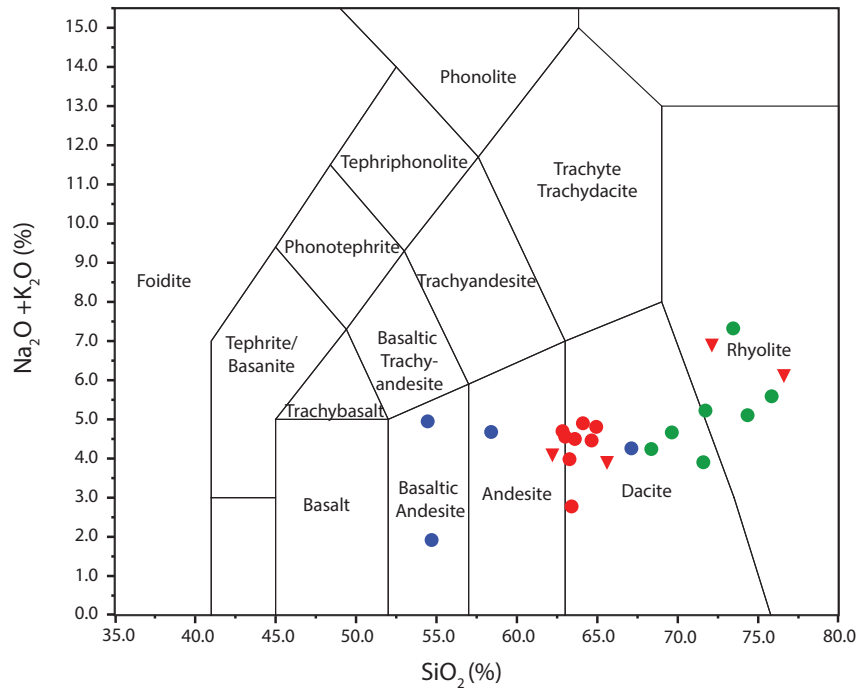


Figure 2.6 A-B: Major and trace element diagram of Middle Jurassic volcanic units. Mederer et al., 2013 whole-rock and trace element data is used as a comparison with dataset produced in present study. Least altered samples are used for classifying volcanic rocks to avoid metasomatic effects. (A) SiO_2 (%) vs $\text{Na}_2\text{O} + \text{K}_2\text{O}$ (%) graph classify Middle Jurassic volcanic rocks as basaltic andesite to rhyolite in composition. TAS classification diagram by LeMaitre (1992); (B) Zr/Ti vs Nb/Y graph classify Middle Jurassic volcanic rocks as basalt to rhyolite dacite (Pearce, 1996).

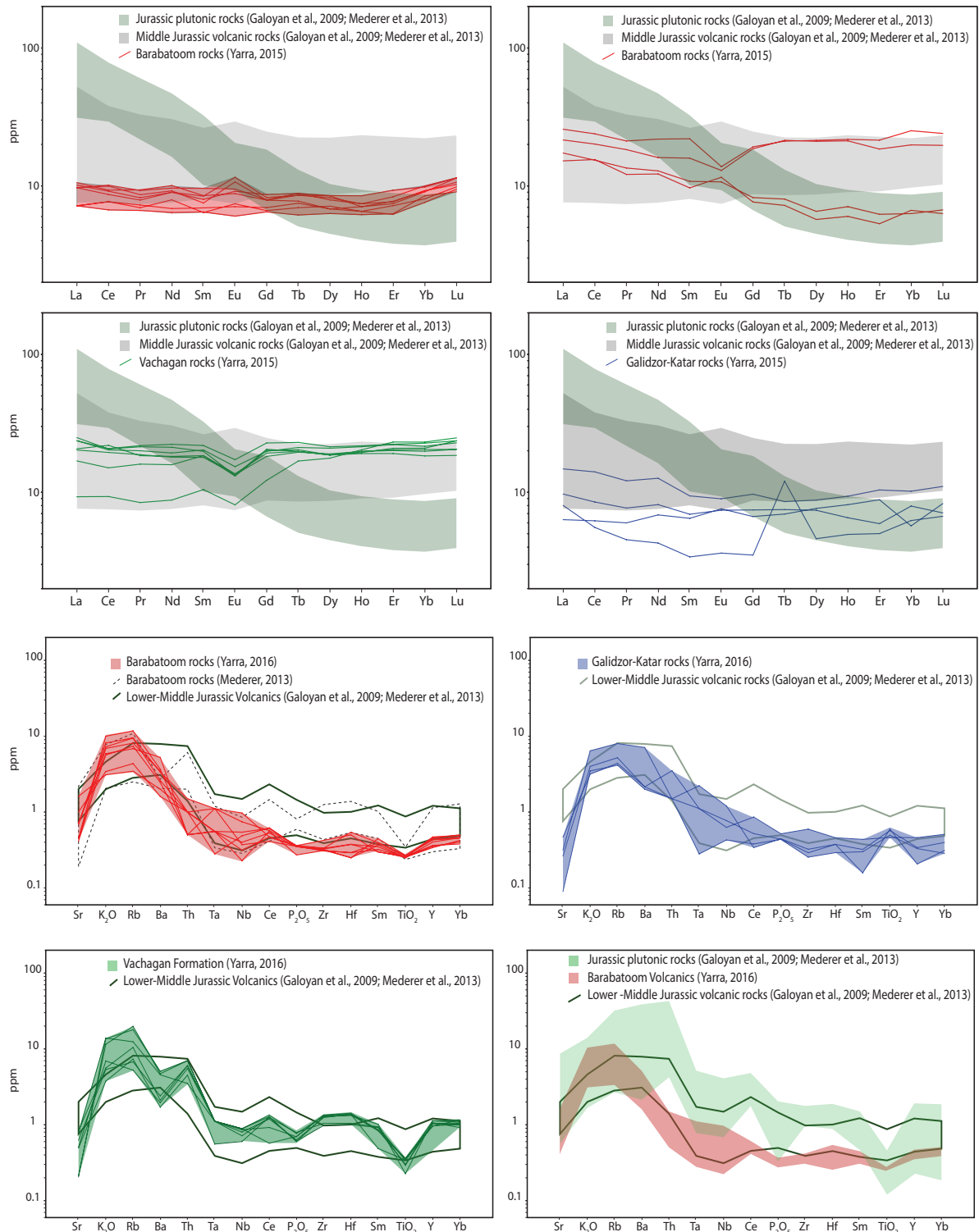


Figure 2.7(A-H) C1 chondrite-normalized rare-earth element plots comparing Middle Jurassic volcanic rocks and Middle to Upper Jurassic intrusive rocks. (E-H) N-MORB normalized trace element spider diagram comparing Middle Jurassic volcanic rocks and Middle to Upper Jurassic intrusive rocks. This study's is compared with data from Mederer et al., 2013, and Galoian et al., 2013. C1 Chondrite and N-MORB values taken from Sun and McDonough (1989).

chondrite normalized diagram. Mederer et al. (2013) observed that rhyolite and tonalite samples have negative Eu anomalies whereas andesite, dacite and basalt samples have positive Eu anomalies. The Galidzor-Katar formation rocks contain no Eu anomalies, except for sample DCC_S004 which has a Tb anomaly. The Tb anomaly is interpreted as an analytical anomaly because Tb does not naturally vary significantly from other HREE's. The Vachagan formation has a negative Eu anomaly and the Barabatom formation generally has a positive Eu anomaly with minor enrichment in HREE's (Yb and Lu). The absence of an Eu anomaly can be explained either by minimal plagioclase crystal fractionation during ascent of magma which would be expected from a hydrous magma and/or by an elevated oxygen fugacity in the magma which would lead to more Eu^{3+} than Eu^{2+} and result in less Eu^{2+} substitution for Ca in plagioclase (Hanson, 1980). The negative Eu anomaly is indicative of early plagioclase fractional crystallization as Eu^{2+} substitutes for Ca into plagioclase (Hanson, 1980). The positive Eu anomaly in the Barabatom formation and the negative Eu anomaly of the Vachagan formation likely indicates the two formations are genetically related, this signature can be produced with plagioclase loss and accumulation through fractional crystallization, respectively.

N-MORB normalized plots of Middle Jurassic volcanics are shown in Figures 2.3.2 (E-H). All samples from the Middle Jurassic complex have characteristics which are typical for subduction-related environments such as negative Nb and Ta anomalies and enrichment in LIL fluid mobile elements such as K, Rb or Ba relative to N-MORB. Incompatible elements such as Hf and Zr are relatively more enriched within the Vachagan formation than the Barabatom or Galidzor-Katar rocks. Vachagan and Barabatom rocks have a negative Ti anomaly and a positive Ti anomaly in the Galidzor-Katar rocks, indicating it is enriched in Galidzor-Katar rocks. Middle to Upper Jurassic intrusive rock analyses (data from Galoyan et al., 2009 and Mederer et al., 2013) have similar trends to the Vachagan formation; however, all elements are rela-

tively more enriched within the intrusive rocks compared to the volcanics.

2.4 Structural Trends, Kapan District

Major faults within the Kapan district (Figure 2.8) are long lived faults that have episodically reactivated since their formation, evidenced by large damage zones (5-20m) adjacent to these faults. These major faults trend north and northeast and will herein be referred to as Fault Set 1 (F1) and Fault Set 2 (F2), respectively.

F1 faults are north trending oblique faults. Some examples of these faults are the Metz-Magarin and Sayad-Kar faults. The Metz-Magarin is a major fault running through the center of the Centralni area separating it into Centralni East and West deposits. It intersects the Bashkend fault in the north, and previous studies have it mapped to intersect the Barabatoom fault in the south. The Metz-Magarin fault has a damage zone varying between 10-30 m in thickness at surface and up to 70 m at depth. It strikes north and is generally sub vertical with a variable dip between 65-90° to the west. Soviet literature indicates a normal offset by approximately 150-300m. The Sayad-Kar fault has a 20m thick damage zone and dips 60-75° towards the east, Soviet literature indicates a normal offset ranging between 10m to 100m calculated based on offset volcanic layers.

F2 faults are northeast trending normal faults that predominantly dip 55-85° to the northwest. Examples of these major northeast faults include the Khotanan, Bashkend and Barabatoom faults. The Khotanan fault is situated north of Arachadzor steeply dips northwest (70- 80°), Soviet geologists indicate a normal offset of approximately 300m. The fault damage zone varies between 5-15m. The Bashkend fault is situated north of Centralni has a 30-40m damage zone and strikes northeast and dips 70-80° to the northwest with an interpreted normal offset of approximately 150m. The Barabatoom fault is located northwest of Shahumyan and strikes northeast and dips

60-70° towards the northwest with a vertical offset of 400-500m.

In addition to F1 and F2 sets, a smaller southeast and east striking oblique F3 faults (normal-dextral faults) are observed locally. F3 faults are smaller than F1 and F2 sets and vary from 5m up to 50m in length and 5cm to 3m in width, and variably dip (65-85°) south to southwest. The dextral component of F3 is interpreted based on limited kinematic indicators and might therefore not represent the original phase of movement. Kinematic indicators when present, are interpreted based on slickenlines (chlorite, clay) and slickensides (calcite).

2.4.1 Folding and Bedding Trends

Volcanic and volcanoclastic rocks within the Kapan district have tilted due to regional and district scale folding. Bedding is best preserved within the volcano-sedimentary members and their contact with volcanic flows within the Kapan region. Bedding measurements were discriminated into three separate domains (Figure 2.8). Domain 1 dips approximately 20-30° to the NE; domain 2 dipping at approximately 20-30° to the southwest; and domain 3 with bedding measurements dipping approximately 30-40° to the SE. The resulting architecture reveals a broad antiform with a southwest trending hinge.

Previous structural studies (e.g Davis, 2006; and Wood et al., 2007) propose, large-scale folding to be a D1 event, that occurred before the formation of Fault Set 2. However, bedding measurements of volcanics and volcanoclastic rocks of Upper Jurassic-Lower Cretaceous and Paleogene complexes have similar bedding trends to measurements within the Middle Jurassic complex indicating that folding likely occurred after the deposition of the Upper Jurassic-Lower Cretaceous and Paleogene complexes. Furthermore, the folding event would have incorporated after the emplacement of southeast to east striking faults and mineralized veins (F3 faults) which

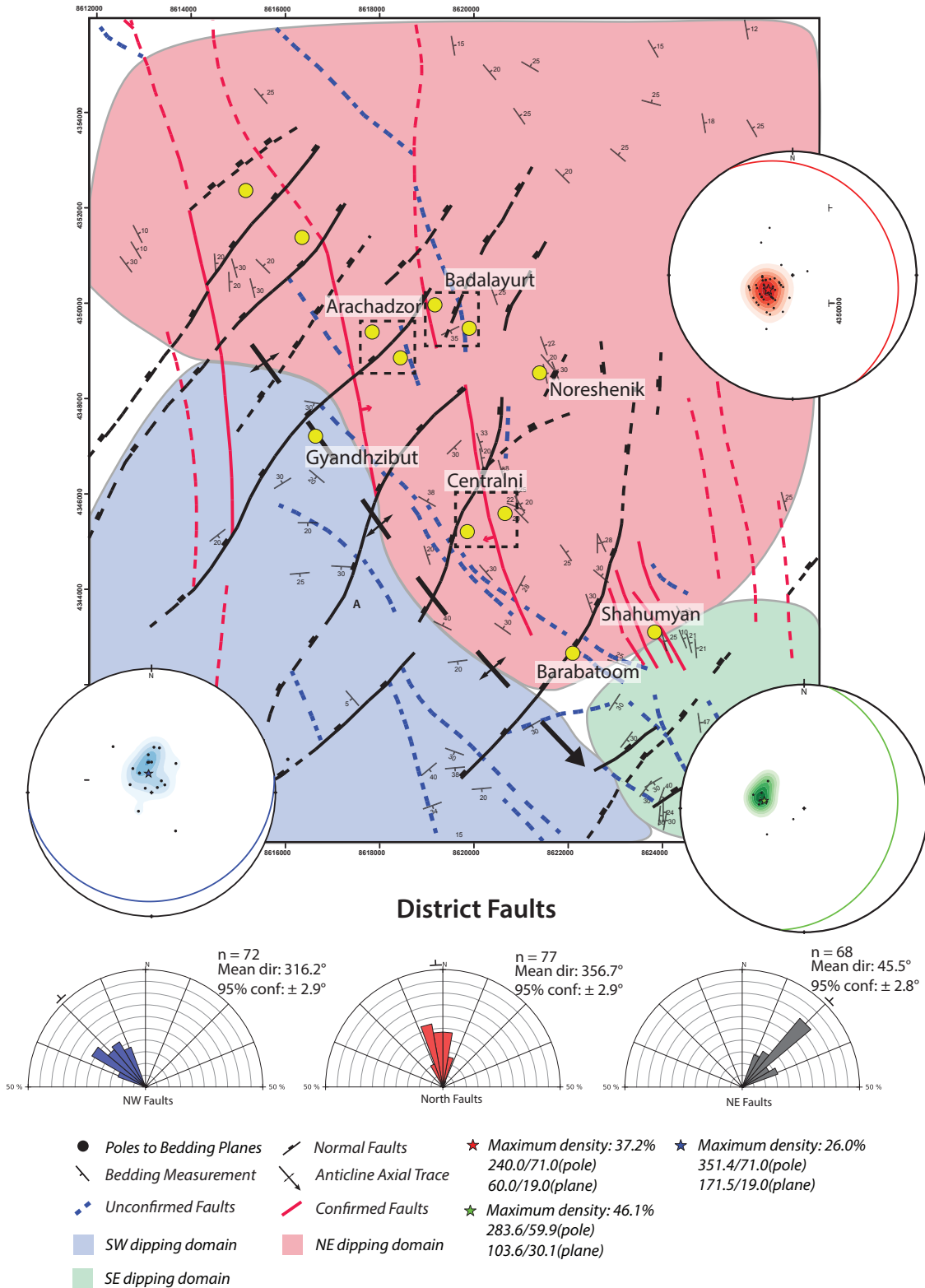


Figure 2.8: Bedding and structural trends within the Kapan District. Three bedding domains are observed: a northeast dipping domain (red); a southwest dipping domain (blue); and a southeast dipping domain (green). This bedding architecture results in a gentle fold with a southeast trending axial hinge. Major faults compiled from historic datasets reveal three main trends: northwest, north and northeast trending faults, only some faults have been ground-truthed.

were dated to Middle-Upper Jurassic (161.78 ± 0.79 to 156.14 ± 0.79 Ma; Mederer et al., 2013).

The Kapan antiform is much younger and can be correlated to regional scale folds within the Lesser Caucasus and Trans Caucasus because of regional deformation during the collision and obduction of the SAB with the Eurasian plate in the Paleocene (Sosson et al., 2010). Sosson et al. (2010), Saintot et al., bracket the folding event in the Lesser Caucasus between the Eocene to Miocene. The Kapan antiform is likely a part of the larger mega-anticlinorium that trends northwest to north within the Lesser Caucasus.

2.5 Mineralized Veins within the Kapan District

Mineralization within the Kapan district is characterized by vein stockworks and narrow (10cm to 2m) subparallel vein clusters. The district has been continuously exploited since the 1800's from surface workings and more advanced underground drift workings in recent times (Table 2.1). Veins within the district trend northeast to east and northwest, and dip steeply to the north and south (Figure 2.9). The district has been known for its Cu rich veins at Centalni, Barabatom, Arachadzor-Badalayurt and Gyangibute; however, Noreshenik and Shahumyan are better known for their polymetallic (Cu, Zn, Pb, Au, Ag) ore. Metal zonation within the district is generally Cu rich in the west, changing progressively to higher Zn,Pb, Au, Ag to the south and southeast (Mederer et al., 2013)

2.5.1 Centralni

The Centralni vein system comprises the East and West deposits; Centralni East was an open pit operation and is characterized by stockwork veining; Centralni West was an underground operation characterized by subparallel east-west vein sets

Deposit	Mineralization Type	Previous Work	Mined Resource	Vein Minerals	Mineralization Type
Noreshenik-Badalayurt	Cu-rich Polymetallic veins	8 Adits->100 DDH- 30,000 m	110,565 t @ 0.87% Cu (4 veins)	Py,Cpy,Sph,Ga	Veins
Arajadzor	Cu,Polymetallic	2 Adits, 30DDH - >10,000 m	656,786 t @ 3.6% Cu (4 Zones)	Py,Cpy,(Bo,En?)	West: Veins; East: Veins and dissemination
Centralni	Cu, Anamolous Au	Very Extensive (UG +Surface)	~27.8Mt @ 1.23% Cu	Py,Cpy,Cc,Bo,En	Veins, stockwork, dissemination
Barabatoom	Cu, Polymetallic	Very Extensive (UG +Surface)	Missing	Py,Cpy,Sph,Ga	Veins and dissemination
Antarashat	Cu, Polymetallic, ± Mo	30DDH- >12,000m	Prospect	Py,Cpy,Sph,Ga	Veins and dissemination
Dzorastan-Gyandzhibut	Cu, Anamolous Mo	1 adit, 5DDH- 1,900m	Prospect	Py,Cpy,Mo	Dissemination and veinlets

Table 2.2: Known historical exploration and mining within the Kapan District. References (N K Kurbanov & Schmidt, 1985 Achikgiozyan et al., 1987- Map)

similar to Shahumyan. Centralni East and West are separated by the north-trending Mets-Magarin oblique (normal) fault dipping 70-80° to the west.

Centralni West veins strike east-west and steeply dip 60°-80° to the south. Locally, mineralization is observed to replace porous and permeable volcanoclastic layers (Mederer et al., 2013). Mederer et al. (2013) has described vein textures to be variable, from hydraulic breccia textures with fragmented sulphides to massive sulphide zones within veins. The main economic minerals at Centralni West consist of chalcopyrite and pyrite with minor amounts of sphalerite, tennantite-tetrahedrite and galena within a quartz rich gangue (Mederer et al., 2013). Trace quantities of tellurobismuthite, hessite, petzite, tetradymite, wittchenite, emplectite and native gold are also reported by Achikigiozyan et al. (1987) and Khachatryan (1958). Vein thicknesses varied from minor veinlets (<1cm) to 1m thick veins. Alteration at Centralni West consists of host rocks altered to sericite, chlorite, carbonate and epidote (Mederer et al., 2013). Ar/Ar dating of hydrothermal muscovite/sericite from Centralni West (Mederer et al., 2013) yielded a mineralization age of 161.78 ± 0.79 Ma.

Centralni East is primarily characterized by stockwork veining at surface and sub-parallel veins similar in architecture to Centralni West dominate at depth. Textures found within veins include: crustiform, colloform, hydraulic breccia and comb quartz textures. Primary sulphide assemblage at Centralni East includes chalcopyrite, pyrite, colusite, tennantite-tetrahedrite, galena and specular hematite. Trace minerals found

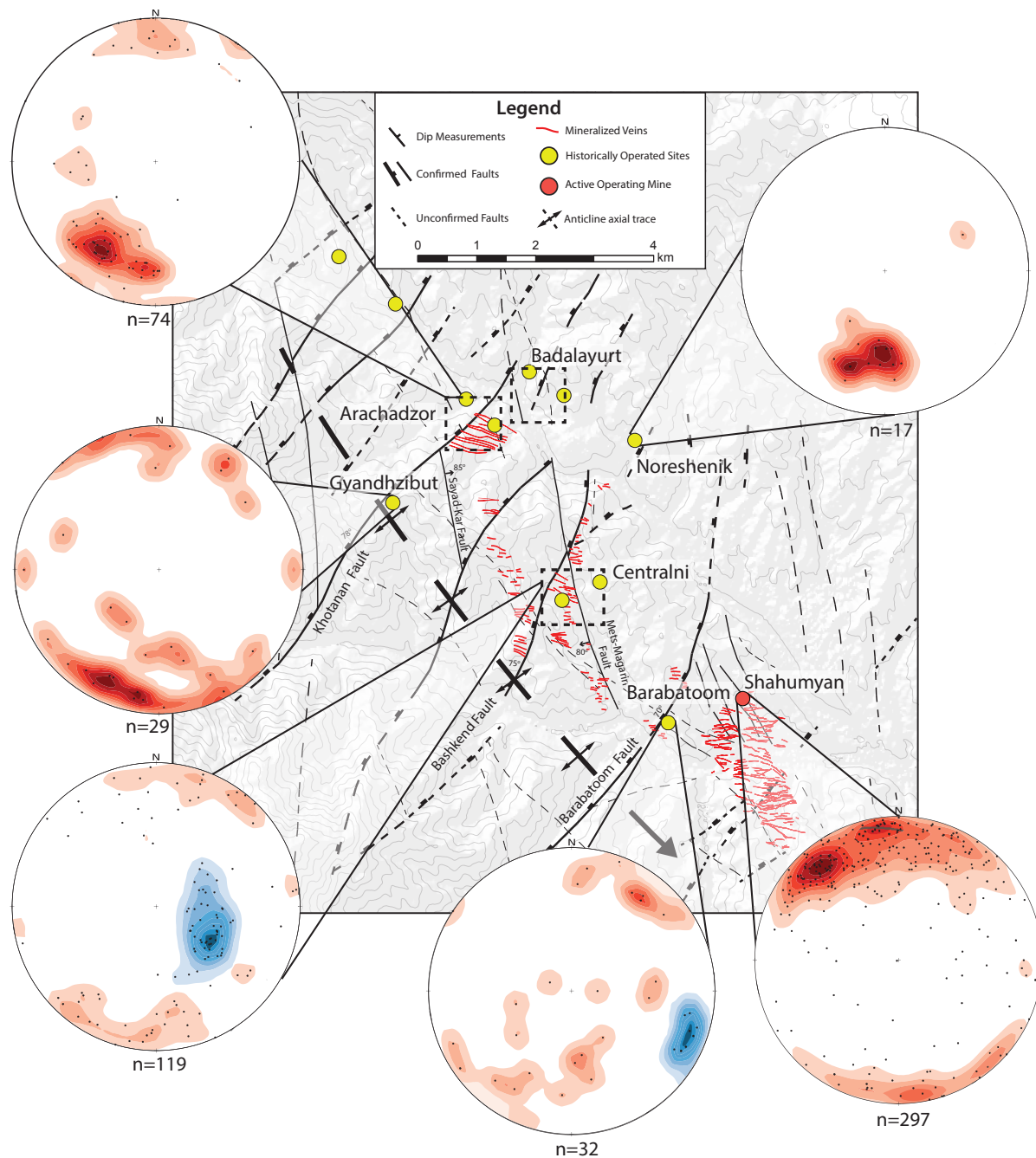


Figure 2.9: Orientation data of mineralized veins within the Kapan district, displayed on an equal area Schmidt net. Bedding domains are also plotted on each stereonet: red for the northeast dipping domain and blue for the southwest dipping domain. The dashed line represents the axial trace of the anticline. It should be noted that vein data is not restored to horizontal based on bedding trends.

at Centralni East include enargite, bornite, sphalerite, covellite, renierite, germanite and native gold (Beaumont, 2006; Khachatryan; 1958). Gangue minerals found within veins include quartz, with barite and gypsum present locally. Stockwork vein thicknesses vary between 2cm to 25cm, larger veins are uncommon but veins can be up

to 50cm thick. Sericite, dickite-kaolinite, diaspora characterize alteration minerals at Centralni East (Khachatryan, 1958) residual quartz is also observed.

2.5.2 Noreshenik

The Middle Jurassic volcanoclastics around the Noreshenik area dip approximately 20-30° to the northeast. Upper Jurassic rocks and Quaternary basalts lie unconformably over altered Middle Jurassic rocks. Mineralized Noreshenik veins are located north of Shahumyan and east of Arachadzor and are hosted within Middle Jurassic andesites. A minor offshoot/splay of the Bashkend fault cuts through the vein system and strikes northeast and steeply dips to the north to northwest (75-80°). Mineralized veins at Noreshenik trend northwest and dip steeply to the North (60-75°). Major vein minerals at Noreshenik include chalcopyrite, pyrite, sphalerite with quartz, and calcite as the main gangue mineral. Vein thicknesses varied from small veinlets (1cm) to larger veins (0.50-1m). Alteration of country rocks consisted of sericite/illite, chlorite and epidote. K-Ar dating of hydrothermal illite yielded an age of 158 ± 4.2 Ma (This Study, Yarra, 2015). Several veins at Noreshenik were mined by small scale methods through several exploration and production adits present in the area. Mineralization within Noreshenik veins is considered to be highly inconsistent along strike and down-dip extents of individual veins and were considered uneconomic for further exploitation.

2.5.3 Arachadzor

Arachadzor is located 4km north of the Centralni deposit and is located near the Arachadzor village. Similar to Centralni, Arachadzor also contains both sub-parallel vein clusters and stockwork type mineralization. Subparallel veins trend west to northwest and moderately dip towards the northeast (45-70°). Major vein minerals

consist of chalcopyrite, pyrite with minor sphalerite and galena within a quartz-carbonate gangue. Vein thicknesses vary between minor <1cm veinlets to larger veins (0.5m-1m). Alteration at Arachadzor is similar to Centralni, with alteration envelopes containing: sericite, chlorite, dickite-kaolinite, epidote and residual quartz.

2.5.4 Barabtoom and Gyangibut

Barabtoom is located south of Centralni and can be seen from the Kapan town center. Local geologists have indicated Barabtoom was once an open pit mine which was subsequently infilled and used for commercial purposes. Veins at Barabtoom have two distinct trends; an east-west trend and a north-south trend which include chalcopyrite and pyrite as the primary ore minerals within a quartz rich gangue.

Gyangibute is located 4 km northwest of Centralni. Veins at Gyangibute are vertical to subvertical dipping both north and south (80-90°) and trend east to south-east. Vein thicknesses at Gyangibute vary from minor veinlets to veins (1cm to 25cm) consisting of pyrite and chalcopyrite with quartz as the main gangue.

3. Mineralization Paragenesis and Structural Evolution of the Vein System at Shahumyan

3.1 Introduction

The Shahumyan deposits is characterized by three main hydrothermal stages within a subparallel anastomosing vein cluster composed of over 120 individual mineralized veins. Shahumyan has an indicated and inferred resource of 15.87 Mt at cut off grades of 2.72 g/t Au, 48.5 g/t Ag, 0.5% Cu, 1.82% Zn and 0.1% Pb (White et al., 2015). Economic mineralization within individual veins is discontinuous and metal proportions are highly variable, confirmed by White et al. (2015). Shahumyan is a base metal rich (Cu-Zn) deposit with anomalously high Ag and Au values, particularly with high Ag:Au ratios. Vein samples have average Ag and Au ratios from 20-40 to ~1000. A closer look at high Ag:Au ratio zones in veins, reveals a second precious metal oreshoot within base metal rich veins.

Faults and joints propagate as curvilinear surfaces that have undulating or corrugated shapes. Many mineral districts have vein patterns resembling the Shahumyan vein system. For example anastomosing faults and veins in the Creede district Colorado (Stevens and Eaton, 1975); the veins of the Fresnillo district, Mexico, (Gemmell et al., 1988); Acupan vein system, Phillipines (Cooke et al., 1996). Anastomosing veins represent stress interplay between faults and are important for exploration and mining of vein-type ore deposits. Bends and other irregularities in veins have been used to predict areas of enhanced vein thickness to identify ore-shoots (Hulin, 1929; Conolly, 1936; Newhouse, 1940).

Detailed mapping of underground workings and a comprehensive paragenetic

study to identify hydrothermal stages was undertaken at Shahumyan. With the goal of unravelling the relationship between the anastomosing nature of veins and high Ag:Au ratios found at Shahumyan. This chapter also examines mineralization paragenesis of the Centralni and Noreshenik deposits providing a comparative analysis of other mineralized veins exploited within the Kapan district.

3.2 Vein Mineralogy and Textures

3.2.1 Ore Minerals

Pyrite [FeS_2] is ubiquitous within the deposit and is found in abundance both in wallrock alteration and vein assemblages. Pyrite associated with wallrock alteration replaces hornblende and pyroxene. Pyrite alteration is observed to be euhedral-subhedral and disseminated. Pyrite textures observed within veins include: sieved sub-euhedral pyrite, blebby anhedral pyrite rimming sub-euhedral sieved grains or intergrown with other sulphides. Blebby pyrite grains are most commonly found to be intergrown with chalcopyrite and sphalerite. Blebby pyrite commonly contains inclusions of chalcopyrite, sphalerite and in rare instances tellurium minerals. Rare occurrences of pyrite needles are observed, with individual crystals having high aspect ratios. The texture is likely a function of accelerated growth or unimpeded growth of pyrite. Richards (1995) suggests this texture is present in low temperature hydrothermal deposits and is found as free growing crystals within cavities. Sulphur isotope studies by Mederer et al. (2013) indicate pyrite $\delta^{34}\text{S}$ values mostly ranging from 4.9-6.4‰_{CDT}.

Chalcopyrite [CuFeS_2] is abundant within veins and accompanied by sphalerite. Blebby-anhedral crystals are intergrown with sphalerite and pyrite. Chalcopyrite can be replaced by tetrahedrite/tennantite (sulphosalts) species. Chalcopyrite exsolution (chalcopyrite disease) is common within sphalerite, occurring as sub-micron

round-elongate blebs, preferentially present along growth zones of honey brown sphalerite. Microscopic fractures containing chalcopyrite and telluride minerals cut through honey brown and yellow sphalerite. Macroscopically, chalcopyrite occurs as individual sulphide bands representative of crustiform texture alternating with sphalerite and/or quartz. Sulphur isotopes taken from Chalcopyrite grains have $\delta^{34}\text{S}$ values ranging between 3.1 and 5.1‰_{CDT} (Mederer et al. 2013).

Sphalerite [(Zn,Fe)S] is the third most abundant sulphide mineral at Shahumyan. Three generations of sphalerite are identified through petrography: dark opaque sphalerite; red to honey brown sphalerite; and light yellow sphalerite. Sphalerite crystals are anhedral-subhedral to fine grained, euhedral sphalerite is rare but present. Some sphalerite crystals contain growth bands containing alternating dark (orange-brown) and light (yellow/white- light orange) bands, boundaries of these growth bands are commonly diffused but can be sharp and distinct. Honey brown and dark opaque sphalerite preferentially contain chalcopyrite disease which is absent within yellow sphalerite. Yellow sphalerite tends to enclose honey brown sphalerite and use it as a nucleus. Studies at the Creede district by Hayba et al. (1997) indicate that these growth zones may correspond to abrupt changes in composition, temperature or salinity of hydrothermal fluids. Dark-opaque sphalerite is commonly intergrown and/or contains inclusions of telluride minerals and chalcopyrite. Dark-opaque sphalerite is chiefly found within secondary fractures present within honey brown or yellow sphalerites. Sulphur isotopes in sphalerite yield $\delta^{34}\text{S}$ values between 3.7 and 4.3‰_{CDT} (Mederer et al. 2013).

Galena [PbS] is rarely observed and does not constitute a major part of economic ore at Shahumyan. It is primarily intergrown with sphalerite and chalcopyrite. In rare occurrences sulphosalts (tetrahedrite/ tennantite) tend to replace galena along micro fractures or grain boundaries. Altaite and hessite are intergrown with galena and

in rare occurrences replace galena.

Sulphosalt species (tetrahedrite-tennantite) have been identified using the SEM in trace amounts. Sulphosalts are present as submicroscopic inclusions in chalcopyrite, sphalerite and galena. They are present as replacement rims around sphalerite and galena grains and rarely around chalcopyrite. Because of their minor abundance, their paragenetic relationship with the other minerals is unclear.

Telluride species $[(\text{Au,Ag,Bi,Pb})_x\text{Te}_y]$ have been identified using the SEM and reflected light microscopy. Tellurides are present within brecciated wallrock or as infill within fractures in sphalerite, chalcopyrite, galena and pyrite. They can also be found as inclusions in pyrite or chalcopyrite in association with yellow-sphalerite. Telluride minerals occasionally contain inclusions of brecciated crystals of pyrite, sphalerite and chalcopyrite. All tellurides species with the exception of hessite are microscopic ($<0.05\text{mm}$). Pure tellurium inclusions in sulphides were identified by Mederer et al. (2013) but not so the present study.

Hessite (Ag_2Te) is the most common telluride mineral observed. Hessite is commonly accompanied by sylvanite, petzite and in some samples coloradoite. Petzite (Ag_3AuTe_2) and sylvanite (Au,Ag-Te_2) calavarite (AuTe_2) are found along fractures in hessite or intergrown with hessite grains. They also occur by themselves as sub-micron inclusions within chalcopyrite pyrite or dark opaque sphalerite. Differentiation between sylvanite and calavarite was made difficult due to their submicron sizes. Altaite (PbTe), is associated with galena and hessite and rarely associated with sphalerite and chalcopyrite. Coloradoite (HgTe), is rare and has only been observed in one sample in contact with hessite, along grain boundaries. Trace amounts of native tellurium is found in pyrite and chalcopyrite.

All tellurides identified are spatially associated with each other microscopical-

ly and macroscopically. This is to be expected as they likely precipitated coevally or due to unstable conditions. Afifi et al. (1988) noted that intergrowths of hessite and petzite are usually a product of the decomposition of χ -phase ($\text{Ag}_{11-x}\text{Au}_{1+x}\text{Te}_6$) at 120°C. Based on petzite distribution and textures this is the most likely scenario at Shahumyan where petzite is usually observed to be intergrown with hessite or found along hessite rims or within fractures.

3.2.2 Gangue Minerals and Textures

3.2.2.1 Major Gangue

Quartz-1 is white in color massive to equigranular fine to medium grained. It is ubiquitous in all veins at Shahumyan, but varies in abundance along vein segments. It ranges from 5% which is limited to a thin selvage between vein opening and wallrock to 50-70% quartz rich zones which comprise a majority of the vein. In thin section, Quartz-1 has undulose extinction, and can appear to be cryptocrystalline with saccharoidal (jigsaw) textures. Saccharoidal and cryptocrystalline textures indicate rapid deposition of quartz. However, in some cases these textures may also indicate recrystallization of massive quartz. Quartz-2 is prismatic-euhedral quartz and is associated with comb quartz and flamboyant and/or feathery textures. In thin section, individual quartz crystals contain zoning patterns with minor inclusions of sulphide preferentially along growth bands, these inclusions range between $<1\mu\text{m} - 3\mu\text{m}$. The presence of sulphide inclusions along growth zones indicate sulphides and Quartz-2 precipitated coevally. Carbonates are ubiquitous in most veins at Shahumyan; however, their abundance varies between vein segments. Carbonate is significantly more abundant within the southern portion of the deposit (veins 17, 20, 20a, 33, 34) and decreases in abundance towards the north (veins 50, 35 and 5). Calcite is the most abundant within the carbonate assemblage however rhodochrosite is also observed locally and

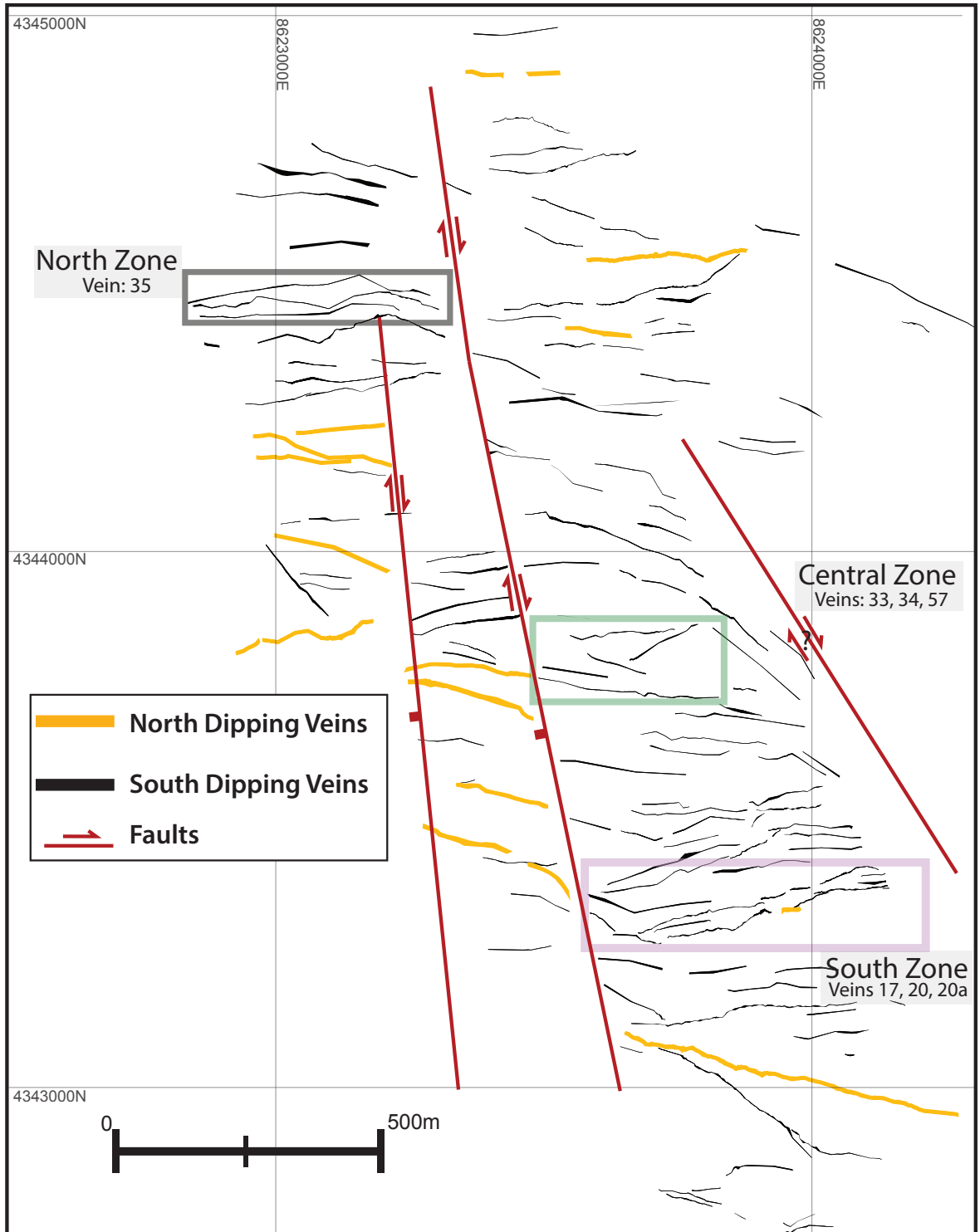


Figure 3.1: A plan view map of Shahumyan veins, projected from 760 level (760 masl). Both north and south dipping veins are present within the deposit. Three zones are looked at in more detailed: South Zone (purple) containing Veins 17, 20 and 20a; Central Zone (green) containing Veins 33,34 and 57; and the North Zone (black) containing Vein 35. The deposit is displaced by north trending faults.

kutnohorite ($\text{Ca}(\text{Mn},\text{Mg},\text{Fe})[\text{CO}_3]_2$) was recognized by Mederer et al. (2013 and 2014). Carbonate abundance ranges from <5% to 50% in mineralized veins. Pure carbonate (calcite) are also observed to crosscut all earlier hydrothermal stages. Isotopic concentration of late calcite is variable ranging from 7.7 to 15.4‰_{VSMOW} for $\delta^{18}\text{O}$ and from -3.0 to 0.7‰_{VSMOW} for $\delta^{13}\text{C}$, with a positive correlation trend in $\delta^{13}\text{C}$ vs $\delta^{18}\text{O}$ space (Mederer et al., 2013). Mederer et al., (2013) propose an influence of meteoric waters mixing with magmatic waters in the waning stages at Shahumyan, depositing massive calcite.

3.2.2.2 *Minor Gangue*

Fluorite at Shahumyan is green in color and is a late stage mineral accompanying massive carbonate. Hydrothermal apatite is identified by Mederer et al. (2014) as a minor gangue mineral along with fluorite. Sericite (illite/clay) is the primary alteration mineral along vein selvages, it is also found as interstitial fill within brecciated veins between calcite, sulphide, and quartz grains. Chlorite is found in trace amounts in a quartz-pyrite rich assemblage. When present, it has a radiating structure and displays clear to light green and light green to medium green pleochroism in plane polarized light with second order anomalous dark blue birefringence. X-ray diffraction and microbeam data (Appendix 2) reveal clinocllore to ripidolite chlorite compositions.

3.3 Mineralization Paragenesis

Shahumyan is characterized by over one hundred subparallel veins with widths up to 3m in thickness and 300-500m along strike length Figure 3.1. Spatial distribution of individual hydrothermal mineral bands (stages) vary along strike making it difficult to trace one band to the next within individual veins (Figure 3.2 A-C). Therefore, the relative timing of hydrothermal stages are differentiated solely by mineralogy and tex-

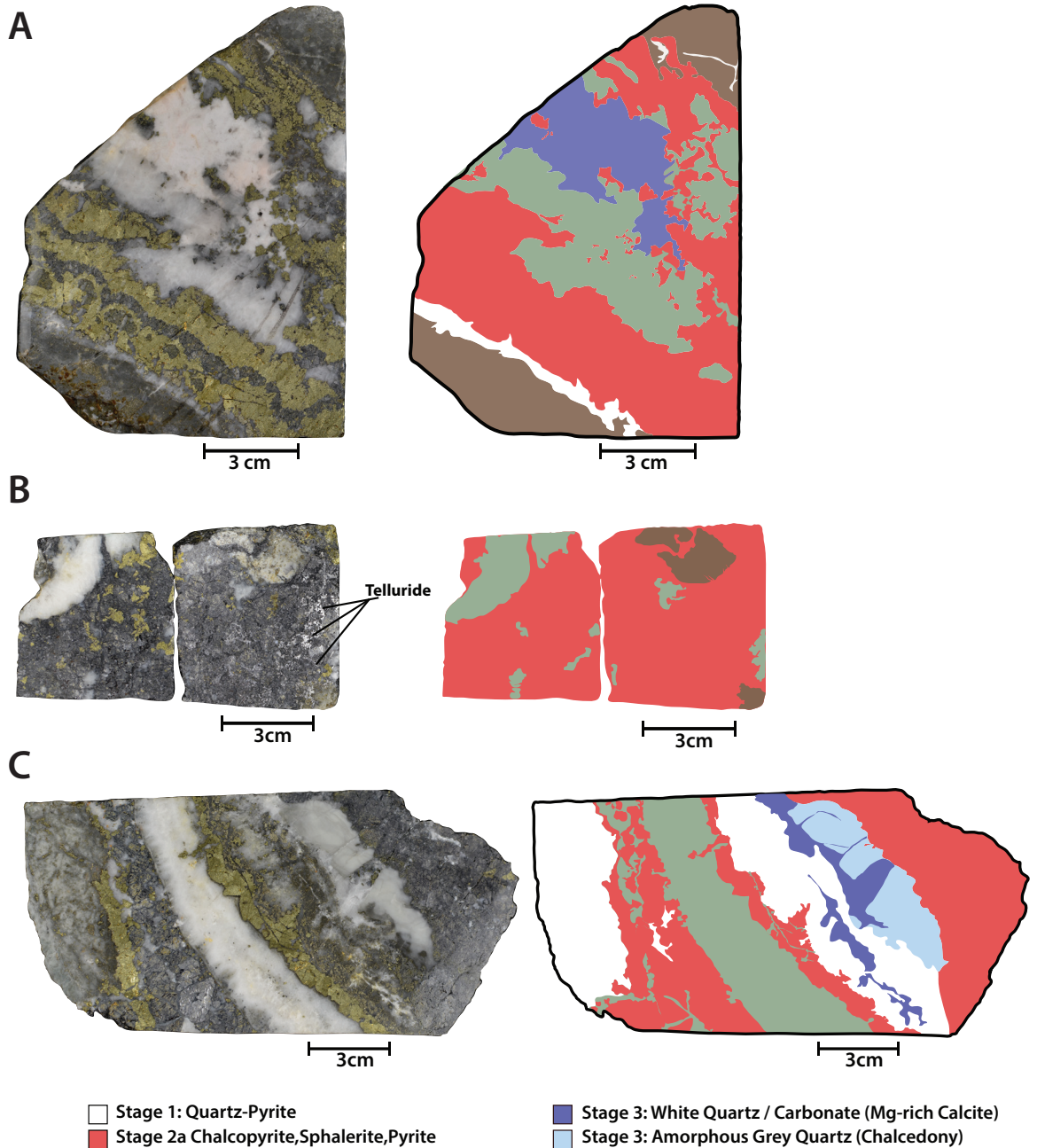


Figure 3.2 A-C: Vein samples from Shahumyan. (A) Sample contains all three stages observed at Shahumyan including colloform banding of sphalerite and chalcopyrite. Hydrothermal stages in this sample young towards the center of the vein, this is not always the case in Shahumyan veins. (B) Two high grade samples consisting of Au-Ag tellurides filling in small microfractures in sphalerite. Wallrock clasts in the sample are completely altered to sericite/illite. (C) Sample showing all three main hydrothermal stages at Shahumyan.

tures rather than crosscutting relationships usually observed in a typical paragenetic studies. The progression of hydrothermal stages and individual minerals within each stage is shown in Table 3.1 and discussed below.

Shahumyan (n= 30)				
mineral	Stage 1	Stage 2a	Stage 2b	Stage 3
Gangue				
Quartz(1)	—————	-----		Chalcedony
Quartz (2)		—————		
Calcite			-----	—————
Fluorite				—————
Illite				—————
Mineralization				
Pyrite	—————	-----		
Chalcopyrite		—————		
Sphalerite		Honey Brown → Light Yellow	Opaque	
Galena		-----		
Tetrahedrite-Tennantite			-----	
Hessite			-----	
Petzite			-----	
Coloradoite			-----	
Altaite			-----	
Sylvanite/Calavarite			---	
Textures				
Massive	—————	-----		-----
Crustiform		-----		
Colloform		-----		
Quartz-Comb		-----		-----
Breccia			?	-----
Wall Rock Alteration				
Quartz		-----		
Chlorite	-----			
Sericite/Illite		-----		-----
Kaolinite		-----		
Calcite				-----

Table 3.1: Paragenetic table of hydrothermal stages, textures and alteration observed at Shahumyan

3.3.1 Stage 1

Stage 1 is characterized mainly by abundant white quartz-pyrite (Quartz-1) veinlets and bands within larger veins. This stage contains trace chlorite and sericite/illite and is considered uneconomic. Within larger veins this hydrothermal stage is typically <1cm to 5cm wide and is present between the vein-wallrock interface. This stage is also observed as isolated quartz-pyrite veinlets (1-5cm) that occur adjacent to major veins, and have a quartz-sericite alteration halo. This hydrothermal stage can

be found as small veins within breccia clasts in larger veins. This would indicate that Stage 1 is paragenetically the earliest.

3.3.2 Stage 2

Stage 2 is broken into two sub stages: Stage 2a and Stage 2b. Stage 2a contains significantly higher proportion of base metal sulphides compared to Stage 2b. Stage 2b contains relatively greater amounts of precious-metal mineralization. Stage 2a is primarily composed of chalcopyrite-sphalerite-pyrite ±galena within a coarse quartz (Quartz-2) gangue. Textures present in this stage include drussy-comb quartz, and crustiform of alternating chalcopyrite, sphalerite, and quartz. Breccias composed of angular to subrounded fragments of adjacent wallrock are suspended within the quartz-sulphide matrix, with colloform bands forming around such clasts. Breccia fragments vary in size ranging from 1 cm sized fragments up to 50cm. Breccia fragments containing truncated Stage 1 veins are observed. On this basis, it is interpreted that Stage 2a followed quartz-pyrite veins of Stage 1. At deposit scale Stage 2a is volumetrically more abundant the northern veins (Vein 5, 35 etc) than southern veins.

Stage 2b primarily consists of Au-Ag-Pb-Hg-Bi tellurides (Figure 3.3 A-F) and sulphosalts are associated with dark-opaque sphalerite and chalcopyrite. Fine aphanitic quartz (Quartz 1) is the principal gangue mineral in addition to fine grained calcite present locally. Tellurides minerals fill in microfractures of brecciated honey brown-yellow sphalerite, galena and rarely chalcopyrite. Hessite contains inclusions of sphalerite, pyrite and chalcopyrite grains. Telluride minerals are intergrown or found as inclusions in dark opaque sphalerite. In decreasing abundance hessite (Ag_2Te), petzite (Ag_3AuTe_2) and sylvanite ($(\text{Ag,Au})\text{Te}_2$) characterize the telluride assemblage with altaite (PbTe), coloradoite (HgTe), and unidentified Bi-Sb-Te minerals found in trace amounts. Macroscopically this brecciation event is indistinguishable within the vein,

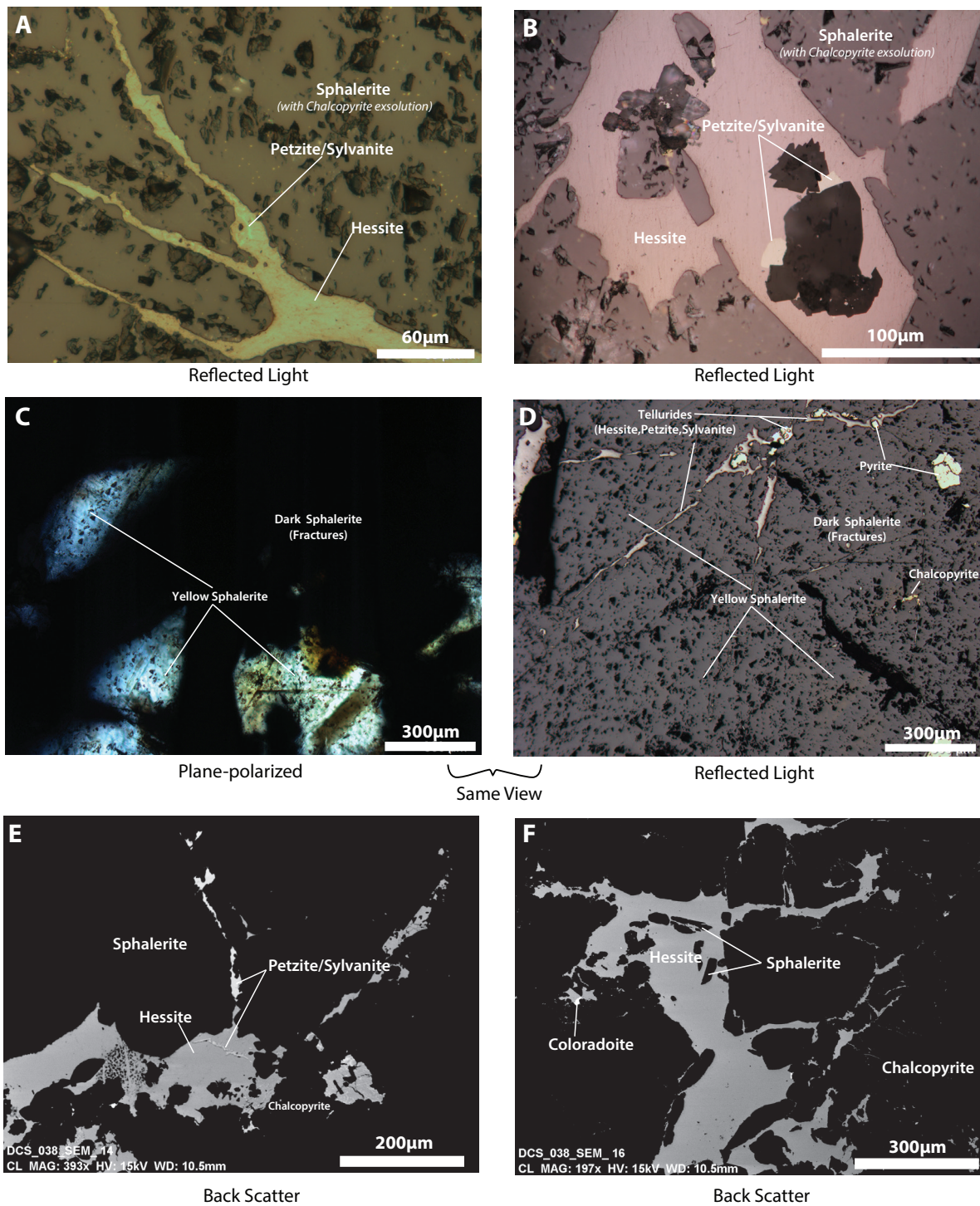


Figure 3.4 A-F: Photomicrographs and SEM imagery of vein samples. (A) Hessite [Ag₂Te] containing petzite/sylvanite [Ag₃AuTe₂/ (Au,Ag)₂Te₄] inclusions, fills a micro-fracture in sphalerite containing chalcopyrite disease. (B) Similar to (A), Hessite containing petzite/sylvanite and coloradoite it also includes brecciated sphalerite grains. (C) Transmitted light photomicrograph of Figure (D) both images together show yellow sphalerite crosscut by later stage fractures filled in with dark opaque sphalerite. Associated with dark-opaque sphalerite are Au-Ag tellurides (hessite, petzite-sylvanite). (E and F) SEM images of tellurides in sphalerite and chalcopyrite. (F) Brecciated grains of sphalerite and chalcopyrite cemented by hessite.

as it is overprinted by subsequent Stage 3 brecciation.

3.3.3 Stage 3

Stage 3 comprises of massive quartz (Quartz 1), coarse crystalline calcite, fluorite and grey amorphous quartz (chalcedony). Sulphide floats and breccia clasts of Stage 1 and Stage 2 are suspended in massive crystalline quartz-carbonate. The presence of sulphides and wall rock clasts suspended in quartz-carbonate gangue indicates the possibility of mechanically transportation of earlier stages during Stage 3. At deposit scale this stage is more abundant by volume % in the southern veins compared to the northern veins. In thin section it is clear that calcite veins crosscut earlier quartz-sulphide-telluride assemblages. Its relative abundance decreases towards the northern veins.

3.4 Centralni and Noreshenik Vein Mineralogy

The Centralni and Noreshenik areas are located to the northeast and northwest of Shahumyan respectively, and fall outside of the Shahumyan mine boundary. These localities are characterized by east trending veins with similar mineralogy to the Shahumyan veins. Several vein samples were collected from drill core to establish a paragenetic sequence in relation to Shahumyan.

3.4.1 Centralni

Centralni is subdivided into two mines: Centralni West and Centralni East. Centralni West is an underground mine characterized by subparallel vein sets similar to Shahumyan, as well as localized massive sulphide lenses found in the tuff layers and Centralni East is an open pit deposit characterized by stockwork veining and disseminated mineralization. The two deposits are separated by the Metz Magarin fault which

Centralni East (n= 4)		
Mineral	Stage 1	Stage 2
Quartz		—————
Chlorite	-----	
Pyrite	—————	—————
Chalcopyrite		—————
Barite		-----
Gypsum		-----

Table 3.2: Paragenetic table of hydrothermal stages and associated minerals at Centralni East

Noreshenik (n= 5)			
Mineral	Stage 1	Stage 2	Stage 3
Quartz		—————	—————
Chlorite	-----		
Pyrite	—————	—————	
Chalcopyrite		—————	
Sphalerite		—————	
Calcite			—————
Sericite		-----	

Table 3.3: Paragenetic table of hydrothermal stages and associated minerals at Noreshenik

variably dips (65-90°) west and is suggested to have a normal offset of approximately 150-300m (Soviet Historic Data, personal communication).

Economic minerals observed by Mederer et al. (2014) at Centralni West include chalcopyrite and pyrite with minor amounts of sphalerite, tennantite-tetrahedrite and galena within a quartz rich gangue. Trace minerals of telluro-bismuthinite, hessite, petzite, tetradymite, wittichenite, emplectite and native gold have also been reported by Achikigiozyan et al. (1987) and Khachatryan (1958).

At Centralni East, main ore minerals include chalcopyrite, pyrite as observed in this study. Mederer et al. (2014) also identified colusite, tennantite-tetrahedrite, galena and specular hematite within veins. Trace minerals found at Centralni East include enargite, bornite, sphalerite, covellite, renierite, germanite and native gold and silver (Beaumont, 2006; Khachatryan; 1958). The paragenesis of the deposit is displayed in Table 3.2. Textures within individual veins and the stockwork include: crustiform, hydraulic breccia and comb-quartz textures. Gangue minerals include quartz, with mi-

nor amounts of barite and gypsum present locally. Vein thicknesses in the stockwork varies between 2cm to 25cm; less commonly, veins extended to 50cm. At Centralni West sulphur isotope values ($\delta_{34}\text{S}$) range from 4.9 to 6.1‰_{CDT} and 2.0 to 4.4‰_{CDT} for pyrite and chalcopyrite respectively (Mederer et al., 2014). Pyrite at Centralni East has $\delta_{34}\text{S}$ values between 3.3 and 6.5‰_{CDT} (Mederer et al., 2014). Alteration at Centralni East primarily consists of sericite, dickite-kaolinite, diaspore (Khachatryan, 1958) and residual quartz.

Key differences in mineralogy at Centralni compared to Shahumyan is the lack of bismuth rich minerals (emphlectite, wittichenite, tetradymite) and the gangue and alteration assemblages such as sericite, dickite-kaolinite, diaspore, and residual. Additionally barite and gypsum are also two minerals present at Centralni in greater abundance than at Noreshenik and Shahumyan, whereas previous reports have reported minor amounts of barite but have not been identified in the present study.

3.4.2 Noreshenik

Minor quartz-pyrite veins are commonly observed at Noreshenik, pyrite is primarily euhedral cubic and occasionally blebby. Quartz-pyrite veins are crosscut by quartz-chalcopyrite-sphalerite-pyrite veins. Ore minerals at Noreshenik are mainly sphalerite and chalcopyrite. Crustiform and massive sulphide textures dominate and locally hydrothermal breccia consists of sulphide and wallrock clasts cemented by quartz-calcite. Major gangue minerals include quartz and calcite while minor gangue includes chlorite, sericite and trace hematite. The paragenesis of Noreshenik veins is shown in Table 3.3.

Key differences in mineralogy at noreshenik compared to Shahumyan include hydrothermal sericite (higher crystallinity) as opposed to hydrothermal illite/sericite (lower crystallinity) found at Shahumyan and the lack of precious metal (Au-Ag) min-

eralization and telluride minerals.

3.5 Vein Geometry, Shahumyan

Individual veins at Shahumyan contain base and precious metal mineralization along strike and dip of a vein; coexisting, localized high grade ore shoots rake (plunge along vein plane) sub-vertical and sub-horizontally within individual veins. Current workings and exploratory drilling indicate vein lengths of 300-500m along strike and vertical continuity of 300m. Veins at Shahumyan are segmented by post mineral faulting making it difficult to ascertain true lengths of individual veins due to their discontinuity. Veins anastomose and comprise of small bends, extensional jogs, soft and hard linked step-overs, pinch and swell structures, vein deflections and cymoid loops (Figure 3.4 A).

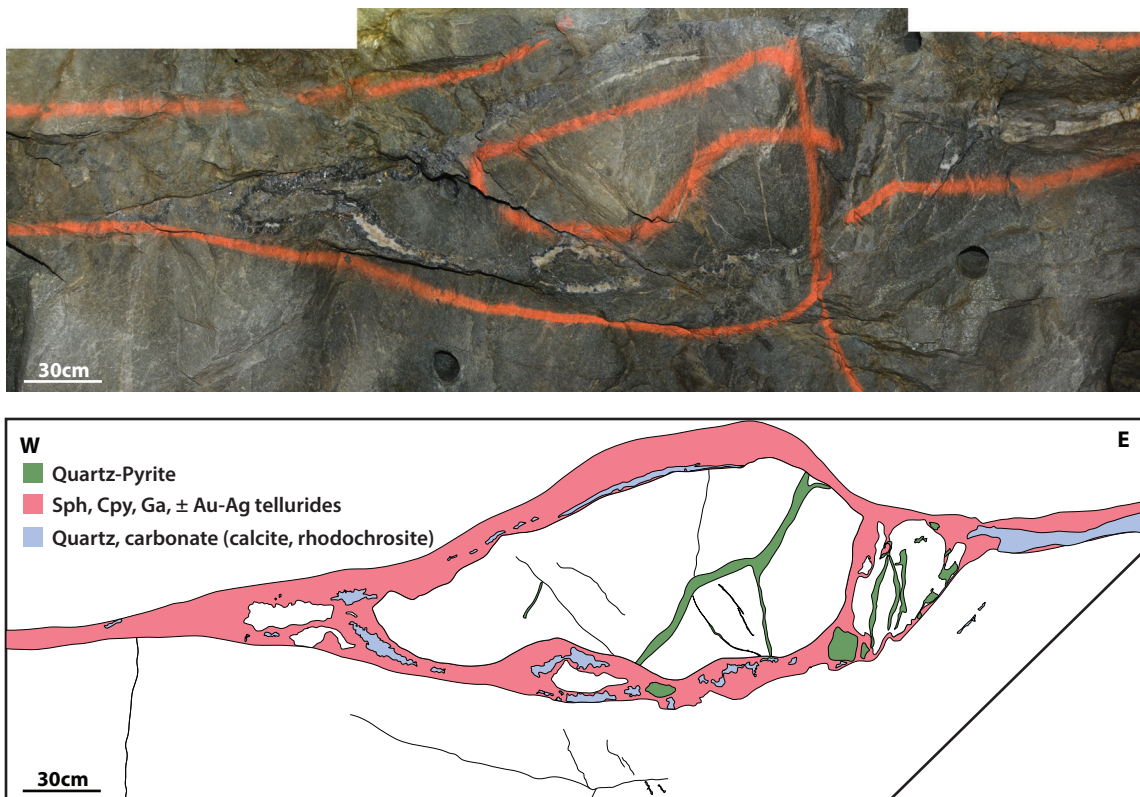


Figure 3.5: A cymoid vein structure in Vein 20 showing brecciated wallrock clasts cemented by Stage 2a and Stage 2b minerals. Wallrock clasts contain Stage 1 quartz-pyrite veins.

Within structurally controlled vein deposits such as the Shahumyan deposit, hydrothermal fluid flow through host rocks is governed by hydraulic gradients and interconnected fluid pathways between discontinuities (Sibson, 1996; Cox, 2005). However the presence of irregularities, jogs, and intersections within these mineralized structures localize fluid pathways for hydrothermal fluids to be focussed and concentrated (Faulkner et al., 2010; Cox, 2005; Rowland and Sibson 2004; Sibson 1996). The presence of highly permeable conduits combined with an efficient ore deposition mechanism, is critical in order to produce economic-grade deposit (Micklethwaite, 2008; Simmons and Brown, 2006; Cox, 2005; Simmons and Browne, 2000). It is therefore crucial in understanding the nucleation and propagation of faults, and how these processes influence vein growth and ore-shoot formation at Shahumyan.

Shahumyan veins were studied by evaluating mine level maps, longitudinal sections, cross-sections, and geometry of interconnecting structures. This preliminary study was followed by detailed mapping at accessible underground levels and drifts at 1:100 scales. Three zones (South, Middle, North) consisting of five veins were chosen for detailed mapping. These veins were selected due to mine accessibility at different depths and their spatial distribution within the mine. Within each vein the distribution of hydrothermal stages, textural and structural variability were examined and mapped. Longitudinal sections showing thickness and grade distribution are created from channel assay database, provided by Dundee Precious Metals. Structural data is plotted and analysed using Open Stereo (Grohmann et al., 2011) and corroborated with Stereonet 9 (Allmendinger et al., 2013), any structural data herein will be given as dip-direction/dip ($278^{\circ}/90^{\circ}$). All collected data and maps of mapped veins are outlined in greater detail in Appendix 5.

3.5.1 South Zone (Vein 17 and 20)

The south zone comprises of Vein 17 and Vein 20 and mapped at levels 690 and 670 (masl). In map view, both Veins 17 and 20 have irregular undulations along strike imparting an anastomosing geometry with frequent changes in orientation. However, when considered as a whole, both veins approximately strike northeast and dip to the southeast (Vein 20:164°/78°; Vein 17:143°/60°), with Vein 17 dipping more shallowly than Vein 20. Vein 17 is significantly thicker (0.50m to 3.0m) than Vein 20 (0.20m to 1m). Veins 17 and 20 are abundant in quartz carbonate gangue comprising up to 30-60% of the vein. The vein-wallrock interface contains no evidence of slip such as gouge or mineral fibers but does contain in-situ breccia (jigsaw breccia) locally. Therefore, initial propagation of veins was likely purely dilational (tensional) with no lateral slip component. Towards the center of the veins 17 and 20, smaller faults (~10cm thick) displace mineral bands dextrally and are sub-parallel to perpendicular to mineral bands. Although rare, oblique-slip (dextral-normal) slickensides are present; indicated by quartz and calcite mineral fibers along exposed fault-vein surfaces. Gouge is also present within these smaller faults, containing rock flour, aphanitic/brecciated quartz-calcite and minor amounts sulphide. Several vein segments of Vein 20 strike to the northwest and steeply dip to the southwest these veins are relatively less mineralized than the main vein segment; similarly assay results from these segments are much lower than the main vein.

Larger northwest striking post mineral faulting crosscut existing veins and have a mean orientation of 235°/72°. These faults mainly dextrally offset of veins in map view. Displacement associated with these faults ranges from 10cm to 10-20m as seen in Vein 20 (L690). Northeast trending gabbro dikes typically crosscut veins but in some cases are parallel to veins. Gabbro dikes strike north to northeast with a mean orientation of 250°/56°.

3.5.2 Middle Zone (Vein 34-33, 57)

The middle zone consists of Veins 34-33 and 57, mapped on levels 760, 748 and 735 (masl). Similar to veins in the south zone veins 34-33 and 57 have an anastomosing geometry with frequent changes in orientation, as a whole they strike approximately east-west. When looked at individually, Vein 57 has a mean orientation of $140^{\circ}/76^{\circ}$ while Veins 33-34 has two sub-populations (east striking, $175^{\circ}/82^{\circ}$ and a southeast striking, $200^{\circ}/80^{\circ}$). Mineralization within these sub-population vein segments are quite similar with similar assay values. Furthermore, small segments along the main vein, drastically change in dip magnitude varying from $45-80^{\circ}$ and direction from south to north or vice versa. These changes are absent in Vein 57. These drastic changes in dip occur with changes in dip-direction and at the edges of cymoid loops these variations sometimes correspond with change in vein textures and breccias between the two vein segments in question. Veins 33-34 are excellent examples of the fractal nature of cymoid loops, where both Veins 33 and 34 are interpreted as individual divergent branches propagating from a single larger vein. Mineralogically, Veins 34-33 and 57 contain 5-20% quartz-carbonate gangue, with the remaining composed of quartz-chalcopyrite-sphalerite and galena. Quartz-carbonate gangue in the middle zone is volumetrically low relative to Veins 17 and 20 in the south zone.

F3 faults described in the previous chapter are identified in the middle zone. F3 faults strike east to southeast and can therefore be subdivided into F3a and F3b sets, respectively. The east striking F3a set has a mean orientation of $190^{\circ}/60^{\circ}$ and characterized as normal faults with a dextral kinematic sense indicated by slicken fibers (calcite and quartz) and slickensides (chlorite-zeolites) this fault set is observed in the more prevalent in the Middle Zone than the South Zone. Measured slickensides rake between $15-25^{\circ}$ southwest ($n=5$) ($\sim 205-215^{\circ}/60^{\circ}$). The east striking fault set has a similar orientation to mineralized veins and is considered syn-mineralization faulting

which likely reactivated multiple times since their formation. Fault material contains significant amounts (1-2%) of pyrite and chalcopyrite in addition to fault gouge and quartz-carbonate material.

The southeast striking F3b set has a mean orientation of $250^{\circ}/82^{\circ}$ and identified as normal faults and in map view displaces veins dextrally. However no kinematic indicators are seen along the fault surface. Therefore, the F3b faults are inferred as normal faults. Fault material consists of fault gouge (rock flour, clay, and hydrothermal mica) and minor carbonate and pyrite.

3.5.3 North Zone (Vein 35)

In the north zone Vein 35 is mapped on level 740 (masl). Vein 35 trends east to southeast with a mean orientation of $198^{\circ}/83^{\circ}$. Only a single fault set is identified in the north zone and strikes north to northeast with a mean orientation of $266^{\circ}/70^{\circ}$. Mineralogically, Vein 35 has significantly less quartz-carbonate gangue than both the south and/or middle zones, making up <1% to 5% of vein material with the rest composed of quartz-chalcopyrite-sphalerite and galena. Additionally there is also an increase in chalcopyrite/pyrite and sphalerite ratios with relatively more chalcopyrite and pyrite in the north zone than the other two zones.

3.5.4 High Grade Ore Shoots

Gold and silver grades within Shahumyan veins is irregular, with high grade Au-Ag mineralization hosted in discontinuous ore shoots. Based on drift mapping these oreshoots are associated with pinch and swell features, bends and cymoid loops. These structural features contain crustiform banding of quartz-sulphides and hydrothermal breccias (Figure 3.5 A-D).

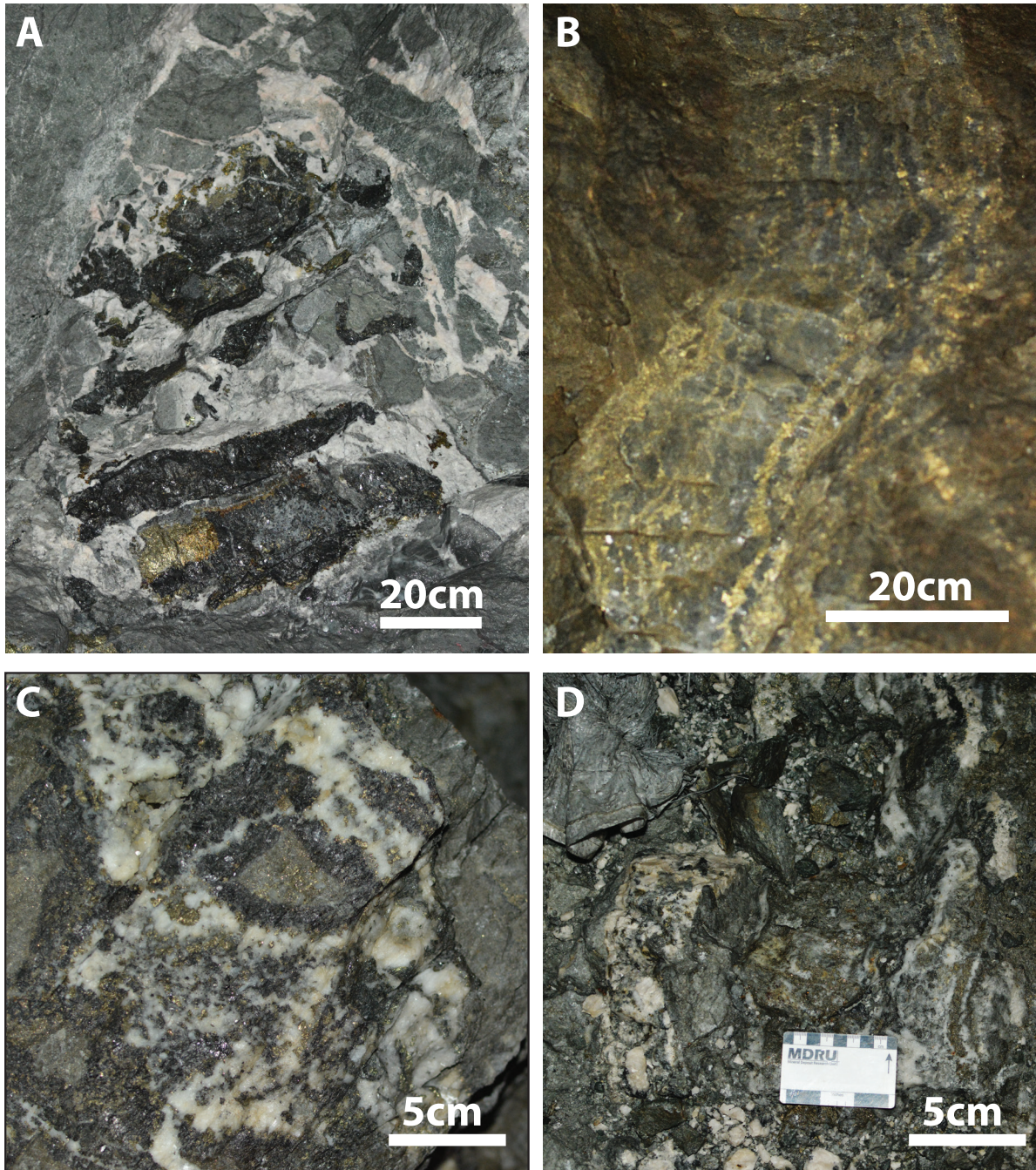


Figure 3.6: Observed vein textures. (A) Brecciated vein pod within a vein, Stage 2a crustiform sphalerite chalcopyrite clasts cemented by Stage 3 quartz-carbonate. (B) Base metal rich vein characterized by crustiform banding of alternating chalcopyrite-sphalerite mineral bands. (C) Early Stage 2 breccia cementing quartz-pyrite stage veins and wallrock with Stage 2 sphalerite and quartz. (D) Vein containing crustiform sulphide bands and displaying multi-stage brecciation.

Each vein examined contains discontinuous high-grade ore shoots which rake sub-vertically and sub-horizontally within the vein. The two general orientation of these ore shoots are: 1) east to west alignment of mineralization pods of higher Au-Ag-Cu-Zn grade which extend 10-25 m horizontally and weakly plunge (10-20°) to the west; and 2) steeply plunging shoots, accommodated by cymoid loops and localized hydrothermal breccia zones extend 20-100m vertically and have a narrow geometry (5-10m thickness) (Figure 3.6). In contrast, the veins themselves have continuous economic base metal mineralization extending 200-500m along strike and dip of the vein. Vein segments with sharp dip and strike changes and strongly brecciated zones tend to have increased Au-Ag grade. However, intersections between faults and extensional fractures only rarely host high Au-Ag grade ore. Vein deflections observed along strike of veins are junctions between two individual, differently oriented veins segments. Vein segments of different orientation and thickness but with similar hydrothermal fill are linked. This would indicate vein segments opened simultaneously and were subsequently linked through further vein propagation.

3.6 Discussion

3.6.1 Hydrothermal Stages

Vein mineralogy at Shahumyan has two main economic ore stages: a base metal stage (Stage 2a) and a precious metal stage (Stage 2b). Stage 2a consists of chalcopyrite, sphalerite (honey brown and yellow), and galena as its main economic minerals. Stage 2b consists of chalcopyrite, opaque sphalerite, sulphosalts, and Au-Ag tellurides as its main economic minerals. Stage 2a is characterized by crustiform colloform and quartz-comb textures while Stage 2b is characterized by localized brecciation of Stage 1 and Stage 2a sulphides and vein segments.

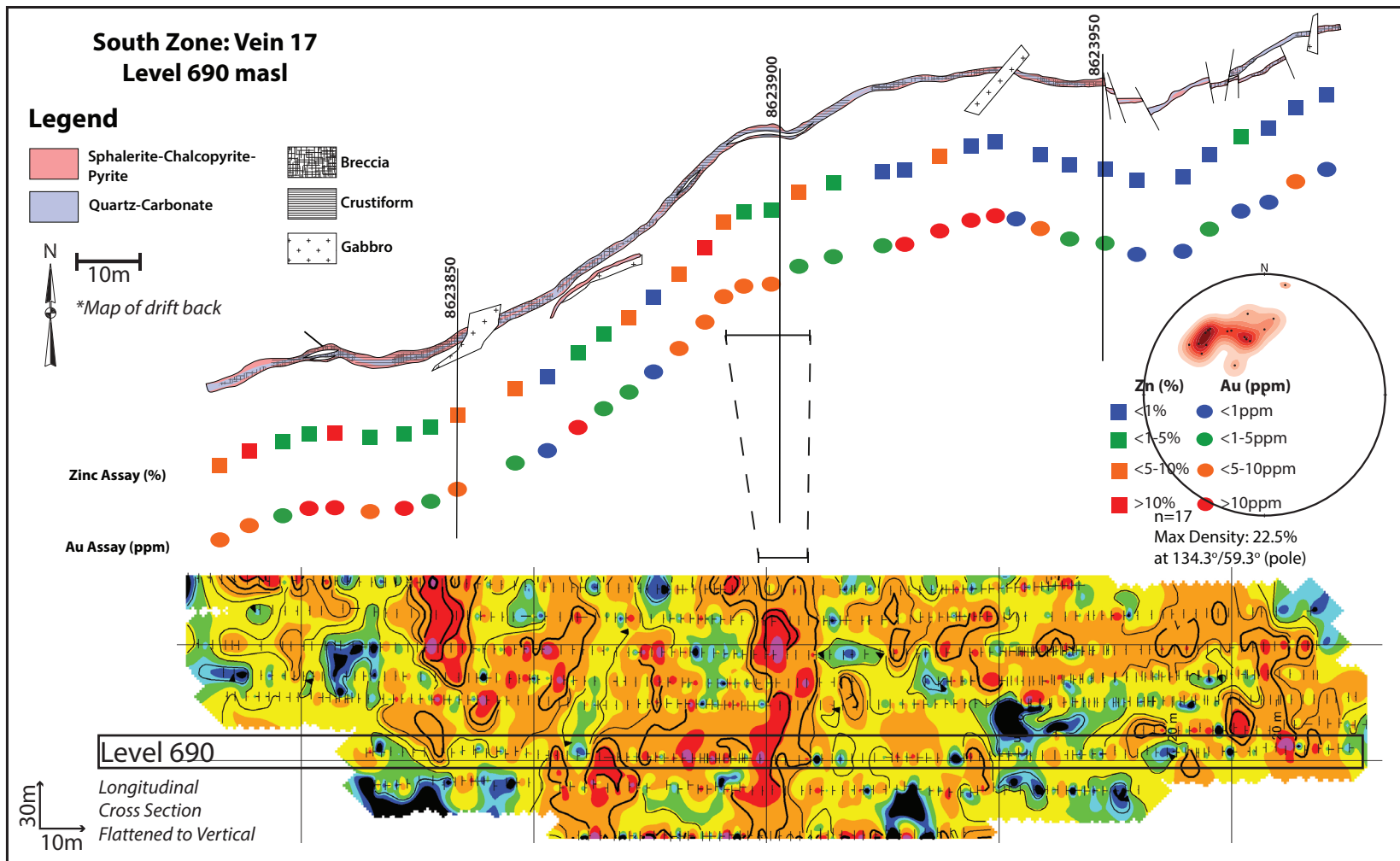


Figure 3.7 A detailed plan view of Vein 17's vein mineralogy, texture, structural features, and metal content (Au, Zn). High grade zones are associated with breccia's and crustiform textures which are typically associated with cymoid loops, and sudden changes in strike and dip of the vein segment. A long section of the vein collapsed to vertical sows contoured Au values normalized to vein thickness which reveals sub-horizontal and sub-vertical ore shoots within the mineralized vein.

3.6.2 Vein Geometry

Epithermal veins commonly form in extensional terranes, which are active either during the relaxation phase following compressional regimes or in back-arc rift settings. Epithermal gold deposits are strongly structurally controlled where mineralization is intimately linked with contemporaneous faulting and volcanism (Begbie et al., 2007; Cox, 2005; Cooke and Simmons, 2000; Páez et al., 2011; Sillitoe and Hedenquist, 2003).

Undulating, veins at Shahumyan can be associated with fracture and vein propagation as through-going fluid pathways form by vein linkage during the development of a hydrothermal system (Sibson, 2001). These sub-vertical veins are tensional in nature, but whether they opened as pure extensional or extensional-shear veins is unknown. A homogeneous host rock and absence of older crosscutting features make it difficult to determine a sense of opening due to a lack of piercing points. However, overall vein geometry (dilatational jogs, cymoid geometry and horse tail terminations) and presence of oblique slickensides indicate that these veins likely propagated or evolved in an extensional to transtensional (normal-dextral) regime during the mineralizing event. An absence of sub horizontal (flat) veins or faults at Shahumyan, and the presence of a sub-vertical extensional/open-space filled veins indicates a vertical principal stress (σ_1). The corresponding least and intermediate stresses axes (σ_3 and σ_2 , respectively) are contained within the plane perpendicular to σ_1 where σ_2 is east to northeast directed and σ_3 is north to northwest directed. This stress regime typically defines an extensional regime. However, with the presence of dextral geometries of veins and a dextral-normal kinematic indicators (slickensides) suggest a transitional regime influenced the evolution of Shahumyan veins. The principal stress would therefore be sub-vertical with the corresponding least and intermediate stresses are sub-horizontal. These stress regimes have been identified to exist in the Lesser and

Trans- Caucasus during the Middle Jurassic to Early Cretaceous by McCann et al. (2010) and Saintot et al. (2006).

3.6.3 Vein and Oreshoot Formation

Extensional fault systems grow and evolve as a consequence of local stresses. Such fault systems begin as tensional fractures perpendicular to the direction of extension producing individual and non-interacting fracture meshes (Trudgill and Cartwright, 1994; Faulds and Varga, 1998; Walsh et al., 2003, Wallier, 2009). With continued extension, individual fractures continue to propagate along strike and begin to overlap and develop curvilinear geometry that mechanically link with one another, forming a dense network of highly permeable conduits for fluid flow (Faulds et al., 2010, 2006; Wallier, 2009; Micklethwaite and Cox, 2004) (Figure 3.7 A). These highly permeable conduits are the focus of continued deformation which are soft-linked at first (Figure 3.7B), where there is no physical connection between segments and create relay ramps, but later become hard linked once segments become physically linked (Fossen, 2010; Walsh et al., 2003; Peacock et al., 2002; Peacock and Sanderson, 1991) (Figure 3.7C). This could result in abandonment of unlinked and smaller structures, as stress is focussed along the newly formed and continuously deforming, linkage zone (Faulds and Varga, 1998; Trudgill and Cartwright, 1994; Acocella et al., 2000; Wallier, 2009). These linkages between structures manifest as fault bends, step-overs, relay ramps or cymoid loops; which, allow for a more localized and repetitive fluid flow (Faulds et al., 2010, 2006; Wallier, 2009; Micklethwaite and Cox, 2004; Trudgill and Cartwright, 1990). In many metalliferous vein deposits these linkage zones also contain the most highly mineralized and prolific parts of the deposit due to the channeled metal-bearing fluid flow because of increased permeability (Micklethwaite, 2009; Wallier, 2009; Cox et al., 2005; Cox and Ruming, 2004; Micklethwaite and Cox, 2004; Sibson 2000).

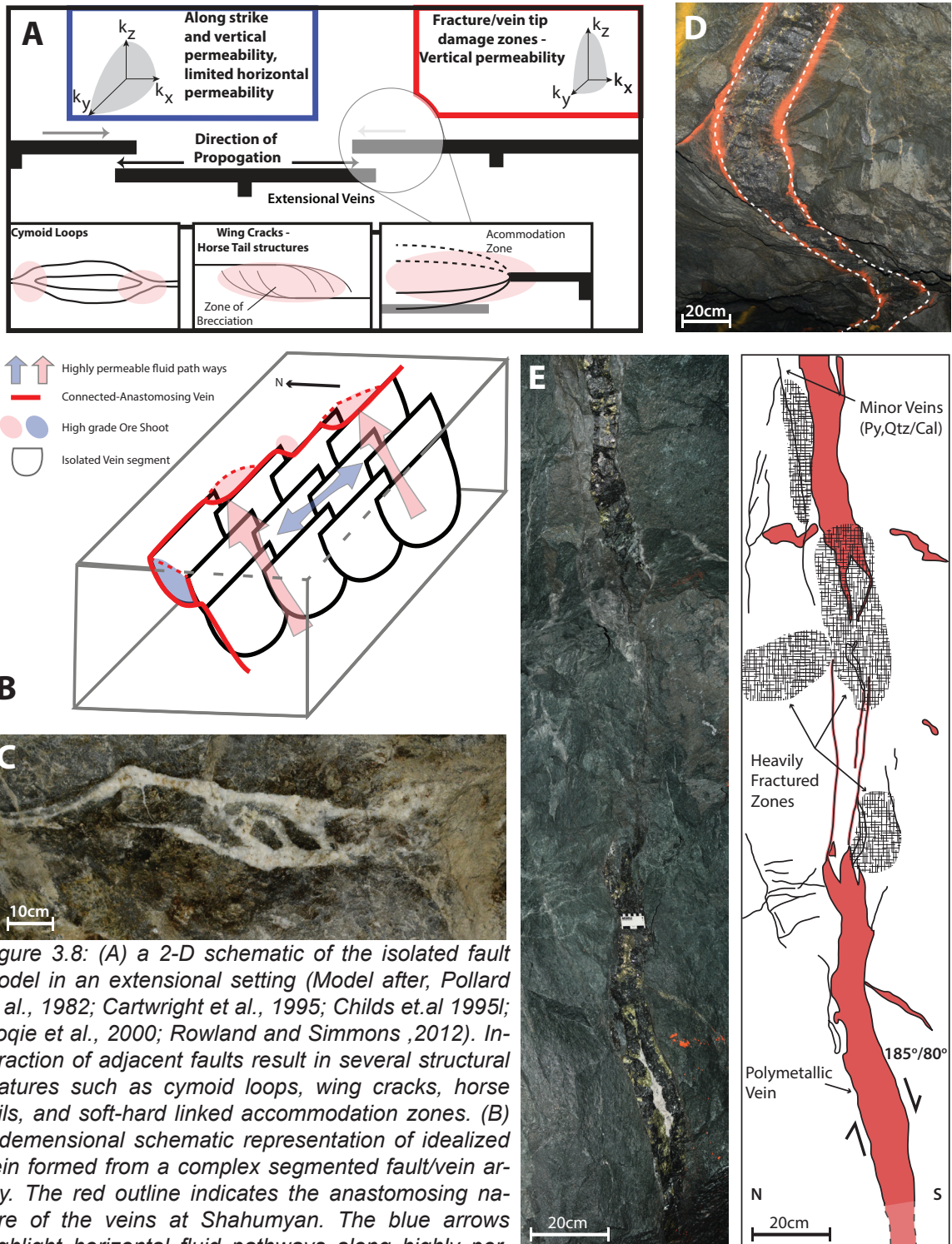


Figure 3.8: (A) a 2-D schematic of the isolated fault model in an extensional setting (Model after, Pollard et al., 1982; Cartwright et al., 1995; Childs et al. 1995; Coqie et al., 2000; Rowland and Simmons, 2012). Interaction of adjacent faults result in several structural features such as cymoid loops, wing cracks, horse tails, and soft-hard linked accommodation zones. (B) 3-dimensional schematic representation of idealized vein formed from a complex segmented fault/vein array. The red outline indicates the anastomosing nature of the veins at Shahumyan. The blue arrows highlight horizontal fluid pathways along highly permeable zones typically found at the intersecting connections of adjacent segments, resulting in either sub-horizontal (blue) oreshoots. High vertical fluid permeability and fluid flow are highlighted in red, and result in narrow vertical ore-shoots. (C): Horse tail structural feature indicative of soft linkage of adjacent veins. (D) Anastomosing nature of veins at Shahumyan. (E): Wing crack and an accommodation zone along a minor vein segment subparallel to a major vein. The accommodation zone is characterized by brecciation and heavy fracturing.

Cymoid loops can be described as vein bifurcations which bind or cement convex shaped lenses of wallrock fragments within hydrothermal vein material. The term cymoid loops had been coined by McKinstry (1948) and has been described in numerous epithermal districts (e.g., Hauraki, New Zealand: Begbie et al., 2007; Caylloma, Peru; Echavarría et al., 2006; Pachuca, Mexico: Thornburg 1945; Grass Valley, California; Johnston, 1940). They have been further described in detail by Marma and Vance (2011) in the Gold Circle district of Midas, Nevada. Marma and Vance (2011) identified three main end-members of cymoid loops: 1) vein-vein cymoid loops, with both branches of the cymoid contain a vein; 2) vein-structure cymoid loops, where one branch of the cymoid loop contains vein material and the other does not and 3) structure-structure cymoid loops, where both branched fractures contain no vein material. Each manifestation is a representation of a halted process towards the formation of a full cymoid loop (vein-vein cymoid). Cymoid loops accompanied by localized brecciation generally indicate the highest grade measured in vein segments; this is doubly true if a sharp change in dip and strike are also observed. All three end members are observed at Shahumyan.

The crossings of cymoid loop branches described above form nodes and represent the intersection of extension and/or shear veins and fractures (Marma and Vance, 2010). As a result, the nodes are highly fractured and intrinsically conducive to fluid flow, therefore producing high grade ore shoots. Micklethwaite and Cox (2004), Rowland and Simmons (2012) and Rowland and Sibson (2004) illustrate the effect of structures on permeability within an active volcanic-hydrothermal setting. After initial linkage of the main driving structure, permeability along the entire fault zone is increased, fluid flow along the main structure occurs diffusely along the entire breadth of the interconnected fractures. However, this is not maintained due to sealing from minerals precipitating from cooling hydrothermal fluids. Fluid flow is therefore localized within the intersection of interconnected faults or at fault tips and generally is protract-

ed through the fractures being continuously reactivated over varied time scales. The intersection zones consequently provide hydrothermal fluids enhanced permeability and sub-vertical conduits that allow for prolonged mineral and metal deposition needed to create high grade ore shoots. Similarly, fault tip interaction can also occur along dip, therefore the along strike and along dip interaction produces a 3D curvilinear fault geometry (Faulkner et al., 2010; Mickethwaite, 2009; Walsh et al., 1999; Childs et al., 1996). Uniquely interconnecting faults along dip of the main rupture zone resulting in sub-horizontal conduits rather than a sub-vertical conduit seen in along strike interaction. Therefore, given the correct fault geometry high grade ore shoots can be either sub-vertical or sub-horizontal.

4. Fluid Characterization, Alteration and Fluid Inclusions

4.1 Introduction

Changes in physicochemical conditions such as temperature, pressure, salinity, pH and eH of hydrothermal fluids are effective mechanisms for precious and base metal precipitation (Zhu et al., 2011, Cooke et al., 2001; Cooke et al., 1996; Spycher and Reed, 1989, 1986) and are therefore important factors to consider for fluid evolution within an ore deposit. Temperature and salinity of mineralizing fluids are measured through fluid inclusion studies. Acidity (pH), sulphur and tellurium fugacities are inferred based on chemical analysis of alteration, and sulphide minerals (sericite/illite/mica, chlorite, sphalerite) and sulphide, telluride mineral relationships (stability fields), respectively.

At Shahumyan, mineralized veins are primarily base metal rich with localized zones enriched in Au-Ag. Vein mapping and petrographic work reveal Au-Ag telluride minerals are enriched in brecciated vein zones. As discussed in previous chapters (Chapter 3.0) high grade Au-Ag oreshoots rake vertically and sub-horizontally within a vein. Cooke and McPhail (2001) suggested magmatic volatile condensation as an effective mechanism for high-grade telluride ore-formation in tellurium rich epithermal deposits; however, in tellurium poor epithermal deposits, boiling is likely to be the principal depositional processes. In the first scenario, tellurium is initially concentrated in magmatic volatiles, which condense into precious metal bearing chloride rich waters reacting with dissolved gold and silver species to deposit telluride minerals such as calaverite (AuTe_2) and hessite (Ag_2Te). In the latter case during boiling, aqueous tellurium species fractionate into a gaseous phase as $\text{HTe}^-_{(\text{aq})}$. Condensation of gaseous $\text{HTe}^-_{(\text{aq})}$ results in saturation and subsequent precipitation of telluride minerals (Cooke

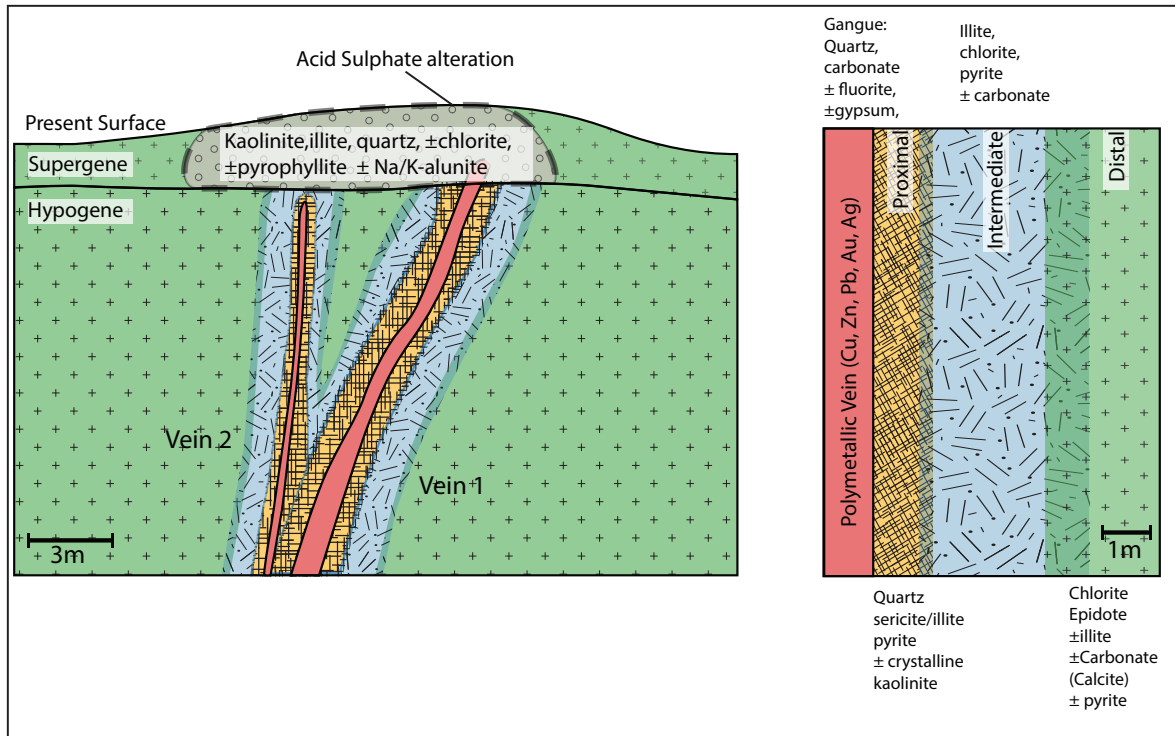


Figure 4.1: A schematic of alteration assemblages observed and mapped at Shahumyan. and McPhail, 2001; Tombros et al., 2010).

In epithermal systems, certain alteration minerals (i.e. anhydrite, rhodonite, chlorite, epidote, carbonates, hydrothermal clays) are effective indicators of paleo-temperatures and/or mineral depositional processes, such as: mixing, boiling, throttling, and wall-rock interaction. An example of this, is steam-heated alteration assemblages which typify host-rocks reacting with acidic waters produced by condensation of vapours from boiled geothermal waters. Detailed mapping of alteration assemblages around veins could help discriminate gas conduits from water conduits and could provide a vector towards high-grade ore-shoots in underground epithermal vein mining operations, such as at Shahumyan.

4.2 Hydrothermal Alteration, Shahumyan

The Barabatoom andesites host the Shahumyan deposit and are ubiquitously

altered. Three main alteration assemblages are identified, with all three assemblages partially overprinting one another. Alteration overprinting is in large part due to fissure veins being used as conduits throughout the lifetime of the evolving hydrothermal system. Alteration haloes are the end-product of prolonged and varied water-rock interaction. The three alteration assemblages are classified based on mineral assemblage extending laterally and vertically outward from veins into country rock, beginning with the proximal assemblage, intermediate assemblage and distal assemblages. (Figure 4.1)

4.2.1 Least Altered Rocks, (Barabatoom Volcanics)

The Shahumyan deposit is hosted in the Barabatoom volcanic group consisting of andesite and andesitic-dacite subvolcanic and volcanic rocks. The Barabatoom andesite-dacites are unique within the Kapan District as they contain bipyramidal quartz crystals ranging from 0.5cm to 5cm with the exception of the interlayered volcanoclastics, which contain mechanically weathered, subrounded to rounded quartz eyes (<0.1-2cm). Bipyramidal quartz within the andesite-dacite are subhedral to euhedral with some crystals showing resorption and/or alteration rings. In decreasing abundance plagioclase, hornblende and pyroxene phenocrysts are also present. Plagioclase and hornblende phenocrysts vary in size (1-10mm) and relative abundance (10-35%), pyroxene phenocrysts are small (1-2mm) with a relative abundance of 1-2%. Locally, hyaloclastite has been reported (Mederer et al., 2013) indicating a sub-aqueous environment was present periodically during the deposition of the Barabatoom andesite-dacites.

4.2.2 Distal Alteration Assemblage

The distal assemblage is characterized by a chlorite, illite/smectite, pyrite, epi-

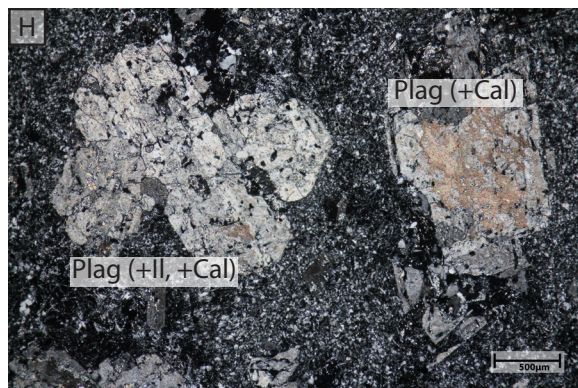
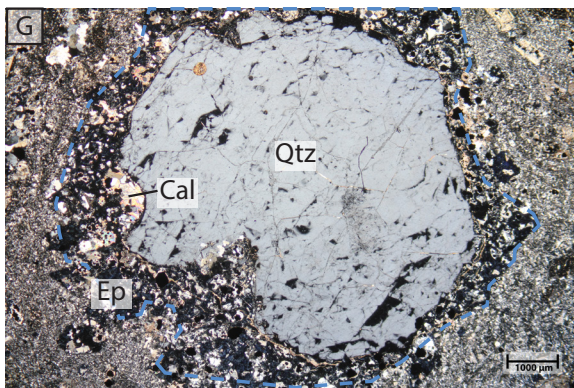
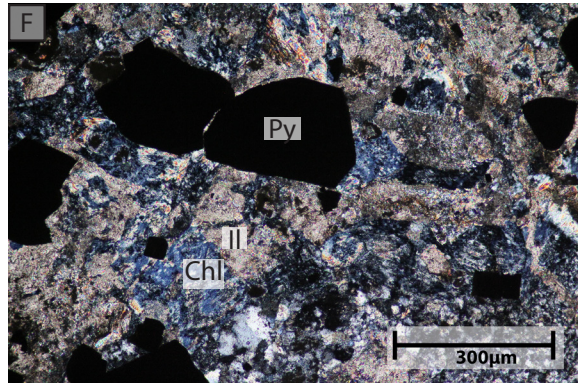
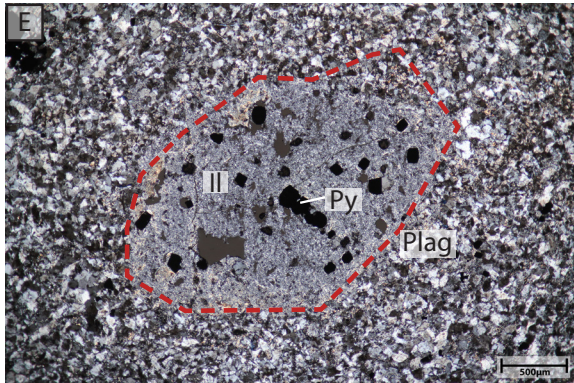
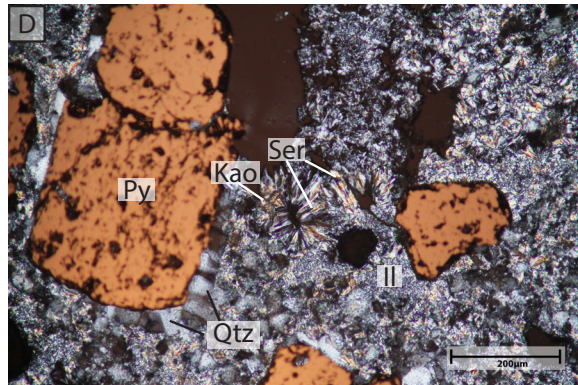
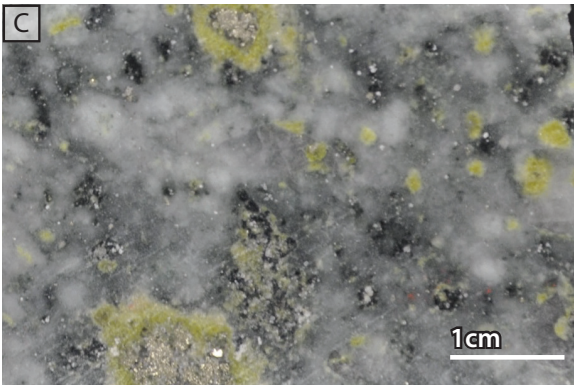
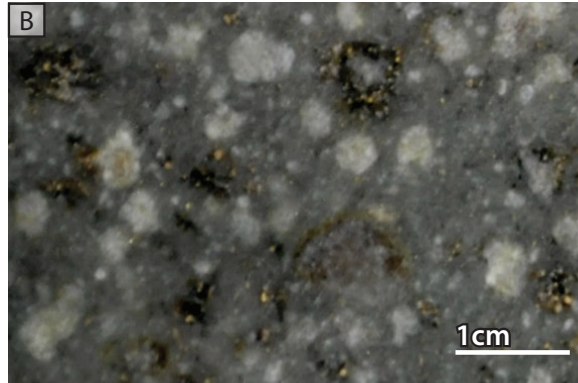
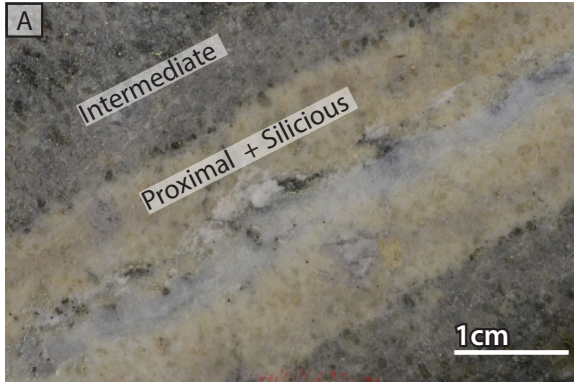


Figure 4.2: (A) Proximal alteration assemblage characterized by quartz-sericite-pyrite adjacent a quartz-pyrite-sphalerite vein. Adjacent the proximal assemblage is the intermediate alteration zone characterized by sericite-chlorite-pyrite. (B) Intermediate alteration zone characterized by chlorite and pyrite after hornblende, sericite/illite after plagioclase. (C) Distal alteration assemblage characterized by pyrite, chlorite after hornblende, and epidote alteration rims around hornblende. (D) Microphotograph of the proximal alteration assemblage. Illite and quartz crystals altering groundmass with sericite alteration with kaolinite altering sericite. (E&F) Microphotograph of the intermediate alteration assemblage. Illite and pyrite alteration after plagioclase. Chlorite-pyrite and illite alteration after hornblende. (G) Photomicrograph of the distal alteration assemblage. Bipyramidal quartz phenocryst with an epidote and calcite alteration rim. (H) Photomicrograph of the distal alteration assemblage. Plagioclase twins and broken plagioclase phenocryst showing sieved-mottled texture with illite and calcite alteration after plagioclase. Abbreviations: Ser: Sericite Kao: Kaolinite Qtz: Quartz Py: Pyrite Ill: Illite Chl: Chlorite Plag: Plagioclase Cal: Calcite Ep: Epidote.

dote and minor calcite (Figure 4.2C,G,K,L) and is texturally-preserving. Distal alteration assemblage halos enclose epithermal veins, proximal, and intermediate alteration envelopes. Due to the dense array of veins at Shahumyan, one vein's distal alteration envelope may overlap or merge with the distal assemblage of an adjacent vein, making it difficult to approximate the extent of this assemblage. Even the least altered volcanic rocks in the deposit contain trace amounts of this assemblage. The Barabatom andesites-dacites altered to this assemblage have a pale to intense green hue. Hornblende, pyroxene and accessory biotite are partially to completely replaced by chlorite, pyrite, epidote and to a lesser degree, leucoxene. Pyrite and leucoxene grains have an anhedral blebby morphology and are disseminated within the relict mafic mineral. Chlorite replaces the rims of hornblende crystals and is present within the rock matrix. Euhedral plagioclase crystals are partially altered to illite/smectite showing a sieve or dusted texture. Illite-smectite alteration is most prevalent at the rims of plagioclase crystals but also occurs within plagioclase crystal cores. Mineralogically destructive mineralogically distal assemblages are only observed locally and primarily only show epidote-chlorite alteration. Accumulations of epidote are primarily observed around mafics, and feldspars and primary quartz phenocrysts to a lesser degree

4.2.3 Intermediate Alteration Assemblage

The assemblage is characterized by sericite, illite, pyrite, chlorite, \pm kaolinite, \pm calcite and is weak to moderately texturally destructive (Figure 4.2 B,E,F,H,J). The alteration envelope extends 50cm to 300cm away from the mineralized vein. Boundaries between the intermediate-proximal assemblages and the intermediate-distal assemblages are indistinct with one assemblage grading into the other. The intermediate assemblage differs from the proximal assemblage with an increase in chlorite and calcite abundance and a decrease in sericite/illite abundance. Primary igneous mafic minerals are replaced by chlorite, sericite/illite, pyrite and minor carbonate (calcite). Chlorite partially to completely alter hornblende and biotite crystals imparting a moderate to strong green coloration on the andesite-dacites. Pyrite blebs are found within hornblende crystals. Very fine grained sericite/illite partially alters biotite and plagioclase crystals resulting in a sieved texture. Very fine grained calcite crystals are disseminated within the groundmass, but are more frequently observed in feldspar crystals (plagioclase). Calcite is rare in intermediate alteration assemblage but occurs more abundantly near late stage calcite rich veins.

4.2.4 Proximal Alteration Assemblage

The proximal alteration is characterized by a quartz-sericite/illite-pyrite \pm kaolinite mineral assemblage (Figure 4.2 A,D,I) and is moderate to intense texturally destructive of host rock. The width of this zone varies with vein width and ranges from 1 to 100cm from the edge of the vein. Very fine grained to medium grained sericite/illite alter primary igneous feldspars and mafic minerals, resulting in a bleached white color to the altered host rock. Fine grained disseminated anhedral quartz crystals are observed in groundmass and feldspar rims. An intense zone of silicification is localized and confined to <0.1-2cm narrow zones from vein margin. This zone is dominated by

quartz (70-80%) with minor amounts of sericite (5-10%) and disseminated pyrite (5-10%). Pyrite occurs as small cubic euhedral and irregular grains disseminated within the groundmass and as aggregates replacing hornblende and biotite. Aggregates of pyrite are also present within relict feldspar crystals. Kaolinite is rare but occurs locally within the proximal assemblage and vein gangue. Spatial distribution of kaolinite along mineralized veins is not well understood due to its sparse occurrence. From mineral relationship and petrographic evidence, kaolinite overprints sericite-illite alteration indicating that kaolinite formed after sericite-illite alteration. It is most easily identified in samples through shortwave infrared (SWIR) spectroscopy.

4.2.5 Lithocap Alteration

Lithocap alteration is present in the eastern part of Shahumyan, above the northern mine entrance. The alteration is distinguished by intense silicification, K-alunite and Na-alunite, diaspore, kaolinite, dickite, and minor hematite and pyrite. Two generations of alunite are observed: a clear to pinkish coarse grained potassium rich alunite in vugs replacing host rocks; and a very fine grained pinkish white Na-rich alunite found exclusively within fractures. Mederer (2013, unpublished) proposes Na-rich alunite as the precursor to K-rich alunite. All alteration minerals are identified through SWIR and XRD analyses. The clay minerals, kaolinite, diaspore and dickite overprint plagioclase phenocrysts completely and quartz primarily replaces groundmass. The lithocap alteration found at Shahumyan is representative of acid-sulfate alteration.

4.3 Mineral Compositions

Alteration minerals identified through petrographic studies are confirmed using SWIR and XRD analyses, particularly to distinguish between various white-mica and

chlorite species. Mineral crystallinity of sericite/illite has been frequently linked with hydrothermal alteration intensity and in turn temperature (i.e. Merriman and Frey, 1999; Ji and Browne, 2000; Harraden et al., 2013 and etc); where, poorly crystalline minerals are associated with weak hydrothermal alteration and low temperatures while the opposite is true for highly crystalline sericite/mica. Additionally, alteration mineral stabilities are sensitive to pH, temperature and exsolution of gases (e.g. fugacity increase or decrease) due to boiling (Simmons and Browne, 2000), and identifying the correct species can lead to constraining such conditions.

4.3.1 White Mica Group

All identified alteration zones at Shahumyan show varying degrees of white-mica alteration (Figure 4.2 D, E, F, G). The white-mica group refers to a group of fine-grained phyllosilicate minerals that includes: illite, paragonite, muscovite and phengite. It is found in a wide variety of rocks due to weathering or hydrothermal alteration. All white micas are spectrally characterized by a prominent absorption feature between 2180-2228nm and two secondary peaks close to 2344 and 2440nm (Figure 4.3 A). The wavelength range indicates a compositional variation from paragonitic (2180 nm), muscovitic (2200 nm) to phengitic (2228 nm). A Dundee Precious Metals SWIR dataset is used in conjunction with one collected during this study to identify prevalent white-mica populations within the deposit. At Shahumyan, white-mica features range between 2,190 to 2,210 nm, consisting of two populations; one concentrated at 2,198 nm and one at 2,207 nm. The 2,198 nm population is relatively more enriched in Zn (> 0.5% Zn) than the 2,207 nm population. In some cases, progressive transition from K-rich illite to phengite indicate alteration vectoring to high-grade ore (Meunier, 2005; Murakami et al., 2005). At Shahumyan white-mica compositions does not directly vector towards higher grades or identify a specific hydrothermal; however, white-mica composition do vary between K-rich and relatively more Fe-rich white-micas. Sericite

crystallinity, is calculated by comparing the depth of the 2200 nm and the 1900 nm features in SWIR analyses and is confirmed through XRD analyses by analysing the Full Wavelength Half Maximum (FWHM) of the 2^θ feature. At Shahumyan, samples containing sericite show increasing crystallinity with depth for white mica (sericite-illite).

4.3.2 Chlorite Group

Chlorites are part of the phyllosilicate group containing Al, Mg and Fe end members; spectrally Mg and Fe can be identified with Mg-OH and Fe-OH absorption features. The spectral positions of the Mg-OH and Fe-OH features depend on the Fe content. Low or High iron content leads to displacement of absorption feature position to either shorter or longer wavelengths (respectively) (Figure 4.3 B). XRD and SWIR analyses of chlorite at Shahumyan indicates Mg-Fe rich chlorite, indicating that chlorite composition is typically clinochlore (rapidolite- a subtype of clinochlore). Chlorite replaces mafic minerals in groundmass and hornblende phenocrysts (Figure 4.2 F, J, K).

4.3.3 Kaolinite Group

Kaolinite is rare but observed locally within the proximal assemblage and vein gangue. From mineral relationship and petrographic evidence, kaolinite overprints sericite-illite alteration indicating that kaolinite formed after sericite-illite alteration. It is most easily identified in samples through shortwave infrared (SWIR) spectroscopy. Kaolinite crystallinity is linked with hydrothermal alteration intensity similar to sericite-illite crystallinity and is calculated from SWIR analysis by comparing depths of the 2180nm and 2160nm doublet feature (Figure 4.3 C). At Shahumyan kaolinite crystallinity ranges from moderate to well crystalline, kaolinite crystallinity is highest within the lithocap assemblage. Kaolinite is observed to replace sericite/illite within proximal

and intermediate alteration assemblages (Figure 4.3C).

4.4 Geochemistry of Alteration Assemblages

Zoned hydrothermal alteration assemblages surrounding ore deposits is the mineralogical expression of compositional gradients and temperature centered on hydrothermal fluid pathways, and in turn relate to processes that form economic ore deposits. These compositional gradients in the sense of gains and losses relative to country rock can vector towards mineralization as shown by previous studies, using trace pathfinder elements and base metals (As, Sb, Hg, Tl, Cu, Zn, Pb) (e.g. White and Hedenquist, 1990,1995; Carlile et al., 1998; Hedenquist et al., 2000). Whole-rock geochemical studies were widely applied to VHMS (e.g. Gemmell and Large, 1992; Whitford and Ashley, 1992; Callahan, 2001; Gemmell and Fulton, 2001; Large et al., 2001a-c) and orogenic gold deposits (e.g. Eilu et al., 1997) and more recently porphyry-epithermal deposits (e.g. Booden et al., 2011; Warren et al., 2007; Gemmell, 2007; Mauk and Simpson, 2007; Bouzari and Clark., 2006; Leavitt and Arehart, 2005) to evaluate compositional gradients associated with hydrothermal alteration.

To classify and evaluate alteration zones and gradients, lithogeochemical analyses of least altered rocks are compared with representative samples from identified alteration assemblages: proximal (n=13); intermediate (n=13); distal (n=13). In addition, three samples from the Mederer et al (2013) sample dataset are used to evaluate geochemical characteristics of least altered samples. Samples from the current study were sent as two separate batches and analysed at Acme Labs, Vancouver British Columbia, Canada. A detailed procedural and analytical framework is outlined in Appendix 1. All samples are taken from the Barabatoom group and are limited to coherent volcanic rocks. Interbedded volcanoclastic layers and samples containing vein vol% greater than 10% within a single sample are avoided as they would not ac-

curately represent mass changes within the host rocks.

4.4.1 Mass Transfer Calculations

Least mobile elements are identified through examination of the concentration ratio of the element between least-altered and altered rocks. Titanium (Ti) and Aluminum (Al) are the least mobile; however Al is chosen as the reference species because it shows least mobility/variation across the different assemblages. Mass change calculations of all mobile constituents is performed between identified alteration zones and least altered rocks using the modified Gresens (1967) equation (Eqn 4.3.1) (Warren et al., 2007; Grant, 1986):

$$\text{(Eqn 4.1): } \Delta X = [(X^{Ai}/X^{Bi}) \times X^B] - X^A$$

where X^A and X^B are the concentrations of an element in fresh and altered rocks, respectively, and (X^{Ai}/X^{Bi}) is the ratio of the concentration of least mobile constituent in unaltered and equivalent altered rock. The modified equation varies from the original as it conserves volume changes and in effect removes any impact of volume change between least-altered and altered rocks. This calculation calculates the absolute mass change between an alteration assemblage and least altered rocks and is most useful for major oxides and metals. However in the case of trace elements and REE's the absolute change is negligible and to identify any trends, a relative mass change percentage must be calculated. Relative mass change percentage is calculated by normalizing mass change values to least mobile element such as Al. Additionally a 95% confidence interval for each trace and rare earth element has been calculated to determine if the calculated mass change is significant enough to indicate true mobility of the element. An element is considered immobile if the 95% confidence interval intersects the zero relative mass % line. These elements are highlighted in Figure 4.4 A-C.

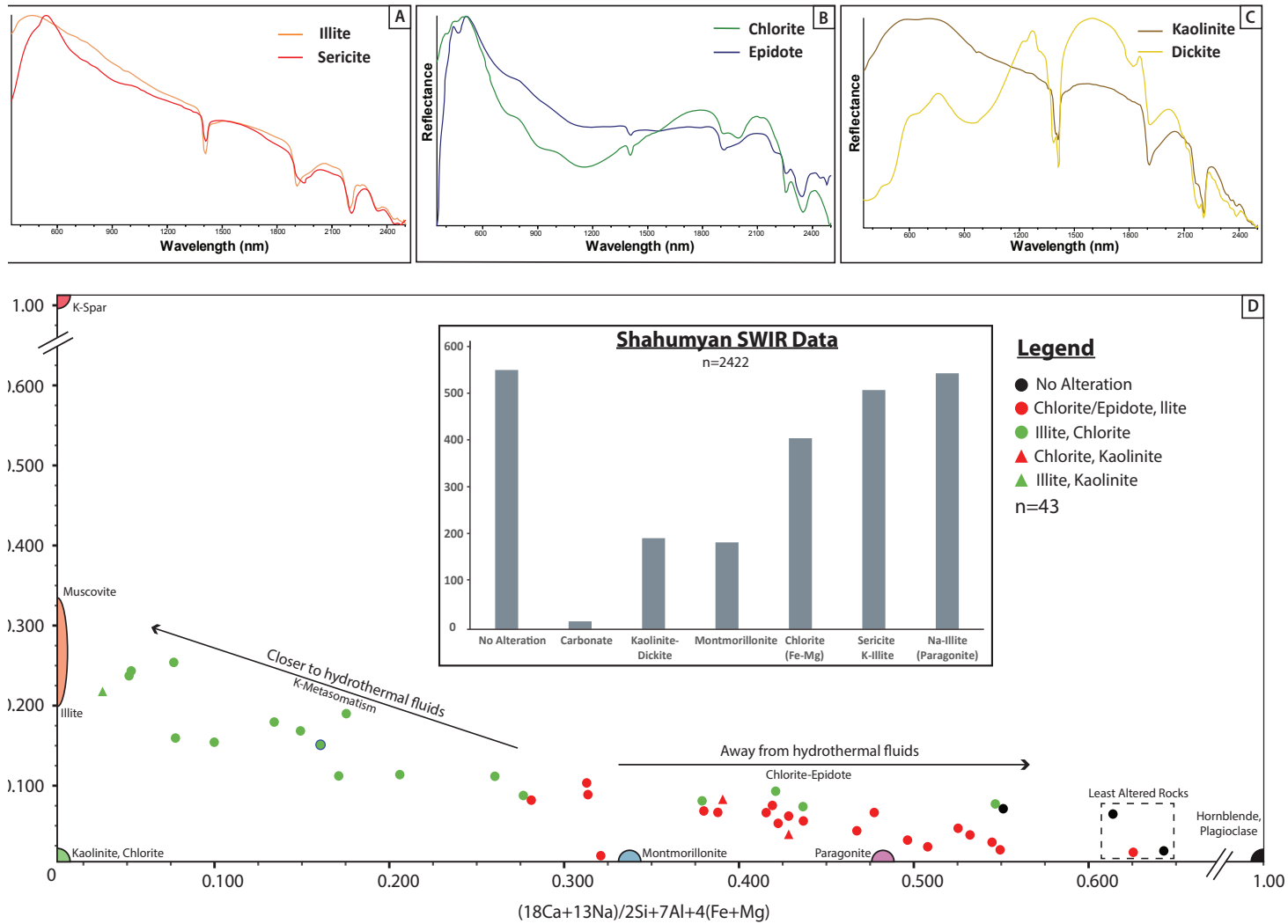


Figure 4.3: (A-C) Shortwave Infrared (SWIR) response for minerals observed at Shahumyan; Sericite-Illite(A), Chlorite-Epidote(B), and Kaolinite-Dickite(C). (D) A molar element ratio diagram is used to graphically evaluate alteration trends observed at Shahumyan. Least altered rock samples or samples further away from the hydrothermal fluids would plot closer to 1.0 on the x-axis. Molar element ratio diagram and relevant indices after Urqueta et al. (2009). Histogram compiles all SWIR analyses at Shahumyan.

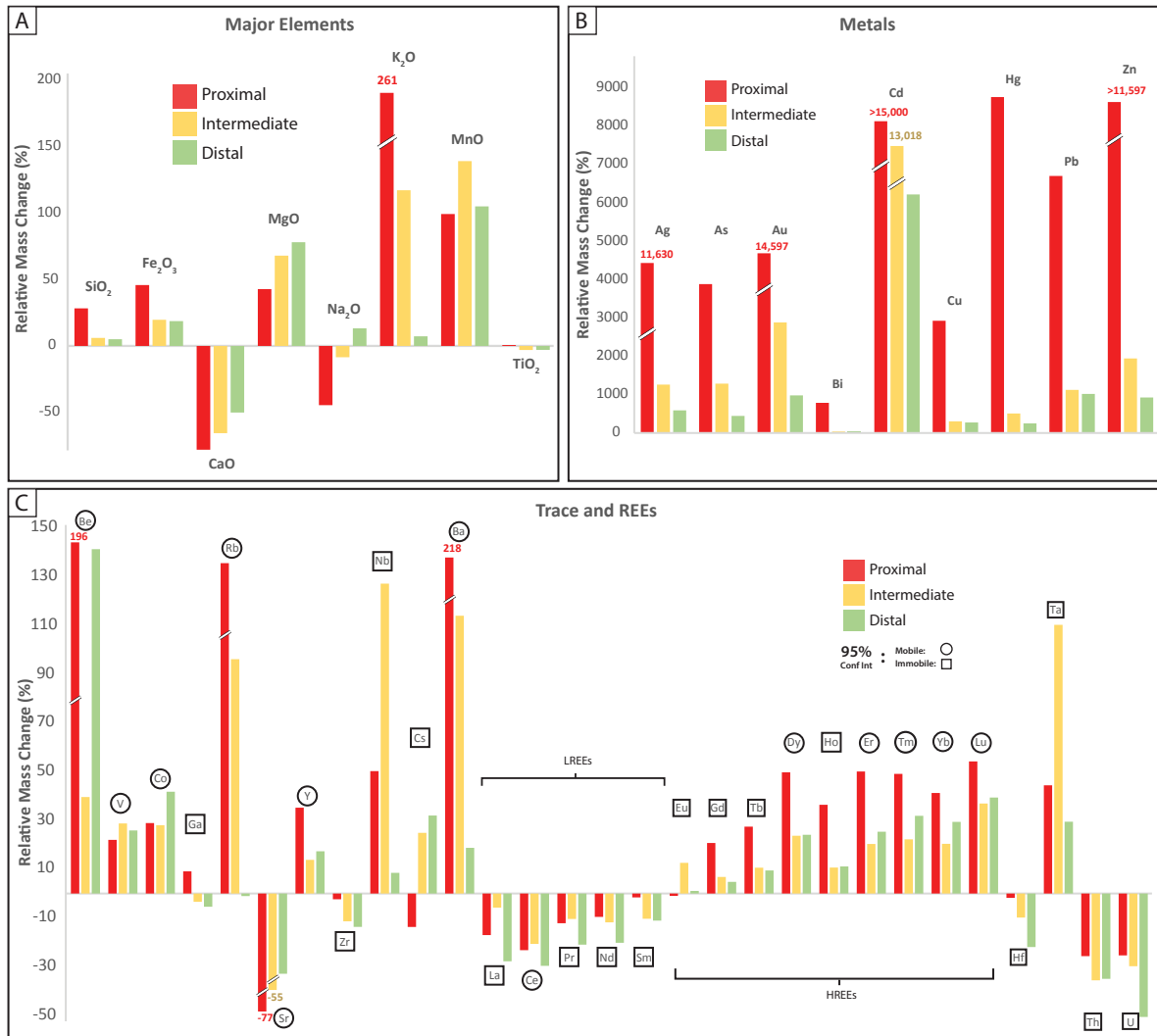


Figure 4.4: (A) Relative mass balance of major elements in the proximal (red), intermediate (yellow), and distal (green) assemblages. (B) Relative mass balance of precious and base metals in observed alteration assemblages. (C) Relative mass balance of trace and REE's in observed alteration assemblages.

4.4.1.1 Major Elements Mass Transfer

All major elements (Si, Fe, Mg, K, Mn) with the exception of Ca and Na are higher in altered rocks relative to least altered rocks (Figure 4.4 A). Addition of Si, Fe, and K is greatest in the proximal assemblage and least in the distal alteration assemblage. A 95% confidence interval analyses indicates K, as immobile in the distal assemblage. Compared to least altered rock, Mg content is highest in the distal assemblage and decreases toward the proximal assemblage. This reflects progressively increasing

abundance of chlorite towards the distal assemblage. Calculated confidence intervals indicate all elements are significantly mobile except for Ti which has already been discussed in previous sections to be another least mobile element along with Al.

Ca and Na are lower in altered rocks compared to least altered rocks, both show significant loss in the proximal assemblage and least loss in the distal assemblage. A 95% confidence interval analyses indicates Na is immobile in the intermediate and distal assemblages compared to least altered rocks.

4.3.1.2 Base and Precious Metal Mass Transfer

Metal concentrations are higher in altered rocks compared to least altered rocks; with highest concentrations found in the proximal assemblage and lowest concentrations in the distal assemblage (Figure 4.4 B). Absolute mass change values indicate Zn as the most significant increase compared to least altered rocks followed by Cu, Pb, Au and Ag. However, relative mass change values show Cd to be significantly added compared to least altered rocks followed by Zn, Au, Ag, Hg, Pb, Cu and As. The primary host mineral for cadmium is sphalerite but may also be hosted in minor amounts by galena, chalcopyrite and pyrite (Schwartz, 2000). The Cd/Zn ratio in sphalerite is dependent on ligand activities, pH and temperature of ore forming fluids (Schwartz, 2000). Calculated confidence intervals indicate all metals with the exception of Pb to significantly vary from least altered rocks in all assemblages. The Pb concentration in distal assemblages is similar in abundance to least altered rocks.

4.3.1.3 Trace Elements and REE Mass Transfer

Significant mass changes in trace elements are limited to Be, V, Ba, Co, Rb and Sr (Figure 4.4 C-D). Additionally, HREEs seem to be added in alteration zones and LREEs are removed in alteration zones. Calculated confidence intervals (95%)

indicate only some REEs to be mobile and others are immobile regardless of relative mass change values. REE concentrations are well within variance and therefore are presumed to be natural variation within the rock and not likely related to hydrothermal alteration. Barium and rubidium both show progressively higher net gains towards veins and reflect K net gains. The REEs can be transported in form of fluoride and chloride complexes in nearly neutral-pH fluids (Wood, 1990; Van Middlesworth and Wood, 1998) which can explain the mobility of Ce, Dy, Er, Tm, Yb, and Lu.

4.4.2 Molar element ratio diagrams and alteration trends

Mass transfer effects are evaluated graphically and related to associated alteration minerals using molar element ratio calculations from whole-rock geochemical data which are fundamentally similar to the Pearce element ratio techniques of Stanley and Madeisky (1994). Molar element ratio diagrams eliminate volume changes when comparing hydrothermally altered rocks to protoliths and express geochemical analyses to mineral stoichiometries of hydrothermal minerals (Stanley and Madeisky, 1994; Madeisky, 1996). This allows geochemical trends to be related to alteration mineralogy and zonation identified from field observations. The molar element ratio diagram evaluating hydrothermal alteration must reflect protolith composition as such a (K/Al) Pearce element ratio has been plotted against an alteration index for andesites: $[(18Ca+13Na)/(2Si+7Al+4(Fe/Mg))]$ outlined by Urqueta et al. (2009) (Figure 4.3 D).

This index is composed of two separate indices: $(18Ca+13Na)$ and $[2Si+7Al+4(Fe/Mg)]$. When plotted against each other the plagioclase-hornblende line will have a control line slope of 1.0 and the epidote control line will have a slope of 2.67. Stoichiometric node points for hornblende, plagioclase for unaltered andesites and kaolinite, chlorite, K-feldspar, biotite, muscovite, paragonite, montmorillonite and illite for altered andesites can be plotted using this index.

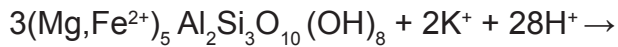
The (K/Al) vs $[(18Ca+13Na)/(2Si+7Al+4(Fe/Mg))]$ plot (Figure 4.3 D) is used to illustrate compositional and spatial trends of alteration zones encompassing mineralized veins at Shahumyan. In the diagram, unaltered or least altered rock occur closest to (1,0) and potassic altered rocks occur at (0,1). Muscovite plots at (0, 0.33), illite plots between 0.2 and 0.33 on the K/Al axes. Kaolin group minerals and chlorite will plot at (0,0). Mixtures of chlorite, illite and or kaolinite which are seen in epithermal deposits plot on the line between 0.2 and 0. This index does not properly distinguish between chlorite and kaolinite group minerals. The overall trend observed in this plot is an increasing K-metasomatism trend associated with the proximal alteration zone. The principal mass change components associated with base and precious metal mineralization are K, Si and Fe. In addition to compositional and spatial trends the plot also delineates K-metasomatism intensity.

4.4.3 Alteration Discussion

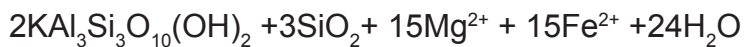
At Shahumyan, alteration minerals progressively replace hornblende, biotite and plagioclase as confirmed from petrography. This sequence employs primary control on alteration mineralogy and whole rock geochemistry of host rocks. Igneous hornblende in the proximal assemblage is completely destroyed and replaced by sericite/illite, chlorite and blebby pyrite whereas distal assemblages show a chlorite, epidote and pyrite assemblage. The chlorite-epidote (distal) alteration front likely progressed during higher temperature fluids and has been overprinted by K-metasomatism, and white-mica minerals at lower temperatures or at lower pH. This is evidenced by the sericite/illite replacement of chlorite which can be represented by the chemical reaction in Eqn 4.5.1 where chlorite is being replaced by sericite/illite with an influx of potassium-rich fluids. The liberated iron reacts with H_2S within hydrothermal fluids to create pyrite, in addition to pyrite formed from hornblende-chlorite alteration. Furthermore

hornblende has been reported to alter directly into interlayered chlorite-illite at lower temperatures of formation compared to chlorite alteration (Rahman, 1995; Schardt et al., 2001); which, represents the intermediate alteration assemblage at Shahumyan.

Eqn 4.2



Chlorite (Clinocllore)



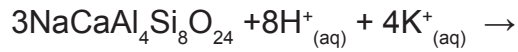
Sericite-Illite

Quartz

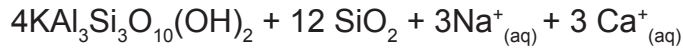
Igneous plagioclase is progressively destroyed by K-metasomatism, leading to loss of Na and Ca and gain of K. Significant loss of both elements reflects the destruction of hornblende and plagioclase in the proximal assemblage which decreases in the intermediate and distal assemblages. A progressive destruction of igneous plagioclase would result in Na and Ca loss and replacement by white mica minerals such as sericite or illite (Eqn 4.5.2) or paragonite. Illite and sericite contain K, and paragonite contains Na. Partial substitution of K into plagioclase could produce interlayered paragonite and K-illite; which, has been identified through SWIR analyses. Proximal assemblages contain narrow silicified zones with higher vein abundance, and disseminated sulphides (pyrite, ± chalcopyrite) which explain the increase in Si and Fe. The proximal assemblage is intensely sericite/illite altered and explains the increase in K, potassium reduces significantly in the intermediate and distal assemblages, which is reflected by sericite-illite content in these assemblages. The significant loss of Ca in the proximal assemblage is attributed to complete destruction of plagioclase and hornblende. Although rare, calcite is observed to replace relict plagioclase after K-metasomatism alteration. It should be noted that although late stage calcite precipitation is prevalent within veins and veinlets of proximal assemblages it does not offset the net

loss of calcium within the altered rocks.

Eqn 4.3



Plagioclase



Sericite-Illite

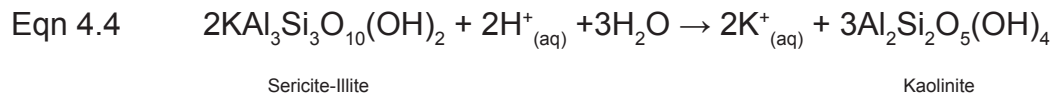
Quartz

The abundance of epidote in the distal assemblage of veins at Shahumyan can be interpreted to be a consequence of lack of dissolved CO₂ with fluids, which stabilized epidote early in the hydrothermal system. Alternatively, if CO₂ had been present in abundance, calcite would be chemically stable over epidote. Formation of epidote is also temperature dependant (220 to 340°C).

K-metasomatism alteration also affects Sr, Ba, V, Co and Rb, where Sr shows mass loss and Ba, Rb and V are enriched. Sr shows progressively lower net loss away from veins and reflects Na loss from plagioclase. Ba and Rb are relatively immobile elements and show inherent enrichment relative to least altered rocks; however, Ba could be significant gained if carbonates are present in samples. Cobalt content may be attributed its substitution in Mg Chlorite. Vanadium has been observed in numerous deposits (e.g., Porgera, Emperor, Tuvatu; Corbett, 2005) to substitute into white mica group minerals. High concentrations of vanadium (>17 wt% V) and potassium crystallize roscoelite, a vanadium rich muscovite (Fleet et al., 2003).

Kaolinite is observed to replace sericite-illite through petrographic studies, however its fineness and minor abundance makes it difficult to identify optically but is easily identified by XRD and SWIR. Hydrothermal kaolinite has been reported to form with increasing acidity of hydrothermal fluids in epithermal deposits (Zhu et al., 2011).

Acidic fluids (i.e., H⁺ metasomatism) can react with sericite/illite to form kaolinite as shown in reaction Eqn 4.5.3. It is also possible to form kaolinite from plagioclase. An increase in acidity of hydrothermal fluids due to fluid-rock interaction can occur once the buffering capacity of the host rock is diminished. Buffering capacity of the host rock is determined by the feldspars (plagioclase) present in the rock. In the proximal alteration assemblage plagioclase has been predominantly altered to sericite/illite, thus reducing the ability of fluids to be buffered and precipitating trace amounts of kaolinite. Boiling is another function by which kaolinite can overprint sericite/illite or plagioclase. Kaolinite overprinting indicates hydrothermal fluids evolved to acid-sulphate composition (H₂S oxidation) as opposed to near-neutral pH fluids which are required to form sericite/illite (Henley and Hedenquist, 1986; DeRonde and Blattner, 1988).



4.5 Fluid Inclusions

Fluid inclusion data provide an estimate of prevailing fluid temperature and salinity during hydrothermal activity which produced Cu-Zn-Pb and Au-Ag telluride mineralization at the Shahumyan deposit. A paragenetic study of Shahumyan veins identified three stages: (Stage 1) a pre-ore Stage, (Stage 2) a main stage; which is subdivided into Stages 2a and 2b, and (Stage 3) a post-ore stage. Stage 2a is predominantly base metal rich consisting of Cu, Zn, and Pb mineralization and Stage 2b is observed to contain Au- Ag telluride mineralization in addition to Cu, Zn and Pb mineralization. A total of thirty-four samples are used in paragenetic studies; of which, six samples containing representative hydrothermal stages of Stage 2a, 2b and 3 are chosen for fluid inclusion work. It should be noted that each of these samples contain multiple hydrothermal stages, which is a result of continuous hydrothermal fluid trans-

Mineral	Fluid Inclusion Type	Observed Frequency	Liquid %	Vapor %	Solid %	Boiling (Y/N)	Inclusion Minerals	Comments
Quartz	Isolated	Common	90-95	5-10	0	N		
	Primary	Common	90-95	5-10	0	N		
	Pseudo-Secondary	Common	90-95	5-10	0	N		
Honey Brown Sphalerite	Primary 1	Abundant	0	0	100	N	Cpy	
	Primary 2	Very Rare	85-95	5-15	0	N		
	Pseudo Secondary	Common	90-95	5-10	0	N		
	Secondary 1	Rare	0-5	95-100	0	Y		Within same trail
	Secondary 2	Rare	85-95	5-15	0	Y		
Yellow Sphalerite	Primary	Very Rare	85-95	5-15	0	N		
	Pseudo Secondary	Common	90-95	5-10	0	N		
	Secondary 1	Rare	0-5	95-100	0	Y		Within same trail
	Secondary 2	Rare	85-95	5-15	0	Y		
Dark Sphalerite	Primary	Adundant	0	0	100	N	Cpy	
Calcite	Isolated	Common	90-95	10-5	0	N		
	Pseudo-Secondary	Rare	90-95	10-5	0	N		

Table 4.1: Summary of observed fluid inclusion assemblages and their characteristics

port throughout the lifetime of the system due to repeated vein opening (see Chapter 3).

4.5.1 Fluid Inclusion Petrography

Primary, isolated, pseudo-secondary, and secondary fluid inclusions are classified using Roedder's (1984) textural criteria. Primary inclusions occur along growth surfaces in crystals, isolated inclusions are distributed randomly within the cores of crystals or between growth planes, pseudo-secondary inclusions crosscut growth planes and occur along minor fractures within a crystal but do not extend to the edges of a crystal, and finally secondary inclusions occur in secondary healed fractures permeating from the edges of a crystal, crosscutting primary inclusions.

Inclusions are observed in three different minerals: quartz, calcite and sphalerite which are sub-divided by color into: honey-brown sphalerite, yellow sphalerite and

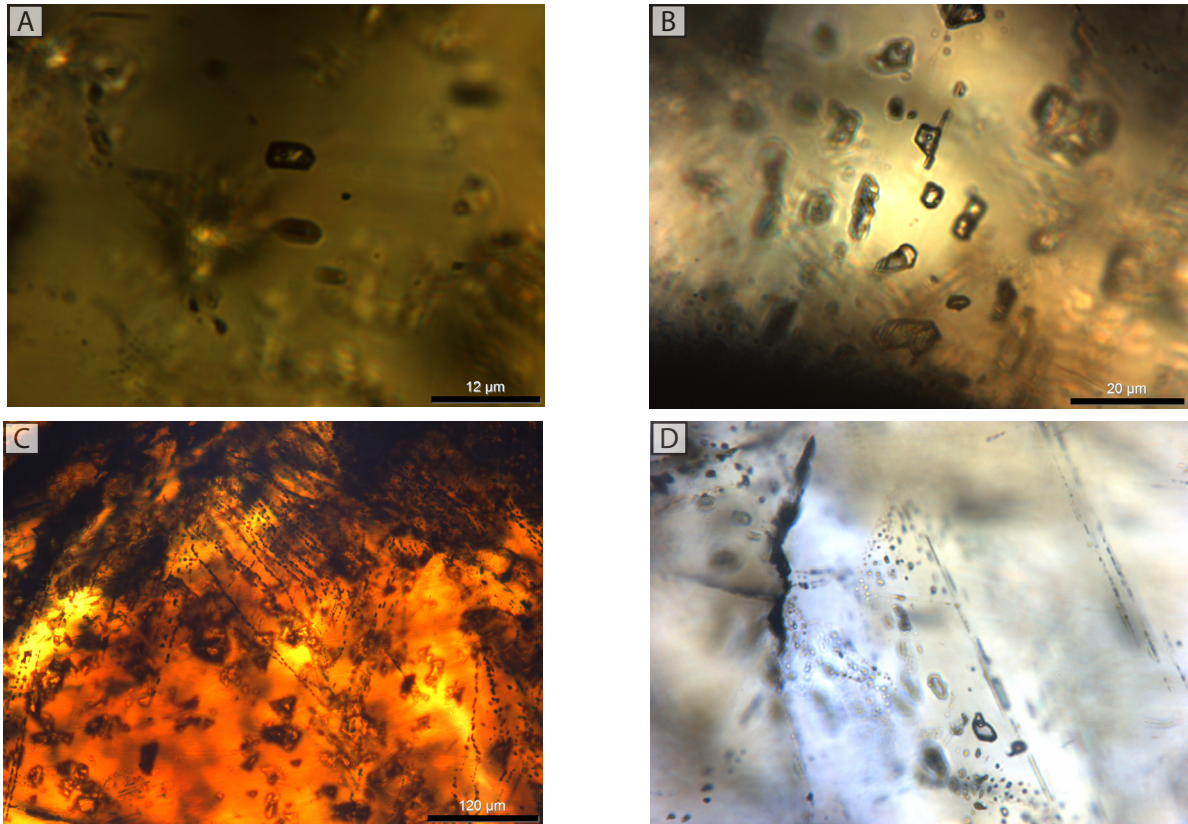


Figure 4.5 (A) pseudo-secondary L-V assemblage in honey brown sphalerite (B) primary L-V assemblage in honey-brown sphalerite (C) Primary solid fluid inclusions in honey brown sphalerite (D) pseudo secondary fluid inclusions in yellow sphalerite.

dark-sphalerite. Coarse crystalline quartz is present in all three hydrothermal stages; however, it is difficult to identify different quartz generations solely from petrography. Cathodoluminescence is a method that can further differentiate specific quartz generations; however, it is not pursued in this study. Honey-brown sphalerite is abundant in stage 2a and increasingly declines into stage 2b, relative to yellow/pale sphalerite. Pale-yellow sphalerite, progressively increases toward the end of stage 2a and into stage 2b. Dark sphalerite is present late in stage 2b and overprints earlier honey-brown sphalerite and pale-yellow sphalerite, it is primarily present along fractures within earlier sphalerites. Dark sphalerite is intergrown with and/or contains inclusions of Au-Ag telluride minerals and is assumed to be paragenetically linked. Dark sphalerite is non-translucent which makes it difficult to identify any assemblages with the exception of solid chalcopyrite inclusions, identified through reflected petrography.

Calcite is abundant in stage 3 and represents the waning stages of the hydrothermal system.

In total, 210 inclusions, within 75 assemblages are measured across all minerals and are further summarized in Table 4.1. Fluid inclusions sizes range from <2-14 μm (long axis) and <1-4 μm (short axis), larger inclusions (>6 μm , short axis) are quite rare, and are limited to primary or isolated inclusions. Sphalerite crystals tend to be zoned and show primary solid and primary liquid-vapour rich inclusions present along growth planes (Figure 4.5 A,B). Primary solid inclusions are predominantly found in honey-brown sphalerite and dark sphalerite, and are composed of chalcopyrite (Figure 4.5 C). Pseudo-secondary assemblages within sphalerite are primarily oriented sub-parallel to perpendicular to growth planes and tend to terminate or propagate from the middle of a mineral grain and are liquid-vapour rich (Figure 4.5 D). Both quartz and calcite predominantly contain isolated and pseudo-secondary inclusions with liquid-vapour inclusions (Figure 4.6 A, B, C, D). Growth zones in both quartz and calcite contain primary inclusions with isolated inclusions in the cores of crystals.

Secondary inclusions are observed in sphalerite crystals and tend to show boiling features (Figure 4.7 B). Vapour-rich inclusions and liquid-vapour rich inclusions occur in a single FI assemblage trail. The presence of multi-phase (liquid-vapour) and single-phase (vapour) inclusions within a single assemblage trail suggests that vapour and liquid coexisted (i.e. fluid was boiling) at the time of trapping. Secondary inclusions are observed in both honey brown and yellow sphalerite; however, are unidentified in calcite and quartz. Secondary assemblages are observed to propagate from fractures containing dark-sphalerite and Au-Ag tellurides and crosscut earlier honey-brown and yellow sphalerite crystals (Figure 4.7 A). This paragenetic evidence would therefore indicate that these secondary assemblages represent an environment in which dark-sphalerite and Au-Ag tellurides were deposited.

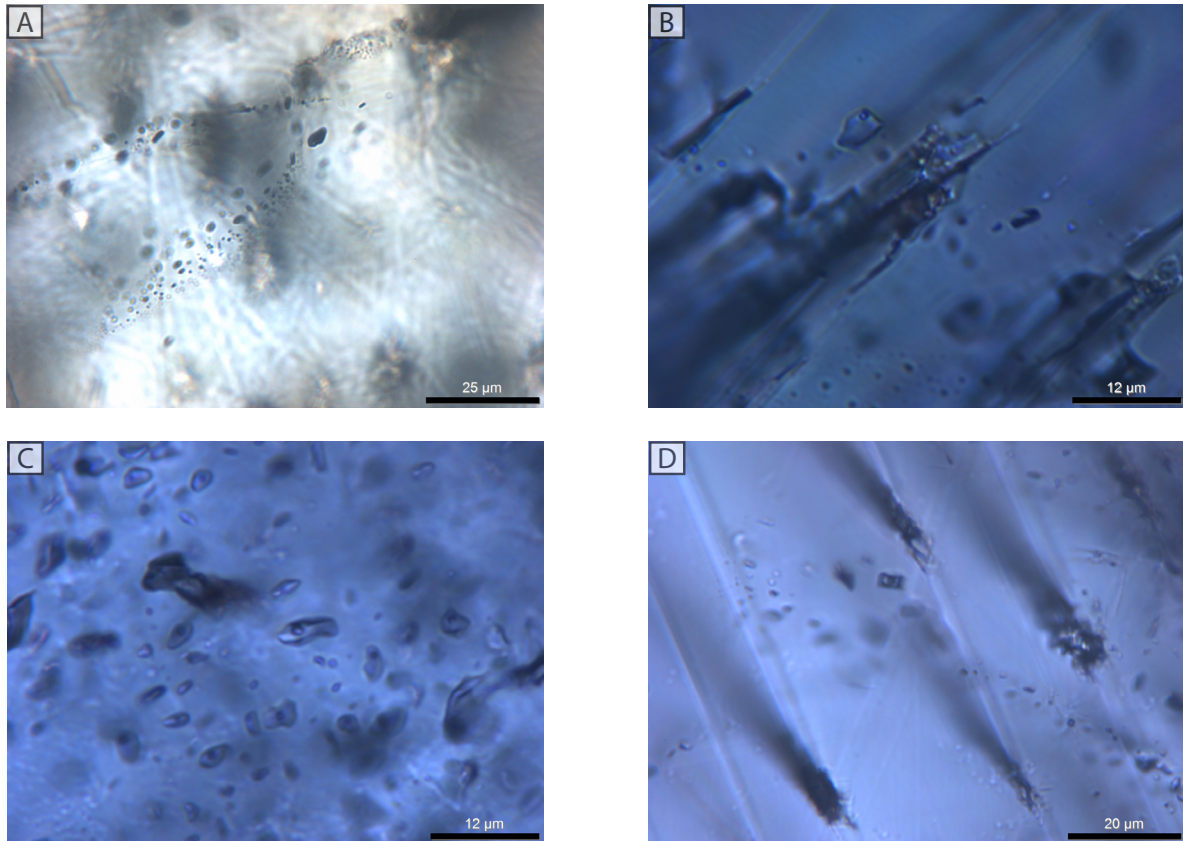


Figure 4.6 (A) Secondary FI assemblage with both L-V and V-L rich inclusions within a single FI trail in sphalerite (B) isolated L-V assemblage in calcite (C) Both isolated and pseudo secondary L-V assemblage in quartz (D) pseudo secondary and isolated L-V inclusions in calcite.

Measured homogenization temperatures represent minimum fluid trapping conditions within fluid inclusions unless the assemblage has been identified as a boiling assemblage in which case the measured homogenization temperature represents the exact trapping temperatures. If boiling is not evident in observed assemblages a pressure correction is needed in order to obtain real formation temperatures. However, there is a lack of an independent geothermometer or geobarometer such as sulphur isotopic data to apply a pressure correction. Therefore all measurements indicated are minimum trapping conditions, with the exception of boiling assemblages. Post-entrapment modification of several fluid inclusion assemblages are observed. These assemblages have not been analysed as they may record post entrapment conditions rather than original fluid conditions. Measured fluid inclusion assemblages within calcite are limited to isolated assemblages rather than primary or pseudo-sec-

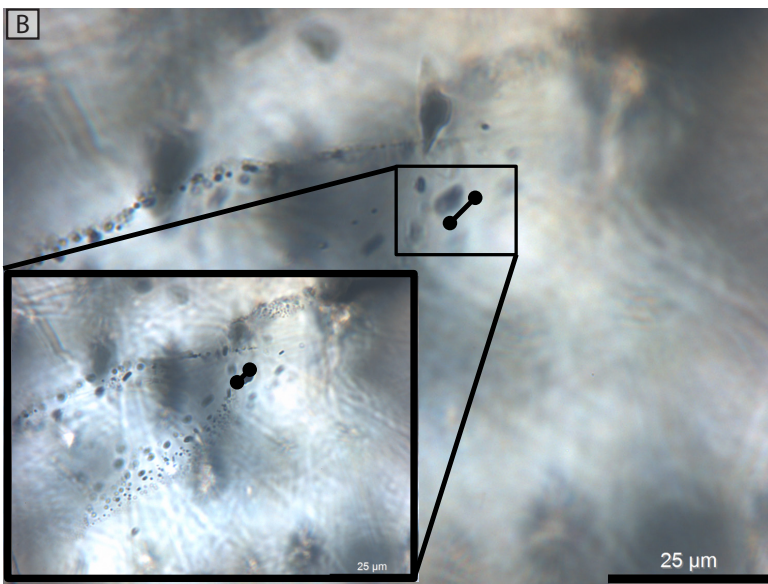
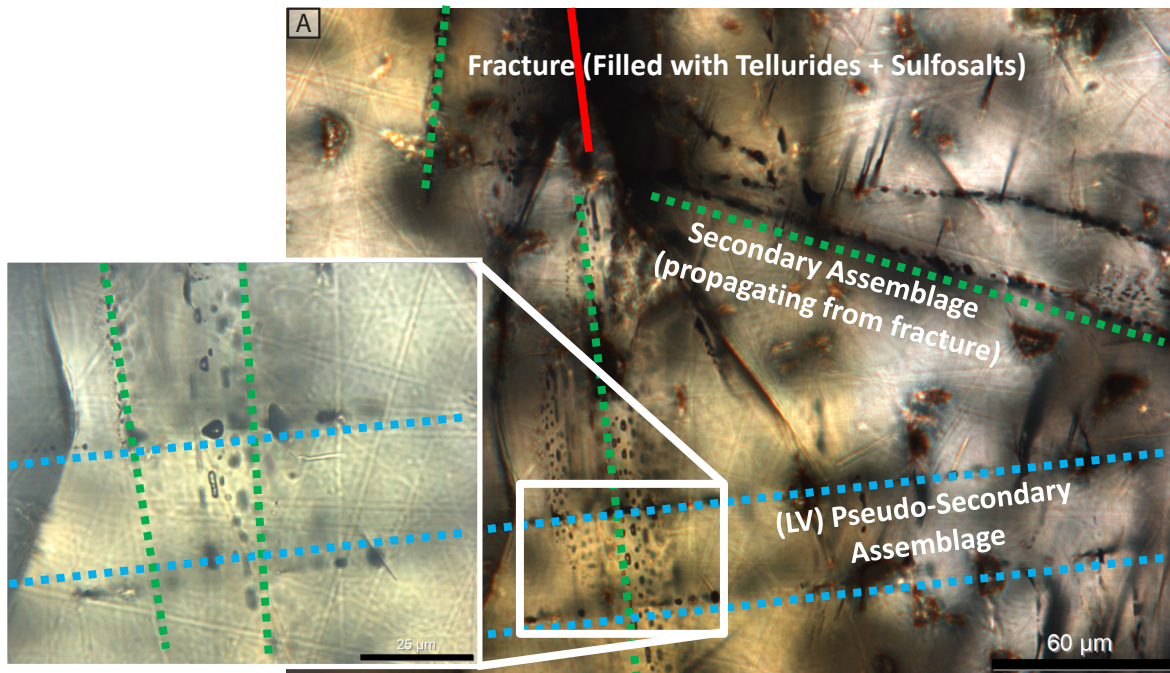


Figure 4.7 (A) Paragenetic sequence of boiling fluid inclusions associated with Au-Ag tellurides found in fracture. Boiling fluid inclusion assemblages (green dashed line) are considered secondary as they propagate from fractures extending across the entire grain and subsequently in filled with dark opaque sphalerite and tellurides. Boiling assemblages also crosscut earlier pseudo-secondary and primary assemblages (blue dashed lines). These boiling assemblages contain both liquid-vapor rich inclusions and low density, vapor-liquid rich inclusions. Presence of both va-

por rich and liquid-vapor rich inclusions is indicative of phase separation (boiling). (B) Vapor rich inclusion within a FI inclusion trail containing both L-V and V-L rich inclusions.

ondary assemblages in order to avoid leakage. Leakage refers to a loss of trapped fluid within the inclusion as a result of the heating and cooling experiments which lead to incorrect measurements.

4.5.2 Fluid Inclusion Results

All pseudo-secondary and primary isolated inclusions measured show relatively similar liquid-vapour ratios with typical liquid fill percentages ranging from 85-95%, indicating that trapped fluids are homogeneous within individual assemblages (Diamond, 2003). In contrast liquid-vapour ratios strongly vary within secondary assemblages indicating that fluids were inhomogeneous and likely in disequilibrium.

The eutectic temperatures (T_e) measured in all inclusions assemblages average approximately -21.6°C . Eutectic temperatures of -21.6°C are representative of a simple NaCl-H₂O system (Borisenko, 1977 and Crawford, 1981) therefore the NaCl-H₂O system is used to model salinities and temperatures (T_h).

Freezing experiments are conducted on sphalerite, quartz and calcite and are summarized in (Figure 4.8 A). Salinities are calculated from measured final ice-melting temperature (T_m) in the H₂O NaCl system using algorithms from Bodnar (1993). Salinities measured in primary and pseudo-secondary inclusions hosted in quartz and calcite range between 1.6 wt.% and 6.0 wt.% NaCl equiv. Salinities within both yellow and honey-brown sphalerite range between 4.0 wt.% to 6.6 wt.% NaCl equiv. However, secondary assemblages identified as boiling assemblages in yellow and honey-brown sphalerite range between 8.4 wt.% and 13.3 wt.% NaCl equiv. which are significantly higher than non-boiling assemblages.

Homogenization temperatures (T_h) measurements are conducted on sphalerite, quartz and calcite and are summarized in (Figure 4.8 B). Temperature (T_h) measurements for isolated inclusions within calcite range between 78°C and 150°C . Primary, isolated and pseudo-secondary inclusions in quartz have large variation of homogenization temperatures between 109°C and 275°C , with a median of 140°C . Measurements from primary and pseudo-secondary inclusions within honey-brown

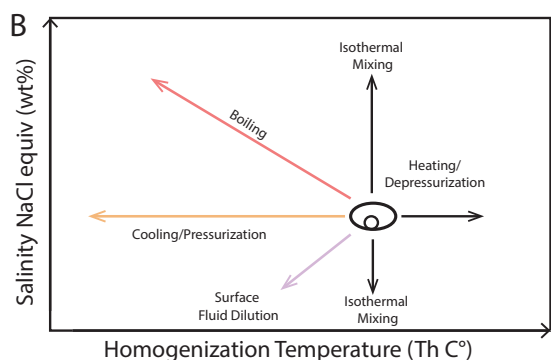
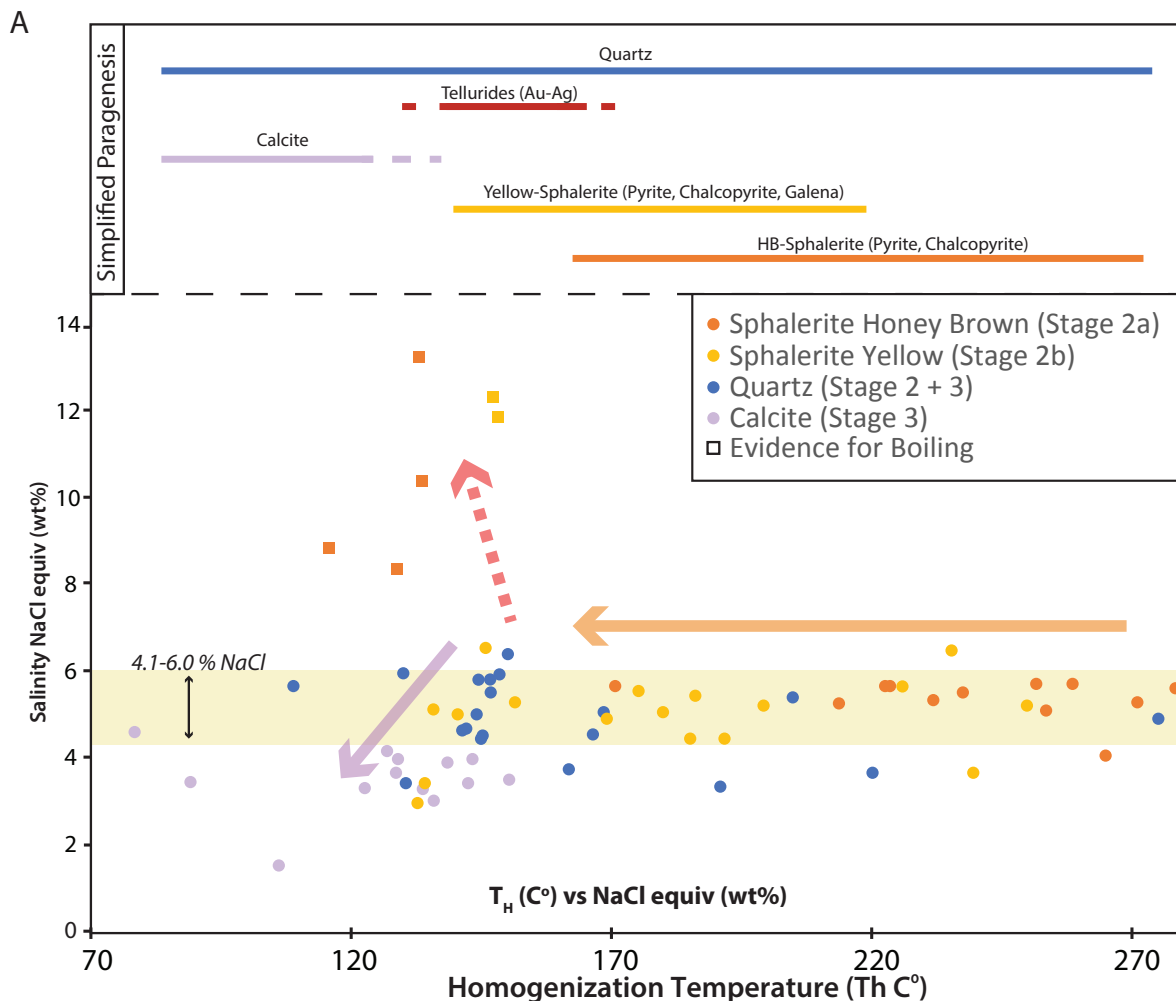


Figure 4.8: (A) homogenization temperature vs salinity graph for all FIA's hosted in quartz, honey brown sphalerite, yellow sphalerite and calcite from studied hydrothermal stages in precious and base metal veins. Arrows depict evolution of fluids and relate to precipitation processes as shown in (4.4.4B). The orange arrow interprets cooling fluids precipitating quartz, yellow and honey brown sphalerite at a steady salinity. The purple arrow infers possible mixing with meteoric waters resulting in dilution and drop in temperature precipitating calcite, quartz and yellow sphalerite. The red

dashed arrow infers boiling of existing hydrothermal fluids to dryness in an open system, resulting in elevated salinities.

sphalerite range between 171°C and 278°C with the median at 250°C Primary and pseudo-secondary measurements from yellow sphalerite range between 110°C and 250°C, with the median at 150°C. Homogenization temperatures of secondary fluid inclusions in honey-brown sphalerite ranges between 116°C and 134°C. Homogeni-

zation temperatures of secondary fluid inclusions in yellow sphalerite ranges between 120°C and 148°C.

4.5.3 Fluid Characteristics- Fluid inclusions

Salinity (wt.% NaCl equiv.) vs temperature of homogenization (T_h) data is plotted in Figure 4.8 (A,B) to identify the depositional processes such as boiling or effervescence, fluid mixing and simple cooling (Wilkinson, 2001). Boiling in a simple NaCl-H₂O system can occur as a result of temperature increase, a pressure decrease or a combination of these. Effervescence in contrast would indicate the fluids contained additional volatiles such as CO₂. Boiling or effervescence results in the production of vapour and in open systems loss of volatiles (i.e. H₂O, H₂S, CO₂ etc.) and partitioning of salts into the liquid-like phase. The residual liquid is more saline than the original fluid before boiling. Additionally, because of adiabatic cooling the liquid phase may also undergo cooling. Fluid mixing can be identified by significant salinity variations, as hydrothermal brines can be diluted by surface-meteoric waters or existing hydrothermal fluids can increase in salinity by influx of magmatic brines or by mechanical mixing of coexisting liquid and vapour.

FI assemblages in honeybrown sphalerite homogenize between 278°C and 170°C with a population peak at 250°C and a salinity between 4-6 wt. % NaCl equiv. Yellow sphalerite, paragenetically deposits after honey-brown sphalerite has T_h measurements of 110°C and 250°C, with a population peak at 150°C. Temperatures measured in quartz crystals, range from 109 to 275°C. Measured salinity in both yellow sphalerite and quartz crystals have similar range to honeybrown sphalerite. The overlap in temperature and salinity ranges allows the assumption that quartz is continuously being deposited in with sphalerite. Petrographic observation of sphalerite inclusions in quartz and vice-versa support this assumption. A gradual cooling trend for

base-metal precipitation beginning at approximately 270°C and ending at approximately 130°C is interpreted.

FI assemblages in Stage 3 calcite and quartz have T_h values between 78.4°C and 150.4°C with salinity measurements ranging from 1.6 to 6.0 wt. % NaCl equiv. A decrease in salinity from approximately 5.0 wt. % NaCl to 3.0 wt. % NaCl equiv. is correlated to a decrease temperature from 150°C to 100°C. This is interpreted as result of fluid mixing and dilution, precipitating Stage 3 quartz and carbonate. It can be argued that (Stage 3) carbonate could have condensed from a low-salinity condensate from boiling which is observed at Shahumyan. However, such processes would leave textural evidence such as bladed or plumose calcite which are absent. Additionally Stage 3 carbonate veins cut Stage 1 and Stage 2 veins indicating it is not related to an earlier stage.

The presence of calcite within the veins at Shahumyan could indicate that CO₂ could be a significant component within fluid inclusions. However, clathrate formation during freezing measurements was not observed in any inclusions; this indicates that CO₂ concentration within fluids is likely <1.5 mol% ($\leq 0.01m$) (Diamond 2001). It is important to identify CO₂ within a system because its presence has a strong effect on measured ice melting temperatures and significantly depresses the melting point of ice. This will result in overestimation of the fluid salinity, particularly in the low-salinity range (Catchpole et al., 2011; Hedenquist and Henley, 1985). However low CO₂ concentration in fluids as is the case at Shahumyan therefore has little effect on the salinity correction.

Boiling assemblages are readily identified as secondary fluid inclusion assemblages in honeybrown and yellow sphalerite and absent in late stage calcite and quartz. Salinities calculated for boiling assemblages (LV-rich) are relatively higher (8.4wt.% - 13.3 wt.% NaCl equiv.) than primary and pseudo-secondary assemblages

in the same minerals. Fluid inclusions measured in boiling assemblages are LV-rich, low density V-rich inclusions are observed but impossible to measure due to the inability to observe phase changes. Boiling assemblages are paragenetically linked to Au-Ag tellurides and are interpreted to represent depositional conditions for Au-Ag mineralization.

An absence of a distinct boiling trend (as shown in Figure 4.9 b) could indicate that boiling was localized and periodic within Shahumyan veins. Localized periodic boiling can be a result of localized faulting and/or fracturing assisted by buildup of pore-fluid pressures in a hydrostatic regime.

4.6 Physiochemical Constraints

4.6.1 Fluid Chemistry, pH and Temperature

Activity-activity and temperature-pH diagrams are constructed using the Geochemists Workbench package (Bethke and Yeakel, 2014) using a modified LLNI thermodynamic database (modified after SOLTHERM database: Spycher and Reed, 1990a, 1990b; Reed and Spycher, 1992) to explain the formation of hydrothermal minerals in response to water-rock interaction (alteration assemblages).

Figure 4.9 shows the stabilities of common phyllosilicates minerals observed at Shahumyan plotted as a function of K^+ , Mg^{2+} , and H^+ ; assuming fluids are quartz- H_2O saturated at temperatures $300^\circ C$ and $250^\circ C$. The diagrams use a white-mica and chlorite base system that plots mineral relationships in an $Mg^{2+}/(H^+)^2$ and K^+/H^+ space. Sericite/Illite activity, chlorite activity, K, Na and CO_2 concentrations are estimated and/or calculated from microprobe and fluid inclusion data to construct Figure 4.9.

Temperature and salinity ranges for each stage are constrained from fluid inclusion measurements. Stage 2a temperatures (T_h) responsible for base-metal mineral-

ization are approximately 250°C (270-230°C) with an average salinity of 4.8 wt% NaCl equiv. Stage 2b fluids responsible for both precious and base-metal mineralization are approximately 150°C (170-130°C) and have a higher salinity range between 8.4 and 13.3 wt% NaCl equiv . These temperatures and salinity ranges are used in the activity and temperature-pH plots for each stage.

The activity of sericite/illites was determined using the relationship equation outlined by Bird and Norton (1981):

$$a_{(ms)} = (X_{K+A})(X_{Al3+M(2)})^2(X_{Al3+T10})(X_{Si4+T1m})(X_{Si4+T2})^2(X_{OH})^2$$

Electron microprobe analyses of sericite-illite grains from vein and vein-alteration assemblages yields an average $a_{(ms)}$ value of 0.55. Sericite grains tend to have similar $a_{(ms)}$ values. However in distal assemblages, $a_{(ms)}$ values are lower, though the actual activity chosen has very little effect on the mica stability field in the activity diagram, unless it is low (<0.1).

Microprobe analyses reveal that chlorite compositions are typically clinochlore (rapidolite- a subtype of clinochlore). The average activity of clinochlore from the illite-chlorite and vein chlorite have been calculated to an average value of 0.023 by assuming $a_{Ch} = (X_{Mg})^5$, where $X_{Mg} = Mg/(Mg+Fe+Mn+Al_{(octohedral)})$ (Cooke et al., 2001). The clinochlore stability field shown in Figure 4.9 for $a_{clinochlore} = 1-0.02$, behaves similarly to $a_{muscovite}$, where a change in $a_{clinochlore}$ has little to no effect on chlorite stability field in the constructed diagram.

At 300°C (Figure 4.9) the $\log (aMg^{2+}/a(H^+)^2)$ is estimated to range between 4-5 and the $\log (aK^+/aH^+)$ ranges between 2.0-3.0. Interaction of hydrothermal fluids with surrounding andesitic host rock increases $\log (aMg^{2+}/(aH^+)^2)$, resulting in chlorite formation. With decreasing temperatures, the stability lines of clinochlore-kaolinite-sericite move up (i.e. increased $\log (aMg^{2+}/(aH^+)^2)$) making it increasingly difficult for hydrothermal fluids to precipitate chlorite in the host rock and allowing sericite/illite

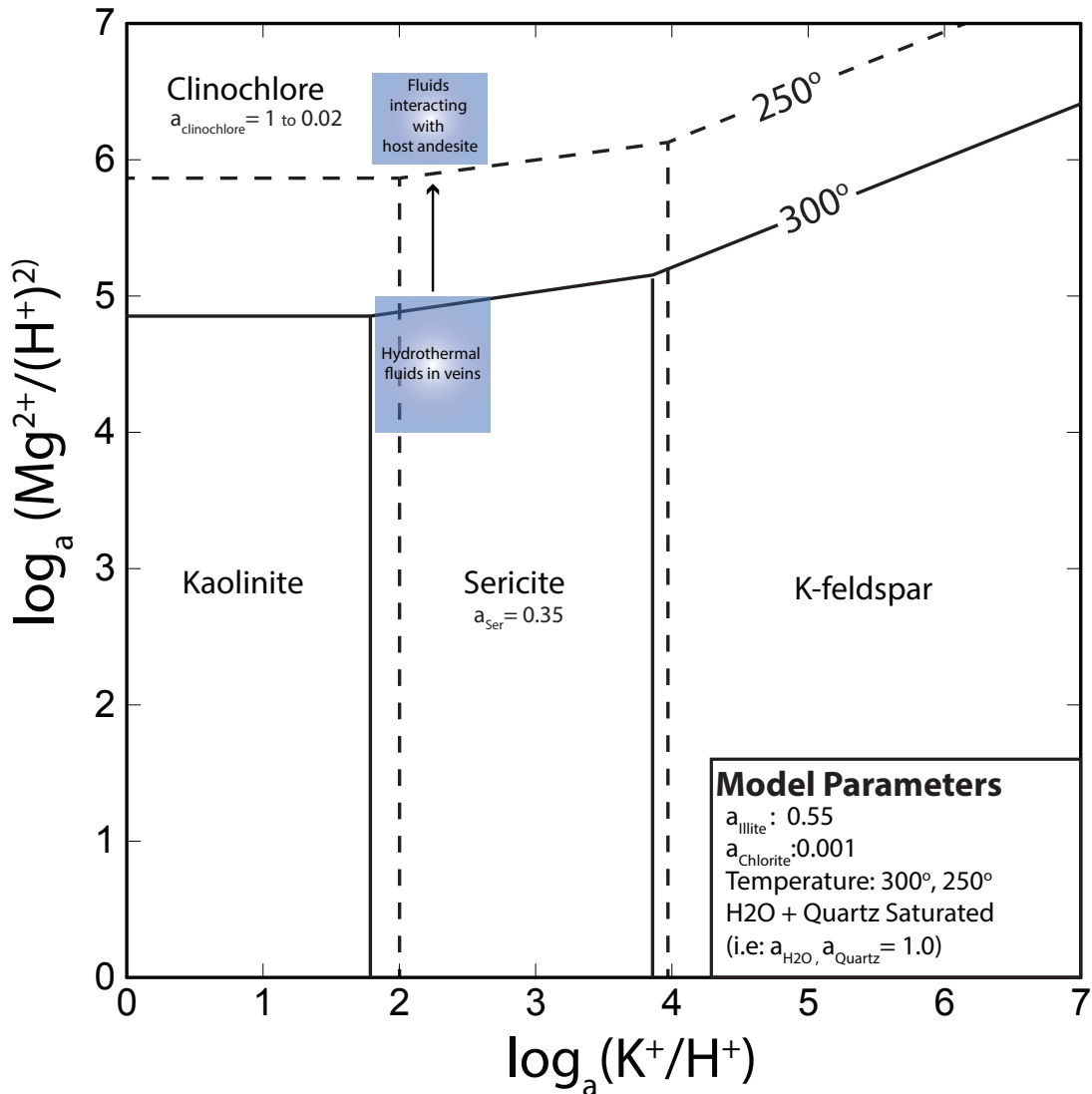


Figure 4.9: Activity diagram for principal phases in an MgO-Al₂O₃-SiO₂-H₂O system. Stability fields at 300°C in solid lines, and 250°C in dashed lines. Field 1 represents possible fluid conditions entering the Shahumyan vein system. Pathway between Field 1 and Field 2 represents fluid-rock interaction with the Barabatoom andesite-dacite, which locally raises $a_{\text{Mg}^{2+}}$ and allows chlorite and sericite/illite to form. At lower temperatures (250°C) a much higher $a_{\text{Mg}^{2+}}$ is needed to form chlorite, suggesting that chlorite more readily formed at high temperatures and sericite/illite forms at lower temperatures. Model parameters are discussed in text. Both chlorite and sericite/illite formation are also function of pH.

to preferentially form. Additionally, decreasing temperatures move stability lines for kaolinite-sericite-K-feldspar (increasing $\log (a_{\text{K}^+}/a_{\text{H}^+})$) to the right, indicating kaolinite-sericite-K-feldspar may precipitate from relatively more alkaline fluids. Assuming that fluid compositions stayed the same based on the narrow salinity range observed from fluid inclusion data; the dominant mineral assemblage at higher temperatures

(chlorite-sericite) would switch to a dominantly kaolinite-muscovite rich assemblage at lower temperatures. The composition of mineralizing fluids vary between the sericite and kaolinite stability fields as both minerals are present. Kaolinite is however less abundant within alteration mineral assemblages relative to sericite/illite. Kaolinite, as described in previous sections occurs prevalently in brecciation zones linked with elevated Au-Ag mineralization. This could therefore indicate that deposition of kaolinite at Shahumyan is not simply a function of temperature (cooling) and may also indicate fluctuations in fluid pH (H^+ metasomatism) and/or composition (a_{K^+}/a_{H^+} ratios).

As highlighted within the fluid inclusion studies, the absence of clathrate formation in all Stage 2 fluid inclusion assemblages limit the concentration of CO_2 in fluid to less than 0.01m (Hedenquist and Henley, 1985; Ulrich and Bodnar, 1988). For Stage 2 fluids carbonate concentration (mCO_2^-) is assumed to be $\leq 0.01m$, because there is a lack of clathrate formation and a lack of calcite within the stage. Low carbonate concentration is also reflected by the formation of epidote in the propylitic halo. If sufficient carbonate was present carbonate would have formed in lieu of epidote as discussed in previous chapters. The presence of massive euhedral calcite in Stage 3 likely indicates an increase in CO_2^- and Ca^{2+} in fluids responsible for Stage 3 mineral assemblages (values for this stage are not been calculated).

An estimate for $a_{(K^+)}$, needed to calculate K^+ mineral fields as a function of pH, is calculated based on the average salinity of chloride waters at Shahumyan (~4-6 wt% NaCl equiv for Stage 2a, 8-12 wt% NaCl equiv. for Stage 2b). This is combined with the assumption that Na/K ratios are 10:1 in hydrothermal fluids (Cooke et al., 1996). This ratio is appropriately within the range of values reported for geothermal waters discharged from wells in New Zealand, North America, the Phillipines and Iceland ($Na^+/K^+ = 4.9-19.4$; Henley, 1984a). Concentrations of 0.068-0.1 mNa and 0.007-0.01 m K^+ are estimated for Stage 2a fluids and 0.14-0.20 mNa and 0.014-0.020 mK for Stage 2b fluids. The Debye-Huckel extended equation is used to calculate the ac-

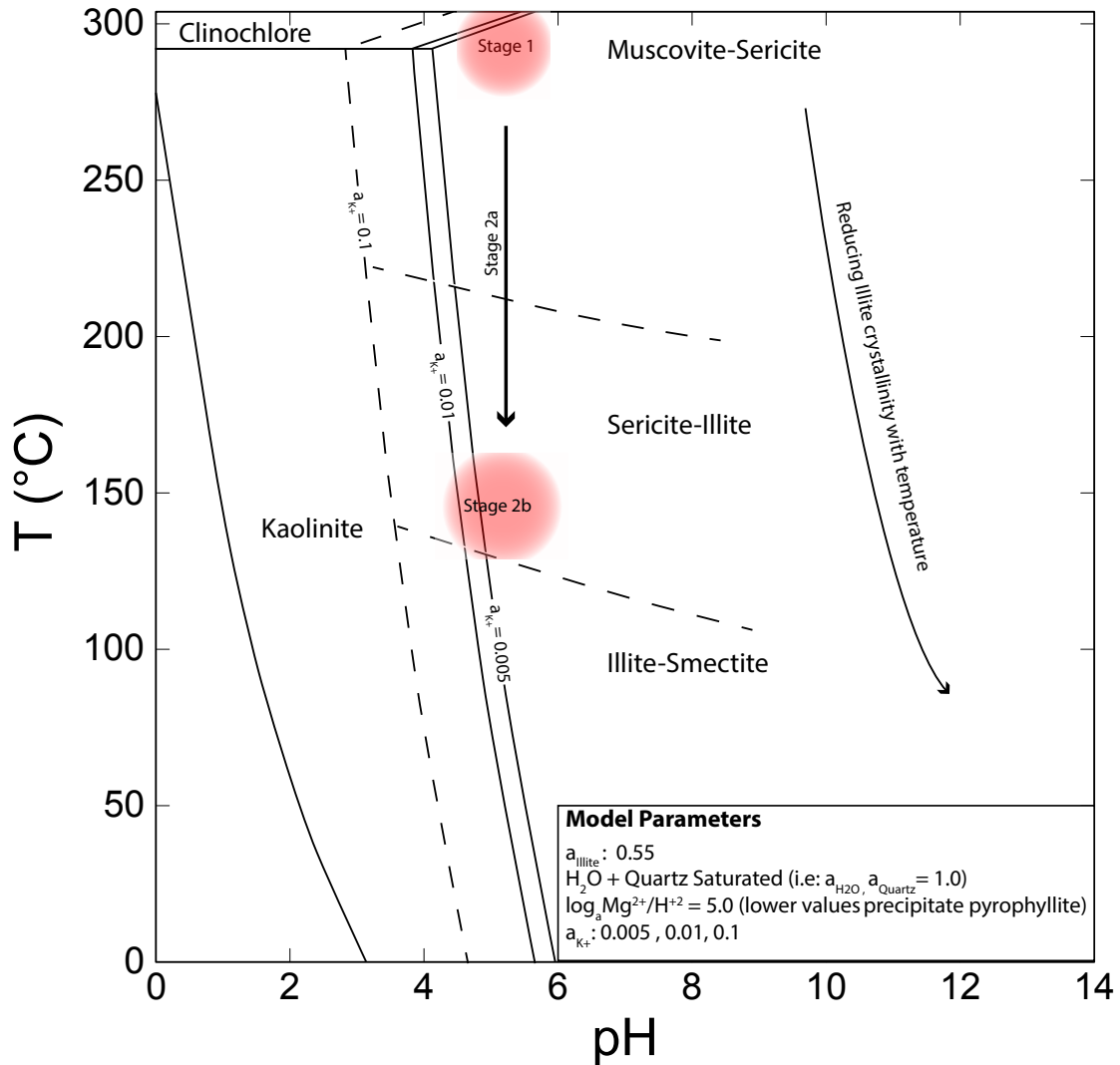


Figure 4.10: An activity-pH diagram showing a potential pathway taken by fluids at Shahumyan. Initial neutral to slightly acidic fluids are inferred based Log (aK/aH) values estimated in Figure 4.9. Model parameters are discussed in text.

tivities of average Na^+ and K^+ concentrations to use within the pH-Temperature GWB model: $\log a_{\text{Na}^+} = -1.25$ ($m_{\text{Na}} = 0.09$) and $\log a_{\text{K}^+} = -2.3$ ($m_{\text{K}} = 0.009$) for Stage 2a fluids assuming fluids were at 300°C . For stage 2b fluids Na and K activities were calculated to: $\log a_{\text{Na}^+} = -0.92$ ($m_{\text{Na}^+} = 0.17$) and $\log a_{\text{K}^+} = -1.93$ ($m_{\text{K}^+} = 0.017$) assuming fluids were at 150°C .

Mineralizing fluids at Shahumyan are estimated to vary between 5.5-6.5 pH, based on observed mineral relationships between sericite (illite), chlorite, quartz and kaolinite. Figure 4.10 is created based on estimated and calculated fluid constituent

parameters highlighted above and summarized in (Table 4.2). An increase in a_k shifts the kaolinite-sericite/illite stability fields to lower pH; a_k^+ values calculated based on fluid inclusion data constrain the a_k^+ to 0.05 to 0.1, thus limiting the pH ranges achieved at Shahumyan. The narrow pH range inferred indicate that hydrothermal fluids fluctuated between the sericite-chlorite fields at high temperatures (>290°C) while at lower temperatures they fluctuated between the sericite-kaolinite fields. Stage 2b hydrothermal fluids have been interpreted to result from boiling of high density fluids relatively rich in Na^+ and K^+ which resulted in a lower pH than Stage 2a fluids.

4.6.2 Constraints on Te and S Fugacities

Thermochemical conditions of ore formation at the Shahumyan deposit is determined from several factors, including the mutual stability and composition of minerals in each stage and the ionic content of various species in the ore-forming solution. Constraining the thermochemical environment of ore deposition will help estimate the composition of mineralizing fluids in an ore-forming environment. This helps predict likely precious metal transporting species and discuss potential depositional processes at Shahumyan. The mineral paragenesis outlined in previous chapters are discussed as separate events. However it is likely that each stage is part of a continuum of hydrothermal processes throughout the entire hydrothermal history. This interpretation is based on overlapping T_h values from fluid inclusion studies (this study) and isotope values (Mederer et al., 2013). Sulphur fugacity for Stage 2a can be determined from the FeS content of sphalerite coexisting with pyrite (Barton and Toulmin, 1966; Scott and Barnes, 1971; Barton and Skinner, 1979) based on the relationship defined by Barton and Skinner (1979) (Eqn 4.5.1). The Fe mole percent content of sphalerite coexisting with pyrite at Shahumyan is 0.19 to 0.29 and is calculated from microprobe measurements ($n= 3$) made on yellow sphalerite by Matveev et al. (2006).

$$\text{Log } X_{\text{Fe(sphalerite)}} = 7.16 - 7730/T - \frac{1}{2} \log f \quad (\text{Eqn 4.5})$$

Where T is temperature in degrees Kelvin and $X_{\text{Fe(Sphalerite)}}$ is the mole fraction of Fe in sphalerite. Sphalerite color and its FeS content are intimately linked; Fe content is the primary cause of color variance of sphalerite (Craig and Vaughan, 1990). The Fe content of the sphalerite (FeS) is controlled by the activity of sulphur and fluid temperature (Craig and Vaughan, 1990) where increasing Fe content (mol % FeS, Fe²⁺ & Fe³⁺) in sphalerite partly relates to an decrease in sulphur fugacity (Leptit et al., 2003).

An average T_h of 175°C (minimum temperature) measured for pale yellow sphalerite was used to determine sulphur fugacity. Sulphur fugacities calculated based from the Barton and Skinner (1979) equation, range between (-14.66 to -15.03 $\log fS_2$). These values represent sphalerite precipitated towards the end of Stage 2a; therefore calculated $fS_{2 \text{ values}}$ do not represent the entirety of Stage 2a. Honeybrown sphalerite interpreted to precipitate earlier in Stage 2a would have higher FeS values. In Stage 2b dark opaque sphalerite would indicate higher FeS values which in turn would indicate lower $fS_{2 \text{ values}}$.

The mole percent FeS of sphalerite in intermediate-sulphidation systems typically vary from < 1 to 10 mol%, however values up to 20 mol% have been reported (e.g. Creede Deposit; Barton et al., 1977; Einaudi et al., 2003). Contrarily, high-sulphidation deposits have FeS contents of 0.05 to 1 mol %, and low sulphidation deposits yield 20 to 40 mol % FeS (Einaudi et al., 2003; Czamanske, 1974; Scott and Barnes, 1971). An increase in FeS mole percent in sphalerite reflects decreasing sulphur fugacity at a given temperature. This would therefore indicate that as sulphur fugacity increases towards the end of Stage2a or beginning of Stage 2b, precipitating low Fe-Sphalerites (yellow sphalerite).

Telluride geochemistry is important as Au-Ag tellurides dominate the Au-Ag rich

ore zones in Shahumyan veins, free gold is rarely observed. The presence of tellurium indicates magmatic sources for mineralizing fluids (Cook et al., 2009; Cooke and Bloom, 1990). Tellurium fugacities can be inferred from telluride mineral assemblages, using mineral relationships and mineral equilibria between sulphide-telluride assemblages such as: sphalerite-pyrite-hessite-altaite-galena or sphalerite-pyrite-hessite-petzite- sylvanite-calaverite-coloradoite assemblages (Afifi et al., 1988; Zhang and Spry, 1994).

Fugacity-fugacity plots (Figure 4.11a-c) modified from Afifi et al (1988) and Zhang and Spry (1992, 1995) are used to estimate fluid conditions during telluride deposition. At Shahumyan, tellurides are interpreted to be deposited between 140-160°C. Sulphur fugacity and tellurium fugacity are used to constrain fluid conditions during sulphide and telluride deposition. Oxygen fugacity is ignored since all common oxides observed (hematite, goethite) are unstable with respect to sulphides and/or tellurides (Afifi et al., 1988). In these diagrams, hessite stability with respect to silver, electrum and/or argentite define the minimum f_{Te_2} - f_{S_2} conditions required for the stability of other telluride minerals (Afifi et al., 1988), therefore minimum f_{Te_2} values required for the formation of other tellurides are set by the stability of hessite at any f_{S_2} vs T condition. Fluids that deposit tellurides must enter a region above the hessite

	Stage 1	Stage 2		Stage 3
		a	b	
Sulfur Fugacity (f_{S_2})	-	~-10.0 to -15.03	~-14.66 to -15.03	-
Te Fugacity (f_{Te_2})	-	~-20 to -18	~-14 to -11	-
Temperature (°C)	300-270*	270-175	175-145	140-78.4
Salinity NaCl_{equiv} (wt.%)		4-6	8.4-13.3	1.56-4
mNa⁺		0.068-0.1	0.14-0.20	0.068-0.1
mK⁺		0.007-0.01	0.014-0.020	0.007-0.01
pH	5.5-6.5*	5.5-6.5	4.5-6.5	5.5-6.5
[CO₂] (mol/L)		<0.01	<0.01	-

Table 4.2: Physiochemical parameters of mineralizing fluids for observed hydrothermal stages.

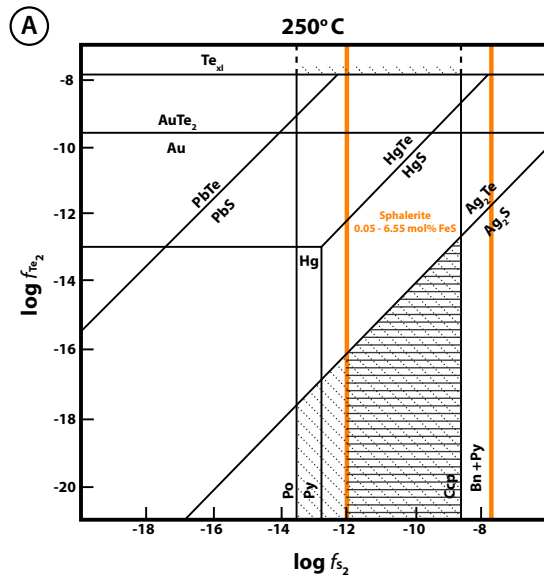
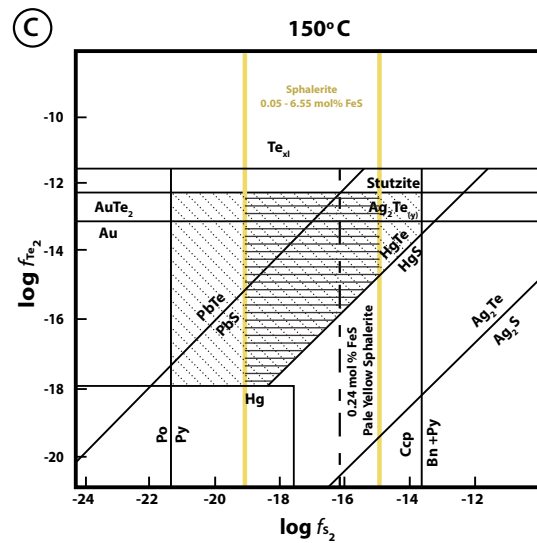
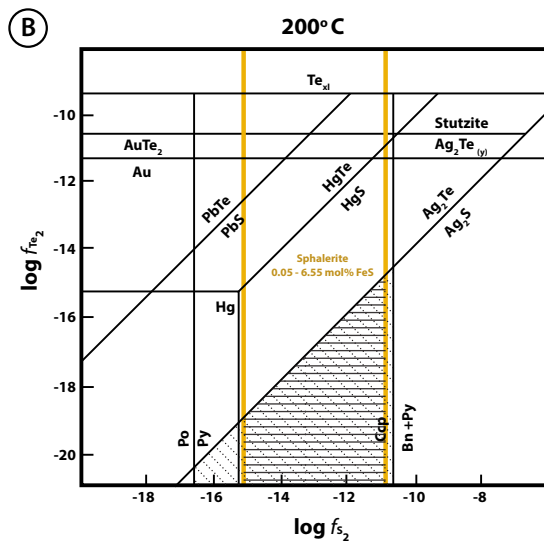


Figure 4.11: Sulfide and telluride equilibrium in f_{Te2}/f_{S2} space. Diagonally striped fields indicate potential fluid conditions for ore-deposition while cross-hatched fields identify stable minerals observed in hydrothermal stages. Abbreviations: Bn: Bornite, Py: Pyrite; Cpy: Chalcocopyrite; Po: Pyrrhotite. Modified from (Pals and Spry 2003; Zhang; 1992; Kovalenker et al., 1991; Afifi et al., 1988(a/b)). FeS mol% content in sphalerite constrains the stability fields in each diagram. (A) Stability diagram at 250°C, this diagram represents Stage 1 and 2a; (B) Stability diagram at 200°C, this diagram represents Stage 2a; (C) Stability diagram at 150°C, this diagram represents Stage 2a and 2b.

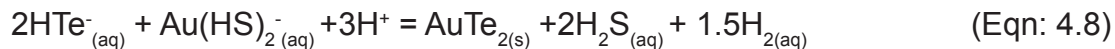
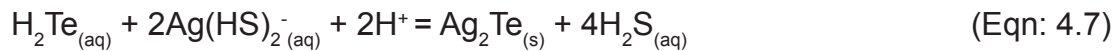


stability field for a given f_{S2} , whereas fluids that do not deposit tellurides are restricted to cooling paths in the telluride undersaturated field (Afifi et al., 1988). This provides an initial basis for distinction of cooling paths resulting in telluride-bearing and telluride-free ore assemblages. Three main $f_{Te2}-f_{S2}$ diagrams are used (250°, 200° and 150°C) (Figure 4.11a-c) constructed from thermodynamic databases provided by Chang (1992), Zhang and Spry (1994a,b) and Afifi et al (1988).

The presence of hessite in equilibrium with altaite in stage 2b (150°C) suggests a minimum $\log f_{Te2} = -10.0$. The common occurrence of galena in relation to altaite indicates low Te_2 fugacities, for the majority of Stage 2. Local increases in $\log f_{Te2}$ and or

$\log f_{\text{H}_2(\text{g})}$ or a decrease in $\log f_{\text{H}_2\text{S}}$ are the most likely causes for the observed distribution of altaite and galena. Similarly coloradoite which is also present in low abundances is a result of increased f_{Te_2} and likely an increase in a_{Hg} . However, the absence of cinnabar indicates a_{Hg} and $f_{\text{H}_2\text{S}}$ values are relatively low. An absence of tellurium-bearing minerals indicate extremely low f_{Te_2} and high $f_{\text{H}_2\text{S}}$ in Stage 2a and relatively higher f_{Te_2} and lower $f_{\text{H}_2\text{S}}$ in Stage 2b. From these observations one can conclude that $\log f_{\text{Te}_2}$ during telluride deposition ranged between -13.0 and -14.0 at 150°C.

Several models (e.g McPhail, 1995; Larocque et al., 1997; Cooke and McPhail, 2001) suggest that tellurium is transported preferentially in vapour ($\text{Te}_{2(\text{g})}$ and $\text{H}_2\text{Te}_{(\text{g})}$) rather than as an aqueous phase. Usually as an precious metals telluride complex or even tellurium-sulphur, tellurium-alkali metals and halides. Numerical simulations by Cooke and McPhail (2001) revealed that the only mechanism capable of tellurium deposition is condensation of $\text{Te}_{2(\text{g})}$ and $\text{H}_2\text{Te}_{(\text{g})}$ into precious metal rich waters. Telluride minerals at Shahumyan may therefore have precipitated (at least in part) in response to cooling of boiled vapours which show high a_{Te_2} . Additionally, other chemical parameters that may have contributed to telluride deposition include pH and aqueous Au and Ag concentrations. Changes in pH affect the relative stabilities of HTe^- and $\text{H}_2\text{Te}_{(\text{aq})}$ and drive precipitation of tellurides by the following reactions.



For the above reactions, a pH decrease is associated with both hessite deposition (Eqn: 4.7) and calaverite deposition (Eqn: 4.8) (Cooke and McPhail, 2001). A pH decrease is possible at Shahumyan; however, evidence of boiling (e.g. multi-phase FI assemblages and crustiform bands) complicates this process. Boiling of fluids would

result in an increase of pH due to CO_2^- effervescence, and is a function of high $[\text{CO}_2^-/\text{H}^+]$ and $[\text{CO}_2^-/\sum\text{SO}_4]$ or $[\text{CO}_2^-/\sum\text{H}_2\text{S}]$ ratios. However, Cole and Drummond (1986) indicate that for fluids with low $[\text{CO}_2^-/\text{H}^+]$ and $[\text{CO}_2^-/\sum\text{SO}_4]$, the pH increase is negligible. It has previously been established (Chapter 4.0) that CO_2^- concentrations at Shahumyan for stage 2 hydrothermal fluids are minimal, as evidenced by lack of carbonates during Stage 2a and only minor amounts in Stage 2b and from a lack of chalcrite formation within fluid inclusions. Therefore, because of low $[\text{CO}_2^-/\text{H}^+]$ and $[\text{CO}_2^-/\sum\text{SO}_4]$ or $[\text{CO}_2^-/\sum\text{H}_2\text{S}]$, fluid pH did not increase as a function of boiling at Shahumyan. Because pH is inferred to remain neutral or slightly acidic at Shahumyan carbonate (calcite) would not be favourable to precipitate. A lack of carbonate would therefore not buffer fluids becoming more acidic as a function of sulphide precipitation. H_2S species would exsolve more readily thus dropping the S fugacity, and potentially decrease pH temporarily in localized areas and precipitating sulphides.

5. Summary and Discussion

5.1 Vein Mineralogy, Alteration and Fluid Inclusions

The three main alteration assemblages at Shahumyan are characterized as proximal, intermediate and distal. Each assemblage is classified based on changes in alteration intensity and mineral assemblages and relative distances to individual mineralized veins.

The proximal assemblage is predominantly characterized by quartz, sericite-illite and pyrite with minor kaolinite. Intermediate assemblages are characterized by sericite, illite, pyrite, chlorite, \pm kaolinite, \pm calcite. The distal assemblage is characterized by chlorite, illite-smectite, pyrite, epidote and minor calcite. Compared to least altered host rocks, Si, K and Fe are major contributors to mass gain in the proximal assemblage and less so in the intermediate and distal assemblages. Mg gain is significantly higher in the distal assemblages decreases towards the proximal assemblage. Ca and Na have relatively higher mass loss in the proximal assemblage and less so in the distal assemblages. All metals show a mass increases in the proximal assemblages which decrease in the intermediate and proximal assemblages. The extent of alteration envelopes at Shahumyan is dependant on the vein size, with distal alteration assemblages from one vein interpreted to overlap the distal assemblage of another.

Three main hydrothermal stages are identified through vein mineralogy in Shahumyan veins: Stage 1, Stage 2a-b, and Stage 3. Stage 1 is a pre-ore stage comprising economically barren quartz pyrite veins. The stage with most significant economic contribution in Shahumyan veins is Stage 2 and is further divided into two substages; a base metal stage (Stage 2a) and a precious metal stage (Stage 2b). Stage 2a is characterized by honey-brown sphalerite, yellow sphalerite, chalcopyrite, galena, sul-

fosalts and rarely pure tellurium, hosted in predominantly a quartz-rich gangue with minor sericite/illite. Yellow sphalerite overgrows honey brown sphalerite cores, indicating that it is paragenetically later. Microthermometry of fluid inclusions in honey brown sphalerite reveal homogenization temperatures ranging between 285°C and 170°C with a population peak at approximately 260°C. Salinity ranges are narrow and range between 4.5 and 8.0 NaCl wt% eqv. with a population average at 5.7 NaCl wt% eqv. Average homogenization temperatures collected from honey brown sphalerites are generally higher than those collected from yellow sphalerites. Salinity measurements, like homogenization temperatures are relatively lower in yellow sphalerites than in honey brown sphalerites.

Stage 2b is characterized by black opaque sphalerite, chalcopyrite, pyrite, and telluride minerals. Silicate gangue minerals are not abundant in this stage; when present the gangue is characterized by quartz, calcite, sericite/illite and kaolinite. Black-opaque sphalerite contains inclusions of chalcopyrite, pyrite, and telluride minerals that crosscut honey brown and yellow sphalerites. Black opaque sphalerite and Au-Ag tellurides are observed to infill fractures in the earlier base metal sulphides of Stage 2a. Infilled fractures are common in earlier sphalerites and less so in chalcopyrite. Microfractured sulphide clasts are cemented by quartz, sulphides and/or tellurides is interpreted to be a localized brecciation event in veins.

Secondary fluid inclusion assemblages in Stage 2b minerals propagate from fractures containing opaque sphalerite, chalcopyrite, pyrite and Au-Ag telluride minerals; thus, directly linking precious metal mineralizing event to these fluid inclusion assemblages. Secondary fluid inclusion assemblages contain both liquid-rich and vapour-rich two-phase inclusions; the two inclusions indicate phase separation of hydrothermal fluids into a vapour during inclusion entrapment. The process of phase separation of a gas phase principally consisting of water vapour from a simple water-salt fluid; either, because of sudden increase in temperature, or sudden decrease

in pressure and is referred to as boiling (Roedder, 1984; Henley et al., 1984). Homogenization temperatures of boiling fluid inclusions average approximately 132°C. Salinities of boiling assemblages are relatively higher than non-boiling assemblages averaging 11.0 NaCl wt% eqv. Measurements were only possible in liquid-rich two phase inclusions as phase changes were unnoticeable in vapour-rich inclusions.

Stage 3 is characterized by quartz, massive calcite, chalcedony, fluorite and Mn-Mg carbonate (rhodochrosite, magnoan calcite). Stage 3 is the last and final stage of the in Shahumyan veins. Stage 3 quartz-carbonates are typically brecciated and contain clasts or rafts of earlier hydrothermal stages and wall rock in addition to mechanically-transported sulphide grains. Mechanical transport is inferred based on the grain/crystal morphology and the presence of jigsaw breccia clast textures and widespread fracturing into wall rock. Jigsaw breccia textures indicate brecciation of wall rock and or hydrothermal bands through implosion within a dilatational zone (Sibson 1986). Similar breccia textures are observed in previous stages but are most prominent in Stage 3. Homogenization temperatures of fluid inclusion assemblages in calcite range between 78°C and 150°C with a population peak at approximately 130°C. Average salinity of inclusions in calcite is 3.5 NaCl wt% eqv. relatively lower than inclusions in sphalerite. Microthermometric measurements recorded in calcite show a decrease in both temperature and salinity, indicating a mixing trend as suggested by Wilkinson (2010). This interpretation is corroborated by carbon and oxygen isotopes from Stage 3 calcite and quartz (Mederer et al. 2013).

5.2 Vein Geometry and Ore Shoots, Shahumyan

Veins at Shahumyan have an anastomosing vein geometry (i.e. anastomosing, undulating etc) both along strike and vertical dip. This geometry is associated with isolated fracture propagation as through-going fluid pathways form via linkage during

the development of a tectonic and hydrothermal systems (Sibson, 2001). Sub-vertical veins at Shahumyan are principally tensional in nature with open space textures such as comb quartz and open space infill. Stage 1 and lesser Stage 2 hydrothermal bands are dextrally displaced in veins, additionally slickensides and slickenlines between vein and wallrock interface, show dextral shear component features locally.

Underground drift mapping of veins reveals an overall vein trend of east to northeast and dipping to the south. Smaller vein segments comprising a larger vein, trend northeast, east, and northwest, and dip steeply to the south or north. Shahumyan veins are approximately 300-500m laterally and 300-400m along dip. Veins locally intersect with neighboring veins to form a vein mesh and make it difficult to determine the true extent at depth of any individual vein. Sudden changes in strike and/or dip occur between linking northeast, east and/or northwest trending vein segments. These sudden changes in orientation locally have associated hydrothermal breccias. These linkages between structures manifest as fault bends, step-overs, relay ramps, dilatational jogs or cymoid loops; which allow for dilation, increased permeability, and more localized and repetitive fluid flow (Faulds et al., 2010, 2006; Wallier, 2009; Micklethwaite and Cox, 2004; Trudgill and Cartwright, 1990).

5.3 Discussion

Epithermal deposits form in the shallow (<2km) and low to moderate temperature (~<400) hydrothermal systems that develop in volcanic arcs. Epithermal deposits can be rich in both precious (Au, Ag) and base metals (Cu, Zn, Pb). Epithermal orebodies occur in a diversity of shapes that reflect the influence of structural and lithological controls, most commonly in the form of steep veins (Simmons et al., 2005). The total precious metal content of some epithermal deposits is substantial (e.g. ~1200t Au and ~7000t Ag, Pueblo Viejo, Dominican Republic, Simmons et al., 2005) and in

some deposits, veins locally have bonanza Au grades ($>30\text{g/t Au}$; Sillitoe, 1993). Most epithermal ores are within a spectrum of Au-rich ($\text{Ag/Au} = <10$, locally <1) to silver-rich ($\text{Ag/Au} = \sim 20\text{-}200$) deposits. Shahumyan is principally Ag-rich and locally Au-rich with individual assay Ag/Au ratios averaging between 20-30.

Some epithermal deposits are Cu-bearing (Au-Ag-Cu) with high to intermediate sulphidation state mineral assemblages such as alunite, kaolinite, pyrophyllite, energite, luzonite, famantinite, orpiment; and others are characterized by Ag-Pb-Zn with low to intermediate sulphidation mineral assemblages dominated by adularia, calcite, illite, chlorite, rhodochrosite, tennantite, tetrahedrite and Fe-poor sphalerite. Both Au-Ag-Cu and Ag-Pb-Zn type deposits form predominantly in calc-alkaline volcanic-magmatic arcs resulting from convergent plate movements and plate subduction (Sawkins, 1990; Sillitoe and Hedenquist, 2003). Au-Ag \pm Te epithermal deposits are also common and are more-closely related to alkaline volcanic rocks derived from oxidized, hydrous mafic magmas (Richards, 1995; Jensen and Barton, 2000) (e.g., Cripple Creek, Ladolam, Emperor, Porgera etc.); however, Au-Ag \pm Te deposits have also been associated with calc-alkaline volcanic rocks (e.g. Kassiteres, Acupan etc.).

Shahumyan contains Cu-Zn-Pb base metal rich veins with localized Au-Ag rich zones and are hosted in calc-alkaline volcanic rocks (andesite-dacite). Other examples of similar deposits are: the St Demetrios deposit and the St Barbara prospect in the Kassiteres-Sapes district, Greece; the Creede deposit, Colorado; or the Acupan deposit in the Philippines. Based on observed mineral relationships between sericite (illite), chlorite, quartz and kaolinite, mineralizing fluids at Shahumyan are estimated to vary between 5.5 and 6.5 pH. Based on the narrow pH range inferred, hydrothermal fluids likely fluctuated between the sericite-chlorite fields at high temperatures ($>290^\circ\text{C}$), at lower temperatures they fluctuated between the sericite-kaolinite fields. Vein mineralogy at Shahumyan, consists of: pyrite, chalcopyrite Fe-rich sphalerite, Fe-poor sphalerite, galena, Au-Ag-Pb tellurides and tetrahedrite-tennantite. This as-

semblage represents intermediate sulphidation deposits

Fluid salinities in intermediate sulphidation deposits range between 0 and 23 wt.% NaCl equiv; whereas, low sulphidation deposits generally have a fluid salinities <2 wt.% NaCl equiv.; (Simmons et al., 2005; Sillitoe and Hedenquist, 2003). At Shahumyan salinities ranging between 1.6 and 13.3 NaCl wt% equiv. This range would characterize Shahumyan as an intermediate sulphidation deposit.

Telluride geochemistry is important as Au-Ag tellurides dominate the Au-Ag rich ore zones in Shahumyan veins, free gold is rarely observed. Au-Ag telluride minerals could precipitate through different mechanisms boiling, mixing, throttling, cooling of magmatic vapours (Cooke and McPhail, 2001; Cooke et al., 1996). Each process is characteristic geochemically, texturally and/or structurally; for example: boiling could produce bladed calcite, colloform bands among other textures and throttling would occur in structural pinch points in a fluid pathway. Identifying the process responsible for Au-Ag telluride deposition would allow for better targeting and exploration within the district and deposit.

The presence of tellurium indicates magmatic sources for mineralizing fluids (Cook et al., 2009; Cooke and Bloom, 1990). Several models (e.g McPhail, 1995; Larocque et al., 1997; Cooke and McPhail, 2001) suggest that tellurium is preferentially transported in vapour ($\text{Te}_{2(g)}$ and $\text{H}_2\text{Te}_{(g)}$) rather than in an aqueous phase. Based on numerical simulations Cooke and McPhail (2001) suggest condensation of $\text{Te}_{2(g)}$ and $\text{H}_2\text{Te}_{(g)}$ vapors into precious metal rich waters is the most effective process for telluride deposition. Telluride minerals at Shahumyan may therefore have precipitated (at least in part) by condensation of boiled vapors which have a relatively high a_{Te_2} .

At Shahumyan fluid inclusion measurements and petrographic observations provide the only evidence for Au-Ag tellurides precipitation via boiling, as no physical textures such as bladed calcite, colloform bands and other boiling textures are ob-

served. Rare occurrences of kaolinite in association with Au-Ag rich zones are the only significant mineralogical indicator for Stage 2b, besides Au-Ag tellurides. It is unclear whether kaolinite directly relates to Stage 2b Au-Ag tellurides due to its sparse nature. Kaolinite may be rare because it changes into illite/muscovite in alkaline conditions (Huang, 1993). Alkaline conditions could have dominated the hydrothermal system in the waning stages of the system, (Stage 3) during the formation of massive calcite. At Shahumyan Au-Ag telluride minerals are observed to be more abundant in structural zones by ~1-2 vol% relative to adjacent vein zones. Au-Ag rich zones are characterized by an increased abundance of microfractures (microbrecciation). Examples of favorable structural zones at Shahumyan include: node points in cymoid loops, pinch and swell structures and relay dilation zones. These zones are interpreted to have formed through the isolated fault model (Chapter 3).

Normal fault relay structures form at all scales as isolated fractures that interact with adjacent fracture planes during growth. Their successive growth and destruction represent the most efficient way for faults to lengthen and concurrently be mineralized through hydrothermal fluid movement. These relay structures are not only paths for lateral fluid flow but the well-developed damage zone also makes them excellent conduits for sustained vertical fluid flow.

Increased permeability and repetitive fluid flow in structurally favorable zones can explain the two main ore shoots identified in Shahumyan veins: 1) steep to moderately ($>60^\circ$) raking ore shoots; and 2) shallow ($20-30^\circ$) raking ore shoots gently plunging to the east. High fluid permeability due to increased microfractures in these zones is interpreted to have been the primary reason for vertical and sub-horizontal semi continuous ore shoots. The formation of microfractures in a relatively coherent sealed vein would create negative space and thus drop pressure allowing hydrothermal fluids to flow through and deposit hydrothermal minerals. This drop-in pressure could initiate localized boiling of small fluid reservoirs, and result in fluids boiling to dryness and in-

creased salinity in measured boiling assemblages. Similar trends have been observed by Simmons and Browne (1997) at the Broadlands-Ohaaki geothermal system and at the Hokko Prospect, Japan by Scott and Watanabe (1998) among others.

Rapid boiling of fluids in the upper 2 km of the crust typically occurs in a closed system where the total heat content of the rising fluid (liquid and steam combined) remains constant but the mass ratio of liquid to steam decreases as temperature and pressure decrease (Henley et al., 1984). These conditions would result in an increase in salinity by 25-30% from the onset of boiling at 300°C to discharge at 100°C (Simmons and Browne, 1995; Hedenquist and Henley 1985). A 25 to 30% increase in salinity of Shahumyan fluids at ~4.0 wt% NaCl equiv. would not produce the salinities observed in boiling assemblages at Shahumyan, and therefore cannot be a viable process to explain the data.

Open system boiling occurs in a fracture dominated system where fracture permeability enables separation of liquid and steam allowing for substantially higher salinities (Simmons and Browne, 1997) through prolonged intermittent boiling. Salinities will especially increase if the liquid is immobilized either in fluid reservoirs, isolated vein segments or in pores adjacent to fractures as steam is lost (Simmons and Browne, 1997). Open system boiling could therefore explain the high salinities at Shahumyan; in which, high salinity fluids are trapped in secondary inclusions in early sphalerite (Stage 2a).

It should be noted that, all Stage 2a fluid inclusions assemblages are liquid rich (~90-10 L-V), with no boiling evidence. This observation could indicate that hydrothermal fluids were below the hydrostatic boiling temperatures and pressures and that fluids ascended under steady state conditions; with sulphides precipitating through simple cooling. Boiling is therefore likely initiated when the hydrothermal system is over pressured and fluids are above the hydrostatic boiling curve.

Fluid pressures can increase if permeability in fractures is decreased through formation of a hydrothermal seal by precipitating minerals. This limits fluid ascent and movement and locally builds pressure. Additionally, the boiling curve could drop below ascending fluids, thus initiating boiling. The water table is intimately linked with the boiling curve, where a drop in the water table would similarly result a drop in the boiling curve. A drop in the water table can be initiated by either climate, topographic or tectonic effects. Examples of climatic effects include tidal changes or glacial activity which effect the water table. Examples of topographic effect includes drainage of a large water body maintaining the water table such as a caldera filled lake or sudden and rapid geological uplift. Tectonic effects include earthquakes as the principal ex-

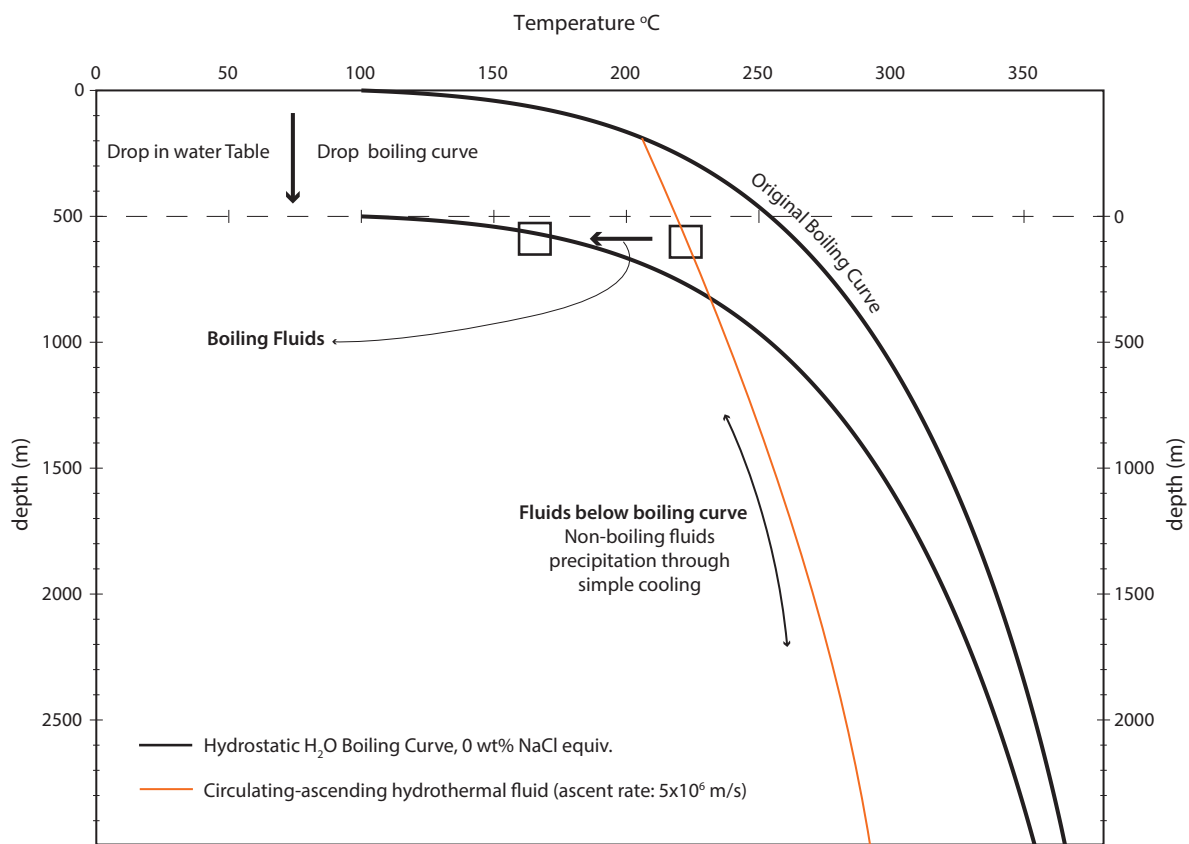


Figure 5.1: A schematic model for boiling fluids induced by water table drop. The fluid ascending curve (orange) is shown to be below the hydrostatic H₂O boiling curve, thus inhibiting boiling. Fluids have a simple cooling path and precipitate minerals, as interpreted from fluid inclusion data. As fluids reach 200-220°C, a sudden drop in the water table would place the fluids to the right of the hydrostatic boiling curve. Pore fluid pressures are thus over pressured and initiate boiling at ~150-170 °C. A drop in water table can be caused by sudden topographic changes or through seismic events or a combination of the two.

amples. Seismic activity causes stress related water table fluctuations. Seismically induced water level fluctuations are called hydroseisms, which are commonly observed following earthquakes. At Shahumyan either rapid uplift or seismic activity or a combination of the two processes is likely responsible for a drop in the water level. Major faults in the Kapan district could represent the trigger for a seismically induced water table drop. Uplift can be attributed to the formation of an arc associated with intense magmatism and volcanism.

At El Indio, Chile and at Fresnillo, Mexico a drop in the water table and initiation of boiling in the system produced acid-sulfate fluids responsible for steam heated blankets. These acid-sulfate fluids produce an alteration assemblage consisting of quartz, kaolinite, alunite and pyrophyllite. At Shahumyan, this alteration assemblage is observed in the lithocap covering the deposit and could further corroborate the interpretation of a drop in the water table.

The schematic diagram (Figure 5.1) shows the potential path for rising fluids below the hydrostatic boiling curve; as fluids reach $\sim 160^{\circ}\text{C}$ a sudden drop in the water table would change the elevation of the boiling curve and which could initiate boiling deeper in the system.

5.4 Conclusions

- The Shahumyan deposit is classified as an Intermediate Sulphidation epithermal vein deposit with structurally controlled Au-Ag rich ore shoots.
- Mineralization occurs in anastomosing east-west striking veins which have a normal-dextral sense of movement.
- Shahumyan polymetallic veins contain two main Au-Ag rich oreshoots in Cu-Zn-Pb rich veins. The two ore shoots are: narrow sub-vertical oreshoots and sub-horizontal oreshoots. These ore shoots are characterized by dilation

zones in the anastomosing veins and can be characterized by pinch and swell veins, cymoid loops (nodes), step over structures and relay ramps. Often accompanying these dilational structures are microbreccia textures.

- Au-Ag mineralization is characterized by Au-Ag tellurides such as petzite, sylvanite and hessite which infill fractures in microbreccia.
- Petrographic observations identify boiling evidence linked to Au-Ag tellurides. Boiling is interpreted to have initiated with a sudden drop in the water table either due to rapid uplift or seismic activity or a combination of the two.
- Based on microthermometric measurements in sphalerite and quartz, mineralizing hydrothermal fluids at Shahumyan range between 285°C and 120 °C and are slightly acidic (5.5-6.5 pH).
- As fluids cooled from approximately 285°C to 150°C, base metals such as Zn, Cu, Pb are deposited. Between 150 °C and 20 °C, physical processes such as boiling changed physiochemical conditions; Te fugacity exceeded S fugacity and precipitated telluride minerals in lieu of other sulphide minerals.
- Deposition of Au-Ag telluride minerals initiated principally as a function of condensing boiled vapors in localized brecciated zones. Telluride minerals precipitated from hydrothermal fluids at approximately 150° C, as evidenced by microthermometric measurements of boiling assemblages linked to Au-Ag telluride hosting fractures.
- Massive calcite deposition marks the waning stages of the hydrothermal system and was precipitated as a function of mixing.

5.5 District Scale Exploration Implications

The Kapan ore district is typified by northeast to east and northwest trending

steep to moderately dipping (60-85°) copper rich to polymetallic (Au-Ag-Zn-Cu-Pb) rich veins. Based on geochronological data, Mederer et al. (2013) suggests distinct magmatic-hydrothermal events to be responsible for mineralization in the different vein systems (Centralni West, Centralni East and Shahumyan). Radiometric age dating (Ar-Ar) of hydrothermal alteration minerals associated with mineralization estimates 161.78 ± 0.79 Ma (hydrothermal muscovite) to 156.14 ± 0.79 Ma (alunite) for mineralization (Mederer et al., 2013). Structural and vein mineralogy from different vein systems presented in the current study, provides evidence for an interconnected fracture system hosting mineralization. Six main vein systems have been exploited in varying degrees within the district: Centralni, Barabatoom, Arachadzor-Badalayurt, Noreshe-nik and Shahumyan, of which Shahumyan is the only operating min. Understanding the extent and displacement of the different vein systems allows geologists to target for economic mineralization within a district which has been over exploited since the 1800's.

The Upper Jurassic to Lower Cretaceous Complex comprising of volcanic, volcanoclastic and intercalated carbonaceous sediments unconformably overlay the middle Jurassic complex. Mineralized veins and associated hydrothermal alteration does not extend or permeate into the Upper Jurassic Complex rocks. Thus, restricting mineralization to the Middle Jurassic Volcanic Complex.

Bedding measurements within the district reveal an anticline with a southeast trending axial hinge. Sosson et al. (2010), Saintot et al., bracket folding events in the Lesser Caucasus between the Eocene to Miocene, linking them to the SAB collision with Eurasia and subsequent collision of Arabia with Eurasia between the Late Cretaceous to Paleocene. Bedding measurements in the Kapan district, of the Middle Jurassic volcanoclastic rocks and Middle Jurassic to Upper Jurassic-Lower Cretaceous unconformity are similar. Furthermore, bedding measurements the Upper Juras-

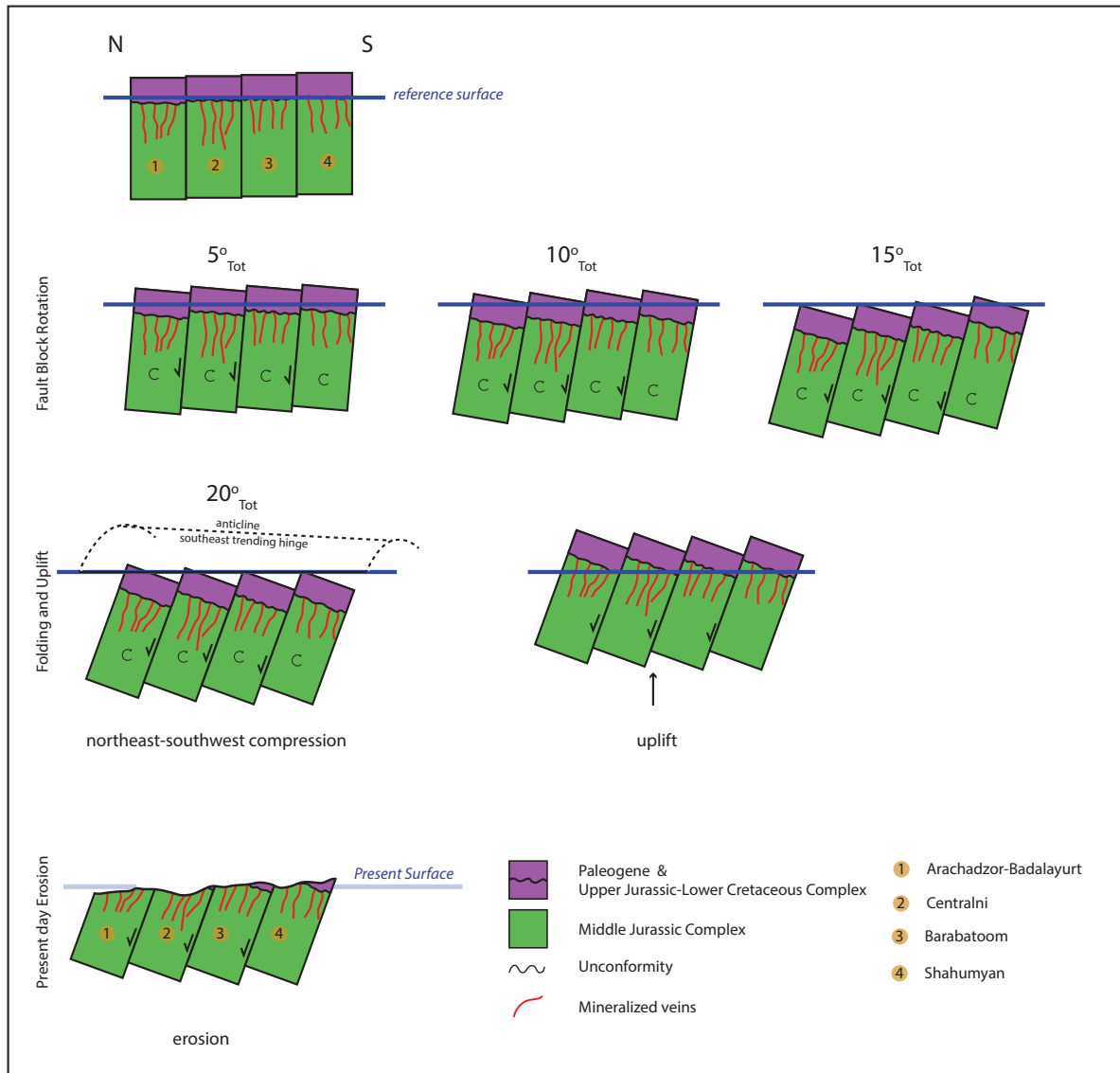


Figure 5.2: Schematic diagram of fault blocks in the Kapan district. Rotation of fault blocks affect existing veins differently at different portions of the district. Veins to the south east would experience much less erosion compare to veins in the northwest.

sic-Lower Cretaceous and Paleogene unconformity also has similar measurements to the lower unconformity. Therefore, the principal compression and subsequent folding event of the Paleogene is inferred to be responsible for the anticline present in the Kapan district. The anticline is part of a larger anticlinorium in the Lesser Caucasus and synclinorium in the Trans Caucasus with similarly trending axial hinge lines.

All veins system identified in the district except for Gyandzhibut veins are located along the northeast limb. As established above, mineralization in the district is re-

stricted to the Middle Jurassic; therefore, subsequent folding in the Paleocene would have rotated and tilted mineralized veins. If bedding is restored back to sub-horizontal, northeast trending, south dipping Shahumyan veins would become steeper, while any north to northeast dipping veins in the district (Arachadzor, Noreshenik) would become slightly shallower (60° - $70^{\circ} \rightarrow 50^{\circ}$ - 60°).

Two major fault-sets, the F1 and F2 are identified in the district. North trending oblique (normal-dextral) F1 set and the northeast trending normal F2 set. Both, F1 and F2 crosscut mineralized veins and offset the Middle Jurassic and the Upper Jurassic-Lower Cretaceous Complexes. Mineralized veins which have been crosscut by F2 and F1 faults cannot be traced from one side of the fault damage zone to the other, it is unknown whether mineralized veins terminate at these faults or if they continue. Damage zones of both fault sets contain discontinuous disseminated mineralization observed at fault-vein intersections. Disseminated mineralization within fault damage zones could indicate that these faults acted as major conduits for fluid flow providing mineralizing fluids for veins. However, it could also indicate existing mineralized veins crosscut by through going faults, which subsequently incorporated mineralization through mechanical degradation of veins over repeated fault reactivation events and/or through remobilization. F2, northeast striking faults in the district impart a fault block or bookshelf type fault architecture in the district. It is evident that faulted blocks have rotated/tilted, shallowing to the northwest. A lack of measurements on reference beds (piercing points) and their continuous reactivation make it difficult to determine the magnitude of fault block rotation and in turn the rotation of mineralized veins. A normal-fault architecture indicates northwestern blocks as hanging wall blocks and southeast blocks as footwall blocks. A simplified schematic is shown in Figure 5.2 to indicate the evolution and the general geometry of fault blocks in the district.

Rotated fault blocks are interpreted to vertically offset the vein systems in such

a way where deeper vein segments are tilted to the northwest and shallower portions towards the southeast. This is further evidenced in vein mineralogy where sulphide and gangue of Arachadzor and Centralni (located more to the NW) contain sulphides requiring higher temperatures and sulphidation states and therefore deeper conditions. Barabatom and Shahumyan (located to the SE) on the otherhand contain calcite, Mg-calcite, minor Mn-carbonates and sulphides requiring relatively lower sulphidation states. This interpretation would thus suggest that a majority of the vein system to the north may have hosted Au-Ag grades in veins on par with Shahumyan, making the district significantly more endowed than current estimates. Erosion is likely the major culprit in the missing upper portion of the district as would be expected in a 165 Ma old deposit. Based on proposed architecture in the district, future exploration in the district for Au-Ag veins should focus in to the southeast of the Shahumyan deposit. Base metal mineralization is also expected to increase at depth for veins at Shahumyan. Further research is required to constrain structural aspects for the proposed interpretation.

5.6 Future Work:

- Establish a better structural understanding of large fault systems fault paragenesis of the Sayed Kar, Barabatom and such fault systems in the Kapan district would help in identifying paleo-stress conditions.
- Identifying the Early- Middle Jurassic age paleo stress conditions would greatly contribute to a better understanding of the Middle Jurassic tectonic environment in The Lesser Caucasus. and would allow for a more precise structural interpretation of similarly aged deposits..
- A more detailed stable isotope and fluid inclusion study of different veins at Shahumyan could help further constrain fluid source and evolution at

Shahumyan. Furthermore, similar work in the district would allow for comparison of the different vein systems mined in the Kapan District.

- A more detailed geochronological and geochemical study of the Lower-Middle Jurassic to Upper Jurassic lower Cretaceous volcanic units.
- Identify whether the TSAVSKI intrusive complex south of the Kapan district have a genetic relationship to mineralization in the Kapan District.

References

- Abdel-Rahman, A. F. M., 1995. Chlorites in a spectrum of igneous rocks: mineral chemistry and paragenesis. *Mineralogical magazine*, 59(1):129-141.
- Achikgiozyan, S.O., Zohrabyan, S.A., Karapetyan, A.I., Mirzoyan, H.G., Sargisyan, R.A., Zaryan, R.N., 1987. The Kapan Mining district. Publishing House of the Academy of Sciences of the Armenian SSR. 198 pp, (in Russian).
- Acocella, V., Gudmundsson, A., & Funicello, R. 2000. Interaction and linkage of extension fractures and normal faults: examples from the rift zone of Iceland. *Journal of Structural Geology*, 22(9):1233-1246.
- Adamia, S., Zakariadze, G., Chkhotua, T., Sadradze, N., Tsereteli, N., Chabukiani, A., & Gventsadze, A. 2011. Geology of the Caucasus: a review. *Turkish Journal of Earth Sciences*, 20(5):489-544.
- Adamia, S.A., Chkhotua, T., Kekelia, M., Lordkipanidze, M., Shavishvili, I., Zakariadze, G. 1981. Tectonics of the Caucasus and adjoining regions: implications for the evolution of the Tethys ocean. *Journal of Structural Geology* 3:437–447.
- Adamia, S.A., Lordkipanidze, M.B., Zakariadze, G.S. 1977. Evolution of an active continental margin as exemplified by the Alpine history of the Caucasus. *Tectonophysics* 40:183–199.
- Afifi, A. M., Kelly, W. C., & Essene, E. J. 1988. Phase relations among tellurides, sulfides, and oxides; Pt. II, Applications to telluride-bearing ore deposits. *Economic Geology*, 83(2):395-404.
- Afifi, A. M., Kelly, W. C., & Essene, E. J. 1988. Phase relations among tellurides, sulfides, and oxides; I, Thermochemical data and calculated equilibria. *Economic Geology*, 83(2):377-394.
- Aghazadeh, M., Hou, Z., Badrzadeh, Z., & Zhou, L. 2015. Temporal–spatial distribution and tectonic setting of porphyry copper deposits in Iran: Constraints from zircon U–Pb and molybdenite Re–Os geochronology. *Ore Geology Reviews*, 70:385-406.
- Akbarpour, A., Gholami, N., Azizi, H., & Torab, F. M. 2013. Cluster and R-mode factor analyses on soil geochemical data of Masjed-Daghi exploration area, northwestern Iran. *Arabian Journal of Geosciences*, 6(9):3397-3408.
- Akopyan, V.T., 1962. Stratigraphy of Jurassic and Cretaceous suites of South-Eastern Zangezur. *Armenian Academy of Sciences SSR*, 265 (in Russian).
- Alavi, M., 1991. Sedimentary and structural characteristics of the Paleo-Tethys remnants in northeastern Iran. *Geological Society of America Bulletin* 103:983–992.
- Alavi, M., 2007. Structures of the Zagros fold–thrust belt in Iran. *American Journal of Science* 307:1064–1095.
- Allmendinger, R. W., Cardozo, N. C., and Fisher, D., 2013, *Structural Geology Algorithms: Vectors & Tensors*: Cambridge, England, Cambridge University Press, 289.

Amiryan, S.H., Pidjyan, G.H., Faramazyan, A.S., 1987. Mineralization stages and ore minerals of Teghut ore deposit. *Izvestia Nauki O Zemle (Proceedings of the National Academy of Sciences, Armenian SSR, Earth Sciences)* 40:31–44 (in Russian).

Amiryan, S.O. and Karapetyan, A.I. 1965. Mineral composition of the ores of Megradzor gold deposit. In *Eksperimental' nometodicheskiye issledovaniya rudnykh mineralov (Experimental-Procedural Investigations of Ore Minerals)*. Nauka Press, 215-222.

Aslanian, A.T. 1958. *Regional Geology of Armenia*. Yerevan: Haipetrat Publishing House, 430 (in Russian).

Avagyan, A., Sosson, M., Karakhanian, A., Philip, H., Rebai, S., Rolland, Y., & Davtyan, V. 2010. Recent tectonic stress evolution in the Lesser Caucasus and adjacent regions. *Geological Society, London, Special Publications*, 340(1):393-408.

Avanesyan, A.S., Leven, E., Uspenskaya, E.A. 1990. About exposure of Middle Jurassic suites in the river Vorotan (Kapan anticlinorium, Lesser Caucasus). *Izvestia Nauki O Zemle. Proceedings of the National Academy of Sciences, Armenian SSR, Earth Sciences*, 43:64–68 (in Russian).

Avanesyan, A.S., Leven, E., Uspenskaya, E.A. 1992. New data about Callovian rocks of Kapan anticlinorium (the Lesser Caucasus). *Izvestia Nauki O Zemle. Proceedings of the National Academy of Sciences, Republic of Armenia, Earth Sciences*, 45:69–73 (in Russian).

Azaryan, N.R. 1978. Determination of Bathonian suites in Kapan Anticlinorium. *Izvestia Nauki O Zemle. Proceedings of the National Academy of Sciences, Armenian SSR, Earth Sciences*, 31:8–15 (in Russian).

Azaryan, N.R. 1978. Determination of Bathonian suites in Kapan Anticlinorium. *Izvestia Nauki O Zemle. Proceedings of the National Academy of Sciences, Armenian SSR, Earth Sciences*, 31:8–15 (in Russian).

Babazadeh, V. M., Ramazanov, V. G., Mammadov, Z. I., Ismailova, A. M. & Abdullayeva, Sh. F. 2007. Geological-geophysical and geochemical fundamentals of the model of ore-magmatic systems of porphyry-copper deposits of the Kedabek ore district. *Proceedings of Scientific Session Dedicated to 100th Anniversary of Academician M. A. Kashkai*. Baku, 58–84.

Baba-Zadeh, V.M., Makhmudov, A.M., Ramazanov, V.G. 1990. Copper-porphyry and molybdenum-porphyry deposits. *Azerneshr, Baku* (in Russian).

Bagdasaryan, G.P., Ghoukassyan, R.K., Kazaryan, K.B. 1978. Comparative study of the age of old metamorphic schists in the Hakhoum River Basin (Armenian SSR) by means of K-Ar and Rb- Sr techniques, in: *Geochronology of the Eastern-European Platform and Junction of the Caucasian-Carpathian System*. Nauka, 47–58 (in Russian).

Bagdasaryan, G.P., Melkonyan, R.L. 1968. New data about petrography and geochronology of some volcanogenic and subvolcanic formations of Alaverdi region. *Izvestia Nauki O Zemle (Proceedings of the National Academy of Sciences, Armenian SSR, Earth Sciences)* 21, 93–101 (in Russian).

Barrier, E., Vrielynck, B. 2008. *Palaeotectonic Maps of the Middle East*. CGMW.

Barton Jr, P. B., & Skinner, B. J. 1979. Sulfide mineral stabilities. *Geochemistry of hydrothermal ore deposits*, 2:278-403.

- Barton, P. B., & Toulmin, P. 1966. Phase relations involving sphalerite in the Fe-Zn-S system. *Economic Geology*, 61(5):815-849.
- Barton, P. B., Bethke, P. M., and Roedder, E. 1977. Environment of ore deposition in the Creede mining district, San Juan Mountains, Colorado; Part III, Progress toward interpretation of the chemistry of the ore-forming fluid for the OH Vein. *Economic geology*, 72:1-24.
- Bazhenov, M.L., Burtman, V.S., Levashova, N.L. 1996. Lower and Middle Jurassic paleomagnetic results from the south Lesser Caucasus and the evolution of the Mesozoic Tethys Ocean. *Earth and Planetary Science Letters*, 141:79–89.
- Beaumont, C. 2006. Feasibility study in to the potential exploitation of Gold from the Central Mine open pit waste dumps, Kapan, Southern Armenia. Unpublished MSc Thesis, University of Exeter, UK.
- Begbie, M. J., Spörli, K. B., & Mauk, J. L. 2007. Structural Evolution of the Golden Cross Epithermal Au-Ag Deposit, New Zealand. *Economic Geology*, 102(5):873-892.
- Belov, A. 1981. Tectonic evolution of the Alpine folded domain in Paleozoic. *Proceedings of Geological Institute of Academy of Sciences of the USSR* 347, 1–212 [in Russian].
- Berger, B. R., and Henley, R. W. 1989. Advances in the understanding of epithermal gold-silver deposits, with special reference to the western United States. *Economic Geology Monograph*, 6: 405-423.
- Berger, B.R., Tingley, J.V., Drew, L.J. 2003. Structural Localization and Origin of Compartmentalized Fluid Flow, Comstock Lode, Virginia City, Nevada. *Economic Geology*, 98:387-408.
- Bethke, C.M. and Yeakel, S., 2014, *The Geochemist's Workbench*, release 10.0.4, Aqueous Solutions LLC, Champaign, IL, USA.
- Bird, D. K., & Norton, D. L. 1981. Theoretical prediction of phase relations among aqueous solutions and minerals: Salton Sea geothermal system. *Geochimica et Cosmochimica Acta*, 45(9): 1479-1494.
- Bodnar, R. J. 1993. Revised equation and table for determining the freezing point depression of H₂O-NaCl solutions. *Geochimica et Cosmochimica Acta*, 57(3):683-684.
- Booden, M. A., Smith, I. E., Black, P. M., & Mauk, J. L. 2011. Geochemistry of the Early Miocene volcanic succession of Northland, New Zealand, and implications for the evolution of subduction in the South-west Pacific. *Journal of Volcanology and Geothermal Research*, 199(1):25-37.
- Borisenko, A. S. 1977. Study of the salt composition of solutions in gas-liquid inclusions in minerals by the cryometric method. *Soviet Geology and Geophysics*, 18(8):11-18.
- Boullier, A. M., and Robert, F. 1992. Palaeoseismic events recorded in Archaean gold-quartz vein networks, Val d'Or, Abitibi, Quebec, Canada. *Journal of Structural Geology*, 14(2):161-179.
- Bouzari, F., & Clark, A. H. 2006. Prograde evolution and geothermal affinities of a major porphyry copper deposit: the Cerro Colorado hypogene protore, I Región, northern Chile. *Economic Geology*, 101(1):95-134.

Brathwaite, R.L., Cargill, H.J., Christie, A.B and Swain, A. 2001. Controls on the distribution of veining in andesite- and rhyolite-hosted gold-silver epithermal deposits of the Hauraki Goldfield, New Zealand. *Mineralium Deposita*, 36:1-12.

Browne, P. R. L. 1978. Hydrothermal alteration in active geothermal fields. *Annual Review of Earth and Planetary Sciences*, 6:229-250.

Browne, P. R. L. 1978. Hydrothermal alteration in active geothermal fields. *Annual Review of Earth and Planetary Sciences*. 6:229-250.

Browne, P.R.L., and Ellis, A.J. 1970. The Ohaki-Broadlands hydrothermal area, New Zealand: Mineralogy and related geochemistry: *American Journal Science*. 269:97-131.

Calagari, A. A. 2003. Stable isotope (S, O, H and C) studies of the phyllic and potassic–phyllic alteration zones of the porphyry copper deposit at Sungun, East Azerbaijan, Iran. *Journal of Asian Earth Sciences*, 21(7):767-780.

Calagari, A. A. 2004. Fluid inclusion studies in quartz veinlets in the porphyry copper deposit at Sungun, East-Azarbaidjan, Iran. *Journal of Asian Earth Sciences*, 23(2):179-189.

Callahan, T., 2001, Geology and host-rock alteration of the Henty and Mount Julia gold deposits, western Tasmania: *Economic Geology*, 96: 1073–1088.

Carlile, J.C., Davey, G.R., Kadir, I., Langmead, R.P., and Rafferty, W.J., 1998, Discovery and exploration of the Gosowong epithermal gold deposit, Halmahera, Indonesia: *Journal of Geochemical Exploration*, 60:207–227.

Catchpole, H., Kouzmanov, K., Fontboté, L., Guillong, M., & Heinrich, C. A. 2011. Fluid evolution in zoned Cordilleran polymetallic veins—Insights from microthermometry and LA-ICP-MS of fluid inclusions. *Chemical Geology*, 281(3):293-304.

Childs, C., Nicol, A., Walsh, J. J., & Watterson, J. 1996. Growth of vertically segmented normal faults. *Journal of Structural Geology*, 18(12):1389-1397.

Cholahyan, L.S., A., S.M., Sarkisyan, R.A., 1972. About the lithology of volcanoclasts of the Upper Bajocian of the left bank of the river Kavart. *Izvestia Nauki O Zemle (Proceedings of the National Academy of Sciences, Armenian SSR, Earth Sciences)* 25:36–41 (in Russian).

Christie, A.B., Simpson, M.P., Brathwaite, R.L., Mauk, J.L., Simmons, S.F. 2007. Epithermal Au-Ag and Related Deposits of the Hauraki Goldfield, Coromandel Volcanic Zone, New Zealand. *Economic Geology*, 102:785-816.

Cole, D. R., & Drummond, S. E. 1986. The effect of transport and boiling on Ag/Au ratios in hydrothermal solutions: a preliminary assessment and possible implications for the formation of epithermal precious-metal ore deposits. *Journal of Geochemical Exploration*, 25(1):45-79.

Cook, N. J., Ciobanu, C. L., Spry, P. G., & Voudouris, P. 2009. Understanding gold-(silver)-telluride-(selenide) mineral deposits. *Episodes*, 32(4):249-263.

Cooke, D. R., and McPhail, D. C. 2001. Epithermal Au-Ag-Te mineralization, Acupan, Baguio district, Philippines: numerical simulations of mineral deposition. *Economic Geology*, 96:109-131.

Cooke, D. R., McPhail, D. C., and Bloom, M. S. 1996. Epithermal gold mineralization, Acupan, Baguio District, Philippines; geology, mineralization, alteration, and the thermochemical environment of ore deposition. *Economic Geology*. 91:243-272.

Cooke, D.R. and Bloom, M.S., 1990, Epithermal and subjacent porphyry mineralization, Acupan, Baguio district, Phillipines: A fluid-inclusion and Paragenetic study: *Journal of Geochemical Exploration*, 35:297-340.

Cooke, D.R., and Simmons, S.F., 2000, Characteristics and genesis of epithermal gold deposits, *Reviews in Economic Geology*, 13:221–244.

Corbett, G. J. 2005. Epithermal Au-Ag deposit types—implications for exploration. In *Proexplo Conference Peru*. Cox, S., Knackstedt, M., Braun, J. 2001. Principles of Structural Control on Permeability and Fluid Flow in Hydrothermal Systems. *Reviews in Economic Geology*. 14:1-24.

Cox, S.F., 2005. Coupling between deformation, fluid pressures, and fluid flow in ore-producing hydrothermal systems at depth in the crust. *Economic Geology*, 100:39-75.

Craig, J. R., & Vaughan, D. J. 1990. Compositional and textural variations of the major iron and base-metal sulphide minerals. In *Sulphide deposits their origin and processing*, Springer Netherlands, 1-16.

Crawford, M. L. 1981. Phase equilibria in aqueous fluid inclusions. *Short course in fluid inclusions: applications to petrology*, 6:75-100.

Czamanske, G. K., and Rye, R. O. 1974. Experimentally determined sulfur isotope fractionations between sphalerite and galena in the temperature range 600 degrees to 275 degrees C. *Economic Geology*, 69:17-25.

Czamanske, GK. 1974. The FeS content of sphalerite along the chalcopyrite-pyrite-bornite sulfur fugacity buffer. *Economic Geology*, 69: 1328-1334.

Czamanske, GK. 1974. The FeS content of sphalerite along the chalcopyrite-pyrite-bornite sulfur fugacity buffer. *Economic Geology*, 69:1328-1334.

Davis, B.K. 2006. Report on the Geology of the Kapan Area with a Focus on the Shahumyan Deposit - Observations and Interpretations Based on a Visit in September 2006. Unpublished report for Dundee Precious Metals.

DeRonde, C. E., & Blattner, P. 1988. Hydrothermal alteration, stable isotopes, and fluid inclusions of the Golden Cross epithermal gold-silver deposit, Waihi, New Zealand. *Economic geology*, 83(5):895-917.

Diamond, L. W. 2003. Introduction to gas-bearing, aqueous fluid inclusions. *Fluid Inclusions: Analysis and Interpretation*, 32:101-158.

Drummond, S. E., & Ohmoto, H. 1985. Chemical evolution and mineral deposition in boiling hydrothermal systems. *Economic geology*, 80(1):126-147.

- Drummond, S. E., and Ohmoto, H. 1985. Chemical evolution and mineral deposition in boiling hydrothermal systems. *Economic geology*, 80:126-147.
- Echavarria, L., Nelson, E., Humphrey, J., Chavez, J., Escobedo, L., & Iriondo, A. 2006. Geologic evolution of the Caylloma epithermal vein district, southern Peru. *Economic Geology*, 101(4):843-863.
- Eilu, P., Mikucki, E.J., and Groves, D.I. 1997. Wall-rock alteration and primary geochemical dispersion in lode-gold exploration: Society for Geology Applied to Mineral Deposits Short Course Series, 1:65.
- Einaudi, M. T., Hedenquist, J. W., and Inan, E. E. 2003. Sulfidation state of fluids in active and extinct hydrothermal systems: transitions from porphyry to epithermal environments. *Special Publication-Society of Economic Geologists*, 10:285-314.
- Faulds, J. E., & Varga, R. J. 1998. The role of accommodation zones and transfer zones in the regional segmentation of extended terranes. *Special Papers-Geological Society of America*, 1:46.
- Faulds, J. E., Coolbaugh, M. F., Benoit, D., Oppliger, G., Perkins, M., Moeck, I., & Drakos, P. 2010. Structural controls of geothermal activity in the northern Hot Springs Mountains, western Nevada: The tale of three geothermal systems (Brady's, Desert Peak, and Desert Queen). *Geothermal Resources Council Transactions*, 34:675-683.
- Faulds, J. E., Coolbaugh, M. F., Vice, G. S., & Edwards, M. L. 2006. Characterizing structural controls of geothermal fields in the northwestern Great Basin: A progress report. *Geothermal Resources Council Transactions*, 30:69-76.
- Faulkner, D. R., C. A. L. Jackson, R. J. Lunn, R. W. Schlische, Z. K. Shipton, C. A. J. Wibberley, and M. O. Withjack. 2010. A review of recent developments concerning the structure, mechanics and fluid flow properties of fault zones, *Journal of Structural Geology*, 32:1557–1575.
- Faulkner, D. R., Jackson, C. A. L., Lunn, R. J., Schlische, R. W., Shipton, Z. K., Wibberley, C. A. J., & Withjack, M. O. 2010. A review of recent developments concerning the structure, mechanics and fluid flow properties of fault zones. *Journal of Structural Geology*, 32(11):1557-1575.
- Fleet, M. E., Deer, W. A., Howie, R. A., & Zussman, J. (Eds.). 2003. *Rock-Forming Minerals: Micas*. Geological Society of London.
- Fossen, H. 2010. Deformation bands formed during soft-sediment deformation: Observations from SE Utah. *Marine and Petroleum Geology*, 27(1):215-222.
- Fossen, H. and Rotevatn, A. 2016. Fault linkage and relay structures in extensional settings – a review. *Earth-Sciences Reviews*, 154:14-28.
- Frost, B. R., Mavrogenes, J. A., & Tomkins, A. G. 2002. Partial melting of sulfide ore deposits during medium-and high-grade metamorphism. *The Canadian Mineralogist*, 40(1):1-18..
- Galoyan, G., Rolland, Y., Sosson, M., Corsini, M., Billo, S., Verati, C., Melkonyan, R., 2009. Geology, geochemistry and $^{40}\text{Ar}/^{39}\text{Ar}$ dating of Sevan ophiolites (Lesser Caucasus, Armenia): Evidence for Jurassic Back-arc opening and hot spot event between the South Armenian Block and Eurasia. *Journal of Asian Earth Sciences*, 34:135 – 153.

Galoyan, G., Rolland, Y., Sosson, M., Corsini, M., Melkonyan, R., 2007. Evidence for superposed MORB, oceanic plateau and volcanic arc series in the Lesser Caucasus (Stepanavan, Armenia). *Comptes Rendus Geoscience*, 339:482 – 492.

Gamkrelidze, I., 1986. Geodynamic evolution of the Caucasus and adjacent areas in Alpine time. *Tectonophysics*, 127:261–277.

Garofalo, P. S., Fricker, M. B., Günther, D., Bersani, D., & Lottici, P. P. 2014. Physical-chemical properties and metal budget of Au-transporting hydrothermal fluids in orogenic deposits. *Geological Society, London, Special Publications*, 402(1):71-102.

Gemmell, J. B. 2007. Hydrothermal alteration associated with the Gosowong epithermal Au-Ag deposit, Halmahera, Indonesia: Mineralogy, geochemistry, and exploration implications. *Economic Geology*, 102(5):893-922.

Gemmell, J.B. 2004. Low and intermediate-sulfidation epithermal deposits, ARC- AMIRAP, Australia, 57-63.

Gemmell, J.B., and Fulton, R., 2001, *Geology, genesis, and exploration implications of the footwall and hanging-wall alteration associated with the Hellyer volcanic-hosted massive sulfide deposit, Tasmania, Australia: Economic Geology*, 96:1003–1035.

Gemmell, J.B., and Large, R.R. 1992. Stringer system and alteration zones underlying the Hellyer volcanic-hosted massive sulfide deposit, Tasmania, Australia: *Economic Geology*, 87:620–649.

Gevorkyan, R., Aslanyan, A. 1997. Armenia, in: Moores, E.M., Fairbridge, R.W. (Eds.), *Encyclopedia of European and Asian Regional Geology*. Chapman and Hall, London, 26–34.

Gialli, S., Moritz, R., Popkhadze, N., Gugushvili, V., Migineishvili, R., Spangenberg, J. 2012. The Madneuli Polymetallic Deposit, Lesser Caucasus, Georgia: A Transitional System with Magmatic Input in a Submarine Environment, in: Hedenquist, J.W., Fontboté, L. (Eds.), *Integrated Exploration and Ore Deposits, Proceedings SEG 2012 Conference, Lima, Peru*. p. Poster 38.

Golonka, J. 2004. Plate tectonic evolution of the southern margin of Eurasia in the Mesozoic and Cenozoic. *Tectonophysics*, 381:235–273.

Grant, J.A. 1986. The isocon diagram—a simple solution to Gresens' equation for metasomatic alteration, *Economic Geology*, 81:1976–1982.

Grohmann, C.H. and Campanha, G.A.C. 2010. OpenStereo: open source, cross-platform software for structural geology analysis. Presented at the AGU 2010 Fall Meeting, San Francisco, CA.

Hakobyan, V. T.1963. Stratigraphy of Jurassic and Cretaceous sedimentary rocks of the north-eastern part of Zangezour, Academy of Science Armenian SSR. Yerevan (in Russian).

Hanson, G.N. 1980 Rare earth elements in petrogenetic studies of igneous systems. *Annual Review of Earth and Planetary Sciences*, 8:371-406.

Hassanpour, S., & Afzal, P. 2013. Application of concentration–number (C–N) multifractal modeling for geochemical anomaly separation in Haftcheshmeh porphyry system, NW Iran. *Arabian Journal of Geosciences*, 6(3):957-970.

Hassanpour, S., Alirezaei, S., Selby, D., & Sergeev, S. (2015). SHRIMP zircon U–Pb and biotite and hornblende Ar–Ar geochronology of Sungun, Haftcheshmeh, Kighal, and Niaz porphyry Cu–Mo systems: evidence for an early Miocene porphyry-style mineralization in northwest Iran. *International Journal of Earth Sciences*, 104(1):45-59.

Hässig, M., Rolland, Y., Sahakyan, L., Sosson, M., Galoyan, G., Avagyan, A., & Müller, C. 2015. Multi-stage metamorphism in the South Armenian Block during the Late Jurassic to Early Cretaceous: Tectonics over south-dipping subduction of Northern branch of Neotethys. *Journal of Asian Earth Sciences*, 102:4-23.

Hässig, M., Rolland, Y., Sosson, M., Galoyan, G., Müller, C., Avagyan, A., & Sahakyan, L. 2013. New structural and petrological data on the Amasia ophiolites (NW Sevan–Akera suture zone, Lesser Caucasus): insights for a large-scale obduction in Armenia and NE Turkey. *Tectonophysics*, 588:135-153.

Hässig, M., Rolland, Y., Sosson, M., Galoyan, G., Sahakyan, L., Topuz, G., & Müller, C. 2013. Linking the NE Anatolian and Lesser Caucasus ophiolites: evidence for large-scale obduction of oceanic crust and implications for the formation of the Lesser Caucasus-Pontides Arc. *Geodinamica acta*, 26(3-4):311-330.

Hayba, D. O. 1997. Environment of ore deposition in the Creede mining district, San Juan Mountains, Colorado; Part V, Epithermal mineralization from fluid mixing in the OH Vein. *Economic Geology*, 92(1):29-44.

Hayba, D. O., Bethke, P. M., Heald, P., and Foley, N. K. 1985. Geologic, mineralogic, and geochemical characteristics of volcanic-hosted epithermal precious-metal deposits. *Reviews in Economic Geology*, 2:129-167.

Heald, P., Foley, N. K., and Hayba, D. O. 1987. Comparative anatomy of volcanic-hosted epithermal deposits; acid-sulfate and adularia-sericite types. *Economic Geology*, 82:1-26.

Hedenquist, J. W., & Henley, R. W. 1985. The importance of CO₂ on freezing point measurements of fluid inclusions; evidence from active geothermal systems and implications for epithermal ore deposition. *Economic geology*, 80(5):1379-1406.

Hedenquist, J. W., & Houghton, B. F. 1987. Epithermal gold mineralisation and its volcanic environments. *The earth resources Foundation the University of Sydney Taupo Vol. Zone, New Zealand*, 15-21.

Hedenquist, J. W., Arribas, A., and Gonzalez-Urien, E. 2000. Exploration for epithermal gold deposits. *Reviews in Economic Geology*, 13:45-77.

Hemley, J. J. 1959. Some mineralogical equilibria in the system K₂O–Al₂O₃–SiO₂–H₂O. *American Journal of Science*, 257(4):241-270.

Hemon, P., Moritz, R., Ramazanov, V. 2012. The Gedabek Epithermal Cu-Au Deposit, Lesser Caucasus, Western Azerbaijan: Geology, Alterations, Petrography and Evolution of the Sulfidation Fluid States, in: Hedenquist, J.W., Fontboté, L. (Eds.), *Integrated Exploration and Ore Deposits, Proceedings SEG 2012 Conference*, Lima, Peru. p. Poster 50.

Henley, R., 1984a, Chemical structure of geothermal systems, Chapter 2 in: Henley, R. W., Truesdell, A. H. and Barton, P. B., *Fluid - mineral equilibria in hydrothermal systems, Reviews in Economic Geology*, Vol. 1 (Robertson, J., series editor), Society of Economic Geology, 9 – 280.

Henley, R. W., & Hedenquist, J. W. (1986). Introduction to the geochemistry of active and fossil geothermal systems. *Guide to the Active Epithermal Systems and Precious Metal Deposits of New Zealand: Monograph Series Mineral Deposits*, Berlin, Gebruder Borntraeger, (26):129-145.

Henley, R. W. 1984b. Hydrolysis reactions in hydrothermal fluids, Chapter 6 in: Henley, R. W., Truesdell, A. H. and Barton, P. B., *Fluid-mineral equilibria in hydrothermal systems, Reviews in Economic Geology*, Vol 1 (Robertson, J., series editor), Society of Economic Geologists, 65-82.

Henley, R.W. 1985. Ore transport and deposition in epithermal environments, In *Stable Isotopes and Fluid Processes in Mineralization*; eds Hubert, H., Golding, S. and Ho, S.E., Geol Dept. and Univ. Extension of Western Australia Publ, 23:51-69.

Hosseinzadeh, G., Mouayed, M., Kalagari, A.A., Hajalilou, B., Moazen, M. 2008. Studies of petrography and petrogenesis of Incheh intrusive body, east of Heris, East-Azerbaijan, 189-206.

Jackson, J. 1992. Partitioning of Strike-Slip and Convergent Motion Between Eurasia and Arabia in Eastern Turkey and the Caucasus. *Journal of Geophysical Research*, 97:12471–12479.

Jamali, H. and Mehrabi, B. 2015. Relationships between arc maturity and Cu-Mo-Au porphyry and related epithermal mineralization at the Cenozoic Arasbaran magmatic belt. *Ore Geology Reviews*, 65:487-867.

Jamali, H., Dilek, Y., Daliran, F., Yaghubpur, A., & Mehrabi, B. 2010. Metallogeny and tectonic evolution of the Cenozoic Ahar–Arasbaran volcanic belt, northern Iran. *International Geology Review*, 52(4-6):608-630.

Johnston Jr, W. D. 1940. *The gold quartz veins of Grass Valley, California* (No. 194). United States Government Printing Office.

Karamyan, K.A. 1978. *Geology, structure and condition of formation copper-molybdenum deposits of Zangezur ore region*. Publishing House of the Academy of Sciences of the Armenian SSR, 179 pp, (in Russian), Yerevan.

Karapetyan, A.I., Amiryan, S.H., Azizbekyan, S., Altunyan, A.Z., Melkonyan, R.L., Guyumjyan, O.P., Paronikyan, V.O., Nalbandyan, E.M., Kaplanyan, P.M., Galstyan, A.R., Grigotyan, L.A., Zohrabyan, S.A. 1982. *Predicting- Metallogenic map of the Alaverdi-Shamlugh-Akhtala ore junction*. Unpublished report of National Academy of Sciences of Armenian SSR, Institute of Geological Sciences.

Kazmin, V., Sbornshikov, I., Ricou, L.E., Zonenshain, L., Boulin, J., Knipper, A. 1986. Volcanic belts as markers of the Mesozoic-Cenozoic active margin of Eurasia. *Tectonophysics*, 123:123–152.

Keith, T. E., & Muffler, L. J. P. 1978. Minerals produced during cooling and hydrothermal alteration of ash flow tuff from Yellowstone drill hole Y-5. *Journal of Volcanology and Geothermal Research*, 3:373-402.

Keith, T.E.C., White, D.E., and Beeson, M.H. 1978. Hydrothermal alteration and self-sealing in Y-7 and Y-8 drill holes in northern part of Upper Geyser basin, Yellowstone National Park, Wyoming: U.S. Geological Survey Professional Paper, 1054:26.

Kekelia, S., Kekelia, M., Otkhmezuri, Z., Özgür, N., Moon, C. 2004. Ore-forming systems in volcanogenic-sedimentary sequences by the example of base metal deposits of the Caucasus and East Pontic Metallotect. *Bulletin of the Mineral Research and Exploration*, 129:1–16.

Khachaturyan, E.A. 1958. About mineralogical composition of the ores of Kapan copper deposit. *Izvestia Nauki O Zemle (Proceedings of the National Academy of Sciences, Armenian SSR, Earth Sciences)* 11:25–40 (in Russian).

Khain, V. 1975. Main stages of tectonic-magmatic evolution of the Caucasus. *Geotectonics*, 1:13–27.

Knipper, A.L., Khain, E.V. 1980. Structural position of ophiolites of the Caucasus. *Ophiolite Special Issue*, 2:297–314.

Konstantinov, M., Kryazhev, S., Ustinov, V. 2010. Characteristics of the ore-forming system of the Zod gold-tellurium deposit (Armenia) according to isotopic data. *Geochemistry International*, 48:946-949.

Kopp, M.L. 1997. Lateral escape structures in the Alpine-Himalayan collision belt (in Russian). *Russian Academy of Sciences Transactions*, 506:1–314.

Kovalenker, V. A., Zalibekyan, M. A., Laputina I. P., Malov, V. S., Sandomirskaya, S.M., Garas'ko M. I., Mkhitarian D. I. 1990. Sulfide-Telluride Mineralization of the Megradzor ore Field, Armenia, *International Geology Review*, 32:705-72.

Kozerenko, S.V. 2004. Hydrothermal system of the Zod gold sulfide deposit, Armenia: Ore sources and formation conditions. *Geochemistry International* 42:188–190.

Large, R.R., Allen, R.L., Blake, M.D., and Herrmann, W. 2001a. Hydrothermal alteration and volatile element halos for the Roseberry K lens volcanic-hosted massive sulfide deposit, western Tasmania, *Economic Geology*, 96:1055–1072.

Large, R.R., Gemmell, J.B., Paulick, H., and Huston, D.L. 2001b. The alteration box plot: A simple approach to understanding the relationship between alteration mineralogy and litho-geochemistry associated with volcanic-hosted massive sulfide deposits, *Economic Geology*, 96:957–971.

Large, R.R., McPhie, J., Gemmell, J.B., Herrmann, W., and Davidson, G.J. 2001c. The spectrum of ore deposit types, volcanic environments, alteration halos, and related exploration vectors in submarine volcanic successions: Some examples from Australia, *Economic Geology*, 96:913–938.

Larocque, A.C.L., Stimac, J.A., and Siebe, C. 1997. An epithermal-like vapor-phase assemblage in pumice from Volcàn Popocatepetl, Mexico [abs.], *Geological Society of America Abstracts with Programs*, 29.

Le Maitre, R. W. 1989. A Classification of Igneous Rocks and Glossary of Terms. Recommendations of the IUGS Commission on the Systematics of Igneous Rocks. Oxford: Blackwell

Leach, T., & Corbett, G. 2008. Fluid mixing as a mechanism for bonanza grade epithermal gold formation. In Paper presented at the Terry Leach Symposium, 17.

Leavitt, E. D., & Arehart, G. B. 2005. Geology, geochemistry, and geochronology of the Midas epithermal gold system, Nevada. In 2005 New Zealand Minerals and Mining Conference Proceedings, 142-149.

Lepetit, P., Bente, K., Doering, T., & Luckhaus, S. 2003. Crystal chemistry of Fe-containing sphalerites. *Physics and Chemistry of Minerals*, 30(4):185-191.

Lindgren, W., 1933. *Mineral Deposits*, 4th ed. McGraw Hill, New York and London. 930 pp.

Lordkipanidze, M., Meliksetian, B., Djarbashian, R. 1989. Mesozoic-Cenozoic Magmatic Evolution of the Pontian-Crimean-Caucasian Region, in: Rakus, M., Dercourt, J., Nairn, A. (Eds.), IGCP project n_198: Evolution of the northern margin of Tethys. *Mémoire de la Société Géologique de France*, Paris. 154(2) of Nouvelle Série: 103–124.

Madeisky, H. E. 1996. A lithogeochemical and radiometric study of hydrothermal alteration and metal zoning at the Cinola epithermal gold deposit, Queen Charlotte Islands, British Columbia. *Geology and ore deposits of the American Cordillera*, 3:1153-1185.

Maghakyan, R., Zakariadze, G., Dmitriev, L., Kolesov, G., Korovina, M. 1985. Geochemistry of the Jurassic-Lower Cretaceous volcanic assemblage of northern Armenia. *Volcanology and Seismology*, 3:39–53 (in Russian).

Marma, J.C., and Vance, R.B. 2010. Importance of Cymoid loops and Implications for Exploration and Development of Epithermal Gold Silver Veins in the Gold Circle District, Midas, Nevada. *Geological Society of Nevada Symposium Publications*, 777-793.

McKinstry, H. E. 1948. *Mining Geology*. Prentice-Hall, Englewood Cliffs, New Jersey.

McPhail, D. C. 1995. Thermodynamic properties of aqueous tellurium species between 25 and 350°. *Geochimica et Cosmochimica Acta*, 59(5):851-866.

Mederer, J. 2013. Regional setting, geological context and genetic aspects of polymetallic hydrothermal ore deposits from the Kapan ore district, southern Armenia: a contribution to the Mesozoic island arc metallogeny of the Lesser Caucasus, Doctoral dissertation, University of Geneva.

Mederer, J., Moritz, R., Ulianov, A., and Chiaradia, M., 2013. Middle Jurassic to Cenozoic evolution of arc magmatism during Neotethys subduction and arc-continent collision in the Kapan Zone, southern Armenia. *Lithos*, 177:61-78.

Mederer, J., Moritz, R., Zohrabyan, S., Vardanyan, A., Melkonyan, R., and Ulianov, A. 2014. Base and precious metal mineralization in Middle Jurassic rocks of the Lesser Caucasus: A review of geology and metallogeny and new data from the Kapan, Alaverdi and Mehmana districts. *Ore Geology Reviews*, 58:185-207.

- Meijers, M. J., Smith, B., Kirscher, U., Mensink, M., Sosson, M., Rolland, Y., Müller, C. 2015. A paleo-latitude reconstruction of the South Armenian Block (Lesser Caucasus) for the Late Cretaceous: Constraints on the Tethyan realm. *Tectonophysics*: 644:197-219.
- Meijers, M. J., Smith, B., Pastor-Galán, D., Degenaar, R., Sadradze, N., Adamia, S., Langereis, C. G. 2015. Progressive orocline formation in the Eastern Pontides–Lesser Caucasus. Geological Society, London, Special Publications, 428: Special Publications428-8.
- Meijers, M.J.M., Vrouwe, B., van Hinsbergen, D.J.J., Kuiper, K.F., Wijbrans, J., Davies, G.R., Stephenson, R.A., Kaymakci, N., Matenco, L., Sainot, A. 2010. Jurassic arc volcanism on Crimea (Ukraine): Implications for the paleo-subduction zone configuration of the Black Sea region. *Lithos*, 119:412–426.
- Melkonyan, R.L., Akopyan, M. 2006. Some aspects of the interrelations between magmatism and ore formation: Evidence from oxygen isotope data on ore-magmatic systems, Armenia. *Petrology*, 14:413–420.
- Meunier, A. 2005. *Clays*, 1st edn. Springer, Berlin.
- Micklethwaite, S., & Cox, S. F. 2004. Fault-segment rupture, aftershock-zone fluid flow, and mineralization. *Geology*, 32(9):813-816.
- Micklethwaite, S. 2009. Mechanisms of faulting and permeability enhancement during epithermal mineralization: Cracow goldfield, Australia. *Journal of Structural Geology*. 31:288-300
- Micklethwaite, S., Ford, A., Witt, W., Sheldon, H. 2015. The where and how of faults, fluids, and permeability – Insights from fault stepovers, scaling properties, and gold mineralization. *Geofluids*. 15:240–51.
- Micklethwaite, S., Sheldon, H.A., and Baker, T. 2010. Active fault and shear processes and their implications for mineral deposit formation and discovery. *Journal of Structural Geology*. 32:151-165.
- Milanovsky, E.E., 1968. *Neotectonics of the Caucasus*. Nedra, Moscow (in Russian).
- Mkrtchian, S. S. 1969. *Geology of the Armenian SSR (Vol.IX - Mineral Waters)*. Academy of Science of the Armenian SSR, Institute of Geological Sciences, Yerevan (in Russian).
- Monin, A.S., Zonenshain, L.P. 1987. *History of the Ocean Tethys*. Moscow Institute of Oceanology (in Russian).
- Moon, C. J., Gotsiridze, G., Gugushvili, V., Kekelia, M., Kekelia, S., Migineishvili R., Othkhmezuri, Z., Ozgur, N. 2001. Comparison of Mineral Deposits between Georgian and Turkish sectors of the Tethyan Metallogenic Belt. In: A. Piestrzynski (ed.), *Mineral Deposits at the Beginning of the 21st Century*. Proceedings. 6th Biennial SGA, Krakow, Poland. 309–312.
- Moritz, R., Rezeau, H., Ovtcharova, M., Tayan, R., Melkonyan, R., Hovakimyan, S., and Putlitz, B. 2015. Long-lived, stationary magmatism and pulsed porphyry systems during Tethyan subduction to post-collision evolution in the southernmost Lesser Caucasus, Armenia and Nakhitchevan. *Gondwana Research*.

Moritz, R., Selby, D., Ovtcharova, M., Mederer, J., Melkonyan, R., Hovakimyan, S.E., Tayan, R., Popkhadze, N., Gugushvili, V., Ramazanov, V. 2012. Diversity of geodynamic settings during Cu, Au and Mo ore formation in the Lesser Caucasus: new age constraints, in: Proceedings 1st triennial EMC meeting, Frankfurt, Germany, 745.

Murakami, T., Inoue, A., Lanson, B., Meunier, A., & Beaufort, D. 2005. Illite-smectite mixed-layer minerals in the hydrothermal alteration of volcanic rocks: II. One-dimensional HRTEM structure images and formation mechanisms. *Clays and Clay Minerals*, 53(5):440-451.

Nikishin, A.M., Ziegler, P.A., Panov, D.I., Nazarevich, B.P., Brunet, M.-F., Stephenson, R.A., Bolotov, S.N., Korotaev, M.V., Tikhomirov, P.L. 2001. Mesozoic and Cenozoic evolution of the Scythian Platform-Black-Sea-Caucasus domain, in: Ziegler, P., Cavazza, W., Robertson, A., Crasquin-Soleau, S. (Eds.), *Peri-Tethys Memoir 6: Peri-Tethyan Rift/Wrench Basins and Passive Margins*. Mémoires du Muséum national d'Histoire Naturelle. 186:295–346.

Oliver, N.S., Bons, P.D., 2001. Mechanisms of fluid flow and fluid-rock interactions in fossil metamorphic hydrothermal systems inferred from vein-wallrock patterns, geometry and microstructure. *Geofluids*, 1:137.

Páez, G. N., Ruiz, R., Guido, D. M., Jovic, S. M., & Schalamuk, I. B. 2011. Structurally controlled fluid flow: High-grade silver ore-shoots at Martha epithermal mine, Deseado Massif, Argentina. *Journal of Structural Geology*, 33(5):985-999.

Peacock, D. C. P., & Parfitt, E. A. 2002. Active relay ramps and normal fault propagation on Kilauea Volcano, Hawaii. *Journal of structural geology*, 24(4):729-742.

Peacock, D. C. P., & Sanderson, D. J. 1991. Displacements, segment linkage and relay ramps in normal fault zones. *Journal of Structural Geology*, 13(6):721-733.

Pearce, J. A. (1996). A user's guide to basalt discrimination diagrams. In: Wyman, D. A. (ed.) *Trace Element Geochemistry of Volcanic Rocks: Applications for Massive Sulphide Exploration*. Geological Association of Canada, Short Course Notes, 12:79–113.

R. J. (1988). Systematics of stretching of fluid inclusions; II, Barite at 1 atm confining pressure. *Economic Geology*, 83(5):1037-1046.

Reed, M. H., and Spycher, N. F. 1985. Boiling, cooling, and oxidation in epithermal systems: a numerical modeling approach. *Reviews in Economic Geology*. 2:249-272.

Reed, M., and Plumlee, G. 1992. Collapse of acid waters into boiling hydrothermal systems and the origin of late stage pyrite and related kaolinite. In *Water-Rock Interaction: Proceedings of the Seventh International Symposium on Water-Rock Interaction*, 1083-1086.

Richards J.P. 1995. Alkalic-type epithermal gold deposits a review. In: Thompson JFH (ed) *Magma, Fluids and ore deposits*. Mineralogical Association of Canada, Short Course Series, 23: 367-400.

Roedder, E. 1984. Fluid inclusions- P. H. Ribbe Ed. Washington, DC: Mineralogical Society of America, 12:12-45.

- Rolland, Y., Billo, S., Corsini, M., Sosson, M., Galoyan, G. 2009a. Blueschists of the Amassia- Stepanavan Suture Zone (Armenia): linking Tethys subduction history from E-Turkey to W-Iran. *International Journal of Earth Sciences*, 98:533–550.
- Rolland, Y., Galoyan, G., Bosch, D., Sosson, M., Corsini, M., Fornari, M., Verati, C. 2009b. Jurassic back-arc and Cretaceous hot-spot series in the Armenian ophiolites – Implications for the obduction process. *Lithos*, 112:163–187.
- Rolland, Y., Galoyan, G., Sosson, M., Melkonyan, R., Avagyan, A. 2010. The Armenian Ophiolite: insights for Jurassic back-arc formation, Lower Cretaceous hot spot magmatism and Upper Cretaceous obduction over the South Armenian Block. *Geological Society, London, Special Publications*, 340:353–382.
- Rolland, Y., Sosson, M., Adamia, S., Sadradze, N. 2011. Prolonged Variscan to Alpine history of an active Eurasian margin (Georgia, Armenia) revealed by $^{40}\text{Ar}/^{39}\text{Ar}$ dating. *Gondwana Research*, 20:798–815.
- Rollison, H. 1993. *Using Geochemical Data: Evaluation, Presentation, Interpretation*: Longman Scientific & Technical, Harlow, 352.
- Rose, A.W. and Burt, D.M. 1979. Hydrothermal alteration. In: H.L. Barnes (Editor) *Geochemistry of Hydrothermal Ore Deposits*. Wiley and Sons, New York, N.Y., 789.
- Rowland, J. V., & Sibson, R. H. 2004. Structural controls on hydrothermal flow in a segmented rift system, Taupo Volcanic Zone, New Zealand. *Geofluids*, 4(4):259-283.
- Rowland, J.V., Sibson, R.H. 2004. Structural controls on hydrothermal flow in a segmented drift system, Taupo Volcanic Zone, New Zealand. *Geofluids*, 4:259-283.
- Saintot, A., & Angelier, J. 2002. Tectonic paleostress fields and structural evolution of the NW-Caucasus fold-and-thrust belt from Late Cretaceous to Quaternary. *Tectonophysics*, 357(1):1-31.
- Sarkisyan, R.A. 1970. About the presence of different age subvolcanic dacite quartz porphyries in Kapan ore field. *Izvestia Nauki O Zemle, Proceedings of the National Academy of Sciences, Armenian SSR, Earth Sciences*, 23:13–17 (in Russian).
- Schardt, C., Cooke, D. R., Gemmill, J. B., and Large, R. R. 2001. Geochemical modeling of the zoned footwall alteration pipe, Hellyer volcanic-hosted massive sulfide deposit, Western Tasmania, Australia. *Economic Geology*, 96(5):1037-1054.
- Schwartz, M.O. 2000. Cadmium in Zinc Deposits: Economic Geology of a Polluting Element, *International Geology Review*, 42:445-469.
- Scott, S. D., & Barnes, H. L. 1971. Sphalerite geothermometry and geobarometry. *Econ. Geol.*, 66(653), 69.
- Scott, S. D., and Barnes, H. L. 1971. Sphalerite geothermometry and geobarometry. *Economic Geologist* 66(653), 69.
- Sengör, A.M.C., Altiner, D., Cin, A., Ustaömer, T., Hsü, K.J. 1988. Origin and assembly of the Tethyside orogenic collage at the expense of Gondwana Land. *Geological Society, London, Special Publications* 37:119–181.

- Seward, T. M. 1989. The hydrothermal chemistry of gold and its implications for ore formation: boiling and conductive cooling as examples. *Economic Geology*, 6:398-404.
- Sibson, R. H. 1996. Structural permeability of fluid-driven fault-fracture meshes. *Journal of Structural Geology*, 18(8):1031-1042.
- Sibson, R. H. 1981. Fluid flow accompanying faulting: field evidence and models, in D. W. Simpson and P. G. Richards, eds., *Earthquake prediction: an international review: American Geophysical Union Maurice Ewing Series*, 4:593– 603.
- Sibson, R. H. 1996, Structural permeability of fluid-driven fault fracture meshes: *Journal of Structural Geology*, 18:1031– 1042.
- Sibson, R. H., Robert, F., & Poulsen, K. H. 1988. High-angle reverse faults, fluid-pressure cycling, and mesothermal gold-quartz deposits. *Geology*, 16:551-555.
- Sibson, R.H. 1987. Earthquake rupturing as a mineralizing agent in hydrothermal systems. *Geology*, 15:701-704.
- Sillitoe, R.H., Hedenquist, J.W., 2003. Linkages between volcanotectonic settings, ore-fluid composition, and epithermal precious-metal deposits. *Society of Economic Geologists*, 101:315-343
- Simmonds, V., Moazzen, M. 2015. Re–Os dating of molybdenites from Oligocene Cu–Mo–Au mineralized veins in the Qarachilar area, Qaradagh batholith (northwest Iran): implications for understanding Cenozoic mineralization in South Armenia, Nakhchivan, and Iran. *International Geology Review*, 57:290–304.
- Simmons, S. F., & Brown, K. L. 2006. Gold in magmatic hydrothermal solutions and the rapid formation of a giant ore deposit. *Science*, 314(5797):288-291.
- Simmons, S.F., and Browne, P.R.L. 2000. Hydrothermal minerals and precious metals in the Broadlands-Ohaaki geothermal system: Implications for understanding low-sulphidation epithermal environments. *Economic Geology*, 95:971-999.
- Simmons, S.F., White, N.C., and John, D.A. 2005. Geological characteristics of epithermal precious and base metal deposits. *Economic Geology*, 29:485-522.
- Simpson, M. P., & Mauk, J. L. 2007. The Favona Epithermal Gold-Silver Deposit, Waihi, New Zealand. *Economic Geology*, 102(5):817-839.
- Sosson, M., Rolland, Y., Müller, C., Danelian, T., Melkonyan, R., Kekelia, S., Adamia, S., Babazadeh, V., Kangarli, T., Avagyan, A., Galoyan, G., Mosar, J., 2010. Subductions, obduction and collision in the Lesser Caucasus (Armenia, Azerbaijan, Georgia), new insights. *Geological Society, London, Special Publications*, 340:329–352.
- Spycher, N. F., and Reed, M. H. 1989. Evolution of a broadlands-type epithermal ore fluid along alternative PT paths; implications for the transport and deposition of base, precious, and volatile metals. *Economic Geology*, 84:328-359.

Stanley, C. R., and Madeisky, H. E. 1994. Litho-geochemical exploration for hydrothermal ore deposits using Pearce element ratio analysis. Alteration and alteration processes associated with ore-forming systems: Geological Association of Canada, Short Course Notes, 11:193-211.

Steiner, A., 1968. Clay minerals in hydrothermally altered rocks at Wairakei, New Zealand. *Clays and Clay Minerals*, 16(3):193-213.

Steiner, A. 1968. Clay minerals in hydrothermally altered rocks at Wairakei, New Zealand. *Clays and Clay Minerals*, 16:193-213.

Stoffregen, R. E. 1987. Genesis of acid-sulfate alteration and Au-Cu-Ag mineralization at Summitville, Colorado. *Economic Geology*, 82:1575-1591.

Thornburg, C.L., 1945, Some applications of structural geology to mining in the Pachuca-Real del Monte area, Pachuca silver district, Mexico. *Economic Geology*. 40:283-297.

Trudgill, B., and Cartwright, J. 1994. Relay-ramp forms and normal-fault linkages, Canyonlands National Park, Utah. *Geological Society of America Bulletin*, 106(9):1143-1157.

Tumanyan, G.A., 1992. Peculiarities of structure and position of Kapan anticlinorium. *Izvestia Nauki O Zemle (Proceedings of the National Academy of Sciences, Republic of Armenia, Earth Sciences)* 45:3–11 (in Russian).

Van Middlesworth, P. E., and S. A. Wood. 1998. The aqueous geochemistry of the rare-earth elements and yttrium. Part 7. REE, Th and U contents in thermal springs associated with the Idaho batholith [J]: *Appl. Geochem.*, 13:861–884.

Vardanyan, A., 2011. Geological Setting of the Drmbon Copper-Gold Deposit, Nagorno Karabakh Republic, Lesser Caucasus, in: *Abstract Volume, 9th Swiss Geoscience Meeting, 11-13 November 2011, Zurich*, 135–136.

Vardanyan, A.V., 2008. Geological structure of Drmbon gold-copperpyrite deposit and peculiarities of its structure. *Izvestia Nauki O Zemle, Proceedings of the National Academy of Sciences, Republic of Armenia, Earth Sciences*, 61:3–13 (in Russian)

Wallier, S. (2009). The geology and evolution of the Manantial Espejo epithermal silver (-gold) deposit, Deseado Massif, Argentina, Doctoral dissertation, University of British Columbia.

Walsh, J. J., Bailey, W. R., Childs, C., Nicol, A., & Bonson, C. G. (2003). Formation of segmented normal faults: a 3-D perspective. *Journal of Structural Geology*, 25(8):1251-1262.

Warren, I., Simmons, S. F., & Mauk, J. L. (2007). Whole-rock geochemical techniques for evaluating hydrothermal alteration, mass changes, and compositional gradients associated with epithermal Au-Ag mineralization. *Economic Geology*, 102(5):923-948.

Weatherley, D. K., and Henley, R. W. 2013. Flash vaporization during earthquakes evidenced by gold deposits. *Nature Geoscience*, 6:294-298.

White, G., Titley, M., Bennett, J., O'Connor, M., 2015. Technical Report Shahumyan Project, Kapan, Republic of Armenia. NI 43-101.

- White, N.C., Hedenquist, J.W., 1990. Epithermal environments and styles of mineralization: Variations and their causes and guidelines for exploration. *J Geochem Explor* 36: 445-474.
- White, N.C., Hedenquist, J.W. 1995. Epithermal gold deposits. Styles, characteristics and exploration. *Society of Economic Geology, News* 23: 1-13.
- Whitford, D.J., and Ashley, P.M. 1992. The Scuddles volcanic-hosted massive sulfide deposit, Western Australia: Geochemistry of the host rocks and evaluation of lithogeochemistry for exploration: *Economic Geology*, 87:873–888.
- Wilkinson, J. J. 2001. Fluid inclusions in hydrothermal ore deposits. *Lithos*, 55(1):229-272.
- Wilkinson, J.J., Johnston, J.D. 1996. Fluid pressure fluctuations, phase separation and gold precipitation during seismic fracture propagation. *Geology*, 24:395–398.
- Winchester, J. A. and Floyd, P. A. 1977. Geochemical discrimination of different magma series and their differentiation products using immobile elements. *Chemical Geology*, 20:325–343.
- Wood, D., Noble, M. 2008. Initial observations and interpretations of mapping from the Shahumyan and Centralni polymetallic vein deposits, Kapan, Armenia. *JIGSAW Geoscience for Dundee Precious Metals*.
- Wood, D., Noble, M., Standing, J., Outhwaite, M. 2008. Observations and interpretations from mapping in the Kapan region, Armenia. Unpublished report. *JIGSAW Geoscience for Dundee Precious Metals*
- Wood, S. A. 1990. The aqueous geochemistry of the rare-earth elements and yttrium 2, Theoretical predictions of speciation in hydrothermal solutions to 350°C at saturation water vapor pressure. *Chemical Geology*. 88:99–125.
- Yilmaz, A., Adamia, S., Chabukiani, A., Chkhotua, T., Erdoğlan, K., Tuzcu, S., Karabiyikoğlu, M., 2000. Structural Correlation of the Southern Transcaucasus (Georgia)-Eastern Pontides (Turkey). *Geological Society, London, Special Publications* 173:171–182.
- Zhang, X. 1992. The geochemistry and mineralogy of the Gies gold-silver telluride deposit, central Montana. *Retrospective Theses and Dissertations*. Paper 10164, (Unpublished)
- Zhang, X., & Spry, P. G. 1994. Calculated stability of aqueous tellurium species, calaverite, and hessite at elevated temperatures. *Economic Geology*, 89(5):1152-1166.
- Zhang, X., & Spry, P. G. 1994. Petrological, mineralogical, fluid inclusion, and stable isotope studies of the Gies gold-silver telluride deposit, Judith Mountains, Montana. *Economic Geology*, 89(3):602-627.
- Zhu, Y., An, F., and Tan, J. 2011. Geochemistry of hydrothermal gold deposits: a review. *Geoscience Frontiers*, 2:367-374.
- Zohrabyan, S.A. 1975. About subvolcanic nature of Barabatoomian quartz andesite dacite of Kapan ore field. *Izvestia Nauki O Zemle (Proceedings of the National Academy of Sciences, Armenian SSR, Earth Sciences)* 33:16–26 (in Russian).

Zohrabyan, S.A. 2005. New Concepts on Stratigraphy of Middle Jurassic Sediments in Southeastern Zangezur. *Izvestia Nauki O Zemle (Proceedings of the National Academy of Sciences, Republic of Armenia, Earth Sciences)* 58:17–22 (in Russian).

Appendix 1: Lithogeochemistry

This appendix contains analytical data. The preparation of lithogeochemical samples was performed by the author at the MDRU lab and analyzed at Acme Labs, Vancouver, Canada. The results are discussed in 2.

Sample Name	DCS-S058	DCS-S059	DCS-S060	DCS-S061	DCS-S062
Hole ID	SHDDR190	SHDDR190	SHDDR190	SHDDR190	SHDDR190
Sequence	Barabatoom	Barabatoom	Barabatoom	Barabatoom	Barabatoom
Deposit	Shahumyan	Shahumyan	Shahumyan	Shahumyan	Shahumyan
Rock Type	QA	QA	QA	QA	QA
Depth	188.7	203.7	207.5	211.4	225.9
Easting	8623848.18	8623848.18	8623848.18	8623848.18	8623848.18
Northing	4342802.18	4342802.18	4342802.18	4342802.18	4342802.18
Datum	Pulkovo 1942 GK 8				
SiO ₂ %	63.600886	62.972564	64.622944	63.267746	64.929563
Al ₂ O ₃ %	17.1079	17.887233	16.823328	17.436678	17.296897
Fe ₂ O ₃ %	6.23352	6.578095	6.152532	6.065877	5.825654
CaO%	3.54393	2.829985	1.922666	3.652571	1.779473
MgO%	4.240059	4.298985	5.223243	4.761387	4.618155
Na ₂ O%	4.039658	3.359257	3.418073	2.500272	3.961445
K ₂ O%	0.464086	1.220566	1.036103	1.500163	0.847368
MnO%	0.32697	0.421257	0.384533	0.391347	0.317763
TiO ₂ %	0.400802	0.388853	0.373852	0.391347	0.381316
P ₂ O ₅ %	0.04219	0.043206	0.042726	0.032612	0.042368
Total (Oxides)	94.81	92.58	93.62	91.99	94.41
Ba (ppm)	40	67	69	73	49
Be (ppm)	3	0.5005	1	3	0.5005
Co (ppm)	11.9	11.4	13.5	12.2	11.9
Cs (ppm)	1.4	1	0.4	0.9	3.4
Ga (ppm)	11.7	11.7	12.2	11.6	13
Hf (ppm)	0.6	1.2	0.9	0.7	0.9
Nb (ppm)	1.7	3.4	1.9	0.8	1.3
Rb (ppm)	6.9	19	16.2	23.5	14.8
Sn (ppm)	0.5005	0.5005	0.5005	0.5005	0.5005
Sr (ppm)	193.7	83.4	53.8	53.9	87
Ta (ppm)	0.0505	0.2	0.1	0.1	0.2
Th (ppm)	0.2	0.3	0.2	0.1005	0.1005
U (ppm)	0.0505	0.0505	0.0505	0.0505	0.0505
V (ppm)	154	119	133	138	132
W (ppm)	1.6	0.5	5.7	0.25005	0.6
Zr (ppm)	28.7	38.2	29.3	28	30
Y (ppm)	13.6	10.9	12.1	13.1	10.2
La (ppm)	2.3	1.7	2.3	2.4	1.7
Ce (ppm)	6.2	4.7	6.1	5.6	4.1
Pr (ppm)	0.88	0.66	0.82	0.78	0.63
Nd (ppm)	4.5	3.7	4.3	4.2	3
Sm (ppm)	1.47	0.98	1.15	1.29	0.99
Eu (ppm)	0.55	0.43	0.62	0.67	0.35
Gd (ppm)	1.63	1.36	1.62	1.69	1.33
Tb (ppm)	0.33	0.26	0.29	0.32	0.23

Sample Name	DCS-S058	DCS-S059	DCS-S060	DCS-S061	DCS-S062
Dy (ppm)	2.01	1.81	1.73	2.15	1.6
Ho (ppm)	0.42	0.37	0.4	0.4	0.35
Er (ppm)	1.38	1.03	1.28	1.23	1.04
Tm (ppm)	0.23	0.18	0.22	0.23	0.18
Yb (ppm)	1.7	1.29	1.56	1.54	1.44
Lu (ppm)	0.29	0.24	0.27	0.29	0.23
Mo (ppm)	0.2	0.0505	0.1	0.0505	0.0505
Cu (ppm)	70	9.9	15.1	216.8	53.4
Pb (ppm)	14.8	30.6	4.7	10.9	2.7
Zn (ppm)	524	795	163	1046	436
Ni (ppm)	1.5	1.6	1.6	1.5	1.6

Sample Name	DCS-S063	DCS-S064	DCS-S081	DCC_S004	DCC_S007
Hole ID	SHDDR190	SHDDR190	SHDDR338	CEDDE-07	CEDDE-07
Sequence	Barabatoom	Barabatoom	Barabatoom	Galidzor-Katar	Galidzor-Katar
Deposit	Shahumyan	Shahumyan	Shahumyan	Centralni	Centralni
Rock Type	QA	QA	QA	BA	BA
Depth	229	241.3	918.5	75.1	193.6
Easting	8623848.18	8623848.18	8623841.46	8619231.40	8619231.40
Northing	4342802.18	4342802.18	4343053.22	4345699.65	4345699.65
Datum	Pulkovo 1942 GK 8				
SiO ₂ %	64.101201	62.839158	63.397255	54.696663	67.114788
Al ₂ O ₃ %	17.061763	17.657912	17.353034	17.07005	14.705274
Fe ₂ O ₃ %	6.367599	6.37074	7.219952	15.25749	8.138573
CaO%	1.934729	3.179944	5.103217	0.213242	0.434333
MgO%	4.889976	4.536575	3.604736	9.361339	4.353671
Na ₂ O%	4.018284	3.581506	2.263439	1.396737	3.660807
K ₂ O%	0.882322	1.085305	0.513465	0.522444	0.599793
MnO%	0.318911	0.303885	0.125747	0.533106	0.237849
TiO ₂ %	0.382694	0.401563	0.37724	0.895618	0.692865
P ₂ O ₅ %	0.042522	0.043412	0.041916	0.053311	0.062048
Total (Oxides)	94.07	92.14	95.43	93.79	96.7
Ba (ppm)	105	52	32	40	43
Be (ppm)	1	0.5005	0.5005	0.5005	0.5005
Co (ppm)	12.7	15.4	13.4	36.1	13.4
Cs (ppm)	1.2	0.8	4.1	1.3	0.2
Ga (ppm)	11.7	12.5	12.9	16.5	12.2
Hf (ppm)	0.7	1.3	0.6	0.9	1.1
Nb (ppm)	1.1	2.6	1.4	4.2	2.2
Rb (ppm)	13.7	18.9	8.7	8.3	10.4
Sn (ppm)	0.5005	0.5005	1	0.5005	0.5005
Sr (ppm)	49.5	83.8	120.4	10.8	31.6
Ta (ppm)	0.1	0.2	0.1	0.4	0.2
Th (ppm)	0.1005	0.2	0.2	0.3	0.7
U (ppm)	0.0505	0.0505	0.0505	0.1	0.3
V (ppm)	128	156	125	460	178
W (ppm)	0.7	0.7	0.25005	1.5	0.7
Zr (ppm)	27.6	30.1	28.5	29.1	53.6
Y (ppm)	10.6	12.9	14.1	6.2	13.8
La (ppm)	1.7	2.5	2.3	1.9	3.5
Ce (ppm)	4.7	5.7	5.3	3.4	8.6
Pr (ppm)	0.69	0.89	0.75	0.43	1.15
Nd (ppm)	3.2	4.7	4.2	2	5.9
Sm (ppm)	1.06	1.3	1.22	0.52	1.44
Eu (ppm)	0.41	0.51	0.53	0.21	0.52
Gd (ppm)	1.43	1.62	1.78	0.72	1.99
Tb (ppm)	0.28	0.32	0.33	0.45	0.32

Sample Name	DCS-S063	DCS-S064	DCS-S081	DCC_S004	DCC_S007
Dy (ppm)	1.73	2.08	2.16	1.17	2.23
Ho (ppm)	0.37	0.42	0.48	0.28	0.53
Er (ppm)	1.19	1.27	1.54	0.83	1.72
Tm (ppm)	0.22	0.24	0.24	0.15	0.28
Yb (ppm)	1.37	1.57	1.67	1.06	1.73
Lu (ppm)	0.25	0.26	0.29	0.17	0.28
Mo (ppm)	0.2	0.0505	0.3	0.0505	0.3
Cu (ppm)	137.7	271.4	65.1	263.7	3.4
Pb (ppm)	9.4	20.9	0.5	1.8	2.2
Zn (ppm)	286	895	59	255	118
Ni (ppm)	2.1	1.6	1.5	23.2	5.8

Sample Name	DCC_S030	DCC-S023	2014_SR_01	2014_SR_11	2014_SR_13
Hole ID	CEDDE-05	CEDDE-02	Surface	Surface	Surface
Sequence	Galidzor-Katar	Galidzor-Katar	Vachagan	Vachagan	Vachagan
Deposit	Centralni	Centralni	Kapan	Kapan	Kapan
Rock Type	BA	BA	A	A	A
Depth	232.4	243.5			
Easting	8619064.54	8619121.59	8615550.16	8615294.35	8615142.23
Northing	4346100.26	4345841.84	4351914.20	4352214.15	4352576.05
Datum	Pulkovo 1942 GK 8				
SiO ₂ %	58.398744	54.453356	75.832306	73.442288	74.336283
Al ₂ O ₃ %	17.320774	19.723512	12.56679	14.198161	12.909943
Fe ₂ O ₃ %	12.77865	11.872098	4.130703	3.677222	4.914107
CaO%	0.334903	0.538202	0.986436	0.418795	1.84279
MgO%	5.232862	7.133812	0.431566	0.367722	0.33316
Na ₂ O%	3.715332	4.474462	4.551993	6.48621	4.549714
K ₂ O%	0.962847	0.474884	1.037813	0.837589	0.562207
MnO%	0.460492	0.422119	0.051377	0.030644	0.041645
TiO ₂ %	0.743066	0.854791	0.339088	0.449438	0.437272
P ₂ O ₅ %	0.052329	0.052765	0.071928	0.091931	0.072879
Total (Oxides)	95.55	94.76	97.32	97.9	96.05
Ba (ppm)	142	43	39	42	34
Be (ppm)	0.5005	0.5005	2	0.5005	1
Co (ppm)	28.2	26.6	4.2	2.7	6.6
Cs (ppm)	0.3	0.4	0.5	1.8	2.3
Ga (ppm)	14.5	17.5	12.5	11.4	9.2
Hf (ppm)	0.7	0.9	3.2	3.2	2.4
Nb (ppm)	1.5	2.7	3.1	3.1	2.1
Rb (ppm)	16	8.8	10.5	20.9	14.7
Sn (ppm)	0.5005	0.5005	0.5005	0.5005	0.5005
Sr (ppm)	37.9	56.2	60.9	100.2	59.2
Ta (ppm)	0.0505	0.2	0.2	0.2	0.1
Th (ppm)	0.3	0.3	1.1	1.2	0.9
U (ppm)	0.0505	0.0505	0.5	0.4	0.2
V (ppm)	386	414	10	63	71
W (ppm)	1.3	1.1	0.25005	0.25005	0.25005
Zr (ppm)	22.9	26.2	114.7	116.3	88
Y (ppm)	9.9	10.2	33.8	31.3	31.9
La (ppm)	1.5	2.3	5.6	4.9	5.9
Ce (ppm)	3.8	5.2	12.7	13.4	12.6
Pr (ppm)	0.57	0.73	2.07	1.75	2.03
Nd (ppm)	3.2	3.8	10.4	8.5	9.9
Sm (ppm)	0.99	1.06	3.34	2.82	3.03
Eu (ppm)	0.44	0.43	1	0.76	0.77
Gd (ppm)	1.37	1.53	4.68	4.13	4.21
Tb (ppm)	0.26	0.28	0.86	0.76	0.74

Sample Name	DCC_S030	DCC-S023	2014_SR_01	2014_SR_11	2014_SR_13
Dy (ppm)	1.94	1.88	5.43	4.74	4.73
Ho (ppm)	0.46	0.37	1.23	1.12	1.08
Er (ppm)	1.46	0.98	3.69	3.32	3.16
Tm (ppm)	0.21	0.18	0.58	0.5	0.49
Yb (ppm)	0.97	1.35	3.86	3.37	3.12
Lu (ppm)	0.21	0.18	0.6	0.52	0.47
Mo (ppm)	0.4	0.4	0.3	0.2	0.3
Cu (ppm)	12.5	56.3	6.3	34.4	11
Pb (ppm)	5.1	2.9	1.5	2	2.2
Zn (ppm)	225	264	91	82	73
Ni (ppm)	6.9	9.5	1.4	2.2	2.8

Sample Name	2014_SR_22	DNS_027	DNS_039	DNS_043
Hole ID	Surface	NEDDE001	NEDDE001	NEDDE001
Sequence	Vachagan	Vachagan	Vachagan	Vachagan
Deposit	Kapan	Noreshenik	Noreshenik	Noreshenik
Rock Type	A	BA	BA	BA
Depth		179.3	219.3	235.5
Easting	8614930.09	8621449.74	8621447.65	8621445.87
Northing	4347806.20	4348762.01	4348740.83	4348725.20
Datum	Pulkovo 1942 GK 8			
SiO ₂ %	71.58625	69.628229	71.718539	68.353883
Al ₂ O ₃ %	14.243667	14.587272	14.905798	14.298075
Fe ₂ O ₃ %	5.150846	5.860113	4.330176	5.753839
CaO%	1.618837	1.281243	0.67659	3.558295
MgO%	2.838221	3.213611	2.466951	3.09323
Na ₂ O%	1.818564	2.940559	3.185177	3.450141
K ₂ O%	2.081362	1.722327	2.040179	0.800346
MnO%	0.063072	0.168032	0.052045	0.086524
TiO ₂ %	0.504573	0.514598	0.541272	0.529959
P ₂ O ₅ %	0.094607	0.084016	0.083273	0.075708
Total (Oxides)	95.13	95.22	96.07	92.46
Ba (ppm)	91	94	101	48
Be (ppm)	0.5005	0.5005	0.5005	0.5005
Co (ppm)	12.8	12.5	12	11.6
Cs (ppm)	0.8	0.4	0.7	0.5
Ga (ppm)	13.1	12.3	12.9	12.5
Hf (ppm)	2.5	3.3	3.4	3.3
Nb (ppm)	2.5	3.1	3	2.8
Rb (ppm)	24.8	39.7	35.8	13.5
Sn (ppm)	0.5005	0.5005	1	0.5005
Sr (ppm)	94	25.8	24.6	75.2
Ta (ppm)	0.2	0.2	0.2	0.2
Th (ppm)	0.7	1.4	1.4	1.2
U (ppm)	0.5	0.5	0.8	0.6
V (ppm)	106	82	85	83
W (ppm)	0.25005	0.25005	0.25005	0.25005
Zr (ppm)	93.9	119.7	120.8	111.9
Y (ppm)	33.8	28.8	30.8	28.9
La (ppm)	5.6	2.2	4	4.8
Ce (ppm)	12.4	5.7	9.2	11.9
Pr (ppm)	1.9	0.8	1.52	1.78
Nd (ppm)	9	4.1	7.4	8.4
Sm (ppm)	3.1	1.6	2.82	2.74
Eu (ppm)	0.89	0.47	0.79	0.78
Gd (ppm)	4.07	2.51	3.95	3.74
Tb (ppm)	0.79	0.63	0.74	0.73

Sample Name	2014_SR_22	DNS_027	DNS_039	DNS_043
Dy (ppm)	5.3	4.49	4.73	4.82
Ho (ppm)	1.21	1.15	1.1	1.12
Er (ppm)	3.67	3.83	3.45	3.37
Tm (ppm)	0.55	0.58	0.54	0.52
Yb (ppm)	3.66	3.93	3.55	3.47
Lu (ppm)	0.58	0.63	0.6	0.52
Mo (ppm)	0.0505	0.4	1.4	0.3
Cu (ppm)	127	61.9	10.3	8.7
Pb (ppm)	0.4	18.7	4.5	3.8
Zn (ppm)	62	181	162	46
Ni (ppm)	4.7	3.9	4.3	4.3

Appendix 2: Geochronology: Ar-Ar and K-Ar

This appendix contains analytical data. This appendix is not discussed in detail in this thesis. Samples for Ar/Ar geochronological analyses were partially prepared at UBC by the author and sent to the University of Geneva, Geneva Switzerland and analysed by Dr. Richard Alan Spikings. Samples for K/Ar geochronological analyses were partially prepared at UBC and sent to Institute for Nuclear Research, Hungarian Academy of Sciences, Debrecen, Hungary for K/Ar analyses and analysed by Drs. Zsolt Benkó and Zoltán Pécskay undertook K/Ar analyses.

Sample 2014-SR-021A															
Step	⁴⁰ Ar/ ³⁹ Ar	±1σ	³⁷ Ar/ ³⁹ Ar	±1σ	³⁶ Ar/ ³⁹ Ar	±1σ	⁴⁰ Ar*/ ³⁹ Ar _k	±1σ	⁴⁰ Ar(mol)	⁴⁰ Ar* (%)	³⁹ Ar _k (%)	Age(Ma)	±2σ (Ma)	K/Ca	±2σ
	30.490	0.07078	0.00791	0.00089	0.01642	0.00035	25.637	0.119	5.420E-15	84.08	15.34	149.62	1.33	54.38	12.30
	27.227	0.07077	0.00516	0.00198	0.00474	0.00069	25.826	0.215	2.064E-15	94.86	6.54	150.68	2.41	83.36	64.11
	27.154	0.06278	0.00441	0.00096	0.00293	0.00050	26.288	0.160	3.177E-15	96.81	10.10	153.27	1.78	97.58	42.43
	27.484	0.05929	0.00544	0.00052	0.00378	0.00020	26.366	0.082	6.752E-15	95.93	21.20	153.70	0.91	79.03	15.00
	27.656	0.06755	0.00339	0.00151	0.00523	0.00054	26.108	0.172	2.442E-15	94.40	7.62	152.26	1.92	126.84	113.13
	28.182	0.07254	0.00892	0.00102	0.00509	0.00036	26.678	0.127	4.242E-15	94.66	12.99	155.45	1.42	48.23	11.07
	27.445	0.07317	0.02205	0.00241	0.00385	0.00084	26.308	0.259	1.551E-15	95.85	4.88	153.38	2.90	19.51	4.26
	26.310	0.07086	0.00103	0.00189	0.00378	0.00064	25.193	0.202	1.863E-15	95.76	6.11	147.14	2.26	416.21	1522.83
	27.925	0.06897	0.00679	0.00192	0.00685	0.00060	25.900	0.188	1.938E-15	92.75	5.99	151.10	2.10	63.31	35.84
	28.321	0.14872	0.00332	0.00330	0.00678	0.00166	26.317	0.509	9.921E-16	92.92	3.02	153.43	5.69	129.71	258.16
	27.221	0.07687	0.01239	0.00226	0.00616	0.00064	25.400	0.203	1.956E-15	93.31	6.20	148.30	2.27	34.71	12.64
Alunite J=0.0033730±5.4E-6					Total Fusion Age 152.04±0.72 Ma										
Plateau Age 153.83±1.05 Ma					Inverse Isochron Age 149.63±6.03 Ma										
Sample SR_S025B															
Step	⁴⁰ Ar/ ³⁹ Ar	±1σ	³⁷ Ar/ ³⁹ Ar	±1σ	³⁶ Ar/ ³⁹ Ar	±1σ	⁴⁰ Ar*/ ³⁹ Ar _k	±1σ	⁴⁰ Ar(mol)	⁴⁰ Ar* (%)	³⁹ Ar _k (%)	Age(Ma)	±2σ (Ma)	K/Ca	±2σ
	24.149	0.06159	0.03304	0.00079	0.00884	0.00021	21.537	0.083	4.703E-15	89.18	9.83	126.73	0.95	13.02	0.62
	21.913	0.04876	0.02396	0.00058	0.00250	0.00023	21.175	0.083	6.485E-15	96.63	14.95	124.68	0.95	17.95	0.87
	22.670	0.05870	0.02607	0.00049	0.00189	0.00012	22.113	0.068	9.323E-15	97.54	20.77	130.00	0.77	16.50	0.62
	23.791	0.05878	0.03052	0.00092	0.00236	0.00029	23.095	0.103	5.052E-15	97.07	10.72	135.57	1.17	14.09	0.85
	23.464	0.05711	0.03087	0.00098	0.00203	0.00023	22.868	0.088	4.650E-15	97.46	10.01	134.28	0.99	13.93	0.88
	23.462	0.06420	0.03519	0.00133	0.00100	0.00037	23.169	0.127	3.362E-15	98.75	7.24	135.98	1.44	12.22	0.92
	24.148	0.05637	0.03094	0.00108	0.00282	0.00050	23.317	0.159	2.510E-15	96.55	5.25	136.82	1.79	13.90	0.97
	24.556	0.06734	0.03990	0.00103	0.00362	0.00029	23.490	0.109	3.602E-15	95.66	7.41	137.79	1.23	10.78	0.56
	23.717	0.06370	0.03031	0.00081	0.00242	0.00046	23.005	0.149	3.282E-15	96.99	6.99	135.05	1.68	14.19	0.76
	31.946	0.11406	0.06290	0.00282	0.03404	0.00098	21.892	0.297	1.659E-15	68.52	2.62	128.75	3.38	6.84	0.61
	24.497	0.06399	0.02639	0.00155	0.01598	0.00068	19.777	0.206	2.046E-15	80.73	4.22	116.70	2.35	16.29	1.91
Alunite, J=0.0034040±5.4E-6					Total Fusion Age 131.04±0.55 Ma										
Weighted Mean Age 135.73±1.19 Ma					Inverse Isochron Age 131.94±3.34 Ma										

Mass discrimination 0.9794±0.051.

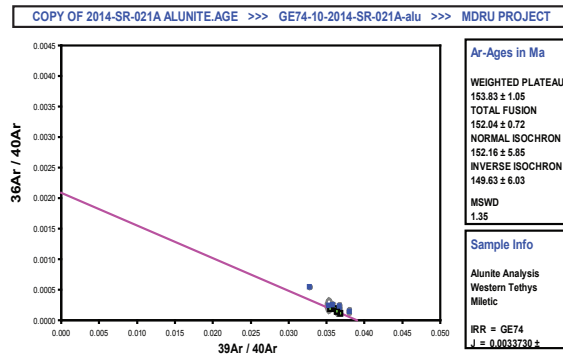
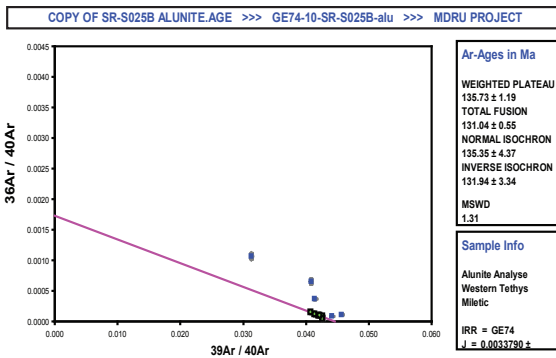
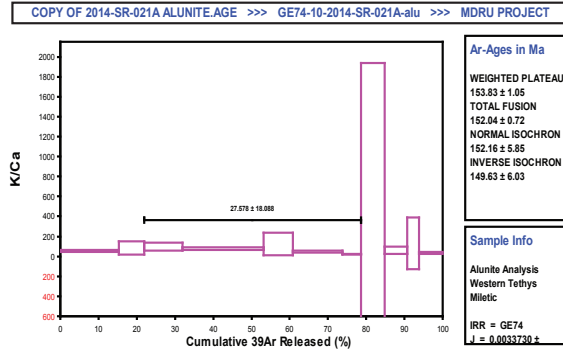
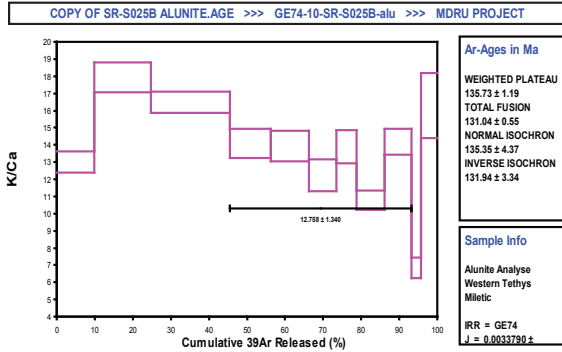
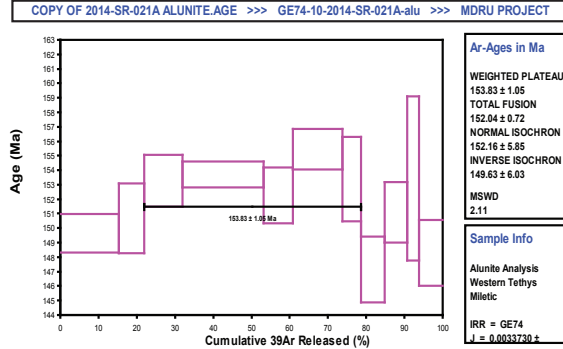
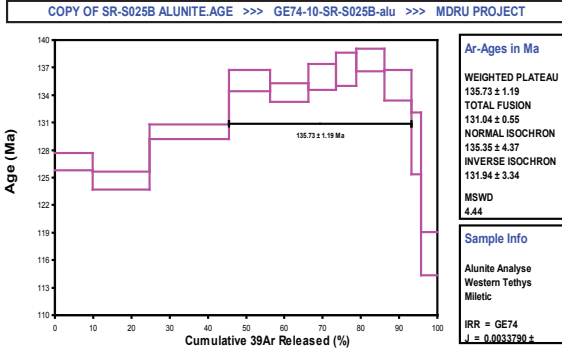
Data are corrected for blanks, interfering nucleogenic reactions and decay of ³⁷Ar and ³⁹Ar.

Irradiated for 12 hours at Oregon State University, TRIGA, CLICIT, ³⁹Ar/³⁷Ar 6.73E-4, ³⁶Ar/³⁷Ar 2.64E-4, ⁴⁰Ar/³⁹Ar 1.01E-3, ³⁸Ar/³⁹Ar 1.138E-2.

Steps highlighted with bold text are included in the calculation of the weighted mean age and the plateau age.

Samples heated with a IR-CO2 laset for 30 seconds, with 5 minutes cleaning with a ST101 and AP10 getter in a stainless teel extraction line.

Data collected with an Argus mass spectrometer. Multi collection with 1E11Ω Faraday (⁴⁰Ar) and 1E12Ω Faradays (³⁹Ar. ³⁸Ar. ³⁷Ar. ³⁶Ar).



Sample Name	Analysed Mineral	Size Fraction	K%	$^{40}\text{Ar}_{\text{rad}} [\text{cm}^{-3} \text{STP} \cdot \text{g}^{-1}]$	$^{40}\text{Ar}_{\text{rad}} (\%)$	K/Ar age [Ma]	Sericite-Crystallinity	FWHM
2014_UG_S021	Sericite	<2 μm	4.23	2.47626×10^{-5}	59	144.7 ± 4.2	2.278	0.433
2014_UG_S021	Sericite	<10 μm	3.46	2.08276×10^{-5}	57	148.5 ± 4.4	2.278	0.433
2014_DNS_021	Sericite	<2 μm	6.56	4.21000×10^{-5}	75	158.0 ± 4.2	1.703	
DCC_S009	Sericite	<2 μm	5.41	3.34061×10^{-5}	48	152.2 ± 4.9	2.383	0.193
DCC_S009	Sericite	<10 μm	4.35	2.93808×10^{-5}	80	165.9 ± 4.2	2.383	0.193
DCS_S077	Sericite	<2 μm	1.27	8.00389×10^{-5}	29	155.5 ± 7.4	1.056	0.228

XRD Results for K-Ar and Ar-Ar Geochronology

**Samples have been treated by ethylene-glycol before XRD analyses.*

2014_UG_S021: The <2 μm size fraction consist of predominantly illite, minor kaolinite, quartz and pyrite. Smectite is present only in trace amount. In the < 10 μm fraction the proportion of the pyrite and quartz is slightly elevated.

2014_DNS_022: The sample consists of illite and chlorite. Quartz and pyrite are present in minor quantity

2014_DNS_021: The sample consists of predominantly well crystallized illite and pyrite in trace amount. In the < 10 μm fraction beside illite quartz, calcite and pyrite are present

DCC_S009: The sample consists of illite and chlorite. The relative proportion of illite is slightly higher. Quartz occurs in trace amount. In the < 10 μm fraction the relative proportion of the quartz is higher, still, minimal.

DCS_S077 : The predominant mineral phase in this sample is chlorite, and in lesser amount illite. In the coarse grained fraction (<10 μm) quartz and feldspar are present in minor amount.

2014_SR_021A: The predominant mineral phase in this sample is K-Alunite and in lesser amounts Na-alunite, kaolinite and illite

SR_S025B: The Predominant mineral phase in this sample is Na-Alunite and in lesser amounts kaolinite and illite.

Geochronology Discussion and Results

Illite in hydrothermal systems are highly sensitive due to their crystal structure (illite-smectite interstratification), broad temperature range at they form (300-180 °C) and the nature of ore forming system (multiple upheating, fluid flow). Multiple fluid circulation may result in incorporation of radiogenic Ar* or loss of Ar* from the crystal structure after the formation of the mineral. Therefore, it is required to carry out the analysis on many different size fractions, from different parts of the hydrothermal system.

The separated samples contain in variable amount illite without smectite interstratification in the illite structure. The separates are free of any magmatic components (feldspar, mica), therefore magmatic mineral contamination did not influence the obtained radiometric ages.

Assuming that all veins within the Kapan district formed at the same time an isochron diagram can be produced to calculate a more accurate age for mineralization within the district. The calculated radiometric ages vary between 144 and 165 Ma (Fig. 6). Majority of the data scatter around 155 Ma. The <10 µm samples give systematically higher ages than the corresponding < 2µm ages (166 vs. 152 Ma and 148 vs.144 Ma). Based on the highly scattered data it is difficult to determine the age of the mineralization. In order to constrain the age of the mineralization, the measured potassium concentrations were plotted against the calculated Ar amount [(given in ccSTP/g = cubic centimeter at standard temperature and pressure (0 °C and one atmosphere)] with their error bars on an isochron diagram (Fig. 7). The major advantage of the isochron diagram is that if the K concentrations are variable, the Ar loss or gain can be easily recognized.

Some samples deviate from the calculated model age considerably. A significant difference in radiometric ages between the <2 and <10 µm size fractions of the sample DCC_S009 was found. It is possible that the coarser grained fraction belongs to an elder phase of the hydrothermal system, which was overprinted by the 153 Ma event. Another possibility is that during the formation of the illite/sericite, Ar* was

incorporated in the structure of the illite (excess Ar) which results in an apparent old age.

The “young” samples (2014_UGS_021) may have suffered some Ar-loss during sample preparation or due to the overprint of a second hydrothermal event.

Isochrons for various model ages (153-156 Ma) were calculated and tested. The best fit was found for the 153 Ma isochron, therefore the most probable age of the mineralization is 153 Ma, Kimmeridgian, Upper Jurassic. This calculated age corresponds with Ar-Ar age of K-Rich coarse alunite, dated to 153.83 ± 1.05 . This alunite sample was taken from the Shahumyan lithocap covering the Shahumyan Veins.

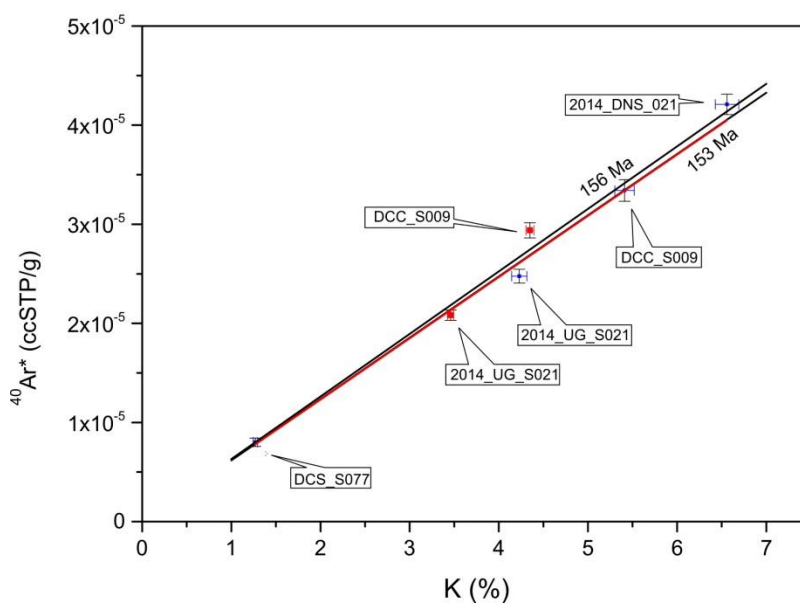


Fig: Isochron diagram of the analyzed samples. The $<2 \mu\text{m}$ samples are plotted with blue, the $<10 \mu\text{m}$ samples with red squares. Black lines are the calculated isochrones for 156 and 153 Ma, respectively, the red line was fitted on the $<2 \mu\text{m}$ size samples.

Appendix 3: Alteration Analysis

This appendix contains analytical data. The preparation of lithogeochemical samples was performed by the author at the MDRU lab and analyzed at Acme Labs, Vancouver, Canada. Further data analysis and interpretation is performed by the author, the results are discussed in 4.

Appendix 3a: Whole Rock Geochemistry for Alteration Analysis

Sample Name	DCS-S018	3-54	5-16	KN-2-82-1
Hole ID	SHDDR0418			
Database	Yarra (2016)	Mederer (2013)	Mederer (2013)	Mederer (2013)
Alteration	Least Altered	Least Altered	Least Altered	Least Altered
Depth	148.4			
Easting	8623432.62	8624374.00	8624458.00	8621513.00
Northing	4344477.11	4343297.00	4342347.00	4342020.00
Datum	Pulkovo 1942 GK 8			
*Least Mobile				
SiO ₂ (%)	61.2	57.76	63.81	58.38
Al ₂ O ₃ (%)	16.76	17.59	17.47	16.4
Fe ₂ O ₃ (%)	5.86	5.12	4.35	6.16
CaO (%)	5.43	5.63	5.31	4.03
MgO (%)	2.96	2.37	1.95	3.27
Na ₂ O (%)	3.19	2.76	3.5	3.26
K ₂ O (%)	0.26	1.05	0.3	1.08
MnO (%)	0.22	0.1	0.2	0.06
TiO ₂ (%)	0.34	0.41	0.34	0.39
P ₂ O ₅ (%)	0.04	0.08	0.08	0.05
Cr ₂ O ₃ (%)	0.0005			
V ₂ O ₅ (%)	0.024			
LOI (%)	3.32	6.68	1.78	6.1
TOT/C (%)	0.27			
TOT/S (%)	0.27			
Total (%)	99.99	99.55	99.09	99.18
Ba (ppm)	44	49	54	50
Be (ppm)	0.5	N/A	N/A	N/A
Co (ppm)	12.2	9	7	12
Cs (ppm)	0.7	2.7	0.8	1.5
Ga (ppm)	11.9	14	14	13
Hf (ppm)	1.1	1.36	1.29	0.9
Nb (ppm)	0.05	1.1	1	0.7
Rb (ppm)	3.6	21	5	19
Sn (ppm)	0.5			
Sr (ppm)	149.3	156	249	53
Ta (ppm)	0.05	0.08	0.06	0.06
Th (ppm)	0.15	0.4	0.4	0.3
U (ppm)	0.05	0.2	0.2	0.1
V (ppm)	110	106	65	145
W (ppm)	0.7			
Zr (ppm)	31.1	44	39	28
Y (ppm)	14.1	11	9	12

Sample Name	DCS-S018	3-54	5-16	KN-2-82-1
La (ppm)	1.9	4.1	3.6	1.9
Ho (ppm)	0.44	0.4	0.34	0.46
Er (ppm)	1.26	1.03	0.88	1.37
Tm (ppm)	0.23	0.15	0.15	0.2
Yb (ppm)	1.6	1.07	1.13	1.53
Lu (ppm)	0.27	0.17	0.16	0.21
Mo (ppm)	0.3	0.6	0.001	0.3
Cu (ppm)	31.8	11	8	8
Pb (ppm)	1.8	2.6	1.9	0.8
Zn (ppm)	57	37	36	37
Ni (ppm)	1.5	4	6	0.001
As (ppm)	5.8	2	6	4
Cd (ppm)	0.05			
Sb (ppm)	0.05	0.3	0.3	0.6
Bi (ppm)	0.05	0.001	0	0.1
Ag (ppm)				
Au (ppm)				
Hg (ppm)				

Sample Name	DCS-S047	DCS-S048	DCS-S056	DCS-S057
Hole ID	SHDDR190	SHDDR190	SHDDR190	SHDDR190
Database	Yarra (2016)	Yarra (2016)	Yarra (2016)	Yarra (2016)
Alteration	Proximal	Proximal	Proximal	Proximal
Depth	88.9	94.3	165.7	176.1
Easting	8623848.18	8623848.18	8623848.18	8623848.18
Northing	4342802.18	4342802.18	4342802.18	4342802.18
Datum	Pulkovo 1942 GK 8			
*Least Mobile				
SiO ₂ (%)	63.2	59.8	58.6	60.2
Al ₂ O ₃ (%)	15.98	15.82	16.41	16.64
Fe ₂ O ₃ (%)	5.33	5.76	6.34	6.27
CaO (%)	1.36	2.09	1.74	0.77
MgO (%)	2.03	4.07	5.19	5.32
Na ₂ O (%)	5.17	3.21	1.99	1.93
K ₂ O (%)	1.14	0.97	1.33	1.75
MnO (%)	0.22	0.34	0.45	0.4
TiO ₂ (%)	0.34	0.34	0.37	0.38
P ₂ O ₅ (%)	0.03	0.04	0.03	0.04
Cr ₂ O ₃ (%)	0.0005	0.0005	0.0005	0.002
V ₂ O ₅ (%)	0.024	0.024	0.024	0.026
LOI (%)	4.76	5.75	6.14	5.51
TOT/C (%)	0.3	0.49	0.32	0.13
TOT/S (%)	3.62	3.56	2.47	2.13
Total (%)	100.46	100.39	100.18	100.29
Ba (ppm)	74	60	77	118
Be (ppm)	0.5	2	0.5	0.5
Co (ppm)	10.5	11.6	14.3	13.8
Cs (ppm)	0.3	0.2	1	1
Ga (ppm)	9.4	10.8	13.3	13.4
Hf (ppm)	1	0.8	1	1
Nb (ppm)	0.05	0.05	2.6	2
Rb (ppm)	21.4	18.2	23.7	31.6
Sn (ppm)	0.5	0.5	0.5	0.5
Sr (ppm)	58.7	41.5	46.5	33.9
Ta (ppm)	0.05	0.05	0.2	0.2
Th (ppm)	0.15	0.15	0.2	0.2
U (ppm)	0.1	0.1	0.1	0.05
V (ppm)	112	115	146	138
W (ppm)	0.6	1.2	0.25	0.6
Zr (ppm)	28.1	26.5	30.1	30
Y (ppm)	12.2	11.8	11.2	11.4

Sample Name	DCS-S047	DCS-S048	DCS-S056	DCS-S057
La (ppm)	1.6	2.1	2.4	1.1
Ho (ppm)	0.38	0.45	0.4	0.37
Er (ppm)	1.17	1.29	1.29	1.25
Tm (ppm)	0.2	0.21	0.2	0.2
Yb (ppm)	1.31	1.57	1.38	1.52
Lu (ppm)	0.24	0.28	0.22	0.24
Mo (ppm)	0.05	0.2	0.2	0.2
Cu (ppm)	30.9	209.6	33.6	28.5
Pb (ppm)	51.1	15.2	8.2	6.1
Zn (ppm)	999	1932	2381	3077
Ni (ppm)	1.4	1.6	1.5	1.6
As (ppm)	286	143.7	87.6	38.7
Cd (ppm)	7.5	15.2	18.8	23.4
Sb (ppm)	0.8	0.2	0.05	0.05
Bi (ppm)	0.05	0.05	0.1	0.05
Ag (ppm)	0.4	2.1	0.6	0.6
Au (ppm)	147.6	211.3	48.9	85.4
Hg (ppm)	0.04	0.03	0.07	0.08

Sample Name	DCS-S061	DCS-S065	708482	708218	708224
Hole ID	SHDDR190	SHDDR190	SHDDR-0285	SHDDR-0460	SHDDR-0460
Database	Yarra (2016)	Yarra (2016)	Yarra (2016)	Yarra (2016)	Yarra (2016)
Alteration	Proximal	Proximal	Proximal	Proximal	Proximal
Depth	211.4	250.8	86	95	127
Easting	8623848.18	8623848.18	8623669.46	8623666.49	8623666.02
Northing	4342802.18	4342802.18	4343410.19	4344438.88	4344423.15
Datum	Pulkovo 1942 GK 8				
*Least Mobile					
SiO ₂ (%)	58.2	62.1	61.5	69	71.2
Al ₂ O ₃ (%)	16.04	15.84	15.01	11.92	11.86
Fe ₂ O ₃ (%)	5.58	5.7	6.28	6.21	6.22
CaO (%)	3.36	0.47	0.71	0.47	0.5
MgO (%)	4.38	5.63	5.53	0.78	0.6
Na ₂ O (%)	2.3	3.05	0.64	0.18	0.15
K ₂ O (%)	1.38	1.2	2.14	2.68	2.6
MnO (%)	0.36	0.27	0.44	0.05	0.03
TiO ₂ (%)	0.36	0.34	0.34	0.23	0.28
P ₂ O ₅ (%)	0.03	0.04	0.03	0.03	0.03
Cr ₂ O ₃ (%)	0.0005	0.002	0.005	0.002	0.0005
V ₂ O ₅ (%)	0.024	0.022	0.028	0.021	0.014
LOI (%)	5.54	5.11	6.57	5.68	5.24
TOT/C (%)	0.74	0.06	0.17	0.15	0.1
TOT/S (%)	2.36	2.62	3.71	6.24	5.6
Total (%)	100.14	100.26	100.09	99.9	99.98
Ba (ppm)	73	81	129	151	137
Be (ppm)	3	1	0.5	0.5	0.5
Co (ppm)	12.2	10.9	14.5	11.2	10.9
Cs (ppm)	0.9	0.3	0.7	1.4	1.7
Ga (ppm)	11.6	11.4	11.4	13.9	11.7
Hf (ppm)	0.7	0.9	0.8	0.7	1.2
Nb (ppm)	0.8	1	0.6	0.5	1
Rb (ppm)	23.5	21	34.5	43	44.5
Sn (ppm)	0.5	0.5	0.5	1	2
Sr (ppm)	53.9	37.6	11.7	15.4	18.8
Ta (ppm)	0.1	0.1	0.05	0.05	0.05
Th (ppm)	0.15	0.15	0.15	0.15	0.3
U (ppm)	0.05	0.05	0.05	0.2	0.2
V (ppm)	138	131	148	104	78
W (ppm)	0.25	1.3	0.7	1.4	1.2
Zr (ppm)	28	27.3	24.6	20.1	38.3
Y (ppm)	13.1	9.5	12	10.2	16.9

Sample Name	DCS-S061	DCS-S065	708482	708218	708224
La (ppm)	2.4	1.7	2	2.1	2.9
Ho (ppm)	0.4	0.34	0.43	0.37	0.65
Er (ppm)	1.23	1	1.31	1.12	1.86
Tm (ppm)	0.23	0.2	0.2	0.18	0.27
Yb (ppm)	1.54	1.24	1.39	1.16	1.92
Lu (ppm)	0.29	0.21	0.24	0.2	0.31
Mo (ppm)	0.05	0.05	0.5	2.2	2.4
Cu (ppm)	216.8	15.3	55.5	464.3	745.1
Pb (ppm)	10.9	24.8	301.4	126.8	297.2
Zn (ppm)	1046	400	1445	10001	6768
Ni (ppm)	1.5	1.4	7.1	4.5	3.4
As (ppm)	163	100.5	91.1	297.4	68.6
Cd (ppm)	8.8	2.9	9.7	151.2	46.6
Sb (ppm)	0.05	0.1	0.8	6	1
Bi (ppm)	0.05	0.05	0.05	0.6	0.4
Ag (ppm)	1.9	2	0.6	5.2	10
Au (ppm)	134.4	181.5	31.2	126.6	282.6
Hg (ppm)	0.03	0.03	0.08	1.64	0.8

Sample Name	708376	708203	708522	708350	DCS-S016
Hole ID	SHDDR-0394	SHDDR-0313	SHDDR-0285	SHDDR-0364	SHDDR0418
Database	Yarra (2016)	Yarra (2016)	Yarra (2016)	Yarra (2016)	Yarra (2016)
Alteration	Proximal	Proximal	Proximal	Proximal	Intermediate
Depth	167	213	320	378	107.4
Easting	8623031.21	8623684.10	8623667.55	8623061.54	8623432.62
Northing	4344540.22	4344574.53	4343520.09	4344424.52	4344477.11
Datum	Pulkovo 1942 GK 8				
*Least Mobile					
SiO ₂ (%)	66.1	70.9	61	63.1	62.7
Al ₂ O ₃ (%)	12.03	10.91	13.84	12.99	16.1
Fe ₂ O ₃ (%)	7.51	6.03	8.73	7.56	6.62
CaO (%)	0.3	0.76	0.3	0.44	0.44
MgO (%)	1.98	0.59	4.93	2.04	3.66
Na ₂ O (%)	0.15	0.19	0.67	1.53	1.26
K ₂ O (%)	2.42	2.56	2.04	2.28	2.67
MnO (%)	0.21	0.05	0.24	0.23	0.29
TiO ₂ (%)	0.25	0.25	0.32	0.28	0.32
P ₂ O ₅ (%)	0.04	0.04	0.03	0.04	0.04
Cr ₂ O ₃ (%)	0.0005	0.0005	0.003	0.0005	0.005
V ₂ O ₅ (%)	0.011	0.014	0.026	0.01	0.02
LOI (%)	8.15	5.13	6.93	5.73	5.54
TOT/C (%)	0.88	0.15	0.06	0.06	0.05
TOT/S (%)	5.84	4.71	4.65	5.85	3.2
Total (%)	99.53	100.07	99.66	100.08	100.08
Ba (ppm)	177	161	175	175	170
Be (ppm)	0.5	3	0.5	2	2
Co (ppm)	5.4	8.1	12.2	5.9	12
Cs (ppm)	0.8	1.4	1	1	2.1
Ga (ppm)	11.2	11.3	12.8	13.1	11.3
Hf (ppm)	1.1	1.1	0.7	1.1	1
Nb (ppm)	0.9	1.5	0.2	1.1	0.05
Rb (ppm)	40.4	36.4	29.6	33.8	46.2
Sn (ppm)	2	2	3	4	0.5
Sr (ppm)	19.5	12.5	14.2	13.8	35.8
Ta (ppm)	0.05	0.05	0.05	0.05	0.05
Th (ppm)	0.15	0.4	0.15	0.15	0.15
U (ppm)	0.05	0.05	0.05	0.05	0.05
V (ppm)	46	89	147	60	96
W (ppm)	0.7	2.2	1.2	0.9	0.9
Zr (ppm)	30.8	36.7	20.8	29.3	27.3
Y (ppm)	17	15.5	11.2	15.6	9.3

Sample Name	708376	708203	708522	708350	DCS-S016
La (ppm)	2.8	1.8	0.7	2	1.6
Ho (ppm)	0.67	0.53	0.43	0.59	0.3
Er (ppm)	1.97	1.59	1.27	1.89	1.05
Tm (ppm)	0.31	0.25	0.2	0.28	0.17
Yb (ppm)	2.1	1.64	1.3	2.06	1.37
Lu (ppm)	0.34	0.26	0.21	0.32	0.22
Mo (ppm)	0.5	5.8	0.3	0.5	0.5
Cu (ppm)	190.4	933.8	43.7	1495	116.8
Pb (ppm)	14.9	330.1	3.4	43.4	18.6
Zn (ppm)	1174	10001	277	10001	547
Ni (ppm)	0.6	2.9	5.5	0.6	1.4
As (ppm)	309.5	82.6	39.6	228.2	65.4
Cd (ppm)	8.1	100.5	1.4	183.6	3.7
Sb (ppm)	0.7	11.1	0.5	1.3	0.3
Bi (ppm)	0.05	1.1	0.7	0.1	0.05
Ag (ppm)	2.4	7.9	7.7	19.6	0.5
Au (ppm)	124.9	160.5	618.8	738.4	55.4
Hg (ppm)	0.06	1.05	0.11	0.34	0.02

Sample Name	DCS-S019	DCS-S022	DCS-S025	DCS-S049	DCS-S051
Hole ID	SHDDR0418	SHDDR0418	SHDDR0418	SHDDR190	SHDDR190
Database	Yarra (2016)	Yarra (2016)	Yarra (2016)	Yarra (2016)	Yarra (2016)
Alteration	Intermediate	Intermediate	Intermediate	Intermediate	Intermediate
Depth	167.6	227.4	310.3	97.4	129
Easting	8623432.62	8623432.62	8623432.62	8623848.18	8623848.18
Northing	4344477.11	4344477.11	4344477.11	4342802.18	4342802.18
Datum	Pulkovo 1942 GK 8				
*Least Mobile					
SiO ₂ (%)	62.3	63	62.7	62.4	60.5
Al ₂ O ₃ (%)	16.44	16.4	16.88	15.42	16.52
Fe ₂ O ₃ (%)	5.71	6.19	5.39	6.14	6.78
CaO (%)	2.12	0.56	0.39	0.71	1
MgO (%)	4.35	4.06	5	4.31	3.91
Na ₂ O (%)	2.95	1.51	1.81	1.21	4.24
K ₂ O (%)	1.04	2.29	1.75	2.4	1.15
MnO (%)	0.31	0.25	0.26	0.45	0.35
TiO ₂ (%)	0.32	0.31	0.33	0.34	0.35
P ₂ O ₅ (%)	0.04	0.04	0.04	0.03	0.04
Cr ₂ O ₃ (%)	0.004	0.0005	0.0005	0.004	0.003
V ₂ O ₅ (%)	0.021	0.025	0.025	0.023	0.025
LOI (%)	4.04	5.51	5.4	5.9	4.97
TOT/C (%)	0.08	0.07	0.04	0.23	0.2
TOT/S (%)	1.2	2.81	1.7	3.3	3.16
Total (%)	100.18	100.58	100.4	100.38	100.81
Ba (ppm)	105	206	126	149	76
Be (ppm)	0.5	0.5	0.5	0.5	2
Co (ppm)	12	12.5	11.6	12.4	12.8
Cs (ppm)	1.5	1.8	1.5	1	0.2
Ga (ppm)	12.8	13.8	13.4	11	10.3
Hf (ppm)	1.1	1.3	0.9	0.8	1
Nb (ppm)	0.05	0.05	0.05	0.05	0.05
Rb (ppm)	18.3	35.3	28.7	38.1	17.8
Sn (ppm)	0.5	0.5	0.5	0.5	0.5
Sr (ppm)	122.6	38.7	35.1	19.9	37.1
Ta (ppm)	0.05	0.05	0.05	0.05	0.05
Th (ppm)	0.15	0.15	0.15	0.15	0.15
U (ppm)	0.1	0.1	0.05	0.1	0.1
V (ppm)	116	137	123	128	128
W (ppm)	0.8	1	0.8	0.7	0.7
Zr (ppm)	32.9	30.1	31.5	26.6	26.5
Y (ppm)	16.2	10.5	14.5	10.6	11

Sample Name	DCS-S019	DCS-S022	DCS-S025	DCS-S049	DCS-S051
La (ppm)	2.6	2.4	1.6	3.6	1.7
Ho (ppm)	0.55	0.34	0.51	0.36	0.38
Er (ppm)	1.5	1.09	1.49	1.12	1.28
Tm (ppm)	0.24	0.19	0.23	0.17	0.18
Yb (ppm)	1.8	1.49	1.68	1.52	1.22
Lu (ppm)	0.31	0.27	0.27	0.25	0.22
Mo (ppm)	0.3	0.2	0.4	0.4	0.05
Cu (ppm)	65.3	34.4	35.6	80	23.6
Pb (ppm)	6.9	17.1	123.2	13.8	16.6
Zn (ppm)	661	424	406	2091	1352
Ni (ppm)	1.4	1.3	1.4	1.4	1.6
As (ppm)	25.1	58.1	28.6	97.2	121.9
Cd (ppm)	5.1	2.6	2.3	14.8	11.1
Sb (ppm)	0.2	0.1	0.3	0.4	0.1
Bi (ppm)	0.05	0.05	0.05	0.05	0.05
Ag (ppm)	0.5	1	0.3	1.8	1.1
Au (ppm)	33.9	63.7	9.2	82.6	96.7
Hg (ppm)	0.02	0.02	0.02	0.08	0.03

Sample Name	DCS-S053	DCS-S055	DCS-S059	DCS-S064	DCS-S067
Hole ID	SHDDR190	SHDDR190	SHDDR190	SHDDR190	SHDDR190
Database	Yarra (2016)	Yarra (2016)	Yarra (2016)	Yarra (2016)	Yarra (2016)
Alteration	Intermediate	Intermediate	Intermediate	Intermediate	Intermediate
Depth	141.7	155	203.7	241.3	171.5
Easting	8623848.18	8623848.18	8623848.18	8623848.18	8623848.18
Northing	4342802.18	4342802.18	4342802.18	4342802.18	4342802.18
Datum	Pulkovo 1942 GK 8				
*Least Mobile					
SiO ₂ (%)	60.9	61.5	58.3	57.9	60
Al ₂ O ₃ (%)	15.48	16.17	16.56	16.27	16.01
Fe ₂ O ₃ (%)	6.57	6.42	6.09	5.87	6.18
CaO (%)	1.91	0.43	2.62	2.93	1.98
MgO (%)	3.83	4.72	3.98	4.18	4.79
Na ₂ O (%)	2.93	2.81	3.11	3.3	2.2
K ₂ O (%)	1.16	1.67	1.13	1	1.53
MnO (%)	0.39	0.34	0.39	0.28	0.4
TiO ₂ (%)	0.33	0.37	0.36	0.37	0.35
P ₂ O ₅ (%)	0.04	0.04	0.04	0.04	0.04
Cr ₂ O ₃ (%)	0.003	0.0005	0.002	0.004	0.0005
V ₂ O ₅ (%)	0.024	0.028	0.025	0.024	0.025
LOI (%)	5.31	5.49	5.53	5.42	5.19
TOT/C (%)	0.29	0.08	0.48	0.56	0.37
TOT/S (%)	2.76	3.22	3.14	2.76	2.36
Total (%)	100.27	100.46	100.11	99.82	100.41
Ba (ppm)	73	135	67	52	107
Be (ppm)	0.5	1	0.5	0.5	0.5
Co (ppm)	11.7	12.4	11.4	15.4	12.7
Cs (ppm)	2	0.5	1	0.8	0.8
Ga (ppm)	10.3	13.6	11.7	12.5	11.9
Hf (ppm)	0.8	1	1.2	1.3	0.9
Nb (ppm)	0.05	7.3	3.4	2.6	3.6
Rb (ppm)	17.9	25.3	19	18.9	25.6
Sn (ppm)	0.5	0.5	0.5	0.5	0.5
Sr (ppm)	89.5	31.9	83.4	83.8	40.5
Ta (ppm)	0.05	0.4	0.2	0.2	0.3
Th (ppm)	0.15	0.4	0.3	0.2	0.2
U (ppm)	0.05	0.3	0.05	0.05	0.1
V (ppm)	121	140	119	156	135
W (ppm)	0.7	0.8	0.5	0.7	3.5
Zr (ppm)	26.4	29.2	38.2	30.1	32.1
Y (ppm)	13.7	13.5	10.9	12.9	11.3

Sample Name	DCS-S053	DCS-S055	DCS-S059	DCS-S064	DCS-S067
La (ppm)	2.8	3.2	1.7	2.5	3.7
Ho (ppm)	0.47	0.49	0.37	0.42	0.37
Er (ppm)	1.38	1.48	1.03	1.27	1.25
Tm (ppm)	0.24	0.24	0.18	0.24	0.21
Yb (ppm)	1.56	1.55	1.29	1.57	1.64
Lu (ppm)	0.25	0.29	0.24	0.26	0.28
Mo (ppm)	0.2	0.2	0.05	0.05	0.2
Cu (ppm)	7.5	54.8	9.9	271.4	21.5
Pb (ppm)	4.8	6.1	30.6	20.9	5.7
Zn (ppm)	151	159	795	895	1921
Ni (ppm)	1.5	1.5	1.6	1.6	1.7
As (ppm)	68	105.2	47.6	39.8	65.1
Cd (ppm)	0.1	0.3	6.9	8.2	15.4
Sb (ppm)	0.05	0.1	0.05	0.05	0.05
Bi (ppm)	0.05	0.05	0.05	0.05	0.05
Ag (ppm)	0.8	0.6	0.2	0.6	0.7
Au (ppm)	78	65.2	21	53.8	73.3
Hg (ppm)	0.01	0.02	0.03	0.03	0.06

Sample Name	708423	708206	DCS-S017	DCS-S020	DCS-S021
Hole ID	SHDDR-0174	SHDDR-0313	SHDDR0418	SHDDR0418	SHDDR0418
Database	Yarra (2016)	Yarra (2016)	Yarra (2016)	Yarra (2016)	Yarra (2016)
Alteration	Intermediate	Intermediate	Distal	Distal	Distal
Depth	123	250	130.1	173.6	223.4
Easting	8623671.73	8623682.24	8623432.62	8623432.62	8623432.62
Northing	4343188.08	4344549.38	4344477.11	4344477.11	4344477.11
Datum	Pulkovo 1942 GK 8				
*Least Mobile					
SiO ₂ (%)	60	61.4	61.2	62.2	61.5
Al ₂ O ₃ (%)	16.31	16.58	16.59	16.86	16.4
Fe ₂ O ₃ (%)	6.12	5.98	5.29	5.56	5.67
CaO (%)	2.43	2.93	2.9	2.58	2.36
MgO (%)	3.94	3.59	3.76	3.74	4.13
Na ₂ O (%)	4.4	2.84	3.3	4.62	4.24
K ₂ O (%)	0.58	0.95	0.67	0.31	0.36
MnO (%)	0.27	0.26	0.45	0.27	0.28
TiO ₂ (%)	0.35	0.32	0.32	0.33	0.33
P ₂ O ₅ (%)	0.04	0.03	0.04	0.04	0.03
Cr ₂ O ₃ (%)	0.002	0.0005	0.0005	0.003	0.004
V ₂ O ₅ (%)	0.025	0.021	0.023	0.022	0.021
LOI (%)	5.32	4.85	5.01	3.28	4.18
TOT/C (%)	0.59	0.19	0.41	0.06	0.12
TOT/S (%)	0.5	1.08	1.32	0.91	0.95
Total (%)	100.46	100.1	100.72	100.16	100.12
Ba (ppm)	42	65	48	57	43
Be (ppm)	0.5	0.5	2	2	2
Co (ppm)	12.6	9.5	10.1	11.7	11.9
Cs (ppm)	5	4.3	5.9	0.7	0.3
Ga (ppm)	11.9	13	12.4	10.9	11.2
Hf (ppm)	0.8	0.9	1.2	1.2	0.8
Nb (ppm)	0.5	0.8	0.05	0.05	0.05
Rb (ppm)	11.4	15.4	14.5	4.5	5.1
Sn (ppm)	0.5	0.5	0.5	0.5	0.5
Sr (ppm)	96.4	96.3	96.4	178.8	143.6
Ta (ppm)	0.05	0.05	0.05	0.05	0.05
Th (ppm)	0.15	0.15	0.15	0.15	0.15
U (ppm)	0.05	0.05	0.05	0.05	0.05
V (ppm)	137	127	98	117	125
W (ppm)	0.6	0.8	0.8	0.6	0.8
Zr (ppm)	28.1	28.5	29.6	31.6	29.3
Y (ppm)	13.2	11.7	15	13.2	13.5

Sample Name	708423	708206	DCS-S017	DCS-S020	DCS-S021
La (ppm)	2.6	2.4	2.6	2.3	2.1
Ho (ppm)	0.48	0.45	0.5	0.43	0.47
Er (ppm)	1.45	1.28	1.5	1.37	1.33
Tm (ppm)	0.23	0.2	0.25	0.24	0.23
Yb (ppm)	1.54	1.47	1.78	1.72	1.79
Lu (ppm)	0.27	0.26	0.29	0.31	0.25
Mo (ppm)	0.1	0.4	0.1	0.4	0.05
Cu (ppm)	48.7	28.4	56.5	37.8	22.1
Pb (ppm)	3.6	4.2	151.6	9.3	3.8
Zn (ppm)	635	207	298	131	129
Ni (ppm)	2.6	1.5	1.3	1.6	1.5
As (ppm)	13.4	32.7	10.3	16.1	26.1
Cd (ppm)	6.4	1.3	1.7	0.05	0.05
Sb (ppm)	0.2	0.2	0.05	0.1	0.1
Bi (ppm)	0.05	0.05	0.05	0.05	0.05
Ag (ppm)	0.05	0.05	0.1	0.1	0.05
Au (ppm)	18.4	13.1	6.3	4.1	3.4
Hg (ppm)	0.02	0.005	0.01	0.005	0.005

Sample Name	DCS-S023	DCS-S024	DCS-S026	DCS-S046	DCS-S058
Hole ID	SHDDR0418	SHDDR0418	SHDDR0418	SHDDR190	SHDDR190
Database	Yarra (2016)	Yarra (2016)	Yarra (2016)	Yarra (2016)	Yarra (2016)
Alteration	Distal	Distal	Distal	Distal	Distal
Depth	244.5	296.8	365.3	69.3	188.7
Easting	8623432.62	8623432.62	8623432.62	8623848.18	8623848.18
Northing	4344477.11	4344477.11	4344477.11	4342802.18	4342802.18
Datum	Pulkovo 1942 GK 8				
*Least Mobile					
SiO ₂ (%)	59.8	62	61.6	60.9	60.3
Al ₂ O ₃ (%)	16.8	16.57	16.55	15.48	16.22
Fe ₂ O ₃ (%)	5.74	5.17	5.27	5.82	5.91
CaO (%)	3.68	1.57	2.02	2.64	3.36
MgO (%)	3.98	4.64	4.15	3.74	4.02
Na ₂ O (%)	2.27	2.58	3.11	4.01	3.83
K ₂ O (%)	0.61	1.36	1.27	0.67	0.44
MnO (%)	0.25	0.24	0.2	0.37	0.31
TiO ₂ (%)	0.33	0.31	0.32	0.33	0.38
P ₂ O ₅ (%)	0.04	0.04	0.04	0.04	0.04
Cr ₂ O ₃ (%)	0.002	0.003	0.002	0.001	0.003
V ₂ O ₅ (%)	0.022	0.022	0.02	0.024	0.026
LOI (%)	6.59	5.04	4.75	4.63	4.17
TOT/C (%)	0.53	0.27	0.3	0.52	0.25
TOT/S (%)	1.06	1.25	1.05	1.73	1.19
Total (%)	100.81	100.59	100.04	100.41	100.07
Ba (ppm)	47	92	84	40	40
Be (ppm)	0.5	0.5	0.5	0.5	3
Co (ppm)	11.7	10.4	11.7	12.5	11.9
Cs (ppm)	2.2	1.1	2	0.8	1.4
Ga (ppm)	12.7	12.3	10.5	10.5	11.7
Hf (ppm)	1.1	1.1	0.9	0.7	0.6
Nb (ppm)	0.05	0.05	0.05	0.05	1.7
Rb (ppm)	9.9	21.5	18.5	12.1	6.9
Sn (ppm)	0.5	0.5	0.5	0.5	0.5
Sr (ppm)	88.7	44.4	80	78.1	193.7
Ta (ppm)	0.05	0.05	0.05	0.05	0.05
Th (ppm)	0.15	0.2	0.15	0.15	0.2
U (ppm)	0.05	0.05	0.05	0.05	0.05
V (ppm)	113	122	113	102	154
W (ppm)	0.7	0.9	0.6	0.5	1.6
Zr (ppm)	30.8	33.8	28.4	26.2	28.7
Y (ppm)	15	15	13.6	13.9	13.6

Sample Name	DCS-S023	DCS-S024	DCS-S026	DCS-S046	DCS-S058
La (ppm)	1.9	2	1.7	1.9	2.3
Ho (ppm)	0.45	0.56	0.44	0.49	0.42
Er (ppm)	1.46	1.51	1.52	1.44	1.38
Tm (ppm)	0.24	0.29	0.24	0.22	0.23
Yb (ppm)	1.72	1.96	1.92	1.65	1.7
Lu (ppm)	0.29	0.31	0.3	0.25	0.29
Mo (ppm)	0.05	0.05	0.3	0.05	0.2
Cu (ppm)	52.1	7.4	9.6	9.5	70
Pb (ppm)	3.8	9.1	7	16.6	14.8
Zn (ppm)	97	131	116	196	524
Ni (ppm)	1.2	1	1.3	1.2	1.5
As (ppm)	19.7	42.4	53.3	71.7	10.7
Cd (ppm)	0.05	0.2	0.05	0.05	4.4
Sb (ppm)	0.05	0.05	0.3	0.3	0.2
Bi (ppm)	0.05	0.05	0.05	0.05	0.05
Ag (ppm)	0.05	0.1	0.2	0.2	0.1
Au (ppm)	2.5	13.5	14	29.7	11.7
Hg (ppm)	0.005	0.005	0.005	0.005	0.005

Sample Name	DCS-S060	DCS-S062	DCS-S063	DCS-S066	DCS-S081
Hole ID	SHDDR190	SHDDR190	SHDDR190	SHDDR190	SHDDR338
Database	Yarra (2016)	Yarra (2016)	Yarra (2016)	Yarra (2016)	Yarra (2016)
Alteration	Distal	Distal	Distal	Distal	Distal
Depth	207.5	225.9	229	356.8	918.5
Easting	8623848.18	8623848.18	8623848.18	8623848.18	8623841.46
Northing	4342802.18	4342802.18	4342802.18	4342802.18	4343053.22
Datum	Pulkovo 1942 GK 8				
*Least Mobile					
SiO ₂ (%)	60.5	61.3	60.3	53.8	60.5
Al ₂ O ₃ (%)	15.75	16.33	16.05	15.47	16.56
Fe ₂ O ₃ (%)	5.76	5.5	5.99	10.25	6.89
CaO (%)	1.8	1.68	1.82	0.44	4.87
MgO (%)	4.89	4.36	4.6	8.54	3.44
Na ₂ O (%)	3.2	3.74	3.78	3.7	2.16
K ₂ O (%)	0.97	0.8	0.83	0.18	0.49
MnO (%)	0.36	0.3	0.3	0.23	0.12
TiO ₂ (%)	0.35	0.36	0.36	0.37	0.36
P ₂ O ₅ (%)	0.04	0.04	0.04	0.03	0.04
Cr ₂ O ₃ (%)	0.004	0.002	0.002	0.007	0.005
V ₂ O ₅ (%)	0.025	0.022	0.024	0.036	0.024
LOI (%)	5.22	4.97	4.73	6.6	4.2
TOT/C (%)	0.33	0.3	0.36	0.29	0.18
TOT/S (%)	2.76	1.47	2.17	4.09	2.29
Total (%)	100.33	100.43	100.33	100.21	100.54
Ba (ppm)	69	49	105	21	32
Be (ppm)	1	0.5	1	1	0.5
Co (ppm)	13.5	11.9	12.7	32.1	13.4
Cs (ppm)	0.4	3.4	1.2	0.1	4.1
Ga (ppm)	12.2	13	11.7	13.1	12.9
Hf (ppm)	0.9	0.9	0.7	0.6	0.6
Nb (ppm)	1.9	1.3	1.1	1.7	1.4
Rb (ppm)	16.2	14.8	13.7	2.9	8.7
Sn (ppm)	0.5	0.5	0.5	2	1
Sr (ppm)	53.8	87	49.5	55.5	120.4
Ta (ppm)	0.1	0.2	0.1	0.1	0.1
Th (ppm)	0.2	0.15	0.15	0.5	0.2
U (ppm)	0.05	0.05	0.05	0.05	0.05
V (ppm)	133	132	128	196	125
W (ppm)	5.7	0.6	0.7	13.2	0.25
Zr (ppm)	29.3	30	27.6	26.9	28.5
Y (ppm)	12.1	10.2	10.6	8.3	14.1

Sample Name	DCS-S060	DCS-S062	DCS-S063	DCS-S066	DCS-S081
La (ppm)	2.3	1.7	1.7	1	2.3
Ho (ppm)	0.4	0.35	0.37	0.3	0.48
Er (ppm)	1.28	1.04	1.19	1.11	1.54
Tm (ppm)	0.22	0.18	0.22	0.19	0.24
Yb (ppm)	1.56	1.44	1.37	1.15	1.67
Lu (ppm)	0.27	0.23	0.25	0.18	0.29
Mo (ppm)	0.1	0.05	0.2	0.5	0.3
Cu (ppm)	15.1	53.4	137.7	37.6	65.1
Pb (ppm)	4.7	2.7	9.4	2	0.5
Zn (ppm)	163	436	286	218	59
Ni (ppm)	1.6	1.6	2.1	13.4	1.5
As (ppm)	44.5	40.2	44.3	21.2	7.6
Cd (ppm)	0.5	4.1	1.2	0.8	0.05
Sb (ppm)	0.05	0.05	0.5	0.05	0.05
Bi (ppm)	0.05	0.05	0.05	0.1	0.3
Ag (ppm)	0.5	0.3	0.8	0.1	0.05
Au (ppm)	31.1	26.5	89.7	8.6	16.9
Hg (ppm)	0.005	0.02	0.01	0.01	0.005

Appendix 3b: Alteration Mass Balance

Element	Average			
	Least Altered	Proximal	Intermediate	Distal
SiO ₂ (%)	60.2875	63.4538	61.0462	60.4538
Al ₂ O ₃ (%)	17.0550	14.2531	16.2415	16.2792
Fe ₂ O ₃ (%)	5.3725	6.4246	6.1585	6.0631
CaO (%)	5.1000	1.0208	1.5731	2.4400
MgO (%)	2.6375	3.3131	4.1785	4.4608
Na ₂ O (%)	3.1775	1.6277	2.6592	3.4262
K ₂ O (%)	0.6725	1.8838	1.4862	0.6892
MnO (%)	0.1450	0.2531	0.3262	0.2831
TiO ₂ (%)	0.3700	0.3138	0.3400	0.3423
P ₂ O ₅ (%)	0.0625	0.0346	0.0385	0.0385
Cr ₂ O ₃ (%)	0.0005	0.0014	0.0023	0.0030
V ₂ O ₅ (%)	0.0240	0.0206	0.0239	0.0239
LOI (%)	4.4700	5.8646	5.2669	4.8746
Total (%)	99.9900	100.0792	100.3123	100.3662
TOT/C (%)	0.2700	0.2777	0.2485	0.3015
TOT/S (%)	0.2700	4.1046	2.3992	1.7108
Ba (ppm)	49.2500	122.1538	105.6154	55.9231
Be (ppm)	0.5000	1.1538	0.7692	1.1538
Co (ppm)	10.0500	10.8846	12.2308	13.5000
Cs (ppm)	1.4250	0.9000	1.7308	1.8154
Ga (ppm)	13.2250	11.9462	12.1154	11.9308
Hf (ppm)	1.1625	0.9308	1.0000	0.8692
Nb (ppm)	0.7125	0.9462	1.4269	0.7269
Rb (ppm)	12.1500	30.8923	24.4538	11.4846
Sn (ppm)	0.5000	1.3462	0.5000	0.6538
Sr (ppm)	151.8250	29.0769	62.3846	97.6846
Ta (ppm)	0.0625	0.0808	0.1192	0.0769
Th (ppm)	0.3125	0.1885	0.1885	0.1923
U (ppm)	0.1375	0.0846	0.0885	0.0500
V (ppm)	106.5000	111.6923	127.9231	127.5385
W (ppm)	0.7000	0.9615	0.9615	2.0731
Zr (ppm)	35.5250	28.5077	29.8077	29.2846
Y (ppm)	11.5250	12.8923	12.2538	12.9308
La (ppm)	2.8750	1.9692	2.4923	1.9846
Ce (ppm)	7.5250	4.7846	5.5077	5.0615
Pr (ppm)	0.9775	0.7115	0.8054	0.7392
Nd (ppm)	5.0750	3.8385	4.1000	3.8769
Sm (ppm)	1.4750	1.2123	1.2162	1.2546
Eu (ppm)	0.5825	0.4946	0.5931	0.5638
Gd (ppm)	1.6900	1.6900	1.6769	1.6954
Tb (ppm)	0.3025	0.3200	0.3108	0.3169
Dy (ppm)	1.6925	2.1015	1.9469	2.0077

Element	Least Altered	Proximal	Intermediate	Distal
Ho (ppm)	0.4100	0.4623	0.4223	0.4354
Er (ppm)	1.1350	1.4031	1.2823	1.3592
Tm (ppm)	0.1825	0.2254	0.2092	0.2300
Yb (ppm)	1.3325	1.5485	1.5154	1.6485
Lu (ppm)	0.2025	0.2585	0.2608	0.2700
Mo (ppm)	0.3003	0.9962	0.2346	0.1808
Cu (ppm)	14.7000	343.2692	61.3769	44.1462
Pb (ppm)	1.7750	94.8846	20.9308	18.1000
Zn (ppm)	41.7500	3807.8462	788.0000	214.1538
Ni (ppm)	2.8753	2.5846	1.5769	2.3692
As (ppm)	4.4500	148.9615	59.0846	31.3923
Cd (ppm)	0.0500	44.4385	6.0154	1.0154
Sb (ppm)	0.3125	1.7423	0.1615	0.1423
Bi (ppm)	0.0378	0.2577	0.0500	0.0731
Ag (ppm)	0.0500	4.6923	0.6308	0.2038
Au (ppm)	1.8000	222.4692	51.1000	19.8462
Hg (ppm)	0.0050	0.3354	0.0281	0.0073

Element	Absolute Mass Change (Average)		
	Proximal (ΔX)	Intermediate (ΔX)	Distal (ΔX)
SiO ₂ (%)	17.9296	3.8591	3.0605
Al ₂ O ₃ (%)	0.0000	0.0000	0.0000
Fe ₂ O ₃ (%)	2.5280	1.1028	1.0050
CaO (%)	-3.9354	-3.4499	-2.5570
MgO (%)	1.1214	1.7519	2.0608
Na ₂ O (%)	-1.3853	-0.3906	0.4207
K ₂ O (%)	1.7231	0.8939	0.0488
MnO (%)	0.1427	0.1988	0.1524
TiO ₂ (%)	0.0052	-0.0127	-0.0108
P ₂ O ₅ (%)	-0.0201	-0.0221	-0.0222
Cr ₂ O ₃ (%)	0.0011	0.0019	0.0026
V ₂ O ₅ (%)	0.0004	0.0011	0.0012
LOI (%)	2.7196	1.0685	0.6488
Total (%)	22.2380	5.4123	5.2378
TOT/C (%)	0.0648	-0.0083	0.0474
TOT/S (%)	4.9632	2.2607	1.5427
Ba (ppm)	105.9138	61.8960	9.2420
Be (ppm)	0.9332	0.3073	0.7067
Co (ppm)	2.9269	2.8068	4.1999
Cs (ppm)	-0.2718	0.3891	0.4564
Ga (ppm)	1.3921	-0.5114	-0.7163
Hf (ppm)	-0.0141	-0.1137	-0.2551
Nb (ppm)	0.4362	0.7857	0.0606
Rb (ppm)	26.8365	13.6167	-0.1264
Sn (ppm)	1.2662	0.0254	0.1910
Sr (ppm)	-118.4848	-86.4308	-49.9700
Ta (ppm)	0.0306	0.0629	0.0184
Th (ppm)	-0.0747	-0.1146	-0.1094
U (ppm)	-0.0311	-0.0444	-0.0851
V (ppm)	25.6440	27.9048	27.5650
W (ppm)	0.5377	0.3131	1.5387
Zr (ppm)	-0.3958	-4.2457	-4.8613
Y (ppm)	4.5035	1.3415	1.9980
La (ppm)	-0.4369	-0.2441	-0.7998
Ce (ppm)	-1.6066	-1.7140	-2.2332
Pr (ppm)	-0.0937	-0.1286	-0.2050
Nd (ppm)	-0.3210	-0.7569	-1.0260
Sm (ppm)	0.0289	-0.1950	-0.1639
Eu (ppm)	0.0175	0.0441	0.0062
Gd (ppm)	0.4100	0.0740	0.0812
Tb (ppm)	0.0948	0.0243	0.0286
Dy (ppm)	0.9260	0.3512	0.4082

Element	Proximal (ΔX)	Intermediate (ΔX)	Distal (ΔX)
Ho (ppm)	0.1679	0.0333	0.0456
Er (ppm)	0.6140	0.2116	0.2879
Tm (ppm)	0.0967	0.0373	0.0582
Yb (ppm)	0.5831	0.2601	0.3918
Lu (ppm)	0.1159	0.0714	0.0798
Mo (ppm)	1.1427	-0.0532	-0.1103
Cu (ppm)	455.7070	49.9042	31.5090
Pb (ppm)	126.9621	19.8269	17.0031
Zn (ppm)	5094.7397	792.0305	183.6080
Ni (ppm)	0.3451	-1.2187	-0.3403
As (ppm)	181.4254	57.9813	28.7250
Cd (ppm)	60.4216	6.3061	1.0171
Sb (ppm)	2.2208	-0.1425	-0.1623
Bi (ppm)	0.3195	0.0148	0.0387
Ag (ppm)	6.2253	0.6205	0.1660
Au (ppm)	278.5820	52.3624	19.2462
Hg (ppm)	0.4712	0.0248	0.0027

Element	Relative Mass Change (Average and 95% Confidence Intervals)					
	Proximal (ΔX)	95% Conf	Inter (ΔX)	95% Conf	Distal (ΔX)	95% Conf
SiO ₂ (%)	29.7402	15.1748	6.4012	2.1724	5.0765	1.6783
Al ₂ O ₃ (%)	0.0000		0.0000		0.0000	
Fe ₂ O ₃ (%)	47.0544	18.4888	20.5274	4.8333	18.7061	15.1624
CaO (%)	-77.1646	9.4169	-67.6452	10.7291	-50.1376	11.6413
MgO (%)	42.5161	41.1469	66.4209	9.1067	78.1363	29.6264
Na ₂ O (%)	-43.5968	26.4661	-12.2924	17.4762	13.2405	13.2815
K ₂ O (%)	256.2228	85.6042	132.9268	53.4644	7.2500	28.6941
MnO (%)	98.4472	53.1472	137.1286	27.3691	105.1209	32.0569
TiO ₂ (%)	1.4042	2.8118	-3.4391	3.2808	-2.9284	4.1253
P ₂ O ₅ (%)	-32.1649	8.2110	-35.3797	3.2096	-35.5356	3.1608
Cr ₂ O ₃ (%)	229.7367	167.4099	380.2514	185.7654	523.9377	197.8140
V ₂ O ₅ (%)	1.5798	12.3272	4.7221	5.0755	4.8279	10.5676
LOI (%)	60.8403	20.1655	23.9039	6.4144	14.5149	11.9177
Total (%)	22.2403	9.7195	5.4128	1.4512	5.2383	1.5694
TOT/C (%)	23.9899	66.1507	-3.0818	39.7261	17.5542	28.2357
TOT/S (%)	1838.2224	487.3200	837.2846	198.8100	571.3614	198.4643
Ba (ppm)	215.0534	77.8554	125.6771	55.5963	18.7654	27.3847
Be (ppm)	186.6394	138.9030	61.4577	61.4819	141.3374	89.5205
Co (ppm)	29.1231	14.8982	27.9288	7.4295	41.7900	33.5994
Cs (ppm)	-19.0766	25.8129	27.3078	54.1316	32.0246	64.4438
Ga (ppm)	10.5265	11.1863	-3.8668	4.3389	-5.4162	4.0989
Hf (ppm)	-1.2119	15.2764	-9.7785	7.9634	-21.9474	9.8120
Nb (ppm)	61.2235	61.8940	110.2748	171.2138	8.5061	61.6128
Rb (ppm)	220.8768	69.9042	112.0717	47.0825	-1.0402	25.5901
Sn (ppm)	253.2350	167.4320	5.0743	1.4441	38.2092	49.7356
Sr (ppm)	-78.0404	5.5433	-56.9279	12.0131	-32.9129	17.0220
Ta (ppm)	49.0063	44.4042	100.6373	104.3069	29.4828	38.7861
Th (ppm)	-23.8930	22.8121	-36.6697	13.4411	-35.0148	17.9954
U (ppm)	-22.5961	31.3946	-32.2675	27.3793	-61.8743	0.5791
V (ppm)	24.0789	15.9787	26.2017	7.5421	25.8827	14.3320
W (ppm)	76.8176	63.3897	44.7356	61.6478	219.8075	298.7107
Zr (ppm)	-1.1140	15.4420	-11.9513	4.6277	-13.6842	2.3511
Y (ppm)	39.0759	23.7509	11.6397	9.0056	17.3365	9.0786
La (ppm)	-15.1975	17.4084	-8.4900	14.6512	-27.8180	7.4966
Ce (ppm)	-21.3506	14.6755	-22.7776	10.2599	-29.6767	7.4511
Pr (ppm)	-9.5899	17.2854	-13.1594	10.9877	-20.9729	8.4558
Nd (ppm)	-6.3244	16.5362	-14.9146	9.9132	-20.2176	8.6011
Sm (ppm)	1.9575	18.9265	-13.2204	9.4050	-11.1100	8.4193
Eu (ppm)	3.0115	19.0729	7.5772	24.2296	1.0684	19.8246
Gd (ppm)	24.2602	21.2909	4.3761	9.3667	4.8022	11.1577
Tb (ppm)	31.3383	22.0940	8.0191	9.2525	9.4683	10.8312
Dy (ppm)	54.7095	28.5966	20.7505	8.8756	24.1171	10.6991

Element	Proximal (ΔX)	95% Conf	Inter (ΔX)	95% Conf	Distal (ΔX)	95% Conf
Ho (ppm)	40.9499	27.3219	8.1171	9.7912	11.1223	8.7356
Er (ppm)	54.0930	28.3646	18.6415	8.0766	25.3663	7.1799
Tm (ppm)	53.0045	24.0979	20.4361	8.7361	31.8982	7.1631
Yb (ppm)	43.7612	23.3330	19.5184	6.6744	29.4008	8.1925
Lu (ppm)	57.2317	22.8087	35.2686	6.9183	39.4128	8.7956
Mo (ppm)	380.5681	444.8773	-17.7267	28.1008	-36.7345	28.1784
Cu (ppm)	3100.0477	2266.5272	339.4846	261.5987	214.3467	134.0676
Pb (ppm)	7152.7919	5315.2686	1117.0078	942.8909	957.9188	1221.4415
Zn (ppm)	12202.9693	7239.2901	1897.0790	862.7873	439.7796	181.9536
Ni (ppm)	12.0032	46.4871	-42.3875	6.2175	-11.8360	67.0022
As (ppm)	4076.9758	1598.0998	1302.9502	413.4788	645.5051	249.0348
Cd (ppm)	120843.2380	89543.4630	12612.2955	5802.6999	2034.1563	1672.0171
Sb (ppm)	710.6487	834.6986	-45.5845	20.7883	-51.9253	25.4462
Bi (ppm)	846.3670	709.9626	39.1713	1.9128	102.5660	99.1735
Ag (ppm)	12450.6856	7873.4411	1240.9937	548.4676	331.9728	245.1687
Au (ppm)	15476.7773	8114.0523	2909.0246	907.6611	1069.2332	716.6842
Hg (ppm)	9423.4038	7878.1565	495.1139	234.6826	53.5095	48.2277

Appendix 3c: Shortwave Infrared

This appendix contains analytical data collected using the SWIR facility at MDRU, UBC under the guidance of Farhad Bouzari and Murray Allan. The results are used to identify alteration minerals and their spectral properties in the SWIR portion of the light spectrum. The results are discussed in Chapter 4.

Sample Name	DCS-S016	DCS-S017	DCS-S018	DCS-S019	DCS-S020
Mineral 1	Illite	IntChlorite	IntChlorite	IntChlorite	IntChlorite
Mineral 2	IntChlorite	Paragonite	Illite	Illite	Illite
w2200	2199.67	2188.17	2201.06	2199.85	2198.82
width2200	33.696	29.653	31.273	35.013	27.268
hqd2200	0.351	0.213	0.0611	0.147	0.112
w2250	2249.86	2252.4	2257.86	2255.41	2253.18
hqd2250	0.179	0.174	0.149	0.273	0.198
w2350	2342.41	2345.79	2351.13	N/A	2343.48
hqd2350	0.227	0.199	0.199	N/A	0.217
width2350	37.656	38.761	36.46	N/A	36.04
hqd1900	0.404	0.386	0.178	0.305	0.277
Crystallinity index	0.869	0.552	0.343	0.481	0.402

Sample Name	DCS-S021	DCS-S022	DCS-S023	DCS-S024	DCS-S025
Mineral 1	IntChlorite	Illite	IntChlorite	IntChlorite	Illite
Mineral 2	Illite	IntChlorite	Kaolinite	Illite	IntChlorite
w2200	2192.78	2199.47	2208.03	2187.71	2199.21
width2200	27.387	31.466	27.42	26.277	33.96
hqd2200	0.107	0.245	0.226	0.145	0.17
w2250	2253.04	2251.3	2254.09	2252.41	2249.62
hqd2250	0.211	0.173	0.245	0.234	0.0563
w2350	2340.02	2338.14	2342.92	2336.82	2346.99
hqd2350	0.203	0.22	0.34	0.232	0.102
width2350	37.339	36.242	38.182	37.5	37.893
hqd1900	0.261	0.258	0.342	0.236	0.203
Crystallinity index	0.409	0.953	0.66	0.612	0.834

Sample Name	DCS-S026	DCS-S046	DCS-S047	DCS-S048	DCS-S049
Mineral 1	IntChlorite	IntChlorite	Illite	IntChlorite	Illite
Mineral 2	Kaolinite	Illite	IntChlorite	Illite	IntChlorite
w2200	2207.19	2200.13	2198	2194.62	2200.89
width2200	33.265	30.324	34.012	31.991	34.196
hqd2200	0.173	0.0861	0.164	0.188	0.247
w2250	2254.49	2253.61	2250.31	2251.38	2250.58
hqd2250	0.0924	0.126	0.0582	0.139	0.122
w2350	2338.11	2340.85	2342.79	2339.69	2343.91
hqd2350	0.156	0.13	0.106	0.178	0.182
width2350	36.406	36.043	36.561	36.186	38.084
hqd1900	0.371	0.145	0.109	0.2	0.216
Crystallinity index	0.466	0.595	1.505	0.941	1.142

Sample Name	DCS-S051	DCS-S053	DCS-S055	DCS-S056	DCS-S057
Mineral 1	IntChlorite	Illite	Illite	Illite	Illite
Mineral 2	Illite	IntChlorite	IntChlorite	IntChlorite	IntChlorite
w2200	2197.73	2194.28	2198.43	2193.5	2199.19
width2200	32.336	32.207	33.461	30.715	32.742
hqd2200	0.19	0.209	0.219	0.275	0.236
w2250	2251.19	2252.26	2250.23	2252.84	2250.03
hqd2250	0.139	0.129	0.106	0.174	0.102
w2350	2342.12	2341.2	2341.74	2340.14	2341.25
hqd2350	0.16	0.159	0.145	0.239	0.143
width2350	36.919	37.631	34.538	40.207	35.84
hqd1900	0.185	0.36	0.234	0.321	0.206
Crystallinity index	1.023	0.581	0.939	0.858	1.144

Sample Name	DCS-S058	DCS-S059	DCS-S060	DCS-S061	DCS-S062
Mineral 1	IntChlorite	Illite	IntChlorite	Illite	IntChlorite
Mineral 2	Illite	IntChlorite	Illite	IntChlorite	Illite
w2200	2193.9	2193.11	2195.73	2193.64	2194.76
width2200	30.095	30.613	30.644	31.807	28.308
hq2200	0.176	0.276	0.305	0.228	0.226
w2250	2251.4	2251.08	2251.3	2251.56	2253.09
hq2250	0.173	0.15	0.24	0.101	0.233
w2350	2342.46	2342.06	2338.38	2335.36	N/A
hq2350	0.224	0.187	0.297	0.14	N/A
width2350	36.739	35.51	35.558	36.564	N/A
hq21900	0.392	0.38	0.337	0.267	0.368
Crystallinity index	0.448	0.727	0.904	0.856	0.615

Sample Name	DCS-S063	DCS-S064	DCS-S065	DCS-S066	DCS-S067
Mineral 1	IntChlorite	IntChlorite	IntChlorite	IntChlorite	IntChlorite
Mineral 2	Illite	Illite	N/A	N/A	Illite
w2200	2193.16	2193.21	N/A	N/A	2194.81
width2200	28.16	29.519	N/A	N/A	30.67
hq2200	0.24	0.256	N/A	N/A	0.269
w2250	2252.72	2250.22	2251.74	2252	2251.06
hq2250	0.241	0.207	0.271	0.187	0.23
w2350	N/A	2337.23	2335.71	2335.25	2345.28
hq2350	N/A	0.219	0.262	0.181	0.29
width2350	N/A	33.518	34.387	35.262	37.417
hq21900	0.326	0.345	0.286	N/A	0.274
Crystallinity index	0.737	0.743	N/A	N/A	0.982

Sample Name	DCS-S081	DCC_S001	DCC_S004	DCC_S007	DCC_S024
Mineral 1	Epidote	Illite	IntChlorite	IntChlorite	IntChlorite
Mineral 2	Illite	Kaolinite	Illite	N/A	N/A
w2200	2197.32	2207.63	2208.24	2207.54	N/A
width2200	29.279	31.521	23.371	27.446	N/A
hqd2200	0.0724	0.146	0.124	0.135	N/A
w2250	2254.03	2249.58	2255.01	2252.295	2253.45
hqd2250	0.171	0.0443	0.197	0.12065	0.171
w2350	2342.56	2350.6	N/A	N/A	2345.84
hqd2350	0.278	0.0814	N/A	N/A	0.181
width2350	37.265	38.619	N/A	N/A	35.558
hqd1900	0.16	0.173	0.196	0.1845	0.102
Crystallinity index	0.453	0.845	0.629	0.737	N/A

Sample Name	DCC_S030	DCC-S023	2014_SR_01	2014_SR_04	2014_SR_11
Mineral 1	IntChlorite	IntChlorite	Illite	Kaolinite	Illite
Mineral 2	N/A	N/A	N/A	Dickite	N/A
w2200	N/A	N/A	2210.21	2208.3	2210.37
width2200	N/A	N/A	26.81	30.651	30.74
hqd2200	N/A	N/A	0.058	0.479	0.118
w2250	2254.63	2254.64	2241.1	N/A	2240.94
hqd2250	0.242	0.241	0.028	N/A	0.105
w2350	2346.55	2344.76	2352.16	2313.39	2350.01
hqd2350	0.251	0.247	0.017	0.106	0.0893
width2350	35.025	35.833	25.466	37.525	32.989
hqd1900	0.185	0.175	0.136	0.185	0.181
Crystallinity index	N/A	N/A	0.427	2.585	0.655

Sample Name	2014_SR_13	2014_SR_22	2014_SR_26	2014_SR_29	2014_SR_33
Mineral 1	Illite	Illite	Topaz	Dickite	Aspectral
Mineral 2	N/A	IntChlorite	Dickite	N/A	N/A
w2200	2209.66	2207.74	2207.46	2205.55	N/A
width2200	29.56	34.057	31.624	34.03	N/A
hqd2200	0.149	0.278	0.164	0.417	N/A
w2250	2243.34	2250.18	N/A	2256.28	2241.1
hqd2250	0.129	0.164	N/A	0.0409	0.028
w2350	2312.83	2346.38	2328.43	2353.38	N/A
hqd2350	0.107	0.199	0.0262	0.119	N/A
width2350	40.02	38.049	37.174	27.37	N/A
hqd1900	0.21	0.393	0.1	0.115	0.625
Crystallinity index	0.711	0.707	1.643	3.644	N/A

Sample Name	2014_SR_34	2014_SR_35	DNS_027	DNS_039	DNS_043
Mineral 1	Aspectral	Aspectral	Muscovite	Illite	IntChlorite
Mineral 2	N/A	N/A	N/A	N/A	Illite
w2200	2210.54	2208.07	2204.82	2208.5	2208.35
width2200	19.56	27.499	31.03	31.468	34.497
hqd2200	0.0632	0.0497	0.151	0.206	0.187
w2250	2248.17	2248.66	N/A	N/A	2252.38
hqd2250	0.0623	0.0489	N/A	N/A	0.188
w2350	2353.73	2337.27	2347.4	2345.37	N/A
hqd2350	0.0624	0.0486	0.0699	0.117	N/A
width2350	31.79	29.544	34.956	36.078	N/A
hqd1900	0.1	0.152	0.112	0.146	0.22
Crystallinity index	0.631	0.327	1.339	1.411	0.849

Sample Name	708482	708218	708423	708224	708226
Mineral 1	Illite	IntChlorite	Illite	Illite	IntChlorite
Mineral 2	FeChlorite	Illite	N/A	N/A	N/A
w2200	2199.49	2194.25	2199.05	2194.56	N/A
width2200	36.313	32.215	32.723	35.451	N/A
hqd2200	0.401	0.185	0.171	0.486	N/A
w2250	N/A	2251.53	N/A	N/A	2247.61
hqd2250	N/A	0.12	N/A	N/A	0.0164
w2350	2343.4	2338.31	2338.66	2340.73	N/A
hqd2350	0.195	0.133	0.066	0.234	N/A
width2350	38.508	36.936	35.221	40.154	N/A
hqd1900	0.444	0.332	0.136	0.408	0.625
Crystallinity index	0.902	0.557	1.253	1.192	N/A

Sample Name	708376	708203	708206	708522	708350
Mineral 1	Illite	Illite	FeChlorite	Illite	Illite
Mineral 2	N/A	Kaolinite	Illite	IntChlorite	IntChlorite
w2200	2198.4	2207.99	2195.83	2203.86	2200.25
width2200	34.279	31.667	31.09	32.694	33.254
hqd2200	0.355	0.35	0.187	0.185	0.263
w2250	N/A	N/A	2250.74	2250.66	2249.77
hqd2250	N/A	N/A	0.161	0.113	0.142
w2350	2344.38	2335	2336.28	2336.58	2341.84
hqd2350	0.168	0.116	0.156	0.139	0.158
width2350	38.651	39.363	38.693	36.605	37.023
hqd1900	0.243	0.115	0.341	0.184	0.244
Crystallinity index	1.461	3.039	0.549	1.005	1.078

Appendix 3d: Illite-Sericite Microprobe Results

This appendix contains analytical data collected using the Microprobe facility at UBC under the guidance of Edith Czech and Jenny Lai. The results are used to identify sericite/illite compositions and model fluid compositions. The results are discussed in Chapter 4.

Sample	DCC_S017	DCC_S017	DCC_S017	DCC_S017
Grain	1	2	3	4
Spot Count (n)	6	4	10	9
SiO ₂	49.6638	49.8838	49.4129	43.4201
Al ₂ O ₃	33.5186	33.9723	33.3124	29.3684
TiO ₂	0.0889	0.0802	0.3148	0.2972
Cr ₂ O ₃	0.0120	0.0074	0.0106	0.0154
FeO	1.1566	1.0620	1.1382	3.4203
MnO	0.0097	0.0120	0.0126	0.0540
MgO	0.8474	0.8540	0.8583	3.5579
CaO	0.2068	0.1790	0.1808	0.1050
Na ₂ O	0.7291	0.8036	0.7524	0.4342
K ₂ O	8.5394	8.4455	8.5348	6.8170
Cl	0.0798	0.0699	0.0348	0.0721
Total	94.9685	95.4758	94.5967	87.6146
Si	3.2642	3.2565	3.2583	3.1418
Al ^{IV}	0.7358	0.7435	0.7417	0.8582
Al ^{VI}	1.8609	1.8704	1.8473	1.6343
Ti	0.0044	0.0039	0.0157	0.0167
Cr	0.0006	0.0004	0.0006	0.0008
Fe	0.0636	0.0580	0.0628	0.2070
Mn	0.0005	0.0007	0.0007	0.0033
Mg	0.0830	0.0832	0.0844	0.3811
Ca	0.0146	0.0125	0.0128	0.0081
Na	0.0930	0.1016	0.0961	0.0601
K	0.7161	0.7034	0.7180	0.6265
OH*	1.9669	1.9706	1.9890	1.9772
F	0.0242	0.0217	0.0071	0.0116
Cl	0.0089	0.0077	0.0039	0.0111
TOTAL	8.8377	8.8358	8.8383	8.9381
Y total	2.0140	2.0183	2.0115	2.2433
X total	0.8237	0.8175	0.8268	0.6948
Al total	2.5967	2.6140	2.5891	2.4925
Fe/Fe+Mg	0.2168	0.2057	0.2125	0.1772
Mn/Mn+Fe	0.0042	0.0055	0.0059	0.0073
Total Al	2.5967	2.6140	2.5891	2.4925
Mg-Li	0.0821	0.0814	0.0844	0.3811
Fe+Mn+Ti-Al ^{VI}	-1.7924	-1.8078	-1.7681	-1.4072
x= (K+ Fe-Mg)	0.7356	0.7285	0.7396	0.8006
Temperature (Battaglia, 2004)	228.5956	226.7126	229.6725	246.0337

Sample	DCC_S026A	DCC_S026A	DCC-009	DCC-009
Grain	5	6	7	8
Count	6	9	2	4
SiO ₂	38.0806	37.0555	48.5105	48.2471
Al ₂ O ₃	26.3830	25.4329	31.7980	32.3783
TiO ₂	0.0927	0.1890	0.1123	0.1288
Cr ₂ O ₃	0.0212	0.0052	0.0233	0.0159
FeO	11.9606	13.1886	2.3794	2.2003
MnO	0.3307	0.3337	0.0374	0.0119
MgO	8.1766	8.7734	1.1410	1.0381
CaO	0.2820	0.0566	0.0636	0.0391
Na ₂ O	0.0783	0.0786	0.1768	0.1432
K ₂ O	5.3237	4.6298	10.5153	10.5276
Cl	0.0278	0.0602	0.0382	0.0228
Total	90.8156	89.9028	94.8443	94.8752
Si	2.7634	2.7249	3.2516	3.2313
Al ^{IV}	1.2366	1.2751	0.7484	0.7687
Al ^{VI}	1.0375	0.9478	1.7639	1.7872
Ti	0.0049	0.0111	0.0057	0.0065
Cr	0.0014	0.0003	0.0012	0.0008
Fe	0.7977	0.8962	0.1334	0.1233
Mn	0.0224	0.0231	0.0021	0.0007
Mg	0.9712	1.0618	0.1140	0.1037
Ca	0.0207	0.0044	0.0046	0.0028
Na	0.0104	0.0107	0.0230	0.0186
K	0.4659	0.4047	0.8990	0.8993
OH*	1.9836	1.9701	1.9853	1.9716
F	0.0130	0.0229	0.0104	0.0259
Cl	0.0034	0.0071	0.0043	0.0026
TOTAL	9.3321	9.3601	8.9469	8.9428
Y total	2.8352	2.9403	2.0204	2.0221
X total	0.4969	0.4198	0.9266	0.9207
Al total	2.2742	2.2229	2.5123	2.5558
Fe/Fe+Mg	0.2277	0.2256	0.2696	0.2719
Mn/Mn+Fe	0.0097	0.0110	0.0078	0.0027
Total Al	2.2742	2.2229	2.5123	2.5558
Mg-Li	0.9712	1.0618	0.1140	0.1037
Fe+Mn+Ti-Al ^{VI}	-0.2125	-0.0175	-1.6228	-1.6568
x= (K+ Fe-Mg)	0.6394	0.5704	0.9184	0.9189
Temperature (Battaglia, 2004)	202.8203	184.3292	277.5903	277.7153

Sample	DCC-009	DCC-009	DCC-009	DCC-009	DCC-009
Grain	9	10	11	12	13
Count	3	3	2	2	2
SiO ₂	48.2986	47.9569	48.1588	59.0856	58.4235
Al ₂ O ₃	32.8958	32.3705	32.2387	25.9957	25.7680
TiO ₂	0.0316	0.0066	0.1264	0.0670	0.0883
Cr ₂ O ₃	0.0297	0.0353	0.0000	0.0514	0.0000
FeO	1.9967	1.9716	2.2902	1.2731	1.3999
MnO	0.0329	0.0068	0.0068	0.0238	0.0000
MgO	0.9177	0.9816	1.0597	0.5140	0.5824
CaO	0.0679	0.0747	0.0364	0.0952	0.0990
Na ₂ O	0.1563	0.1956	0.2221	5.8061	5.8240
K ₂ O	10.5652	10.1021	10.4876	5.2054	5.2406
Cl	0.0234	0.0761	0.0846	0.0233	0.0389
Total	95.0960	93.8680	94.7185	98.1804	97.5344
Si	3.2225	3.2359	3.2312	3.6897	3.6736
Al ^{IV}	0.7775	0.7641	0.7688	0.3747	0.3806
Al ^{VI}	1.8094	1.8102	1.7807	1.5755	1.5782
Ti	0.0016	0.0003	0.0064	0.0033	0.0044
Cr	0.0016	0.0019	0.0000	0.0024	0.0000
Fe	0.1114	0.1112	0.1284	0.0700	0.0783
Mn	0.0018	0.0004	0.0004	0.0013	0.0000
Mg	0.0912	0.0988	0.1060	0.0504	0.0581
Ca	0.0048	0.0054	0.0026	0.0062	0.0066
Na	0.0202	0.0256	0.0288	0.6771	0.6750
K	0.8992	0.8694	0.8977	0.4368	0.4510
OH*	1.9804	1.9719	1.9888	1.9898	1.9819
F	0.0170	0.0194	0.0016	0.0076	0.0140
Cl	0.0027	0.0087	0.0096	0.0026	0.0041
TOTAL	8.9414	8.9232	8.9509	8.8876	8.9057
Y total	2.0171	2.0228	2.0219	1.7030	1.7189
X total	0.9243	0.9004	0.9291	1.1201	1.1326
Al total	2.5870	2.5744	2.5495	1.9503	1.9588
Fe/Fe+Mg	0.2748	0.2645	0.2738	0.3454	0.2938
Mn/Mn+Fe	0.0080	0.0015	0.0014	0.0047	0.0000
Total Al	2.5870	2.5744	2.5495	1.9503	1.9588
Mg-Li	0.0912	0.0988	0.1060	0.0504	0.0581
Fe+Mn+Ti-Al ^{VI}	-1.6946	-1.6983	-1.6455	-1.5009	-1.4956
x= (K+ Fe-Mg)	0.9194	0.8829	0.9201	0.4564	0.4712
Temperature (Battaglia, 2004)	277.8635	268.0606	278.0495	153.7836	157.7579

Sample	DCS-S029	DCS-S029	DCS-S029	DCS-S029	DCS-S029
Grain	14	15	16	17	18
Count	6	5	7	4	6
SiO ₂	49.5559	50.2807	50.5997	50.6682	50.2241
Al ₂ O ₃	34.9137	35.9601	34.8508	35.2408	35.3933
TiO ₂	0.0542	0.0524	0.0522	0.0531	0.0565
Cr ₂ O ₃	0.0014	0.0060	0.0152	0.0128	0.0206
FeO	0.3631	0.3066	0.3743	0.3194	0.3479
MnO	0.0102	0.0334	0.0425	0.0213	0.0228
MgO	0.6118	0.6631	0.7303	0.7307	0.6378
CaO	0.1250	0.1615	0.1363	0.1987	0.1813
Na ₂ O	0.4626	0.4558	0.3798	0.3881	0.3985
K ₂ O	8.6151	9.0729	8.6647	8.7442	8.9803
Cl	0.0768	0.0179	0.0269	0.0243	0.0589
Total	94.8934	97.0726	95.9511	96.5345	96.3828
Si	3.2398	3.2173	3.2665	3.2541	3.2363
Al ^{IV}	0.7602	0.7827	0.7335	0.7459	0.7637
Al ^{VI}	1.9316	1.9298	1.9185	1.9217	1.9248
Ti	0.0027	0.0025	0.0025	0.0026	0.0027
Cr	0.0001	0.0003	0.0008	0.0006	0.0011
Fe	0.0199	0.0164	0.0202	0.0172	0.0187
Mn	0.0006	0.0018	0.0023	0.0012	0.0012
Mg	0.0594	0.0632	0.0703	0.0699	0.0612
Ca	0.0088	0.0111	0.0094	0.0137	0.0125
Na	0.0590	0.0565	0.0475	0.0484	0.0499
K	0.7184	0.7409	0.7136	0.7162	0.7380
OH*	1.9702	1.9855	1.9812	1.9702	1.9811
F	0.0213	0.0126	0.0159	0.0271	0.0124
Cl	0.0085	0.0019	0.0030	0.0027	0.0064
TOTAL	8.8003	8.8226	8.7852	8.7915	8.8101
Y total	2.0142	2.0140	2.0146	2.0132	2.0097
X total	0.7862	0.8086	0.7706	0.7783	0.8004
Al total	2.6918	2.7125	2.6520	2.6676	2.6884
Fe/Fe+Mg	0.1278	0.1016	0.1118	0.0986	0.1173
Mn/Mn+Fe	0.0139	0.0508	0.0491	0.0299	0.0326
Total Al	2.6918	2.7125	2.6520	2.6676	2.6884
Mg-Li	0.0594	0.0632	0.0703	0.0699	0.0612
Fe+Mn+Ti-Al ^{VI}	-1.9085	-1.9090	-1.8934	-1.9009	-1.9021
x= (K+ Fe-Mg)	0.7580	0.7877	0.7637	0.7690	0.7805
Temperature (Battaglia, 2004)	234.5942	242.5720	236.1295	237.5566	240.6280

Sample	DCS-S029	DNS_S011	DNS_S011	DNS_S011	DNS_S011
Grain	19	20	21	22	23
Count	8	2	2	3	3
SiO ₂	50.2713	49.8393	49.9916	50.0904	49.5764
Al ₂ O ₃	36.0303	32.0942	32.8544	31.2705	32.3961
TiO ₂	0.0613	0.0343	0.0034	0.0308	0.0312
Cr ₂ O ₃	0.0171	0.0277	0.0000	0.0000	0.0099
FeO	0.3016	1.6948	1.3996	1.8470	1.5629
MnO	0.0132	0.0206	0.0481	0.0080	0.0412
MgO	0.6382	0.9248	0.8398	1.2111	0.9263
CaO	0.1589	0.1453	0.0865	0.1729	0.1767
Na ₂ O	0.4679	0.1645	0.1707	0.2748	0.1722
K ₂ O	9.1880	9.9960	9.9961	9.8132	10.0479
Cl	0.0294	0.0342	0.0226	0.0687	0.0547
Total	97.2399	95.1326	95.4221	94.9488	95.0877
Si	3.2139	3.3024	3.2895	3.3278	3.2857
Al ^{IV}	0.7861	0.6976	0.7105	0.6722	0.7143
Al ^{VI}	1.9291	1.8090	1.8376	1.7761	1.8163
Ti	0.0029	0.0017	0.0002	0.0015	0.0016
Cr	0.0009	0.0015	0.0000	0.0000	0.0005
Fe	0.0161	0.0939	0.0770	0.1026	0.0867
Mn	0.0007	0.0012	0.0027	0.0005	0.0023
Mg	0.0608	0.0914	0.0824	0.1200	0.0915
Ca	0.0109	0.0103	0.0061	0.0123	0.0125
Na	0.0580	0.0211	0.0218	0.0354	0.0221
K	0.7494	0.8449	0.8390	0.8315	0.8495
OH*	1.9840	1.9632	1.9955	1.9584	1.9746
F	0.0128	0.0329	0.0020	0.0339	0.0193
Cl	0.0032	0.0038	0.0025	0.0077	0.0061
TOTAL	8.8288	8.8749	8.8667	8.8800	8.8830
Y total	2.0105	1.9986	1.9998	2.0008	1.9989
X total	0.8182	0.8763	0.8669	0.8792	0.8842
Al total	2.7151	2.5066	2.5481	2.4483	2.5306
Fe/Fe+Mg	0.1059	0.2533	0.2416	0.2309	0.2425
Mn/Mn+Fe	0.0190	0.0057	0.0168	0.0020	0.0128
Total Al	2.7151	2.5066	2.5481	2.4483	2.5306
Mg-Li	0.0608	0.0914	0.0824	0.1200	0.0915
Fe+Mn+Ti-Al ^{VI}	-1.9093	-1.7123	-1.7577	-1.6715	-1.7257
x= (K+ Fe-Mg)	0.7941	0.8525	0.8444	0.8489	0.8543
Temperature (Battaglia, 2004)	244.2665	259.9294	257.7478	258.9636	260.4227

Sample	DNS_S011	DNS_S011	DNS_S011	DNS_S011	DNS_S011
Grain	24	25	26	27	28
Count	1	2	1	4	2
SiO ₂	45.9225	49.8003	50.8991	49.1619	48.7466
Al ₂ O ₃	29.6579	32.6312	32.2721	32.4925	32.0779
TiO ₂	0.0235	0.0678	0.0022	0.0242	0.0397
Cr ₂ O ₃	0.0000	0.0000	0.0723	0.0149	0.0000
FeO	1.9595	1.8998	2.1012	1.7051	1.6132
MnO	0.0514	0.0137	0.0446	0.0249	0.0138
MgO	1.0572	0.8748	1.3243	0.9584	0.8031
CaO	0.0969	0.1061	0.0882	0.1388	0.1424
Na ₂ O	0.5149	0.2067	0.3875	0.3951	0.2619
K ₂ O	9.5532	9.9995	9.1961	9.8075	10.0976
Cl	0.2361	0.0342	0.1870	0.1567	0.0635
Total	89.0826	95.7003	96.5746	95.0364	94.0305
Si	3.2744	3.2804	3.3120	3.2677	3.2761
Al ^{IV}	0.7256	0.7196	0.6880	0.7323	0.7239
Al ^{VI}	1.7670	1.8140	1.7872	1.8132	1.8171
Ti	0.0013	0.0034	0.0001	0.0012	0.0020
Cr	0.0000	0.0000	0.0037	0.0008	0.0000
Fe	0.1169	0.1047	0.1143	0.0948	0.0907
Mn	0.0031	0.0008	0.0025	0.0014	0.0008
Mg	0.1124	0.0859	0.1285	0.0950	0.0805
Ca	0.0074	0.0075	0.0061	0.0099	0.0102
Na	0.0712	0.0264	0.0489	0.0510	0.0341
K	0.8689	0.8401	0.7633	0.8316	0.8656
OH*	1.9693	1.9823	1.9794	1.9493	1.9563
F	0.0021	0.0138	0.0000	0.0331	0.0365
Cl	0.0285	0.0038	0.0206	0.0177	0.0072
TOTAL	8.9480	8.8827	8.8545	8.8995	8.9015
Y total	2.0006	2.0087	2.0362	2.0070	1.9915
X total	0.9474	0.8740	0.8183	0.8925	0.9100
Al total	2.4926	2.5336	2.4752	2.5455	2.5409
Fe/Fe+Mg	0.2549	0.2746	0.2355	0.2499	0.2649
Mn/Mn+Fe	0.0129	0.0036	0.0105	0.0071	0.0042
Total Al	2.4926	2.5336	2.4752	2.5455	2.5409
Mg-Li	0.1124	0.0859	0.1285	0.0946	0.0799
Fe+Mn+Ti-Al ^{VI}	-1.6458	-1.7052	-1.6702	-1.7157	-1.7236
x= (K+ Fe-Mg)	0.8733	0.8589	0.7774	0.8355	0.8759
Temperature (Battaglia, 2004)	265.5096	261.6439	239.7951	255.3626	266.1846

Sample	DNS_S011	DNS_S011	DNS_S037	DNS_S037	DNS_S037
Grain	29	30	31	32	33
Count	3	4	7	2	2
SiO ₂	50.2521	49.6138	49.3509	47.3839	48.6422
Al ₂ O ₃	31.7035	32.1155	34.3052	32.6085	33.0179
TiO ₂	0.0191	0.0527	0.0129	0.0245	0.0044
Cr ₂ O ₃	0.0298	0.0075	0.0043	0.0321	0.0000
FeO	1.8475	1.8153	0.5101	0.6142	0.4357
MnO	0.0423	0.0344	0.0452	0.0361	0.0155
MgO	1.0979	0.9477	0.6940	0.7013	0.7569
CaO	0.0891	0.0843	0.0962	0.0878	0.1180
Na ₂ O	0.1801	0.2217	0.2082	0.2117	0.2197
K ₂ O	10.0469	10.1672	9.7431	9.0604	9.2804
Cl	0.0568	0.0804	0.0168	0.0372	0.0198
Total	95.4728	95.2423	95.1867	90.9887	92.6971
Si	3.3195	3.2909	3.2427	3.2545	3.2736
Al ^{IV}	0.6805	0.7091	0.7573	0.7455	0.7264
Al ^{VI}	1.7883	1.8012	1.8998	1.8939	1.8926
Ti	0.0009	0.0026	0.0006	0.0013	0.0002
Cr	0.0016	0.0004	0.0002	0.0018	0.0000
Fe	0.1020	0.1008	0.0280	0.0350	0.0245
Mn	0.0024	0.0019	0.0025	0.0022	0.0009
Mg	0.1080	0.0938	0.0679	0.0721	0.0759
Ca	0.0063	0.0060	0.0068	0.0066	0.0085
Na	0.0231	0.0285	0.0266	0.0282	0.0286
K	0.8467	0.8602	0.8168	0.7932	0.7966
OH*	1.9710	1.9694	1.9565	1.9538	1.9576
F	0.0226	0.0215	0.0416	0.0417	0.0401
Cl	0.0064	0.0091	0.0019	0.0045	0.0023
TOTAL	8.8793	8.8955	8.8501	8.8344	8.8306
Y total	2.0033	2.0008	2.0000	2.0063	1.9968
X total	0.8760	0.8947	0.8501	0.8281	0.8338
Al total	2.4688	2.5103	2.6571	2.6395	2.6190
Fe/Fe+Mg	0.2435	0.2594	0.1466	0.1637	0.1219
Mn/Mn+Fe	0.0113	0.0100	0.0406	0.0331	0.0157
Total Al	2.4688	2.5103	2.6571	2.6395	2.6190
Mg-Li	0.1080	0.0938	0.0671	0.0721	0.0732
Fe+Mn+Ti-Al ^{VI}	-1.6829	-1.6959	-1.8686	-1.8555	-1.8670
x= (K+ Fe-Mg)	0.8580	0.8726	0.8567	0.8303	0.8480
Temperature (Battaglia, 2004)	261.4096	265.3031	261.0463	253.9898	258.7300

Sample	DNS_S037	DNS_S037	DNS_S037	DNS_S037
Grain	34	35	36	37
Count	2	1	2	3
SiO ₂	47.7956	49.2850	48.9424	48.6130
Al ₂ O ₃	33.1023	33.4064	33.8920	33.3691
TiO ₂	0.0146	0.0000	0.0403	0.0246
Cr ₂ O ₃	0.0321	0.0300	0.0236	0.0071
FeO	0.5059	0.3296	0.4245	0.4163
MnO	0.0155	0.0000	0.0086	0.0115
MgO	0.6760	0.7940	0.6450	0.7262
CaO	0.1088	0.1499	0.1241	0.1802
Na ₂ O	0.1760	0.2279	0.2575	0.2764
K ₂ O	9.6123	9.3717	9.3661	9.3401
Cl	0.0295	0.0266	0.0384	0.0503
Total	92.2884	93.8798	93.8822	93.1554
Si	3.2448	3.2758	3.2516	3.2583
Al ^{IV}	0.7552	0.7242	0.7484	0.7417
Al ^{VI}	1.8924	1.8930	1.9054	1.8940
Ti	0.0007	0.0000	0.0020	0.0012
Cr	0.0017	0.0016	0.0012	0.0004
Fe	0.0288	0.0183	0.0235	0.0234
Mn	0.0009	0.0000	0.0005	0.0007
Mg	0.0684	0.0787	0.0639	0.0727
Ca	0.0080	0.0107	0.0088	0.0130
Na	0.0233	0.0294	0.0332	0.0360
K	0.8316	0.7945	0.7937	0.7980
OH*	1.9498	1.9426	1.9701	1.9644
F	0.0468	0.0544	0.0255	0.0298
Cl	0.0035	0.0030	0.0044	0.0057
TOTAL	8.8587	8.8274	8.8323	8.8394
Y total	1.9959	1.9928	1.9965	1.9924
X total	0.8628	0.8346	0.8358	0.8470
Al total	2.6476	2.6172	2.6538	2.6357
Fe/Fe+Mg	0.1479	0.0944	0.1311	0.1219
Mn/Mn+Fe	0.0142	0.0000	0.0074	0.0114
Total Al	2.6476	2.6172	2.6538	2.6357
Mg-Li	0.0654	0.0774	0.0639	0.0727
Fe+Mn+Ti-Al ^{VI}	-1.8620	-1.8747	-1.8795	-1.8687
x= (K+ Fe-Mg)	0.8712	0.8549	0.8341	0.8473
Temperature (Battaglia, 2004)	264.9321	260.5651	255.0012	258.5367

Sample	DNS_S037	DNS_S037	DNS_S037	DNS_S037
Grain	38	39	40	41
Count	2	1	3	2
SiO ₂	49.9998	49.8842	49.3793	49.2263
Al ₂ O ₃	33.1851	34.6031	32.8556	33.4719
TiO ₂	0.0029	0.0441	0.0442	0.0695
Cr ₂ O ₃	0.0193	0.0342	0.0256	0.0385
FeO	0.4492	0.3232	1.1466	1.1591
MnO	0.0000	0.0344	0.0057	0.0000
MgO	0.8706	0.6601	0.8723	0.9893
CaO	0.2474	0.0602	0.1076	0.1001
Na ₂ O	0.2880	0.1907	0.1907	0.1617
K ₂ O	8.7437	9.7785	9.6757	9.9209
Cl	0.0324	0.0202	0.0247	0.0040
Total	94.0679	95.7482	94.4711	95.2412
Si	3.3029	3.2503	3.2782	3.2460
Al ^{IV}	0.6971	0.7497	0.7218	0.7540
Al ^{VI}	1.8875	1.9078	1.8497	1.8476
Ti	0.0001	0.0022	0.0022	0.0034
Cr	0.0010	0.0018	0.0013	0.0020
Fe	0.0250	0.0176	0.0636	0.0639
Mn	0.0000	0.0019	0.0003	0.0000
Mg	0.0859	0.0641	0.0863	0.0972
Ca	0.0176	0.0042	0.0077	0.0071
Na	0.0370	0.0241	0.0246	0.0207
K	0.7370	0.8127	0.8195	0.8344
OH*	1.9483	1.9740	1.9674	1.9786
F	0.0481	0.0238	0.0298	0.0209
Cl	0.0036	0.0022	0.0028	0.0004
TOTAL	8.7913	8.8363	8.8552	8.8763
Y total	1.9997	1.9953	2.0035	2.0142
X total	0.7916	0.8410	0.8518	0.8622
Al total	2.5846	2.6575	2.5715	2.6016
Fe/Fe+Mg	0.1111	0.1077	0.2119	0.1973
Mn/Mn+Fe	0.0000	0.0487	0.0026	0.0000
Total Al	2.5846	2.6575	2.5715	2.6016
Mg-Li	0.0857	0.0641	0.0863	0.0972
Fe+Mn+Ti-Al ^{VI}	-1.8624	-1.8861	-1.7836	-1.7802
x= (K+ Fe-Mg)	0.7979	0.8592	0.8422	0.8677
Temperature (Battaglia, 2004)	245.3074	261.7177	257.1730	264.0086

Sample	DNS_S037	DNS_S037	DNS_S037	DNS_S037
Grain	42	43	44	45
Count	1	3	1	5
SiO ₂	50.1089	48.6797	50.4347	49.3679
Al ₂ O ₃	33.5562	31.8771	33.7569	32.4672
TiO ₂	0.0120	0.0747	0.0408	0.0017
Cr ₂ O ₃	0.0513	0.0284	0.0385	0.0128
FeO	0.8143	1.2431	0.5736	0.4816
MnO	0.0000	0.0309	0.0000	0.0220
MgO	0.7944	1.1884	0.8927	0.8981
CaO	0.0381	0.0892	0.0639	0.0931
Na ₂ O	0.0934	0.1905	0.1592	0.1855
K ₂ O	10.2086	9.8295	10.0632	9.1649
Cl	0.0153	0.0099	0.0000	0.0362
Total	95.8840	93.4700	96.3203	92.7980
Si	3.2783	3.2797	3.2799	3.3109
Al ^{IV}	0.7217	0.7203	0.7201	0.6891
Al ^{VI}	1.8661	1.8116	1.8675	1.8763
Ti	0.0006	0.0038	0.0020	0.0001
Cr	0.0027	0.0015	0.0020	0.0007
Fe	0.0446	0.0700	0.0312	0.0271
Mn	0.0000	0.0017	0.0000	0.0013
Mg	0.0775	0.1194	0.0865	0.0900
Ca	0.0027	0.0065	0.0045	0.0068
Na	0.0118	0.0249	0.0201	0.0242
K	0.8519	0.8449	0.8348	0.7833
OH*	1.9587	1.9502	1.9390	1.9818
F	0.0396	0.0487	0.0610	0.0140
Cl	0.0017	0.0011	0.0000	0.0042
TOTAL	8.8578	8.8850	8.8529	8.8097
Y total	1.9913	2.0088	1.9936	1.9955
X total	0.8664	0.8762	0.8593	0.8142
Al total	2.5877	2.5319	2.5876	2.5654
Fe/Fe+Mg	0.1826	0.1844	0.1325	0.1154
Mn/Mn+Fe	0.0000	0.0113	0.0000	0.0212
Total Al	2.5877	2.5319	2.5876	2.5654
Mg-Li	0.0775	0.1186	0.0822	0.0900
Fe+Mn+Ti-Al ^{VI}	-1.8209	-1.7361	-1.8343	-1.8478
x= (K+ Fe-Mg)	0.8848	0.8943	0.8901	0.8462
Temperature (Battaglia, 2004)	268.5914	271.1258	270.0028	258.2378

Sample	DNS_S037	DNS_S037	DNS_S037	DNS_S037
Grain	46	47	48	49
Count	2	2	3	1
SiO ₂	48.9583	49.7275	49.6893	49.6366
Al ₂ O ₃	33.3021	34.2319	34.1169	34.6829
TiO ₂	0.0198	0.0304	0.0133	0.0123
Cr ₂ O ₃	0.0000	0.0129	0.0242	0.0385
FeO	0.4594	0.6028	0.5885	0.5257
MnO	0.0069	0.0138	0.0275	0.0206
MgO	0.6640	0.6992	0.7070	0.6878
CaO	0.0634	0.0412	0.0643	0.0860
Na ₂ O	0.2518	0.1846	0.2093	0.2637
K ₂ O	9.5314	9.8580	9.8499	9.8173
Cl	0.0279	0.0105	0.0107	0.0016
Total	93.3519	95.6325	95.4764	95.8880
Si	3.2718	3.2533	3.2558	3.2356
Al ^{IV}	0.7282	0.7467	0.7442	0.7644
Al ^{VI}	1.8952	1.8931	1.8907	1.9004
Ti	0.0010	0.0015	0.0007	0.0006
Cr	0.0000	0.0007	0.0013	0.0020
Fe	0.0257	0.0330	0.0323	0.0287
Mn	0.0004	0.0008	0.0015	0.0011
Mg	0.0661	0.0682	0.0691	0.0668
Ca	0.0045	0.0029	0.0045	0.0060
Na	0.0326	0.0234	0.0266	0.0333
K	0.8125	0.8226	0.8232	0.8163
OH*	1.9827	1.9534	1.9625	1.9761
F	0.0141	0.0455	0.0363	0.0237
Cl	0.0032	0.0012	0.0012	0.0002
TOTAL	8.8381	8.8498	8.8509	8.8552
Y total	1.9884	2.0009	1.9965	1.9996
X total	0.8497	0.8489	0.8544	0.8556
Al total	2.6234	2.6399	2.6349	2.6648
Fe/Fe+Mg	0.1406	0.1639	0.1590	0.1501
Mn/Mn+Fe	0.0066	0.0104	0.0208	0.0191
Total Al	2.6234	2.6399	2.6349	2.6648
Mg-Li	0.0661	0.0644	0.0680	0.0668
Fe+Mn+Ti-Al ^{VI}	-1.8681	-1.8579	-1.8563	-1.8700
x= (K+ Fe-Mg)	0.8530	0.8578	0.8601	0.8544
Temperature (Battaglia, 2004)	260.0480	261.3490	261.9557	260.4473

Sample	DNS_S037	DNS_S037	DNS_S037	DNS_S037
Grain	50	51	52	53
Count	2	1	2	1
SiO ₂	49.6636	49.2333	48.1017	49.4139
Al ₂ O ₃	33.9532	33.4576	31.9916	33.5914
TiO ₂	0.0228	0.0148	0.0091	0.0000
Cr ₂ O ₃	0.0386	0.0000	0.0278	0.0000
FeO	0.5137	0.5663	0.8233	0.6205
MnO	0.0189	0.0310	0.0310	0.0103
MgO	0.7058	0.7754	0.8940	0.6800
CaO	0.0645	0.0884	0.1278	0.0774
Na ₂ O	0.1582	0.2569	0.1816	0.1760
K ₂ O	9.7824	9.3751	9.2541	10.1046
Cl	0.0198	0.0057	0.0468	0.0024
Total	94.9988	93.8045	91.4934	94.6765
Si	3.2636	3.2699	3.2849	3.2654
Al ^{IV}	0.7364	0.7301	0.7151	0.7346
Al ^{VI}	1.8933	1.8891	1.8602	1.8819
Ti	0.0011	0.0007	0.0005	0.0000
Cr	0.0020	0.0000	0.0015	0.0000
Fe	0.0283	0.0315	0.0469	0.0343
Mn	0.0011	0.0017	0.0018	0.0006
Mg	0.0692	0.0768	0.0909	0.0670
Ca	0.0046	0.0063	0.0094	0.0055
Na	0.0202	0.0331	0.0241	0.0226
K	0.8199	0.7942	0.8060	0.8517
OH*	1.9857	1.9994	1.9935	1.9997
F	0.0121	0.0000	0.0010	0.0000
Cl	0.0022	0.0006	0.0054	0.0003
TOTAL	8.8395	8.8334	8.8412	8.8635
Y total	1.9948	1.9998	2.0018	1.9837
X total	0.8447	0.8336	0.8394	0.8798
Al total	2.6297	2.6192	2.5753	2.6165
Fe/Fe+Mg	0.1447	0.1453	0.1688	0.1693
Mn/Mn+Fe	0.0160	0.0263	0.0169	0.0083
Total Al	2.6297	2.6192	2.5753	2.6165
Mg-Li	0.0692	0.0768	0.0909	0.0670
Fe+Mn+Ti-Al ^{VI}	-1.8628	-1.8552	-1.8111	-1.8470
x= (K+ Fe-Mg)	0.8608	0.8395	0.8500	0.8844
Temperature (Battaglia, 2004)	262.1541	256.4526	259.2561	268.4781

Sample	DNS_S037	DNS_S037	DNS_S037	DNS_S037
Grain	54	55	56	57
Count	1	2	5	1
SiO ₂	48.8032	47.3644	48.6728	49.5892
Al ₂ O ₃	33.1637	30.8471	33.1000	32.9212
TiO ₂	0.0028	0.1106	0.0408	0.0520
Cr ₂ O ₃	0.0000	0.0128	0.0000	0.0213
FeO	0.7591	1.5006	1.1324	1.5037
MnO	0.0447	0.0292	0.0227	0.0790
MgO	0.7319	1.1526	0.7945	1.0770
CaO	0.1093	0.0872	0.0747	0.0516
Na ₂ O	0.1762	0.2508	0.2515	0.1728
K ₂ O	9.4971	9.7422	9.8734	10.1316
Cl	0.0428	0.0941	0.0337	0.0419
Total	93.3308	91.4482	94.0842	95.7748
Si	3.2663	3.2765	3.2508	3.2644
Al ^{IV}	0.7337	0.7235	0.7492	0.7356
Al ^{VI}	1.8826	1.7909	1.8565	1.8187
Ti	0.0001	0.0058	0.0020	0.0026
Cr	0.0000	0.0007	0.0000	0.0011
Fe	0.0425	0.0874	0.0633	0.0828
Mn	0.0025	0.0017	0.0013	0.0044
Mg	0.0730	0.1190	0.0790	0.1057
Ca	0.0078	0.0065	0.0054	0.0036
Na	0.0229	0.0335	0.0326	0.0221
K	0.8108	0.8601	0.8411	0.8507
OH*	1.9951	1.9330	1.9779	1.9675
F	0.0000	0.0558	0.0183	0.0278
Cl	0.0049	0.0112	0.0038	0.0047
TOTAL	8.8422	8.9084	8.8812	8.8917
Y total	2.0008	2.0084	2.0021	2.0153
X total	0.8415	0.9001	0.8791	0.8764
Al total	2.6162	2.5144	2.6057	2.5544
Fe/Fe+Mg	0.1839	0.2103	0.2232	0.2196
Mn/Mn+Fe	0.0281	0.0105	0.0091	0.0253
Total Al	2.6162	2.5144	2.6057	2.5544
Mg-Li	0.0730	0.1161	0.0790	0.1057
Fe+Mn+Ti-Al ^{VI}	-1.8374	-1.6961	-1.7899	-1.7290
x= (K+ Fe-Mg)	0.8413	0.8918	0.8569	0.8736
Temperature (Battaglia, 2004)	256.9241	270.4471	261.1023	265.5819

Sample	DNS_S037	DNS_S037
Grain	58	59
Count	2	1
SiO ₂	50.2197	49.3426
Al ₂ O ₃	32.4061	33.5501
TiO ₂	0.0742	0.0082
Cr ₂ O ₃	0.0107	0.0000
FeO	1.4309	1.4409
MnO	0.0464	0.0000
MgO	1.1685	0.7951
CaO	0.0620	0.0712
Na ₂ O	0.1717	0.1791
K ₂ O	9.9899	9.9134
Cl	0.0117	0.0145
Total	95.7344	95.4198
Si	3.2991	3.2505
Al ^{IV}	0.7009	0.7495
Al ^{VI}	1.8085	1.8557
Ti	0.0037	0.0004
Cr	0.0006	0.0000
Fe	0.0787	0.0794
Mn	0.0026	0.0000
Mg	0.1144	0.0781
Ca	0.0044	0.0050
Na	0.0219	0.0229
K	0.8370	0.8330
OH*	1.9690	1.9766
F	0.0297	0.0218
Cl	0.0013	0.0016
TOTAL	8.8717	8.8744
Y total	2.0084	2.0135
X total	0.8633	0.8609
Al total	2.5094	2.6051
Fe/Fe+Mg	0.2029	0.2521
Mn/Mn+Fe	0.0166	0.0000
Total Al	2.5094	2.6051
Mg-Li	0.1144	0.0781
Fe+Mn+Ti-Al ^{VI}	-1.7236	-1.7759
x= (K+ Fe-Mg)	0.8727	0.8343
Temperature (Battaglia, 2004)	265.3493	255.0518

Appendix 3e: Chlorite Microprobe Results

This appendix contains analytical data collected using the Microprobe facility at UBC under the guidance of Edith Czech and Jenny Lai. The results are used to identify chlorite compositions and model fluid compositions. The results are discussed in Chapter 4.

Label	DCC-009	DCC-009	DCC-009	DCC-009	DCC-009	DCC-009	DCC-009
#	1	2	3	4	5	6	7
Count	1	1	6	6	2	2	3
Deposit	Centralni	Centralni	Centralni	Centralni	Centralni	Centralni	Centralni
Area	Wallrock	Wallrock	Vein	Vein	Vein	Wallrock	Wallrock
SiO ₂	27.8382	27.6738	27.1031	27.0786	26.7364	27.0073	26.9550
TiO ₂	0.0419	0.0000	0.0145	0.0119	0.0094	0.0353	0.0208
Al ₂ O ₃	21.7989	20.1969	19.1619	19.0663	18.3845	21.0490	20.8885
Cr ₂ O ₃	0.1040	0.0000	0.0038	0.0267	0.0000	0.0345	0.0612
Fe ₂ O ₃	2.4245	1.4742	0.5155	0.5233	0.0243	1.5400	1.3557
FeO	20.5874	21.5666	24.5863	24.3498	26.8536	21.8197	22.9705
MnO	0.8374	0.7068	0.8506	0.8194	0.8297	0.7838	0.8076
MgO	14.5768	15.6240	15.5704	15.6375	14.9376	15.0202	14.6345
CaO	0.0119	0.0511	0.0380	0.0217	0.0311	0.0521	0.0885
Na ₂ O	0.0000	0.0314	0.0048	0.0020	0.0156	0.0145	0.0185
K ₂ O	0.1284	0.1226	0.0339	0.0284	0.0040	0.0429	0.0511
H ₂ O*	11.6483	11.5006	11.3982	11.3693	11.2636	11.4687	11.4634
TOTAL	99.9978	98.9480	99.2808	98.9348	99.0897	98.8679	99.3152
Si	5.6906	5.7432	5.6930	5.7032	5.6913	5.6221	5.6162
Al ^{IV}	2.3094	2.2568	2.3070	2.2968	2.3087	2.3779	2.3838
Al ^{VI}	2.9814	2.7081	2.4446	2.4443	2.3052	2.8111	2.7678
Ti	0.0064	0.0000	0.0023	0.0019	0.0015	0.0055	0.0033
Cr	0.0168	0.0000	0.0006	0.0044	0.0000	0.0057	0.0101
Fe ³⁺	0.3730	0.2302	0.0809	0.0828	0.0039	0.2413	0.2124
Fe ²⁺	3.5196	3.7432	4.3271	4.2897	4.7869	3.7987	4.0032
Mn	0.1450	0.1242	0.1514	0.1462	0.1495	0.1382	0.1425
Mg	4.4419	4.8336	4.8747	4.9097	4.7393	4.6610	4.5457
Ca	0.0026	0.0114	0.0086	0.0049	0.0071	0.0116	0.0197
Na	0.0000	0.0253	0.0039	0.0016	0.0129	0.0117	0.0148
K	0.0670	0.0649	0.0181	0.0153	0.0022	0.0228	0.0271
OH*	16.0000	16.0000	16.0000	16.0000	16.0000	16.0000	16.0000
Total	35.5537	35.7409	35.9122	35.9008	36.0086	35.7076	35.7467
Fe/Fe+Mg	0.4670	0.4512	0.4745	0.4710	0.5026	0.4643	0.4812
Chlorie T (°C)-Al ^{IV} ¹⁴ O	1.1547	1.1284	1.1535	1.1484	1.1544	1.1889	1.1919
T (°C)-Cathelineau (1988)	309.8665	301.4022	309.4796	307.8480	309.7600	320.8929	321.8457
Fe ⁺² (¹⁴ O)	1.7598	1.8716	2.1635	2.1449	2.3935	1.8993	2.0016
Mg ⁺² (¹⁴ O)	2.2210	2.4168	2.4373	2.4549	2.3696	2.3305	2.2729
Al ^{IV} (Jowett, 1991)	1.1989	1.1720	1.2004	1.1950	1.2046	1.2338	1.2387
T (°C)-Jowett (1991)	313.4478	304.8818	313.9428	312.2181	315.2667	324.5917	326.1501

Label	DCC-009	DCC_S026A	DCC_S026A	DNS_S011	DNS_S011	DNS_S011
#	8	9	10	11	12	13
Count	2	15	10	5	5	2
Deposit	Centralni	Centralni	Centralni	Noreshenik	Noreshenik	Noreshenik
Area	Wallrock	Vein	Vein	Vein	Vein	Vein
SiO ₂	26.9722	26.4501	26.6760	26.2713	26.4478	26.9696
TiO ₂	0.0034	0.0330	0.0308	0.0281	0.0218	0.0218
Al ₂ O ₃	20.5647	20.2545	20.4611	21.2009	21.2595	21.1918
Cr ₂ O ₃	0.0613	0.0132	0.0142	0.0037	0.0243	0.0000
Fe ₂ O ₃	1.1985	1.0351	0.9724	1.0671	1.1868	1.3485
FeO	22.6544	22.4906	22.0955	25.3833	23.8690	23.4721
MnO	0.7878	0.6240	0.5695	0.7599	0.7152	0.8001
MgO	15.0125	15.1404	15.4310	13.4641	14.2510	14.5648
CaO	0.1358	0.0188	0.0274	0.0678	0.0966	0.0772
Na ₂ O	0.0296	0.0242	0.0095	0.0111	0.0000	0.0125
K ₂ O	0.0726	0.0505	0.2623	0.0029	0.0108	0.0000
H ₂ O*	11.4356	11.2679	11.3496	11.3849	11.4239	11.5275
TOTAL	98.9282	97.4022	97.8993	99.6452	99.3068	99.9857
Si	5.6348	5.6065	5.6129	5.5165	5.5341	5.5899
Al ^{IV}	2.3652	2.3935	2.3871	2.4835	2.4659	2.4101
Al ^{VI}	2.7193	2.6907	2.7091	2.7828	2.7954	2.7872
Ti	0.0005	0.0052	0.0049	0.0045	0.0034	0.0034
Cr	0.0101	0.0022	0.0024	0.0006	0.0040	0.0000
Fe ³⁺	0.1885	0.1615	0.1524	0.1684	0.1870	0.2102
Fe ²⁺	3.9589	3.9978	3.8940	4.4654	4.1771	4.0695
Mn	0.1394	0.1122	0.1014	0.1349	0.1268	0.1405
Mg	4.6747	4.7913	4.8444	4.2087	4.4448	4.5001
Ca	0.0304	0.0043	0.0062	0.0151	0.0217	0.0171
Na	0.0238	0.0197	0.0077	0.0092	0.0000	0.0100
K	0.0386	0.0273	0.1386	0.0016	0.0058	0.0000
OH*	16.0000	16.0000	16.0000	16.0000	16.0000	16.0000
Total	35.7842	35.8123	35.8609	35.7912	35.7660	35.7379
Fe/Fe+Mg	0.4701	0.4646	0.4549	0.5240	0.4953	0.4874
Chlorie T (°C)-Al ^{IV} ¹⁴ O	1.1826	1.1967	1.1935	1.2418	1.2329	1.2051
T (°C)-Cathelineau (1988)	318.8459	323.4089	322.3730	337.9005	335.0644	326.0835
Fe ⁺² (¹⁴ O)	1.9794	1.9989	1.9470	2.2327	2.0885	2.0347
Mg ⁺² (¹⁴ O)	2.3374	2.3957	2.4222	2.1044	2.2224	2.2500
Al ^{IV} (Jowett, 1991)	1.2284	1.2421	1.2380	1.2932	1.2814	1.2525
T (°C)-Jowett (1991)	322.8704	327.2379	325.9313	343.5395	339.7556	330.5582

Label	DNS_S011	DNS_S011	DNS_S011	DNS_S011	DNS_S011	DNS_S011
#	14	15	16	17	18	19
Count	2	5	1	3	3	5
Deposit	Noreshenik	Noreshenik	Noreshenik	Noreshenik	Noreshenik	Noreshenik
Area	Vein	Vein	Vein	Vein	Vein	Vein
SiO ₂	27.0392	26.7565	26.4140	26.5314	26.3133	26.3441
TiO ₂	0.0053	0.0245	0.0561	0.0251	0.0241	0.0317
Al ₂ O ₃	21.6876	20.9419	20.7231	21.5093	21.5522	21.0026
Cr ₂ O ₃	0.0191	0.0138	0.0306	0.0114	0.0037	0.0100
Fe ₂ O ₃	1.7766	1.1222	0.7270	1.0879	1.2715	1.1897
FeO	22.8918	23.4453	23.9204	24.6868	25.1158	24.0118
MnO	0.7200	0.8112	0.7054	0.7294	0.6636	0.7989
MgO	14.0767	14.6857	15.0969	14.0829	13.3003	13.9599
CaO	0.0922	0.0834	0.0472	0.0656	0.0557	0.0749
Na ₂ O	0.0176	0.0515	0.0291	0.0272	0.0199	0.0146
K ₂ O	0.0099	0.0121	0.0173	0.0123	0.0008	0.0005
H ₂ O*	11.5345	11.4591	11.4215	11.5065	11.4104	11.3450
TOTAL	99.8702	99.4071	99.1887	100.2756	99.7314	98.7838
Si	5.5937	5.5806	5.5340	5.5123	5.5095	5.5498
Al ^{IV}	2.4063	2.4194	2.4660	2.4877	2.4905	2.4502
Al ^{VI}	2.9089	2.7473	2.6635	2.7972	2.8501	2.7845
Ti	0.0008	0.0038	0.0088	0.0039	0.0039	0.0050
Cr	0.0032	0.0023	0.0051	0.0019	0.0006	0.0017
Fe ³⁺	0.2761	0.1763	0.1146	0.1702	0.1996	0.1886
Fe ²⁺	3.9620	4.0891	4.1913	4.2895	4.4069	4.2331
Mn	0.1262	0.1433	0.1252	0.1283	0.1177	0.1428
Mg	4.3417	4.5658	4.7150	4.3615	4.1464	4.3815
Ca	0.0205	0.0186	0.0106	0.0146	0.0124	0.0169
Na	0.0140	0.0416	0.0236	0.0219	0.0162	0.0120
K	0.0052	0.0065	0.0092	0.0065	0.0004	0.0003
OH*	16.0000	16.0000	16.0000	16.0000	16.0000	16.0000
Total	35.6586	35.7947	35.8670	35.7956	35.7543	35.7662
Fe/Fe+Mg	0.4939	0.4830	0.4773	0.5055	0.5260	0.5025
Chlorie T (°C)-Al ^{IV} ¹⁴ O	1.2031	1.2097	1.2330	1.2438	1.2453	1.2251
T (°C)-Cathelineau (1988)	325.4655	327.5840	335.0839	338.5718	339.0271	332.5401
Fe ⁺² (¹⁴ O)	1.9810	2.0446	2.0956	2.1448	2.2035	2.1166
Mg ⁺² (¹⁴ O)	2.1708	2.2829	2.3575	2.1808	2.0732	2.1907
Al ^{IV} (Jowett, 1991)	1.2508	1.2570	1.2801	1.2934	1.2967	1.2743
T (°C)-Jowett (1991)	330.0162	331.9679	339.3417	343.6006	344.6548	337.4931

Label	DNS_S011	DNS_S011	DNS_S011	DNS_S011	DNS_S011	DNS_S011
#	20	21	22	23	24	25
Count	3	2	8	6	3	5
Deposit	Noreshenik	Noreshenik	Noreshenik	Noreshenik	Noreshenik	Noreshenik
Area	Vein	Vein	Vein	Vein	Vein	Vein
SiO ₂	26.1072	26.7034	26.8125	27.2850	27.4836	26.4527
TiO ₂	0.0301	0.0182	0.0089	0.0260	0.0056	0.0263
Al ₂ O ₃	21.1708	21.2026	20.8156	20.5096	20.8425	21.7578
Cr ₂ O ₃	0.0074	0.0153	0.0095	0.0224	0.0971	0.0251
Fe ₂ O ₃	0.9150	1.3081	1.2377	1.4139	1.6360	1.4323
FeO	26.3711	23.6227	23.9318	23.4042	23.3099	25.2275
MnO	0.7818	0.7633	0.8090	0.8330	0.7319	0.6636
MgO	13.0554	14.2223	14.3216	14.5786	14.4025	13.0382
CaO	0.0866	0.1160	0.0815	0.0825	0.1005	0.0882
Na ₂ O	0.0063	0.0386	0.0073	0.0260	0.0286	0.0077
K ₂ O	0.0130	0.0000	0.0015	0.0012	0.0124	0.0175
H ₂ O*	11.3651	11.4521	11.4384	11.4862	11.5558	11.4557
TOTAL	99.9097	99.4623	99.4755	99.6684	100.2062	100.1925
Si	5.4939	5.5707	5.6025	5.6740	5.6774	5.5150
Al ^{IV}	2.5061	2.4293	2.3975	2.3260	2.3226	2.4850
Al ^{VI}	2.7619	2.8049	2.7475	2.7221	2.7762	2.8851
Ti	0.0048	0.0028	0.0014	0.0040	0.0009	0.0042
Cr	0.0013	0.0025	0.0016	0.0037	0.0159	0.0041
Fe ³⁺	0.1447	0.2054	0.1947	0.2212	0.2545	0.2243
Fe ²⁺	4.6499	4.1215	4.1823	4.0706	4.0264	4.4025
Mn	0.1392	0.1349	0.1432	0.1468	0.1280	0.1171
Mg	4.0881	4.4228	4.4605	4.5193	4.4350	4.0504
Ca	0.0195	0.0259	0.0182	0.0184	0.0223	0.0196
Na	0.0051	0.0312	0.0060	0.0209	0.0228	0.0062
K	0.0071	0.0000	0.0008	0.0007	0.0065	0.0093
OH*	16.0000	16.0000	16.0000	16.0000	16.0000	16.0000
Total	35.8217	35.7520	35.7562	35.7276	35.6886	35.7230
Fe/Fe+Mg	0.5399	0.4945	0.4953	0.4871	0.4913	0.5335
Chlorie T (°C)-Al ^{IV} ¹⁴ O	1.2531	1.2147	1.1988	1.1630	1.1613	1.2425
T (°C)-Cathelineau (1988)	341.5424	329.1732	324.0562	312.5493	311.9909	338.1438
Fe ⁺² (¹⁴ O)	2.3250	2.0607	2.0911	2.0353	2.0132	2.2013
Mg ⁺² (¹⁴ O)	2.0440	2.2114	2.2303	2.2596	2.2175	2.0252
Al ^{IV} (Jowett, 1991)	1.3063	1.2629	1.2472	1.2104	1.2089	1.2946
T (°C)-Jowett (1991)	347.7064	333.8604	328.8418	317.1182	316.6341	343.9777

Label	DNS_S011	DNS_S011	DNS_S011	DNS_S011	DNS_S011	DNS_S011
#	26	27	28	29	30	31
Count	2	2	2	2	1	1
Deposit	Noreshenik	Noreshenik	Noreshenik	Noreshenik	Noreshenik	Noreshenik
Area	Vein	Vein	Vein	Vein	Vein	Vein
SiO ₂	27.1129	26.4296	26.5815	26.7790	24.8498	26.7912
TiO ₂	0.0289	0.0336	0.0112	0.0000	0.0097	0.0150
Al ₂ O ₃	21.0851	21.2675	21.3485	21.0312	21.0457	21.0046
Cr ₂ O ₃	0.0556	0.0249	0.0629	0.0039	0.0112	0.0460
Fe ₂ O ₃	1.5124	0.9144	1.2962	1.1185	1.3632	1.1717
FeO	23.3248	24.3150	24.4744	23.6493	28.8140	23.6451
MnO	0.8377	0.8189	0.6743	0.7658	0.4779	0.8996
MgO	14.3346	14.4765	13.7551	14.7751	9.4896	14.4580
CaO	0.1438	0.1275	0.0744	0.0733	0.0434	0.1304
Na ₂ O	0.0052	0.0220	0.0400	0.0000	0.0375	0.0438
K ₂ O	0.0148	0.0056	0.0000	0.0167	0.0049	0.0049
H ₂ O*	11.5221	11.4787	11.4477	11.4898	10.8532	11.4747
TOTAL	99.9775	99.9138	99.7660	99.7024	97.0001	99.6849
Si	5.6194	5.5075	5.5476	5.5723	5.4679	5.5799
Al ^{IV}	2.3806	2.4925	2.4524	2.4277	2.5321	2.4201
Al ^{VI}	2.7930	2.7457	2.8201	2.7471	2.9501	2.7550
Ti	0.0045	0.0053	0.0017	0.0000	0.0016	0.0023
Cr	0.0092	0.0041	0.0104	0.0006	0.0019	0.0076
Fe ³⁺	0.2357	0.1435	0.2037	0.1752	0.2257	0.1836
Fe ²⁺	4.0434	4.2374	4.2717	4.1156	5.3025	4.1186
Mn	0.1471	0.1445	0.1192	0.1350	0.0891	0.1587
Mg	4.4294	4.4968	4.2789	4.5831	3.1127	4.4888
Ca	0.0320	0.0285	0.0166	0.0163	0.0102	0.0291
Na	0.0042	0.0178	0.0324	0.0000	0.0320	0.0354
K	0.0078	0.0030	0.0000	0.0088	0.0028	0.0026
OH*	16.0000	16.0000	16.0000	16.0000	16.0000	16.0000
Total	35.7063	35.8264	35.7547	35.7817	35.7286	35.7817
Fe/Fe+Mg	0.4914	0.4935	0.5113	0.4835	0.6398	0.4894
Chlorie T (°C)-Al ^{IV} ¹⁴ O	1.1903	1.2463	1.2262	1.2139	1.2660	1.2101
T (°C)-Cathelineau (1988)	321.3404	339.3552	332.8998	328.9217	345.7202	327.6994
Fe ⁺² (¹⁴ O)	2.0217	2.1187	2.1358	2.0578	2.6512	2.0593
Mg ⁺² (¹⁴ O)	2.2147	2.2484	2.1395	2.2915	1.5563	2.2444
Al ^{IV} (Jowett, 1991)	1.2380	1.2948	1.2762	1.2612	1.3291	1.2579
T (°C)-Jowett (1991)	325.9371	344.0372	338.1035	333.3171	354.9679	332.2774

Appendix 4: Fluid Inclusion Study

Appendix 4a: Fluid Inclusion Results

Fluid inclusion analyses was conducted by the author on selected vein samples. This appendix contains analytical data collected to identify minimum homogenization temperatures of precipitating minerals in each hydrothermal stage. Methodology and results are discussed in Chapter 4.

#	Assemblage	Sample Name	Mineral	Type	L %	V %	Morphology	Size (A-AXIS)	T(mice)	Th	Salinity	Sphalerite Color	Boiling Evidence
1	1	UGS_S011a	SPH	S	90	10	Tabular Elongated	6.82	N/A	109.6		Y	
2	2	UGS_S011a	SPH	S	90	10	Tabular Elongated	9.44	N/A	126		Y	Y
3	2	UGS_S011a	SPH	S	90	10	Tabular Elongated	5.65	N/A	114.7		Y	Y
4	3	UGS_S011a	QTZ	PS	90	10	Planar Elongated	8.75	N/A	124.9			
5	3	UGS_S011a	QTZ	PS	95	5	Planar Elongated	8.6	N/A	124.6			
6	4	UGS_S011a	SPH	S	90	10	Tabular Rounded	5.15	-11.2	135.3	15.17	Y	Y
7	4	UGS_S011a	SPH	S	95	5	Tabular Equant	3.54	-9	130.5	12.85	Y	Y
8	4	UGS_S011a	SPH	S	95	5	Tabular Equant	4.62	-8.2	133.2	11.93	Y	Y
9	5	UGS_S011a	SPH	S	90	10	Tabular Rounded	3.1	-8.5	152.9	12.28	Y	Y
10	5	UGS_S011a	SPH	S	90	10	Tabular Rounded	3.1	-8.4	144.7	12.16	Y	Y
11	5	UGS_S011a	SPH	S	90	10	Tabular Rounded	3.2	-8.5	143.2	12.28	Y	Y
12	5	UGS_S011a	SPH	S	90	10	Tabular Rounded	4.34	-9	148	12.85	Y	Y
13	6	UGS_S011a	QTZ	PS	90	10	Tabular Elongated	2	-3	150.6	4.96		
14	6	UGS_S011a	QTZ	PS	90	10	Tabular Equant	2.35	-2.5	139.9	4.18		
15	7	UGS_S011a	SPH	PS	90	10	Tabular Elongated	3.06	-3.8	136.1	6.16	Y	
16	7	UGS_S011a	SPH	PS	90	10	Tabular Elongated	3.2	-2.5	135.5	4.18	Y	
17	8	UGS_S011a	SPH	S	90	10	Tabular Equant	6.73	-8.2	148.2	11.93	Y	Y
18	9	UGS_S012b	QTZ	PS	90	10	Tabular Elongated		N/A	145.7			
19	10	UGS_S012b	QTZ	PS	90	10	Tabular Elongated		-3.5	108.9	5.71		
20	11	UGS_S012b	SPH	PS	90	10	Tabular Elongated	4.5	N/A	111		Y	
21	11	UGS_S012b	SPH	PS	90	10	Tabular Elongated	4.3	N/A	131.1		Y	
22	11	UGS_S012b	SPH	PS	90	10	Tabular Elongated	4.3	N/A	152.6		Y	
23	12	UGS_S012b	SPH	PS	85	15	Tabular Rounded	3.5	-2.5	283.5	4.18	HB	
24	12	UGS_S012b	SPH	PS	85	15	Tabular Rounded	4.33	-3	285.5	4.96	HB	
25	12	UGS_S012b	SPH	PS	85	15	Tabular Rounded	4.5	-3.1	287.7	5.11	HB	
26	13	UGS_S012b	SPH	PS	85	15	Tabular Rounded	4	-2.5	237	4.18	HB	
27	13	UGS_S012b	SPH	PS	80	20	Tabular Equant	5.04	-4.1	224.3	6.59	HB	
28	13	UGS_S012b	SPH	PS	90	10	Tabular Equant	3	N/A	234.1		HB	
29	13	UGS_S012b	SPH	PS	85	15	Tabular Rounded	-4.33	-2.7	191.7	4.49	Y	
30	14	UGS_S012b	SPH	PS	90	10	Tabular Elongated	7.49	-2.4	256.8	4.03	HB	
31	14	UGS_S012b	SPH	PS	85	15	Tabular Elongated	7.84	-2.5	261.4	4.18	HB	
32	14	UGS_S012b	SPH	PS	90	10	Tabular Elongated	4.66	N/A	276.5		HB	
33	15	UGS_S012b	SPH	PS	90	10	Tabular Equant	2.12	-3.1	179.9	5.11	Y	

	Assemblage	Sample Name	Mineral	Type	L %	V %	Morphology	Size (A-AXIS)	T _(mice)	Th	Salinity	Sphalerite Color	Boiling Evidence
34	16	UGS_S012b	QTZ	PS	90	10	Tabular Equant	7.96	-3.1	178.1	5.11		
35	16	UGS_S012b	QTZ	PS	90	10	Equant Planar	3.68	-2	162.1	3.39		
36	16	UGS_S012b	QTZ	PS	85	15	Tabular Rounded	4.53	-3.7	161.2	6.01		
37	16	UGS_S012b	QTZ	PS	90	10	Equant Planar	5.11	-2.3	164.3	3.87		
38	17	UGS_S012b	CAL	I	90	10	Equant Planar	6.95	-2.2	147.1	3.71		
39	17	UGS_S012b	CAL	I	90	10	Equant Planar	17.18	-2	153.6	3.39		
40	18	UGS_S012b	SPH	PS	90	10	Angular	5.53	-2.7	185.1	4.49	Y	
41	19	UGS_S012b	SPH	PS	90	10	Angular	2.94	-2.3	239.5	3.87	Y	
42	19	UGS_S012b	SPH	PS	90	10	Angular	3.6	-2.5	239.1	4.18	Y	
43	19	UGS_S012b	SPH	PS	90	10	Angular	5.54	-1.9	239.8	3.23	Y	
44	19	UGS_S012b	SPH	PS	90	10	Angular	3.68	-2.2	240	3.71	Y	
45	19	UGS_S012b	SPH	PS	90	10	Angular	2.67	-2.1	239	3.55	Y	
46	20	UGS_S012b	QTZ	I	90	10	Angular	1.78	-3.1	168.5	5.11		
47	21	UGS_S012b	CAL	I	90	10	Angular	1.98	-1.98	122.6	3.36		
48	22	UGS_S012b	CAL	I	90	10	Angular	3.87	-0.9	106.1	1.57		
49	23	UGS_S012b	SPH	PS	90	10	Tabular Equant	3.38	-3.2	251.3	5.26	HB	
50	23	UGS_S012b	SPH	PS	90	10	Tabular Equant	6.72	-3.5	257	5.71	HB	
51	23	UGS_S012b	SPH	PS	90	10	Tabular Equant	11.24	-2.9	255.7	4.80	HB	
52	23	UGS_S012b	SPH	PS	90	10	Tabular Equant	3.9	-2.9	249.9	4.80	HB	
53	24	UGS_S012b	SPH	PS	90	10	Tabular Equant	7.72	-3.5	170.7	5.71	HB	
54	25	2014_UGS_S012A	QTZ	PS	90	10	Tabular	4.1	-2.1	128.9	3.55		
55	25	2014_UGS_S012A	QTZ	PS	90	10	Tabular	4.1	-2	131.4	3.39		
56	25	2014_UGS_S012A	QTZ	PS	90	10	tabular	4.4	-1.9	131.5	3.23		
57	25	2014_UGS_S012A	QTZ	PS	90	10	Tabular	4.6	-2.2	130.2	3.71		
58	25	2014_UGS_S012A	QTZ	PS	90	10	Tabular	4.8	-2.1	131.1	3.55		
59	25	2014_UGS_S012A	QTZ	PS	90	10	Tabular	4.2	-2	129.9	3.39		
60	26	2014_UGS_S012A	SPH	I	90	10	Tabular Equant	4.1	-3.4	154.4	5.56	Y	
61	26	2014_UGS_S012A	SPH	I	90	10	Tabular Equant	4.2	-3.1	148.5	5.11	Y	
62	27	2014_UGS_S012A	QTZ	I	90	10	Tabular Equant	3.2	-2.5	138.5	4.18		
63	27	2014_UGS_S012A	QTZ	I	90	10	Tabular Equant	5.72	-2.7	148.9	4.49		
64	27	2014_UGS_S012A	QTZ	I	90	10	Tabular Equant	4.1	-3.1	137.8	5.11		
65	27	2014_UGS_S012A	QTZ	I	90	10	Tabular Equant	3.1	-3	140.1	4.96		
66	28	2014_UGS_S012A	CAL	I	90	10	Tabular Equant	4.2	-2	146.4	3.39		

	Assemblage	Sample Name	Mineral	Type	L %	V %	Morphology	Size (A-AXIS)	T(mic)	Th	Salinity	Sphalerite Color	Boiling Evidence
67	28	2014_UGS_S012A	CAL	I	90	10	Tabular Equant	3.8	-2.1	138.5	3.55		
68	29	2014_UGS_S012A	CAL	PS	90	10	Tabular Rounded	7.41	-1.7	145.2	2.90		
69	29	2014_UGS_S012A	CAL	PS	90	10	Tabular Rounded	2.3	-1.9	130.7	3.23		
70	29	2014_UGS_S012A	CAL	PS	90	10	Tabular Rounded	3.29	-2	132.8	3.39		
71	29	2014_UGS_S012A	CAL	PS	90	10	Tabular Rounded	2.56	-1.6	133.9	2.74		
72	29	2014_UGS_S012A	CAL	PS	90	10	Tabular Rounded	2.85	-1.75	135.5	2.98		
73	29	2014_UGS_S012A	CAL	PS	90	10	Tabular Rounded	4.23	-1.85	137	3.15		
74	30	2014_UGS_S012A	CAL	I	90	10	Equant Planar	4.5	-2.5	144.6	4.18		
75	30	2014_UGS_S012A	CAL	I	90	10	Equant Planar	4.02	-2.3	142	3.87		
76	31	2014_UGS_S012A	CAL	I	90	10	Tabular Equant	8.51	-2.4	129.9	4.03		
77	31	2014_UGS_S012A	CAL	I	90	10	Tabular Equant	4.25	N/A	128.1			
78	33	2014_UGS_S012A	CAL	I	85	15	Equant Planar	4.46	-2.8	78.4	4.65		
79	34	2014_UGS_S012A	QTZ	I	90	10	Tabular Equant	2.9	-2.1	229.4	3.55		
80	34	2014_UGS_S012A	QTZ	I	90	10	Tabular Equant	3	-2.3	210.9	3.87		
81	35	2014_UGS_S012A	QTZ	I	90	10	Tabular Rounded	3.4	-2.1	156.6	3.55		
82	35	2014_UGS_S012A	QTZ	I	90	10	Tabular Rounded	3.29	-2.4	167	4.03		
83	36	2014_UGS_S012A	CAL	PS	90	10	Equant Planar	5.63	-2.4	135.7	4.03		
84	36	2014_UGS_S012A	CAL	PS	90	10	Equant Planar	5.2	-2.3	141.3	3.87		
85	37	2014_UGS_S012A	QTZ	I	90	10	Tabular Rounded	5.62	-2	190.9	3.39		
86	38	2014_UGS_S012A	SPH	PS	90	10	Tabular Rounded	5.86	-1.5	133	2.57	Y	
87	38	2014_UGS_S012A	SPH	PS	90	10	Tabular Rounded	4.31	-2	132.8	3.39	Y	
88	38	2014_UGS_S012A	SPH	PS	90	10	Tabulae Rounded	3.84	-1.8	132.4	3.06	Y	
89	39	2014_UGS_S012A	SPH	PS	85	15	Tabular Equant	4.21	-3.6	212.7	5.86	HB	
90	39	2014_UGS_S012A	SPH	PS	85	15	Tabular Equant	4.1	-3.5	211.8	5.71	HB	
91	39	2014_UGS_S012A	SPH	PS	85	15	Tabular Equant	4.9	-3.4	243.2	5.56	HB	
92	40	2014_UGS_S012A	SPH	PS	95	5	Tabular Equant	7.32	-2	132.1	3.39	Y	
93	40	2014_UGS_S012A	SPH	PS	95	5	Tabular Equant	4.32	-2.1	136.2	3.55	Y	
94	41	2014_UGS_S012A	SPH	PS	85	15	Tabular Equant	12.04	-4	229.2	6.45	Y	
95	41	2014_UGS_S012A	SPH	PS	85	15	Tabular Equant	5.07	-3	222.6	4.96	Y	
96	42	2014_UGS_S012A	SPH	PS	85	15	Tabular Equant	8.23	-3.2	199.2	5.26	Y	
97	43	2014_UGS_S012A	SPH	PS	80	20	Tabular Equant	12.21	-3.3	259.2	5.41	Y	
98	43	2014_UGS_S012A	SPH	PS	90	10	Tabular Equant	4.2	-3.1	240.4	5.11	Y	
99	44	2014_UGS_S012A	SPH	S	95	5	Tabular Equant	5.18	-6.9	134.4	10.36	HB	Y

	Assemblage	Sample Name	Mineral	Type	L %	V %	Morphology	Size (A-AXIS)	T(mice)	Th	Salinity	Sphalerite Color	Boiling Evidence
100	44	2014_UGS_S012A	SPH	S	95	5	Tabular Equant	4.02	-7.1	139.2	10.61	HB	Y
101	44	2014_UGS_S012A	SPH	S	95	5	Tabular Equant	3.59	-6.9	129.2	10.36	HB	Y
102	44	2014_UGS_S012A	SPH	S	95	5	Tabular Equant	3.9	-7	131.5	10.49	HB	Y
103	45	2014_UGS_S012A	SPH	PS	90	10	Tabular Equant	5.4	-4.8	250.8	7.59	Y	
104	45	2014_UGS_S012A	SPH	PS	90	10	Tabular Equant	4.61	-3.6	228.8	5.86	Y	
105	45	2014_UGS_S012A	SPH	PS	90	10	Tabular Equant	4.81	-3.8	226.3	6.16	Y	
106	46	2014_UGS_S008	SPH	S	85	15	Tabular Rounded	6.83	-5.8	116.2	8.95	HB	Y
107	46	2014_UGS_S008	SPH	S	95	5	Tabular Rounded	2.21	-6	118.1	9.21	HB	Y
108	46	2014_UGS_S008	SPH	S	90	10	Tabular Rounded	4.28	-5.5	113.1	8.55	HB	Y
109	47	2014_UGS_S008	SPH	S	90	10	Tabular Rounded	3.3	-5.3	133.2	8.28	HB	Y
110	47	2014_UGS_S008	SPH	S	90	10	Tabular Rounded	5.95	-5.5	124.3	8.55	HB	Y
111	48	2014_UGS_S008	QTZ	PS	90	10	Tabular Rounded	3.56	-3.9	139.9	6.30		
112	48	2014_UGS_S008	QTZ	PS	90	10	Tabular Rounded	2.26	-3.5	130.2	5.71		
113	48	2014_UGS_S008	QTZ	PS	95	5	Tabular Rounded	2.04	N/A	126.7			
114	48	2014_UGS_S008	QTZ	PS	90	10	Tabular Rounded	3.27	N/A	123.2			
115	49	2014_UGS_S008	QTZ	PS	90	10	Tabular Equant	2.75	-3.4	144.2	5.56		
116	49	2014_UGS_S008	QTZ	PS	90	10		2.43	-3.3	148.3	5.41		
117	49	2014_UGS_S008	QTZ	PS	90	10		3.12	-3.5	147.9	5.71		
118	50	2014_UGS_S008	SPH	P	80	20	Tabular Rounded	4.03	-3.4	259.7	5.56	HB	
119	50	2014_UGS_S008	SPH	P	90	10	Tabular Rounded	3.33	-3.5	240.5	5.71	HB	
120	50	2014_UGS_S008	SPH	P	80	20	Tabular Rounded	4.44	-3.7	254.6	6.01	HB	
121	51	2014_UGS_S008	SPH	P	90	10	Tabular Rounded	3.35	-3.5	223.5	5.71	HB	
122	52	2014_UGS_S008	SPH	PS	90	10	Tabular Rounded	7.03	-3	169.1	4.96	Y	
123	53	2014_UGS_S008	SPH	PS	90	10	Tabular Rounded	3.2	-4.1	145.8	6.59	Y	
124	54	2014_UGS_S008	QTZ	PS	85	15	Tabular Rounded	4.37	-3.8	150.1	6.16		
125	54	2014_UGS_S008	QTZ	PS	90	10	Tabular Rounded	2.33	N/A	148.5			
126	54	2014_UGS_S008	QTZ	PS	90	10	Tabular Rounded	5.2	-3.6	141.2	5.86		
127	54	2014_UGS_S008	QTZ	PS	85	15	Tabular Rounded	3.2	-3.5	143.4	5.71		
128	54	2014_UGS_S008	QTZ	PS	90	10	Tabular Rounded	2.5	-3.4	142.3	5.56		
129	54	2014_UGS_S008	QTZ	PS	85	15	Tabular Rounded	2.8	-3.6	144.2	5.86		
130	54	2014_UGS_S008	QTZ	PS	90	10	Tabular Rounded	3	-3.7	141.3	6.01		
131	55	2014_UGS_S008	QTZ	PS	90	10	Tabular Rounded	3.27	N/A	137.3			
132	55	2014_UGS_S008	QTZ	PS	90	10	Tabular Rounded	3.94	-2.6	146.8	4.34		

	Assemblage	Sample Name	Mineral	Type	L %	V %	Morphology	Size (A-AXIS)	T(mice)	Th	Salinity	Sphalerite Color	Boiling Evidence
133	55	2014_UGS_S008	QTZ	PS	90	10	Tabular Rounded	4.9	-2.8	147.2	4.65		
134	55	2014_UGS_S008	QTZ	PS	90	10	Tabular Rounded	3.66	N/A	144.8			
135	55	2014_UGS_S008	QTZ	PS	90	10	Tabular Rounded	2.37	-2.5	145.2	4.18		
136	55	2014_UGS_S008	QTZ	PS	90	10	Tabular Rounded	3.62	-2.9	148.3	4.80		
137	56	2014_UGS_S008	QTZ	I	90	10	Equant Planar	5.32	-3.6	146.7	5.86		
138	57	2014_UGS_S008	QTZ	PS	90	10		5.11	-3.6	147.6	5.86		
139	57	2014_UGS_S008	QTZ	PS	90	10		6.65	-3.5	147.3	5.71		
140	57	2014_UGS_S008	QTZ	PS	90	10		5.56	-3.5	146.9	5.71		
141	57	2014_UGS_S008	QTZ	PS	90	10		6.42	-3.7	148.1	6.01		
142	57	2014_UGS_S008	QTZ	PS	90	10		2.99	-3.6	147.8	5.86		
143	57	2014_UGS_S008	QTZ	PS	90	10		4.47	-4.2	153.2	6.74		
144	57	2014_UGS_S008	QTZ	PS	90	10		3.61	-4	150.1	6.45		
145	58	2014_UGS_S008	SPH	PS	90	10	Tabular Elongated	24.19	-3.5	190.4	5.71	Y	
146	58	2014_UGS_S008	SPH	PS	90	10	Tabular Elongated	16.16	-3.2	181.8	5.26	Y	
147	59	2014_UGS_S008	SPH	P-I	80	20	Prismatic Elongated	23.29	-3.1	214.9	5.11	HB	
148	59	2014_UGS_S008	SPH	P-I	80	20	Prismatic Elongated	21.61	-3.3	219.9	5.41	HB	
149	59	2014_UGS_S008	SPH	P-I	80	20	Prismatic Elongated	22.2	-3.3	206.3	5.41	HB	
150	59	2014_UGS_S008	SPH	P-I	90	10	Prismatic Elongated	18.34	-3.7	167.4	6.01	Y	
151	59	2014_UGS_S008	SPH	P-I	90	10	Prismatic Elongated	15.28	-3.5	199.7	5.71	Y	
152	59	2014_UGS_S008	SPH	P-I	80	20	Prismatic Elongated	28.32	-2.9	182.4	4.80	Y	
153	59	2014_UGS_S008	SPH	P-I	70	30	Prismatic Elongated	28.17	-4	181.9	6.45	Y	
154	59	2014_UGS_S008	SPH	P-I	80	20	Prismatic Elongated	29.4	-3.7	177.5	6.01	Y	
155	59	2014_UGS_S008	SPH	P-I	80	20	Prismatic Elongated	24.1	-3.1	183.1	5.11	Y	
156	60	2014_UGS_S008	SPH	PS	90	10	Tabular Rounded	4.79	-3.7	176.2	6.01	Y	
157	60	2014_UGS_S008	SPH	PS	90	10	Tabular Rounded	6.68	-3.8	174.2	6.16	Y	
158	60	2014_UGS_S008	SPH	PS	90	10	Tabular Rounded	7.22	-3.3	171.1	5.41	Y	
159	60	2014_UGS_S008	SPH	PS	90	10	Tabular Rounded	7.86	-2.9	179.2	4.80	Y	
160	61	2014_UGS_S012b	CAL	I	90	10	Planar Equant	7.94	-2.3	128.8	3.87		
161	61	2014_UGS_S012b	CAL	I	90	10	Planar Equant	3.83	-2.1	128.4	3.55		
162	62	2014_UGS_S012b	QTZ	PS	90	10	Tabular Rounded	4.19	-3.1	146.5	5.11		
163	62	2014_UGS_S012b	QTZ	PS	90	10	Tabular Rounded	4.58	-3	147.1	4.96		
164	62	2014_UGS_S012b	QTZ	PS	90	10	Tabular Rounded	2.67	-3.1	146.9	5.11		
165	62	2014_UGS_S012b	QTZ	PS	90	10	Tabular Rounded	5.7	-3	145.7	4.96		

	Assemblage	Sample Name	Mineral	Type	L %	V %	Morphology	Size (A-AXIS)	T _(mice)	Th	Salinity	Sphalerite Color	Boiling Evidence
166	62	2014_UGS_S012b	QTZ	PS	90	10	Tabular Rounded	4.53	-2.9	141.1	4.80		
167	62	2014_UGS_S012b	QTZ	PS	90	10	Tabular Rounded	5.02	-3.3	137.3	5.41		
168	63	2014_UGS_S012b	CAL	PS	90	10	Tabular Rounded	8.72	-1.9	128.9	3.23		
169	63	2014_UGS_S012b	CAL	PS	90	10	Tabular Rounded	4.21	-2	134.2	3.39		
170	63	2014_UGS_S012b	CAL	PS	90	10	Tabular Rounded	3.29	-2	138.2	3.39		
171	64	2014_UGS_S012b	CAL	I	80	20	Planar	3.02	-2	88.9	3.39		
172	64	2014_UGS_S012b	CAL	I	85	15	Planar	2.36	-2.1	90.2	3.55		
173	64	2014_UGS_S012b	CAL	I	80	20	Planar	2.97	-2.1	88.3	3.55		
174	65	2014_UGS_S012b	CAL	PS	90	10	Planar Rounded	3.31	-2.4	127.3	4.03		
175	65	2014_UGS_S012b	CAL	PS	90	10	Planar Rounded	2.35	-2.8	128.9	4.65		
176	65	2014_UGS_S012b	CAL	PS	90	10	Planar Rounded	3.29	-2.8	127.9	4.65		
177	65	2014_UGS_S012b	CAL	PS	90	10	Planar Rounded	5.45	-2.4	125.4	4.03		
178	65	2014_UGS_S012b	CAL	PS	90	10	Planar Rounded	3.29	-2.2	128.3	3.71		
179	65	2014_UGS_S012b	CAL	PS	90	10	Planar Rounded	3.8	N/A	123.5			
180	66	2014_UGS_S012b	QTZ	I	90	10	Planar Rounded	4.47	-2.9	143	4.80		
181	66	2014_UGS_S012b	QTZ	I	90	10	Planar Rounded	3.76	-2.8	141.2	4.65		
182	67	2014_UGS_S012b	SPH	PS	90	10	Tabular Rounded	5.71	-3.1	139.6	5.11	Y	
183	67	2014_UGS_S012b	SPH	PS	90	10	Tabular Rounded	4.78	-3	139.9	4.96	Y	
184	67	2014_UGS_S012b	SPH	PS	90	10	Tabular Rounded	4.32	-3.1	141.8	5.11	Y	
185	68	2014_UGS_S006	QTZ	I	90	10	Planar Equant	4.66	-3.3	212.5	5.41		
186	68	2014_UGS_S006	QTZ	I	80	20	Planar Equant	3.92	-3.5	201.9	5.71		
187	68	2014_UGS_S006	QTZ	I	90	10	Planar Equant	2.93	-3.3	205.3	5.41		
188	68	2014_UGS_S006	QTZ	I	90	10	Planar Equant	3.05	-3.2	199.6	5.26		
189	69	2014_UGS_S006	QTZ	I	90	10	Planar Rounded	4.48	-3.1	271.2	5.11		
190	69	2014_UGS_S006	QTZ	I	90	10	Planar Rounded	4.24	-2.9	278.9	4.80		
191	70	2014_UGS_S006	SPH	PS	90	10	Tabular Rounded	4.94	-3.4	258.4	5.56	HB	
192	70	2014_UGS_S006	SPH	PS	90	10	Tabular Rounded	4.02	-3.6	260.1	5.86	HB	
193	70	2014_UGS_S006	SPH	PS	85	15	Tabular Rounded	3.77	-3.6	257.2	5.86	HB	
194	71	2014_UGS_S006	SPH	P	85	15	Prismatic Elongated	27.18	-3.3	242.3	5.41	HB	
195	71	2014_UGS_S006	SPH	P	80	20	Prismatic Elongated	13.9	-3.6	230.3	5.86	HB	
196	71	2014_UGS_S006	SPH	P	80	20	Prismatic Elongated	10.82	-3.5	232.3	5.71	HB	
197	71	2014_UGS_S006	SPH	P	75	25	Prismatic Elongated	8.5	-3.2	245.1	5.26	HB	
198	72	2014_UGS_S006	SPH	P	75	25	Prismatic	5.94	-3.2	272.2	5.26	HB	

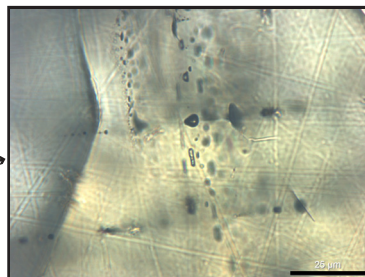
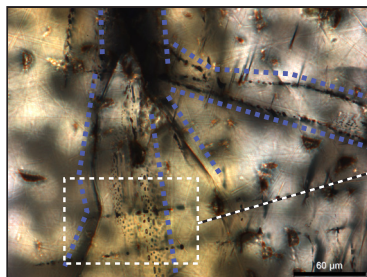
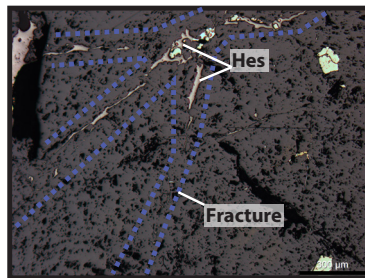
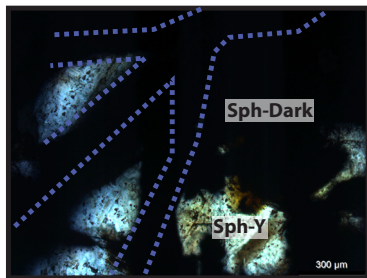
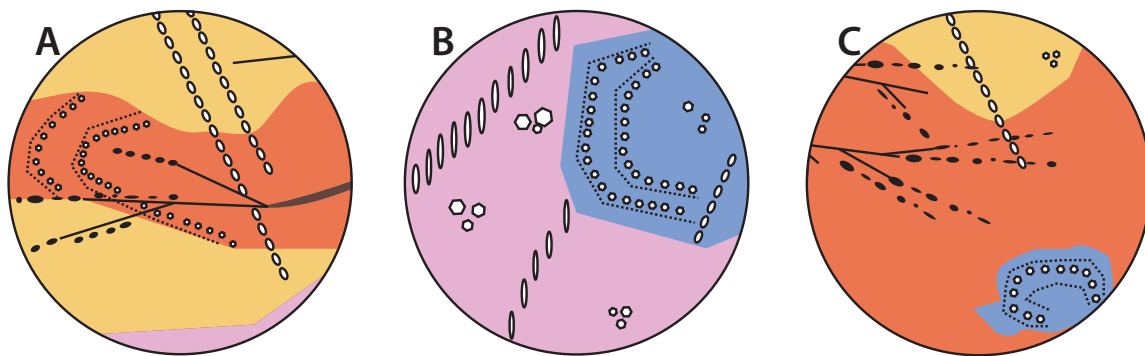
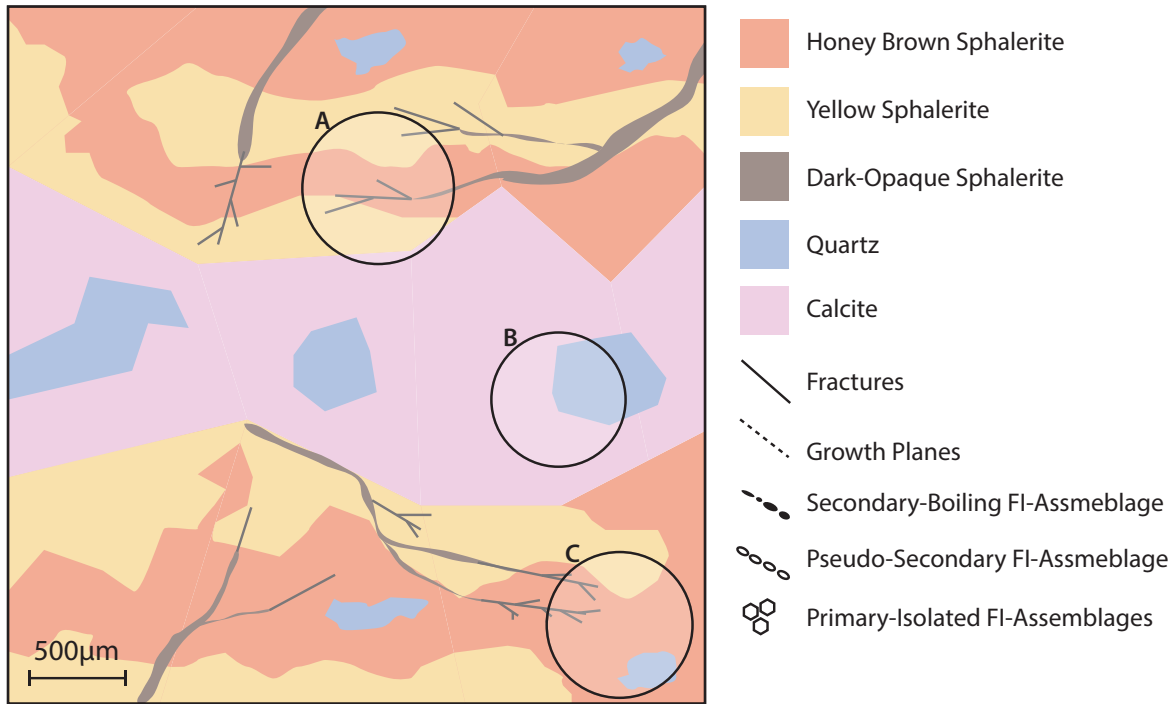
	Assemblage	Sample Name	Mineral	Type	L %	V %	Morphology	Size (A-AXIS)	T(m _{lce})	Th	Salinity	Sphalerite Color	Boiling Evidence
199	72	2014_UGS_S006	SPH	P	90	10	Prismatic	3.48	-3.3	269.8	5.41	HB	
200	73	2014_UGS_S006	SPH	PS	85	15	Prismatic	6.35	-3.7	277.7	6.01	HB	
201	73	2014_UGS_S006	SPH	PS	90	10	Prismatic	3.58	-3.4	275.6	5.56	HB	
202	73	2014_UGS_S006	SPH	PS	85	15	Prismatic	11.12	-3.5	298.2	5.71	HB	
203	73	2014_UGS_S006	SPH	PS	85	15	Prismatic	8.94	-3.2	272.6	5.26	HB	
204	73	2014_UGS_S006	SPH	PS	90	10	Prismatic	7.35	-3.4	278.1	5.56	HB	
205	73	2014_UGS_S006	SPH	PS	90	10	Prismatic	3.47	-3.6	267.9	5.86	HB	
206	74	2014_UGS_S006	SPH	S	90	10	Tabular Rounded	2.34	N/A			HB	Y
207	74	2014_UGS_S006	SPH	S	90	10	Tabular Rounded	2.87	N/A			HB	Y
208	74	2014_UGS_S006	SPH	S	90	10	Tabular Rounded	3.22	N/A			HB	Y
209	75	2014_UGS_S006	SPH	S	90	10	Tabular Rounded	2.93	N/A			HB	Y
210	75	2014_UGS_S006	SPH	S	90	10	Tabular Rounded	3.56	N/A			HB	Y

Bin	Sphalerite HB	Boiling	Quartz	Stage 3 Carbonate	Spahlerite Y
0	0	0	0	0	0
2	0	0	0	1	0
4	0	0	12	22	9
6	34	0	41	8	23
8	3	0	7	0	10
10	0	5	0	0	0
12	0	6	0	0	0
14	0	5	0	0	0
16	0	1	0	0	0
>16	0	0	0	0	0
Total	37	17	60	31	42

Bin	Sphalerite HB	Boiling	Quartz	Stage 3 Carbonate	Spahlerite Y
50	0	0	0	0	0
70	0	0	0	1	0
100	0	0	1	4	1
120	0	7	6	12	1
140	0	11	41	15	13
160	0	1	10	1	4
180	1	0	1	0	11
200	1	0	4	0	4
220	6	0	3	0	4
240	9	0	0	0	6
260	12	0	0	0	2
280	9	0	2	0	0
300	1	0	0	0	0
>300	0	0	0	0	0
Total	39	19	68	33	46

Appendix 4b: Fluid Inclusion Petrography

Fluid inclusion petrography was conducted by the author on selected vein samples prior to microthermometric measurements. This appendix contains observational data used to identify fluid inclusion assemblages as discussed in Chapter 4.



Summary of Observed Fluid Inclusion Assemblages

Mineral	Fluid Inclusion Type	Observed Frequency	Liquid %	Vapor %	Solid %	Boiling (Y/N)	Inclusion Minerals	Comments
Quartz	Isolated	C	90-95	10-5	0	N		
	Pseudo-Secondary	C	90-95	10-5	0	N		
Honey Brown Sphalerite	Primary 1	A	0	0	100	N	Cpy	
	Primary 2	VR	85-95	15-5	0	N		
	Pseudo Secondary	C	90-95	10-5	0	N		
	Secondary 1	R	5-0	95-100	0	Y		Within same trail
	Secondary 2	R	85-95	15-5	0	Y		
Yellow Sphalerite	Primary	VR	85-95	15-5	0	N		
	Pseudo Secondary	C	90-95	10-5	0	N		
	Secondary 1	R	0-5	95-100	0	Y		Within same trail
	Secondary 2	R	85-95	15-5	0	Y		
Dark Sphalerite	Primary	A	0	0	100	N	Cpy	
Calcite	Isolated	C	90-95	10-5	0	N		
	Pseudo-Secondary	R	90-95	10-5	0	N		

Appendix 5: Underground Vein Maps

Underground vein maps were produced by author during the 2013-2014 field season. All underground mapping was conducted at a 1:100 scale and show drift backs. All measured structural features are shown on map and are formatted to dip direction/dip.

South Zone: Vein 17 Level 690

Legend

- Quartz-Carbonate (calcite)
- Sphalerite-Chalcopyrite-Pyrite
- Breccia
- Crustiform
- Gabbro

- | | |
|---------------|----------------|
| Zn (%) | Au(ppm) |
| ■ <1% | ● <1ppm |
| ■ <1-5% | ● <1-5ppm |
| ■ <5-10% | ● <5-10ppm |
| ■ >10% | ● >10ppm |

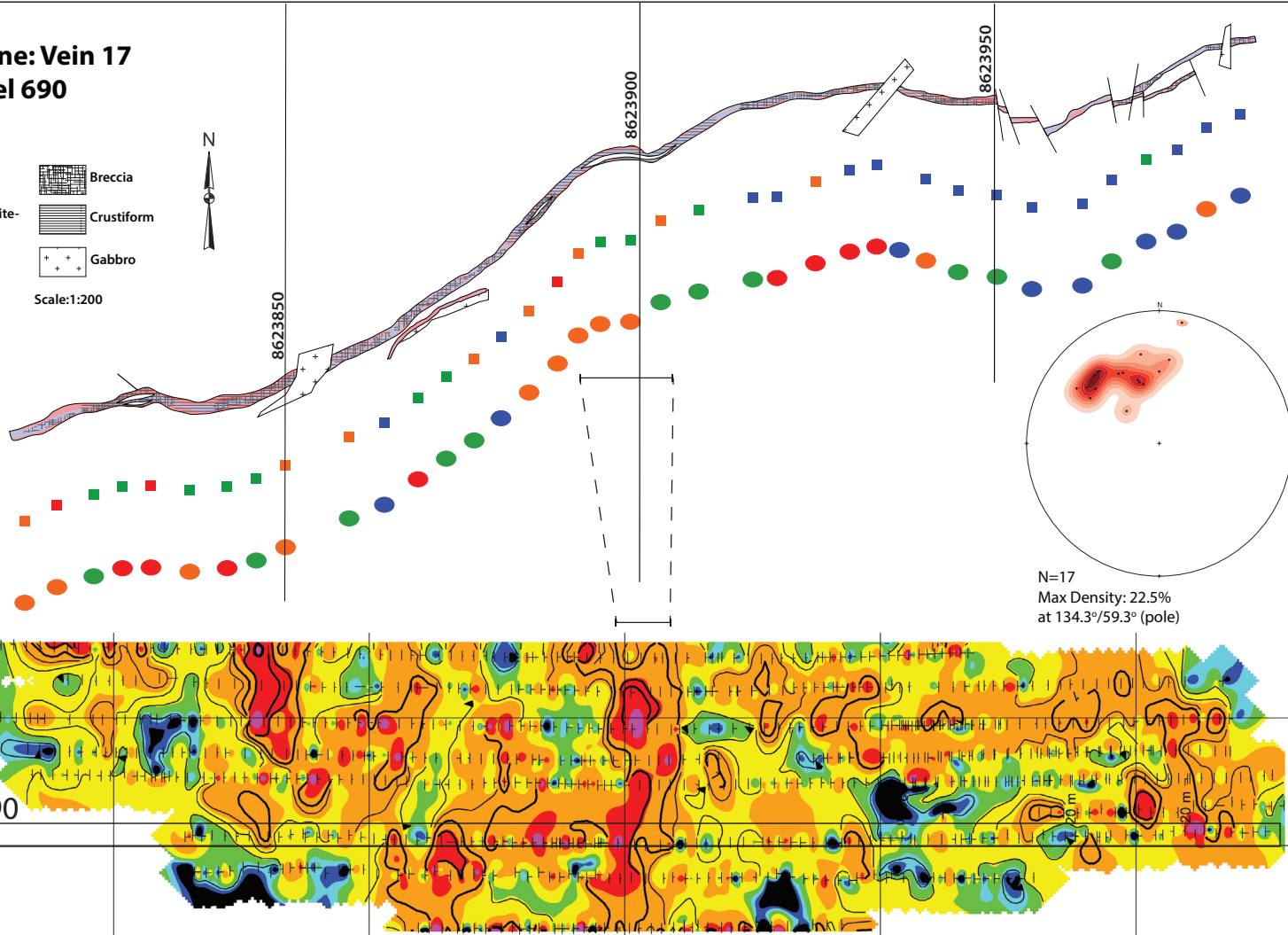
Scale: 1:200



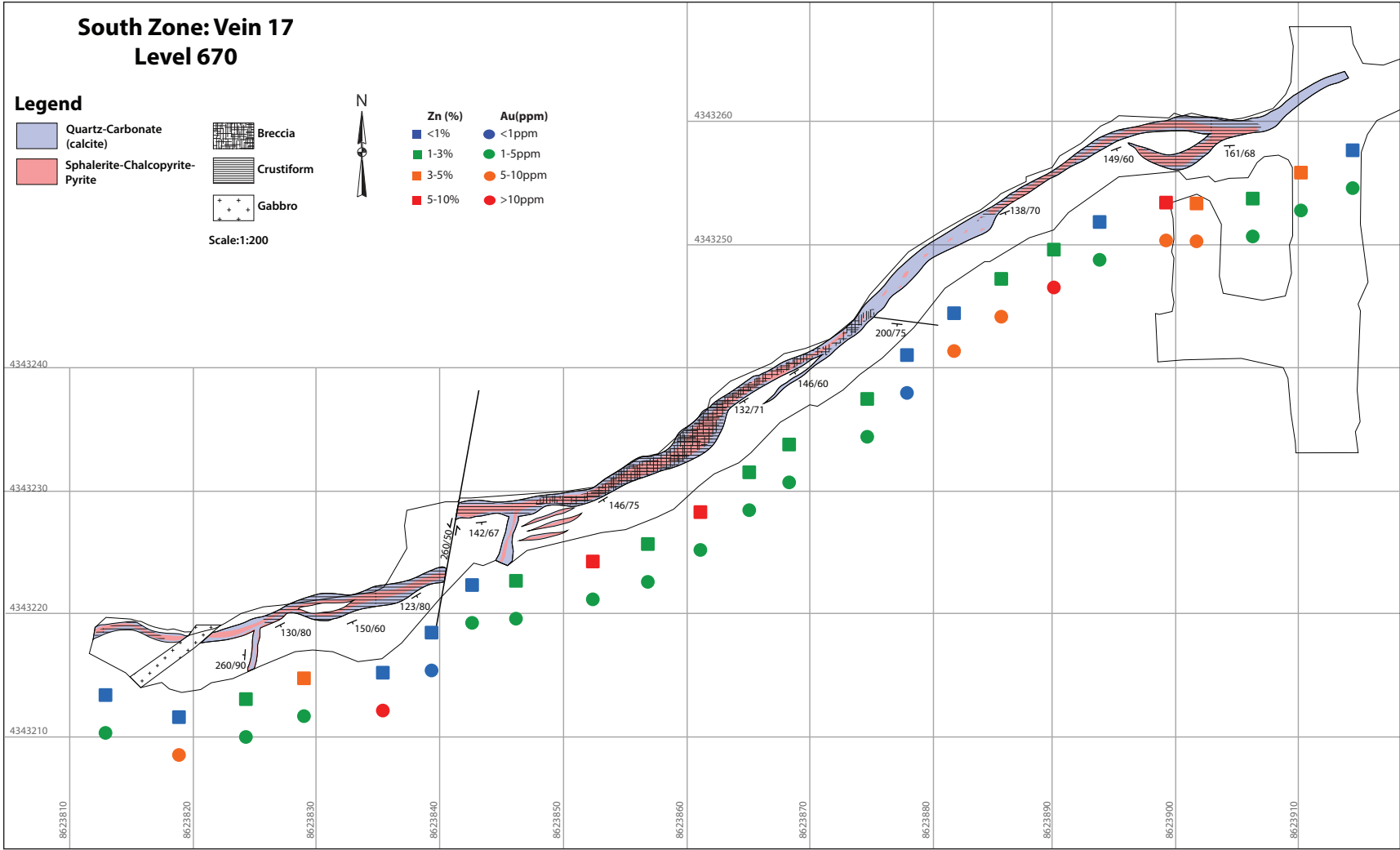
Zinc Assay (%)

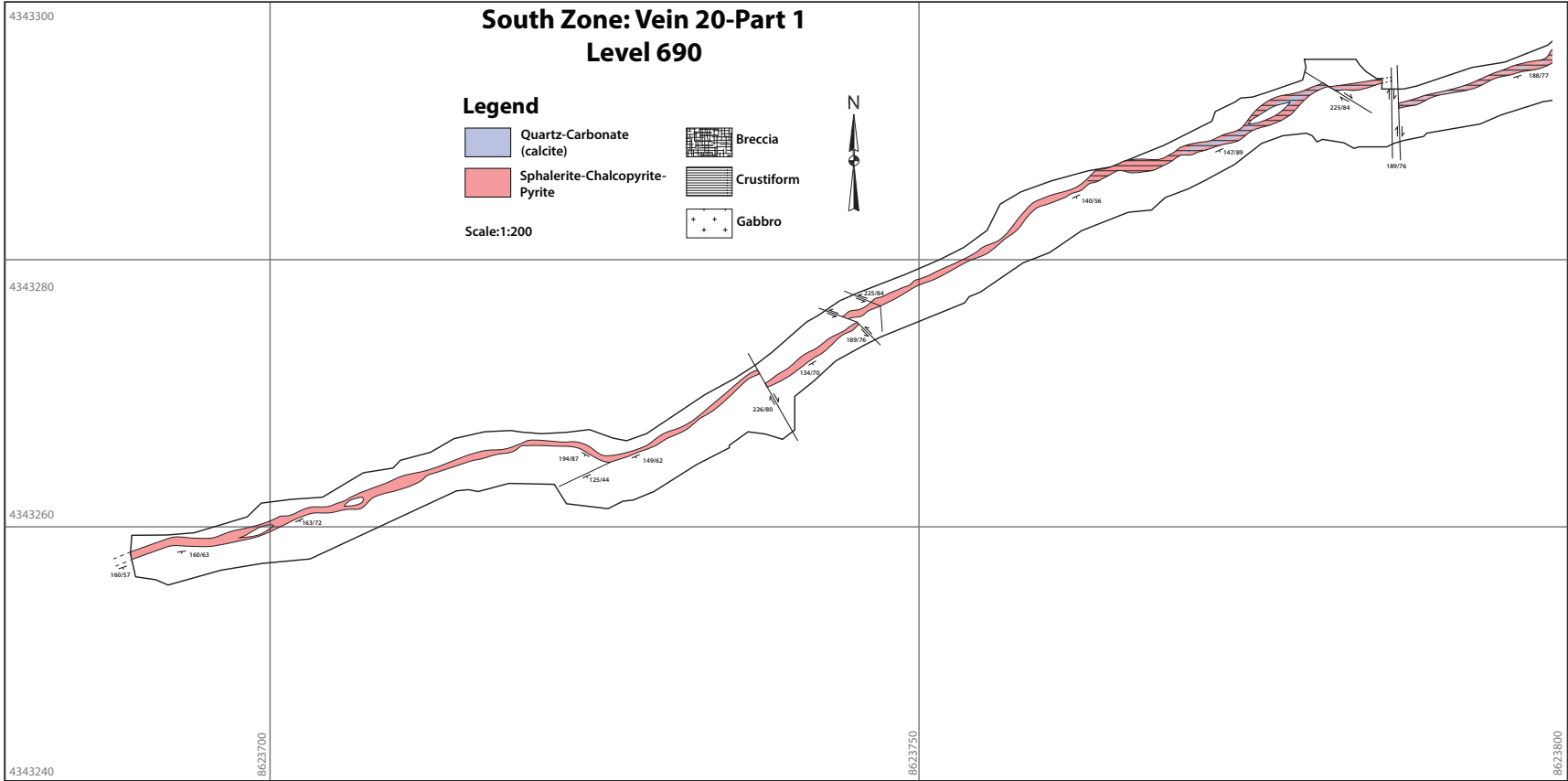
Au Assay (ppm)

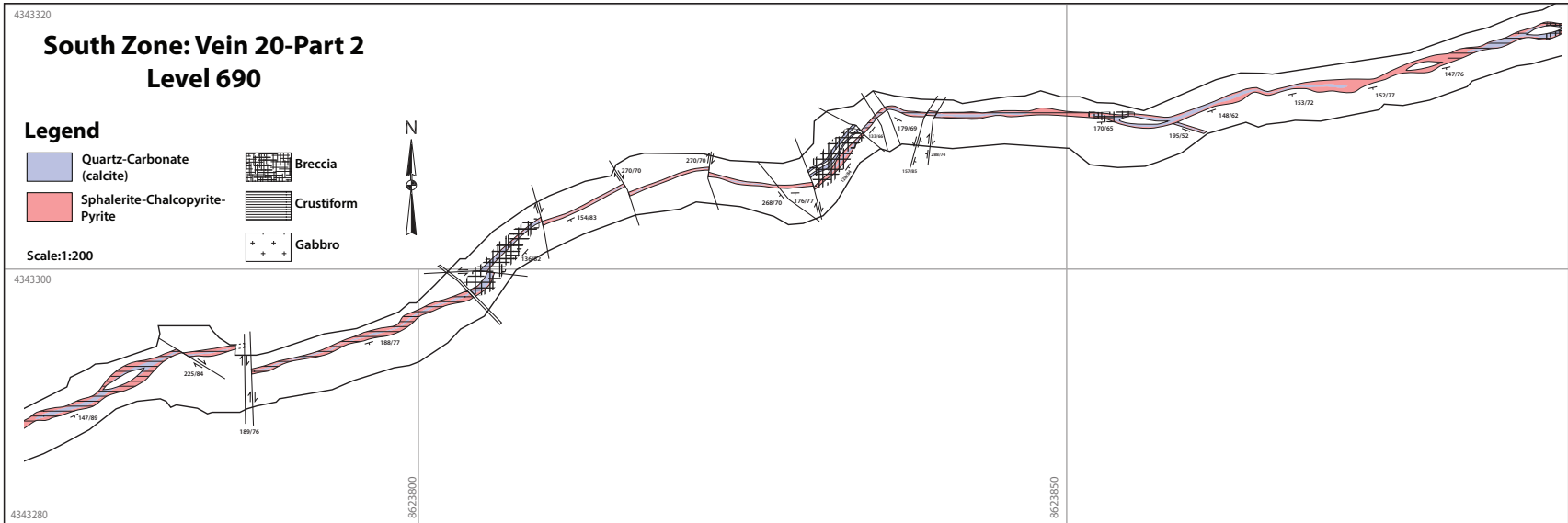
Level 690

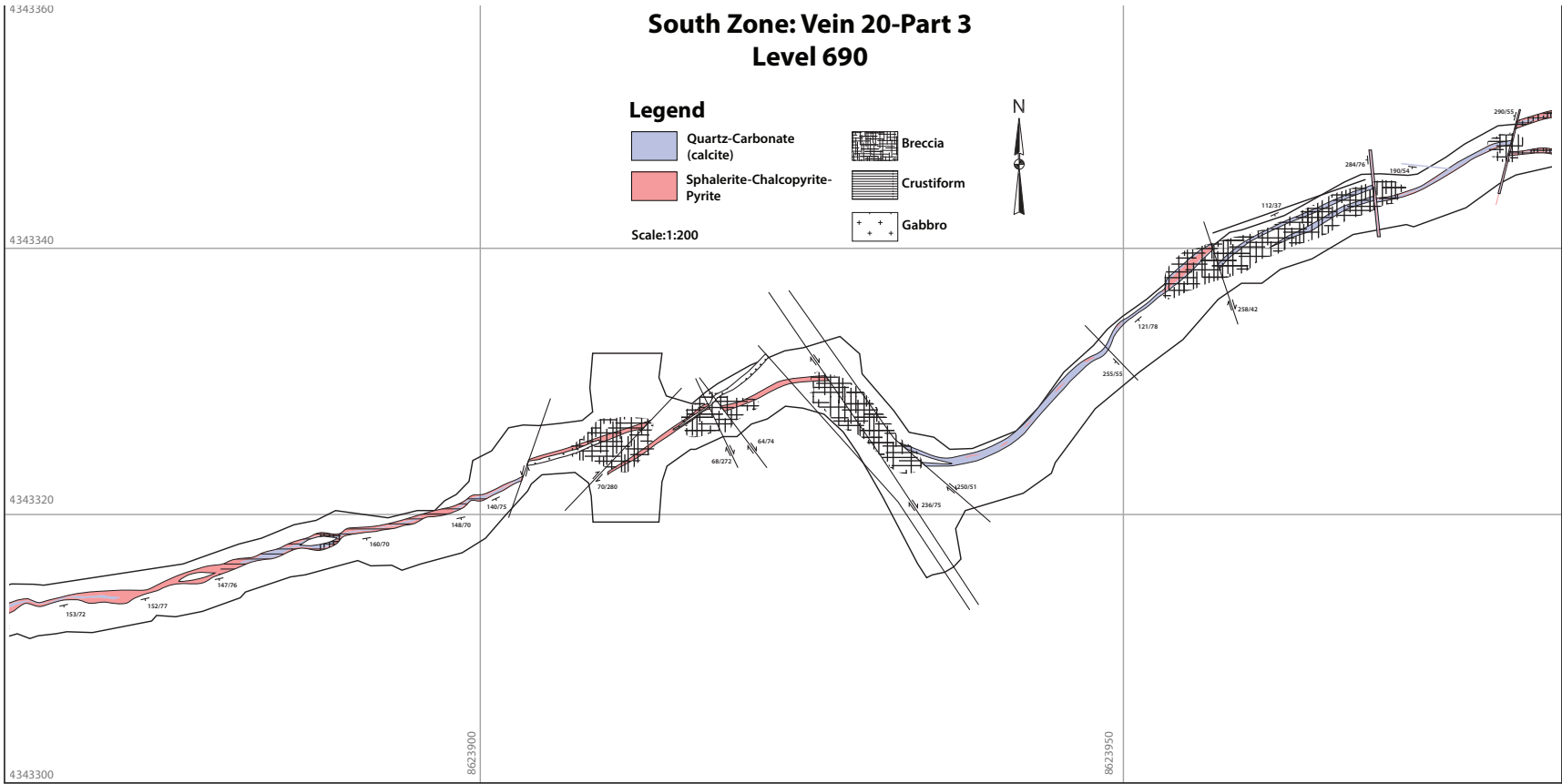


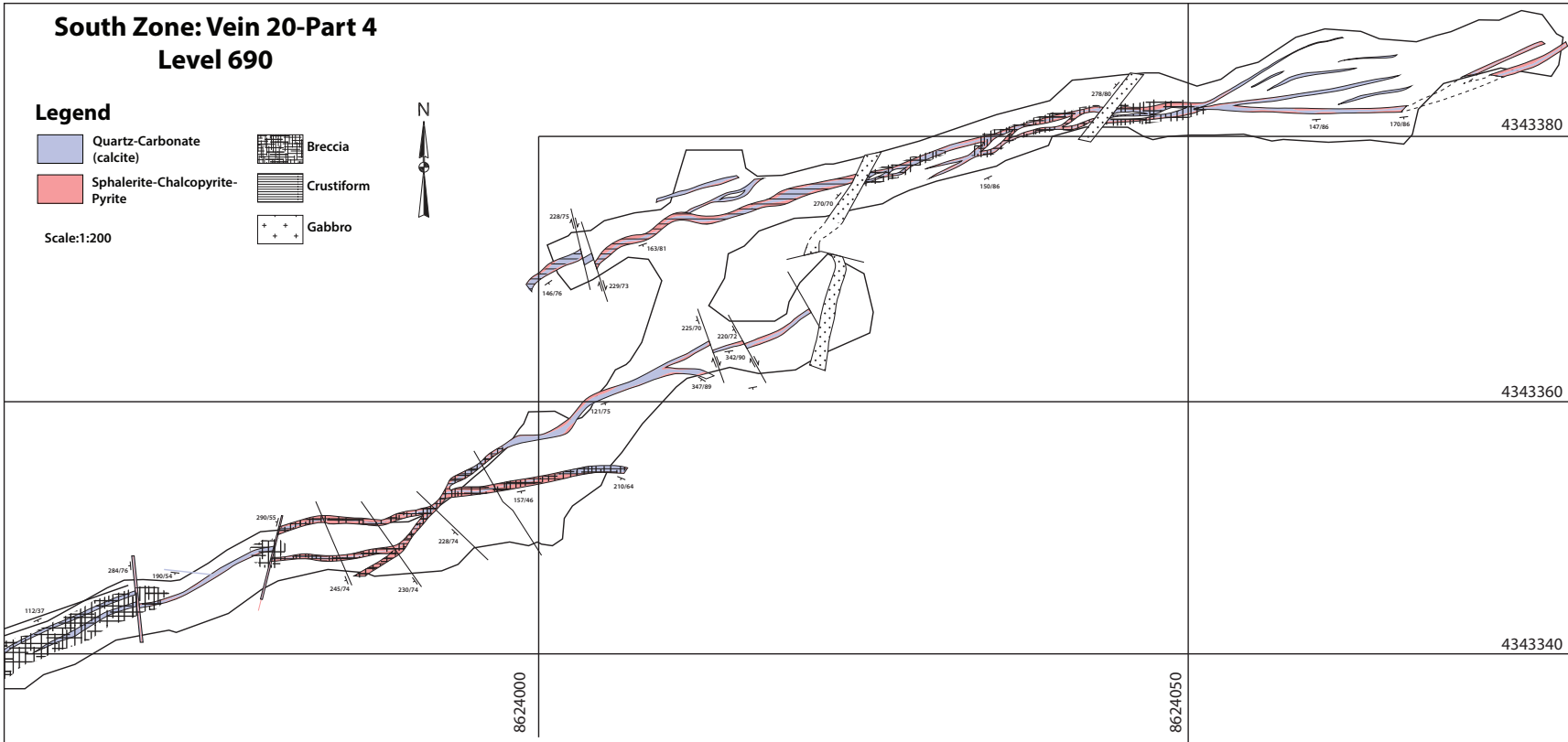
N=17
Max Density: 22.5%
at 134.3°/59.3° (pole)

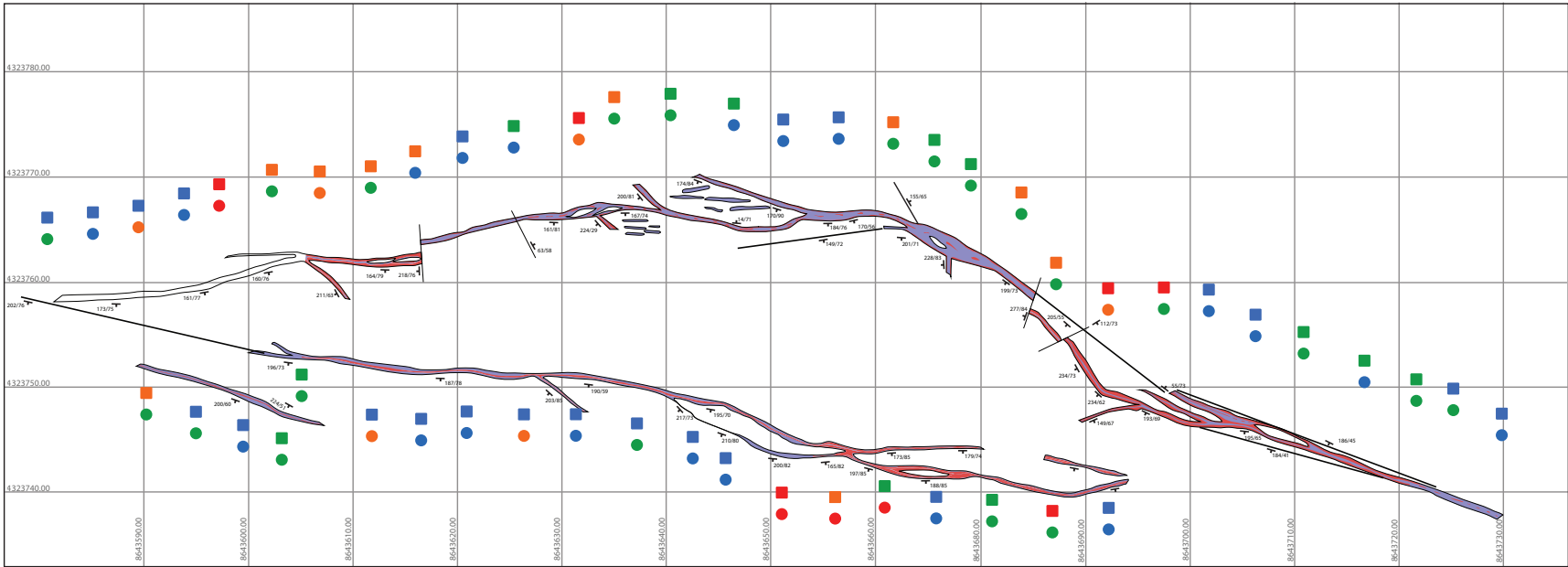












**South Zone: Vein 33-34
Level 735**

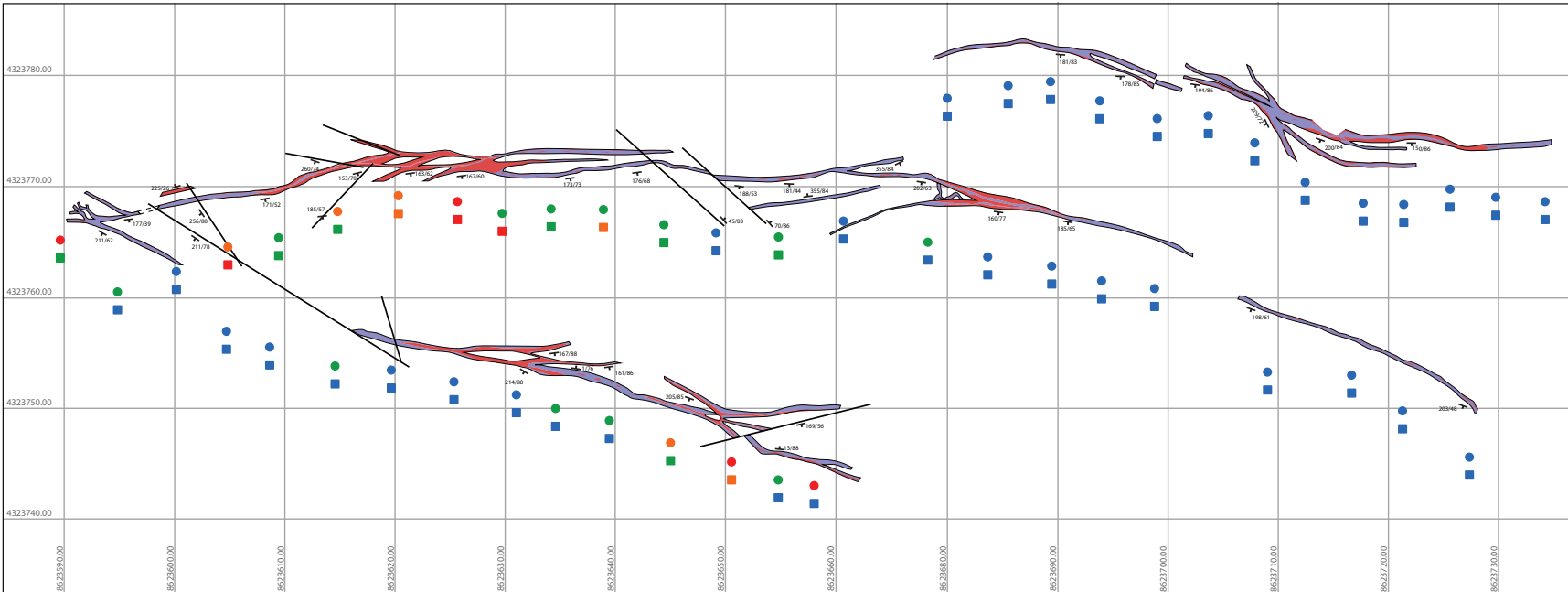
Legend

- Quartz-Carbonate (calcite)
- Sphalerite-Chalcopyrite-Pyrite
- Breccia
- Crustiform
- Gabbro

Scale:1:200



- | Zn (%) | Au(ppm) |
|--|---|
| <1% | <1ppm |
| 1-3% | 1-5ppm |
| 3-5% | 5-10ppm |
| 5-10% | >10ppm |



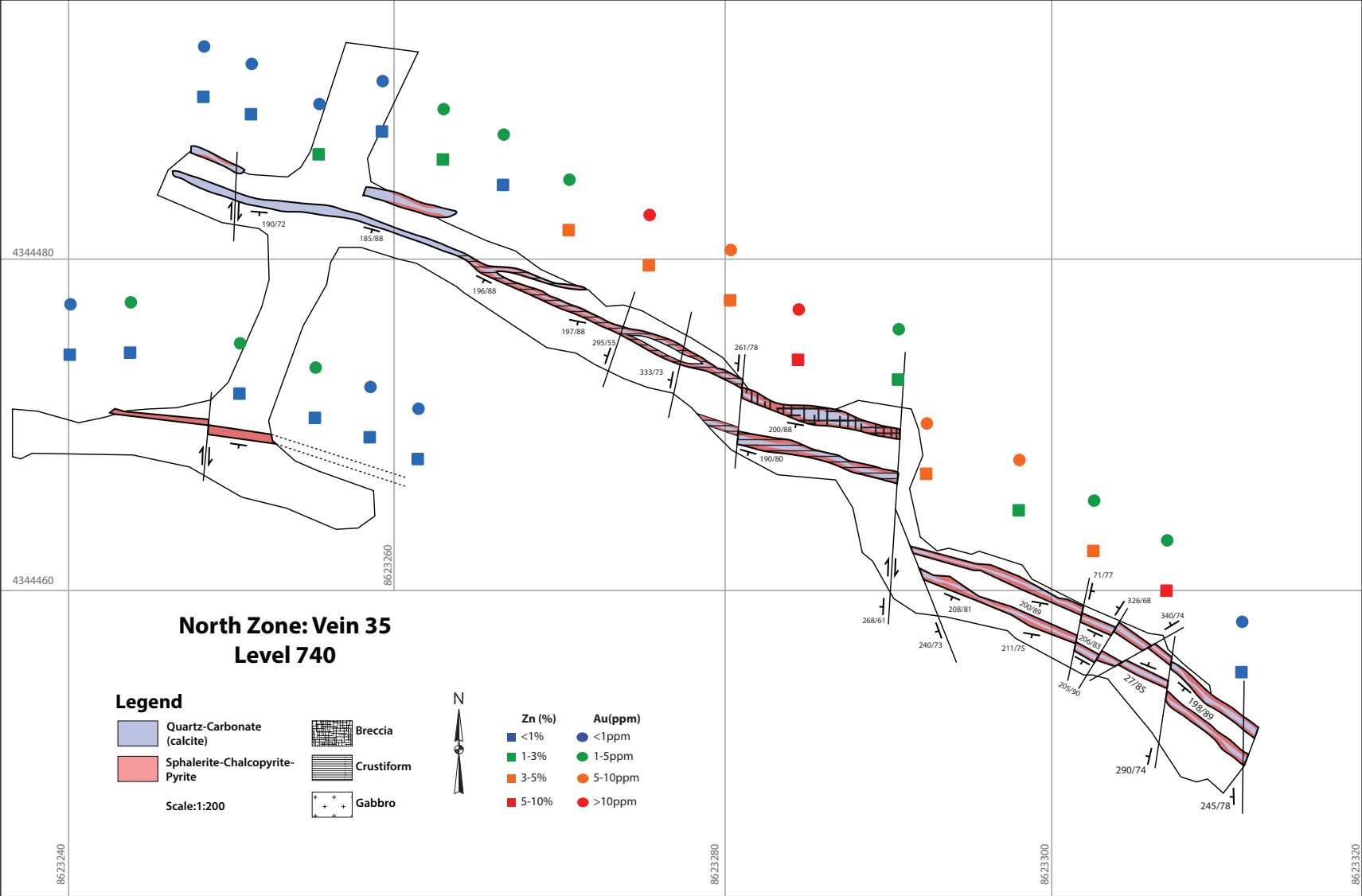
**South Zone: Vein 33-34
Level 748**

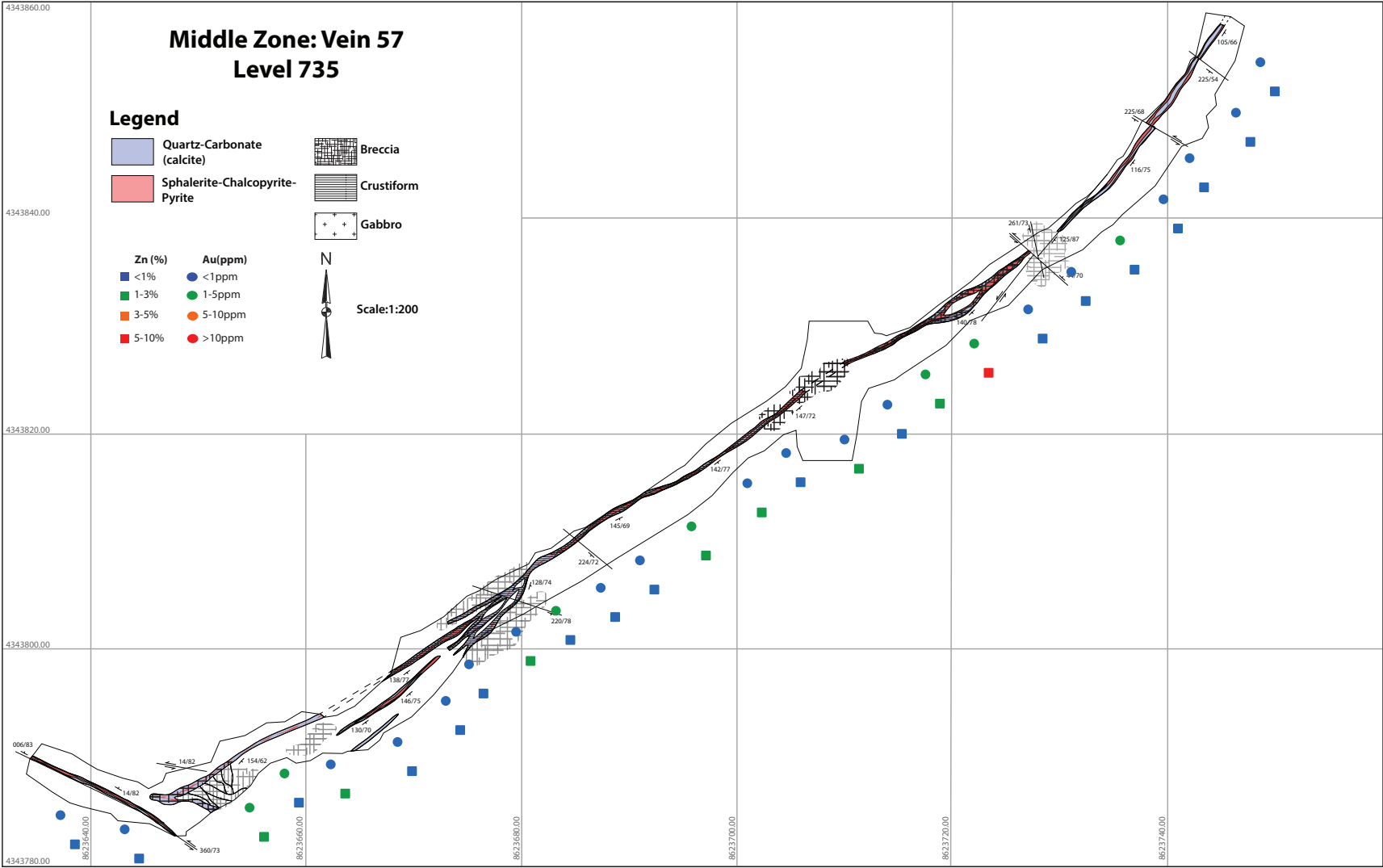
Legend

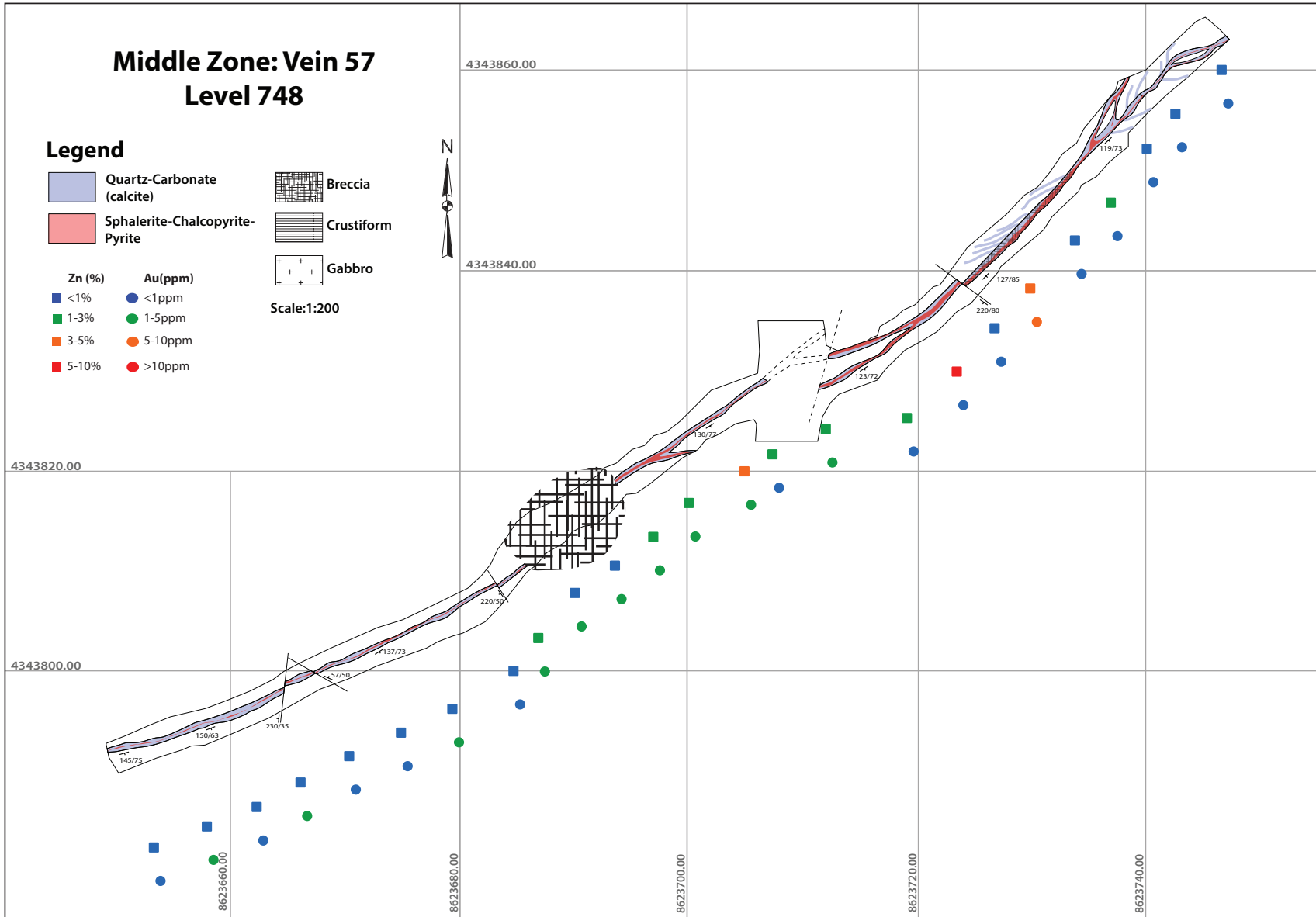
- Quartz-Carbonate (calcite)
 - Sphalerite-Chalcopyrite-Pyrite
 - Breccia
 - Crustiform
 - Gabbro
- Scale: 1:200

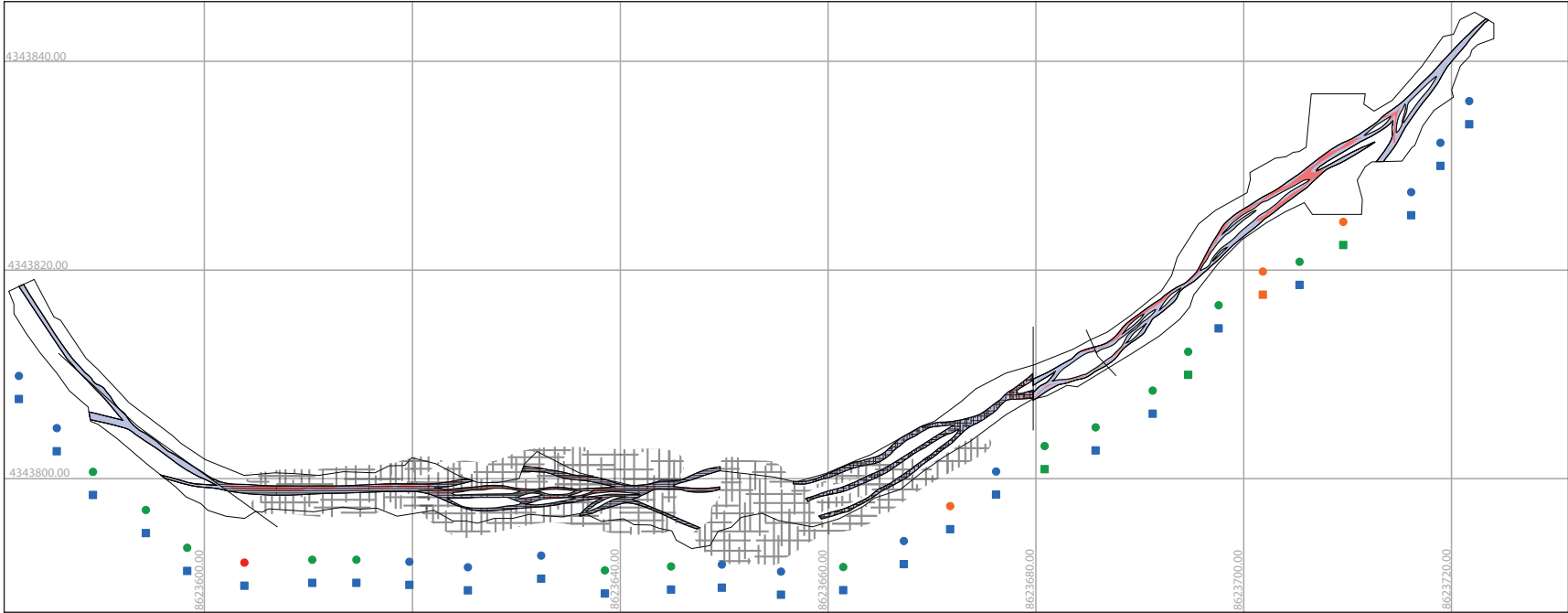


- | Zn (%) | Au(ppm) |
|--|--|
| <1% | <1ppm |
| 1-3% | 1-5ppm |
| 3-5% | 5-10ppm |
| 5-10% | >10ppm |







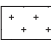














**Middle Zone: Vein 57
Level 760**

Legend

-  Quartz-Carbonate (calcite)
 -  Sphalerite-Chalcopyrite-Pyrite
 -  Breccia
 -  Crustiform
 -  Gabbro
 -  Zn (%) <1%
 -  Zn (%) 1-3%
 -  Zn (%) 3-5%
 -  Zn (%) 5-10%
 -  Au(ppm) <1ppm
 -  Au(ppm) 1-5ppm
 -  Au(ppm) 5-10ppm
 -  Au(ppm) >10ppm
- Scale:1:200



Appendix 6: Ore Petrography

Ore petrography was conducted by the author on selected vein and host rock samples. This appendix contains observational data used to produce the Shahumyan vein paragenesis, discussed in Chapter 3. A representative subset of 20 samples out of 41 samples is presented in this appendix.

Glossary

Cy: Mica / Clay, indistinguishable using optical microscopy likely sericite and or illite or a combination.

Py: Pyrite

Cpy: Chalcopyrite

Pg: Plagioclase

Sph: Sphalerite

Tt-Tn(?): Tetrahedrite/ Tennantite (solid solution of unknown composition)

Te (?): Telluride of unknown composition

He: Hessite

Ga: Galena

Qtz(1): Cryptocrystalline to sacchroidal fine grained quartz

Qtz(2): Prismatic/euhedral quartz

Ca: Calcite

F: Fluorite

Hb: Hornblend

Chl: Chlorite

-T: Transmitted light (*postscript, e.g XPL-T*)

-RL: Reflected light (*postscript, e.g XPL-RL*)

XPL: Cross polarized light

PPL: Plane Polarized light

Blebbly: texture comprising scattered small clots irregularly shaped with a bubble like texture.

Exsolution: Process through which an initially homogeneous solid solution separates into two different crystalline minerals

Chalcopyrite Disease : consists of a multitude of submicron - micron- sized blebbs of Chalcopyrite concentrated along fracture so rims or in relatively iron-rich bands of sphalerite Crystals.

----- : Observed inconsistently / lower confidence

——— : Observed consistently/ high confidence

Sample Locations

Hole ID	Depth(m)	Easting(GK)	NorthingGK)
SHDDR020	139.5	8623436.72	4344456.78
SHDDR247	192.8	8623189.94	4344158.62
SHDDR0231	382.45	8623434.90	4344152.75
SHDDR0233	324.3	8623426.91	4344074.63
Vein 20a	712	8624014.36	4343370.66
SHDDR0177	321.9	8623831.34	4343457.51
SHDDR0177	321.9	8623831.34	4343457.51
SHDDR0190	150.2	8623848.18	4342802.18
Vein 20a	712	8624003.48	4343365.02
Vein 17	703	8623850.32	4343252.01

Hole ID	Depth(m)	Easting(GK)	Northing(GK)
SHDDR0231	99.3	8623434.90	4344152.75
SHDDR0016	235.8	8623433.99	4344397.96
Vein 17	703	8623897.69	4343285.30
SHDDR0403	107.85	8624158.48	4342816.55
SHDDR0129	308.4	8623429.13	4344344.89
SHDDR0129	194.9	8623429.13	4344344.89
Vein 13	703	8623539.17	4344756.28
CEDDE06	146.9	8619465.00	4346080.00
CEDDE05	222.3	8619087.90	4346087.50
CEDDE07	225.5	8619120.40	4345708.00

Sample ID: UG S01

Sample taken from an exposed underground vein 20aE approximately ~1.5m in width from level 712.

Handsample Description:

Sample shows massive honey colored sphalerite intergrown with chalcopyrite, pyrite and minor amounts of galena. Late stage calcite vein cutting sulphide assemblage.

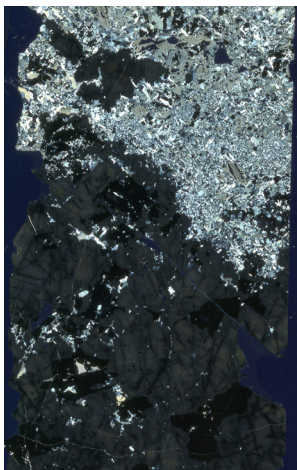


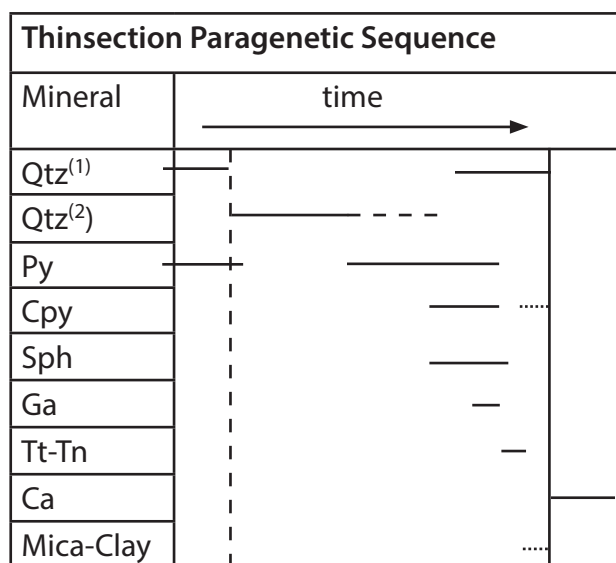
Fig 1: XPL scanned thinsection

Mineralogy:

Mineral	Relative%	Textural Description
Sphalerite (Sph)	30%	Massive euhedral light brown in ppl-dark grey in xpl. Cpy as replacement/exsolution and intergrown.
Chalcopyrite (Cpy)	10%	Anhedral heavily pitted blebbs intergrown with py-sph. Also present as replacement/exsolution in py and sph (cpy-disease)
Galena (Ga)	10%	Blebby anhedral and intergrown with sphalerite. Ga contains py inclusions. Strongly distinguished by its pinkish white color and triangular pits.
Pyrite (Py)	7%	Masive anhedral blebbs occur as individual grains or intergrown with Sph, Cpy, Ga. Tt-tn and cpy sparsely replaces py
Tetrahedrite (Tt-Tn)	tr	Partial-complete replacement of cpy. partial replacement of sphalerite is occasionally observed
Quartz (1) (Qtz ⁽¹⁾)	20%	Very fine grained irregular anhedral quartz
Quartz (2) (Qtz ⁽²⁾)	20%	Prismatic/euhedral quartz associated with sph and cpy. Shows open space growing textures (comb-quartz)
Calcite (Ca)	5%	Interstitial with sulphide and qtz assemblages. Also late stage vein material. Coarse grained with distinct cleavage.
Mica/clay (Cy)	tr	Difficult to differentiate clays Interstitial to sulphides and quartz assemblages.

Summary and Interpretation

This sample is represented by both coarse and fine grained quartz. Coarse grained prismatic quartz is spatially associated (in contact) with sulphide mineralization, often sulphide blebbs are observed inside the quartz indicating the sulphides precipitated coevally with the quartz. Pyrite is euhedral-disseminated to anhedral-blebby. Anhedral-blebby pyrite is intergrown with chalcopyrite and sphalerite. Chalcopyrite is intergrown with pyrite and is associated with sphalerite as either replacement rims near Sph boundaries and as submicron replacement bodies known as chalcopyrite disease. Partial replacement of chalcopyrite by sulfosalts (tetrahedrite-tennantite) is common, while partial replacement of sphalerite is rare in this sample but present. Calcite is present as late stage interstitial infill, often shows perfect cleavage. Hydrothermal mica/clay is also observed to be interstitial fill.



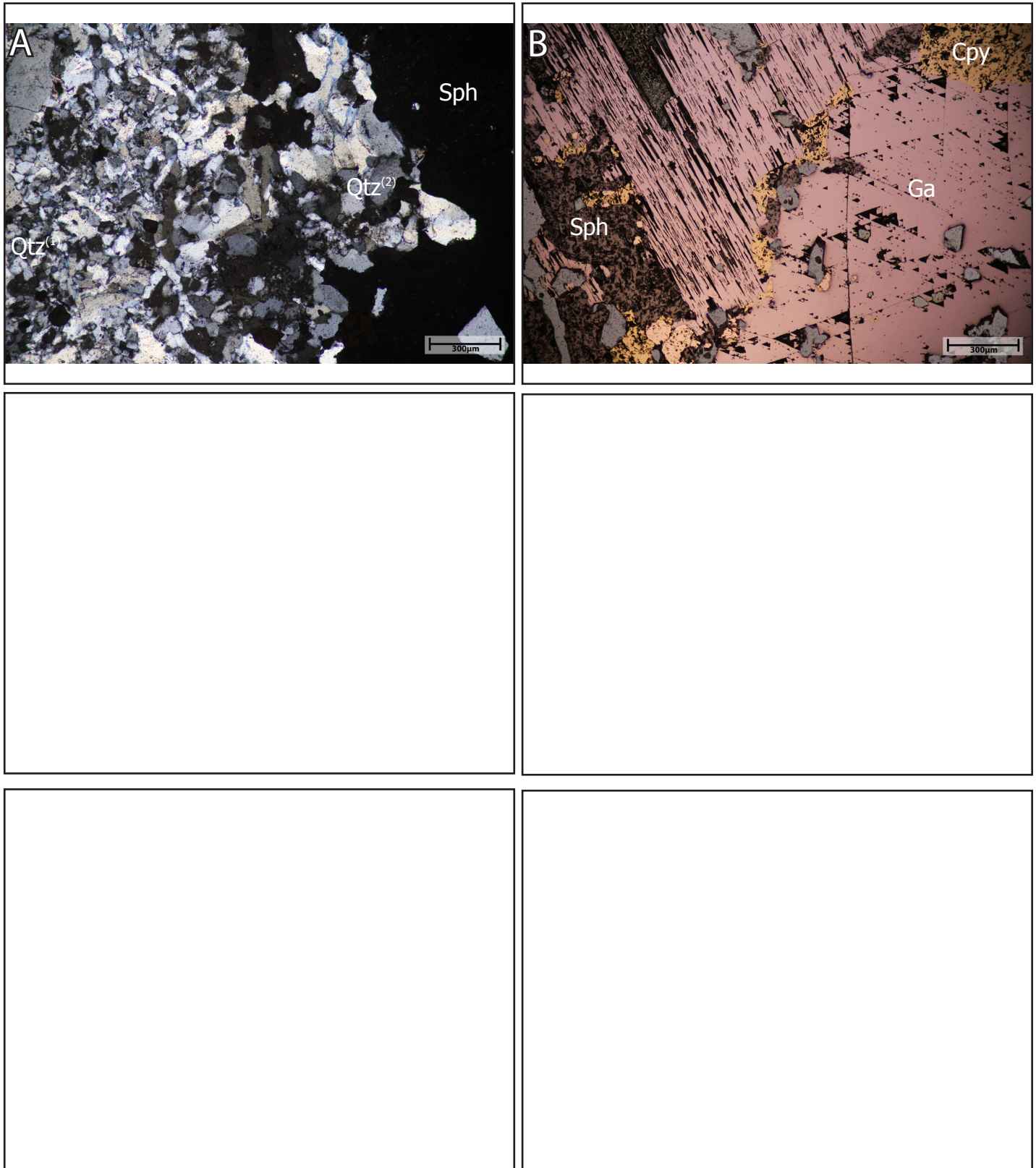


Fig 2A: Fine grained quartz present closest to the wallrock, precedes prismatic quartz (quartz-2) growth that may show euhedral open growth textures. Quartz -(2) stage is associated with sulphide mineralization (Sph, Chalcopyrite). **Fig2B:** Sphalerite is intergrown with galena and chalcopyrite. Galena shows triangular pits due to poor polishing. Chalcopyrite appears to be growing inbetween galena grains.

Sample ID: UGS S020:

Sample taken from an exposed underground vein 17, level 703. This sample was taken from the inner core of the vein.

Handsample Description Smokey white-grey quartz and calcite matrix contains embayed sulphide floats. anhedral pyrite-sphalerite and chalcopyrite are present.

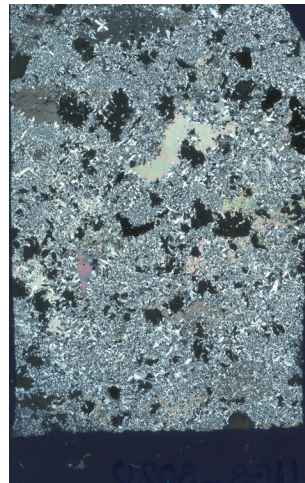


Fig 3: XPL scanned thinsection

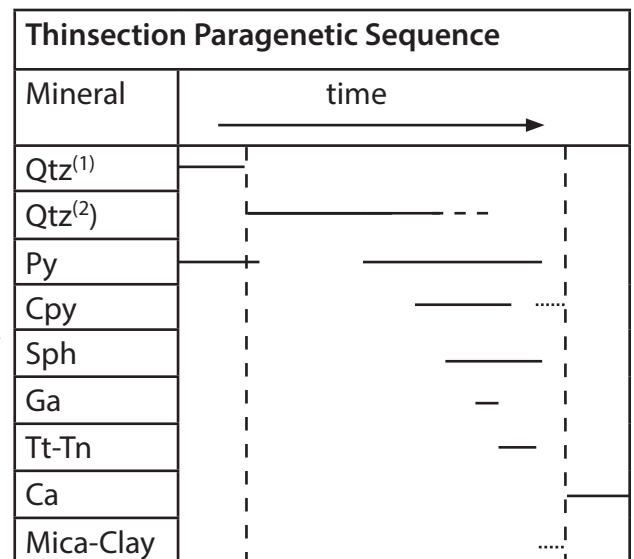
Mineralogy:

Mineral	Relative %	Textural Description
Sphalerite (Sph)	5%	Anhedral blebbs of light brown in ppl-dark grey in xpl. Cpy as replacement/exsolution and intergrown.
Chalcopyrite (Cpy)	5%	Anhedral heavily pitted blebbs intergrown with py-sph. Also present as replacement/exsolution in py and sph (cpy-disease)
Pyrite (Py)	3%	Anhedral blebbs- euhedral disseminated crystals. occurs as individual grains or interrown with sph, cpy, ga. Tt-tn and cpy replaces Py along fractures and rims.
Galena (Ga)	tr	Anhedral blebbs intergrown with cpy and sph.
Quartz (1) (Qtz ⁽¹⁾)	50%	Very fine grained irregular anhedral quartz
Quartz (2) (Qtz ⁽²⁾)	20%	Prismatic/euhedral quartz associated with sph and cpy. Shows open space growing textures (comb-quartz)
Calcite (Ca)	5%	Interstitial with sulphide and qtz assemblages. Also late stage vein material. Coarse grained with distinct cleavage.
Mica/clay (Cy)	5%	Very fine grained mica/clay, difficult to differentiate. Interstitial to sulphides and quartz assemblages.

Summary and Interpretation

Sphalerite is heavily fractured and brecciated, fragments of sphalerite are embayed in a quartz-calcite rich matrix. Calcite is present as interstitial infill between quartz-sulphide assemblages.. Qtz⁽²⁾ grains show random orientation of growing, in contrast to other samples which show a unidirectional orientation of growth into open space. Quartz grains may have grown in suspension rather than from wall-rock interface.

Disseminated euhedral pyrite present in sample does not show any relationship with other sulphide minerals. Chalcopyrite is present as massive grains in contact with pyrite and sphalerite. Chalcopyrite disease is observed within sphalerite. Small grains of galena (1-5 microns) are in contact with sphalerite and chalcopyrite.



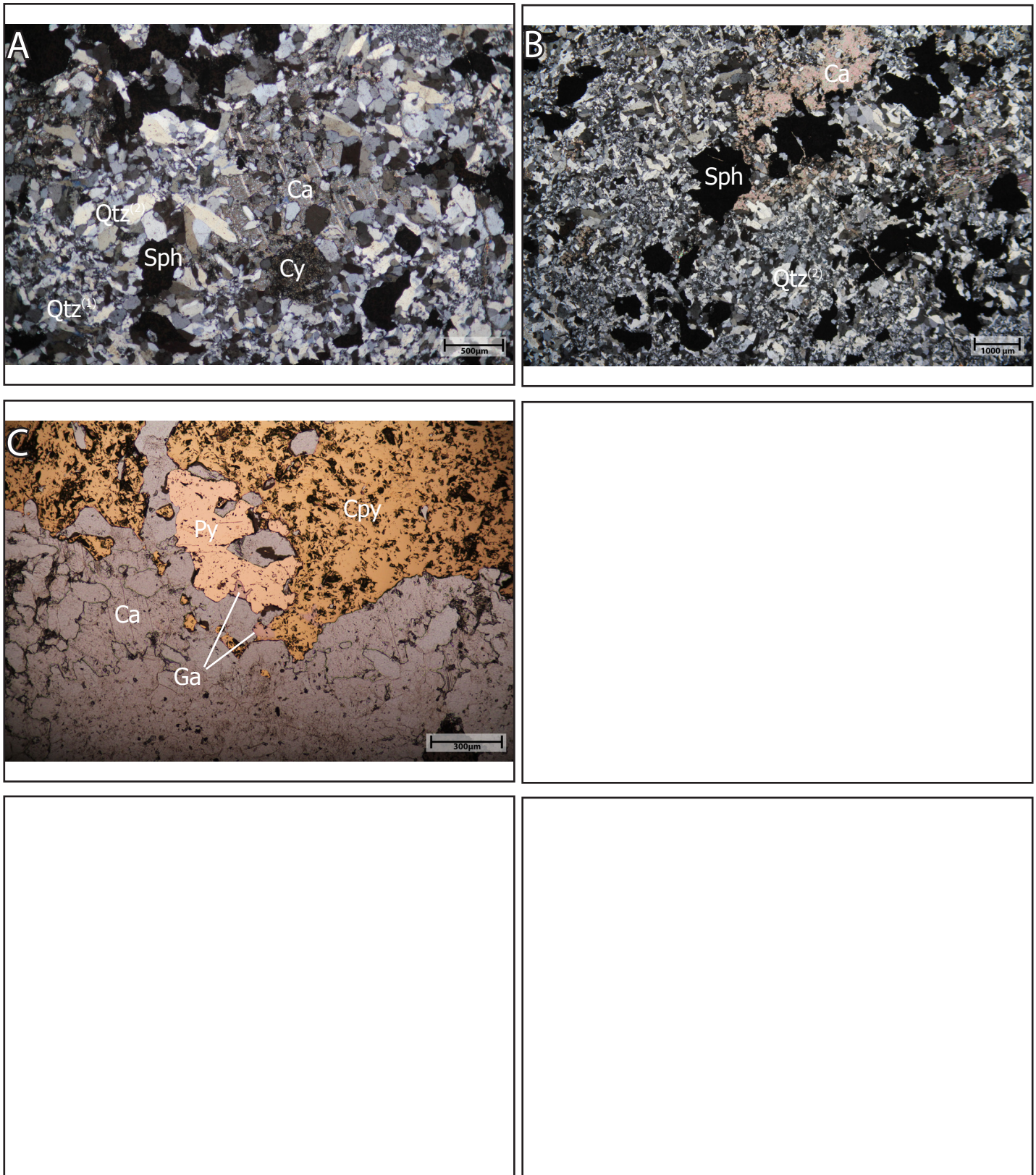


Fig 4A(PPL-T): late stage calcite and Mica/Clay alteration interstitial to earlier quartz-sulphide phases. Sphalerite associated with quartz-2, Fig4B: Quartz 2 filling in open fractures in quartz-1 matrix, similar mineral associations to Fig 4A. Fig4C: Galena,pyrite and chalcopyrite intergrown together. Galena is distinguished by its piskish white color and often contains triangular pit marks.

Sample ID: UG S007

Sample was taken close to vein-selvage and vein core interface from vein 17, level 703

Handsample Description:

Chalcopyrite rich vein, sample retrieved from pug-filled vein. Pyrite and chalcopyrite intergrown with sphalerite. Interstitial quartz-carbonate.

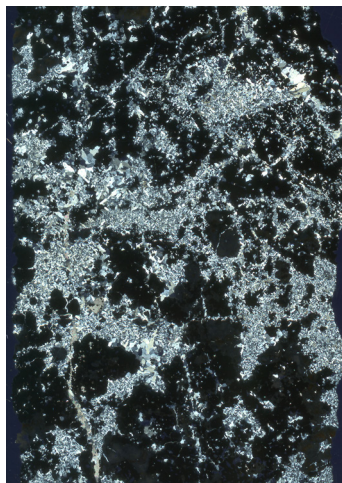


Fig 5: XPL scanned thinsection

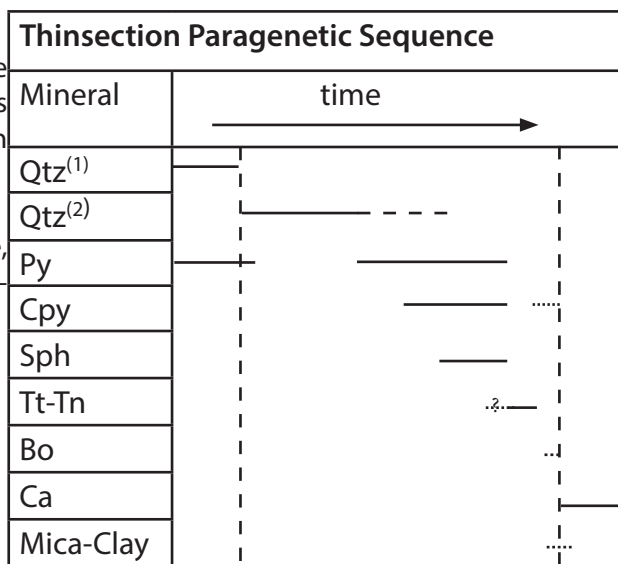
Mineralogy:

Mineral	Relative %	Textural Description
Sphalerite (Sph)	10%	Fractured / subhedral light brown Sph intergrown with cpy and py. Rarely shows Cpy disease.
Chalcopyrite (Cpy)	22%	Anhedral heavily pitted blebbs intergrown with py.
Pyrite (Py)	23%	Cumulate anhedral-subhedral pyrite assemblages, intergrown with Sph. Intergrown Cpy-Py boundaries show Tt-Tn replacement.
Tetrahedrite (Tt-Tn)	8%	Primarily replacing Cpy and occasionally replacing Sph.
Bornite(Bo)	Tr	Replacing Tt-Tn and Cpy in pyrite.
Quartz (1) (Qtz ⁽¹⁾)	22%	Very fine grained irregular anhedral quartz.
Quartz (2) (Qtz ⁽²⁾)	8%	Prismatic/euhedral quartz associated with Sph and Cpy. Shows open space growing textures (comb-quartz).
Calcite (Ca)	3%	Interstitial with sulphide and Qtz assemblages. Also late stage vein material. Coarse grained with distinct cleavage.
Mica/clay (Cy)	tr	Very fine grained mica/clay, difficult to differentiate. Interstitial to sulphides and quartz assemblages.

Description and Interpretation

Micron sized sphalerite inclusions seen in Qtz⁽²⁾ indicates sphalerite likely precipitated coevally with Qtz⁽²⁾. Unknown sulfosalt (Tt-Tn?) is replacing chalcopyrite and occasionally sphalerite this is rarely seen in pyrite but present.

New hydrothermal fluids may have been introduced at a later stage, inducing disequilibrium with existing sulphide assemblages. Resulting in replacement of Chalcopyrite and sphalerite.



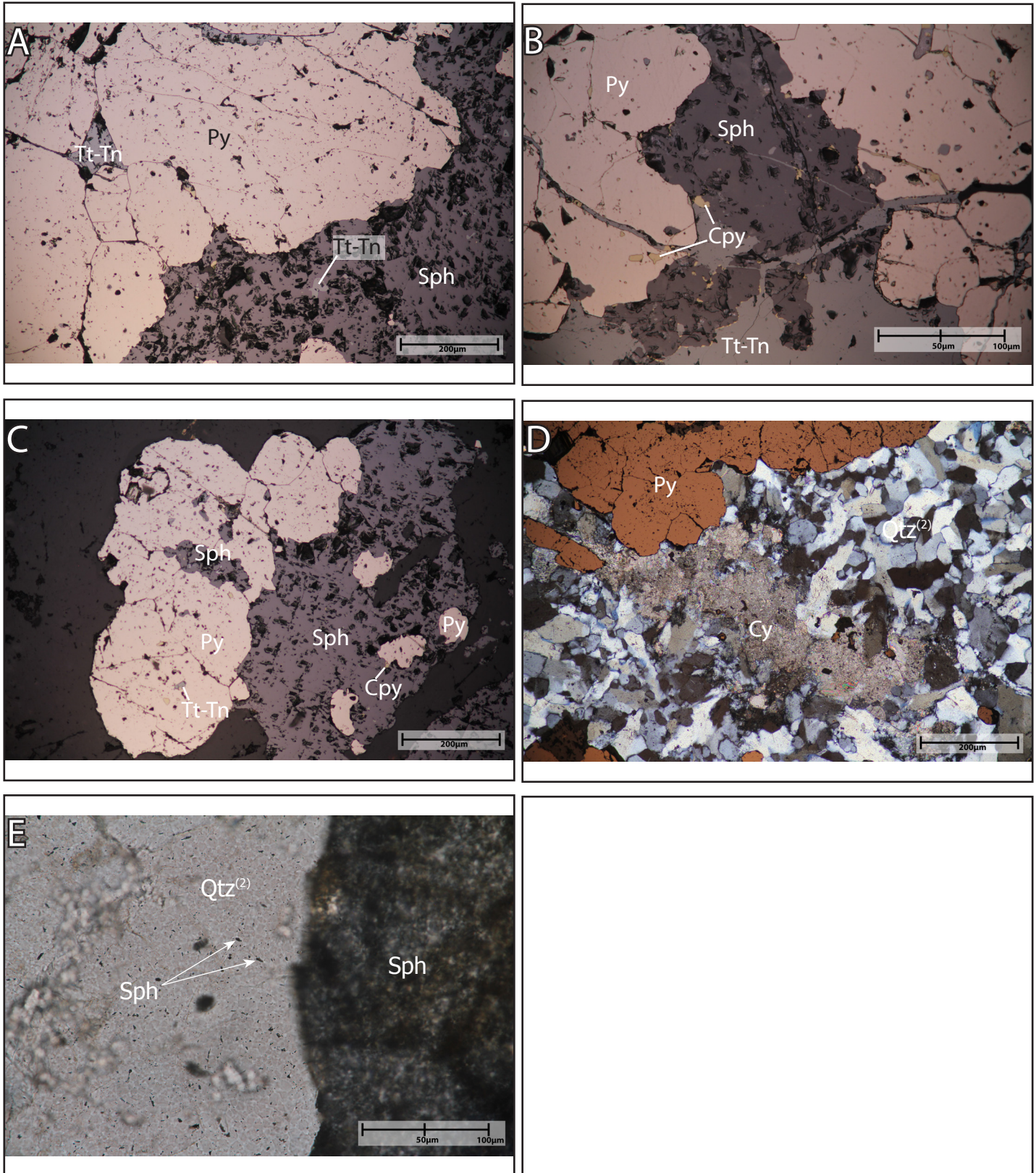


Fig 6A(PPL-R): Tetrahedrite replacing/ forming along fractures in pyrite, tetrahedrite similarly present in sphalerite. Chalcopyrite disease present in sphalerite, and as inclusions(?) in pyrite. **Fig 6B (PPL-R):** Tetrahedrite-Tennantite present in fractures in sphalerite and pyrite, and surrounds both Py, and Sph. Chalcopyrite is present inbetween sph and Tt-Tn grain boundaries (replacement). **Fig6C:** Pyrite and Sphalerite intergrown with chalcopyrite disease in sphalerite, Tt-Tn present in pyrite pits or along fractures. **Fig6D:** Coarse grained blebby-anhedral pyrite associated with quartz-2, mica/clay as late stage interstitial material. **Fig6E:** Quartz-2 showing inclusions of micron sized Sph.

Sample ID: DCS S029

Hole ID: SHDDR020

Depth: 139.55

Assay: 0.017% Cu, 0.145%Zn, 0.22ppmAu,
5ppm Ag

Handsample Description:

Wallrock is strongly sericite-pyrite altered, primary lithology texture is eliminated. Quartz-carbonate vein with pyrite, ± chalcopyrite selvage cutting through host rock.

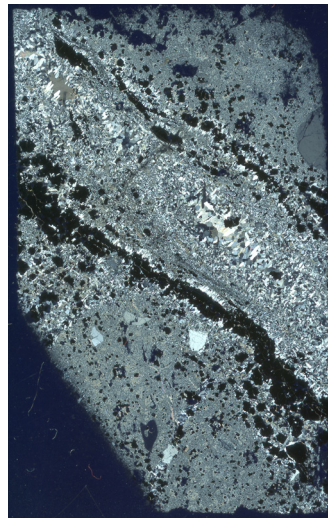


Fig 7: XPL scanned thinsection

Mineralogy:

Mineral	Relative%	Textural Description
Pyrite (Py)	17%	Anhedral blebbs- euhedral disseminated crystals. occurs as individual grains or interrown with sph, cpy, ga. Tt-tn and cpy sometimes shows replacement of py
Chalcopyrite (Cpy)	2%	Anhedral heavily pitted blebbs intergrown with py-sph. Also present as replacement/exsolution in py and sph (cpy-disease)
Sphalerite (Sph)	1%	Massive euhedral light brown in ppl-dark grey in xpl. Cpy as replacement/exsolution and intergrown.
Tetrahedrite (Tt-Tn)	tr	Partial-complete replacement of cpy.
Galena (Ga)	tr	Blebby anhedral and intergrown with sphalerite. Ga contains py inclusions. Strongly distinguished by its pinkish white color and triangular pits.
Quartz (1) (Qtz ⁽¹⁾)	25%	Very fine grained irregular anhedral quartz
Quartz (2) (Qtz ⁽²⁾)	13%	Prismatic/euhedral quartz associated with sph and cpy. Shows open space growing textures (comb-quartz)
Calcite (Ca)	5%	Interstitial with sulphide and qtz assemblages. Also late stage vein material. Coarse grained with distinct cleavage.
Mica/clay (Cy)	2%	Very fine grained mica/clay, difficult to differentiate. Interstitial to sulphides and quartz assemblages.
Wallrock		
Plagioclase (Pg)	6%	Plagioclase phenocrysts partial-complete replacement by clay ± carbonate
Quartz (Qtz ⁽³⁾)	6%	Embayed quartz phenocryst. Rimmed with carbonate,pyrite/sericite
Aphanitic Matrix	15%	VFG plagioclase quartz and relict hornblende replaced by pyrite
Wall Alteration		
Mica/Clay	6%	Replacing primary Pg and present as very fine grained overprint in matrix. Shows radial growth occasionally.
Quartz	2%	Rimming plagioclase and pyrite grains present in wallrock.

Summary and Interpretation

Wallrock is Intensely altered; undifferentiated mica/clay alteration replace plagioclase and overprint aphanitic matrix. Silica alteration shows quartz rimming pyrite and plagioclase grain boundaries. Pyrite is most abundant while other sulphides are minor constituents.

This vein sample was examined because it was identified as a separate vein type during field observation. However petrographic analyses revealed it to contain similar sulphide mineralogies as main stage sulphide veins but at lower relative abundances. This may indicate that sulphide rich veins initially identified in field are infact similar to main stage veins. I interpret this to indicate that certain veins were closed to subsequent hydrothermal fluids.

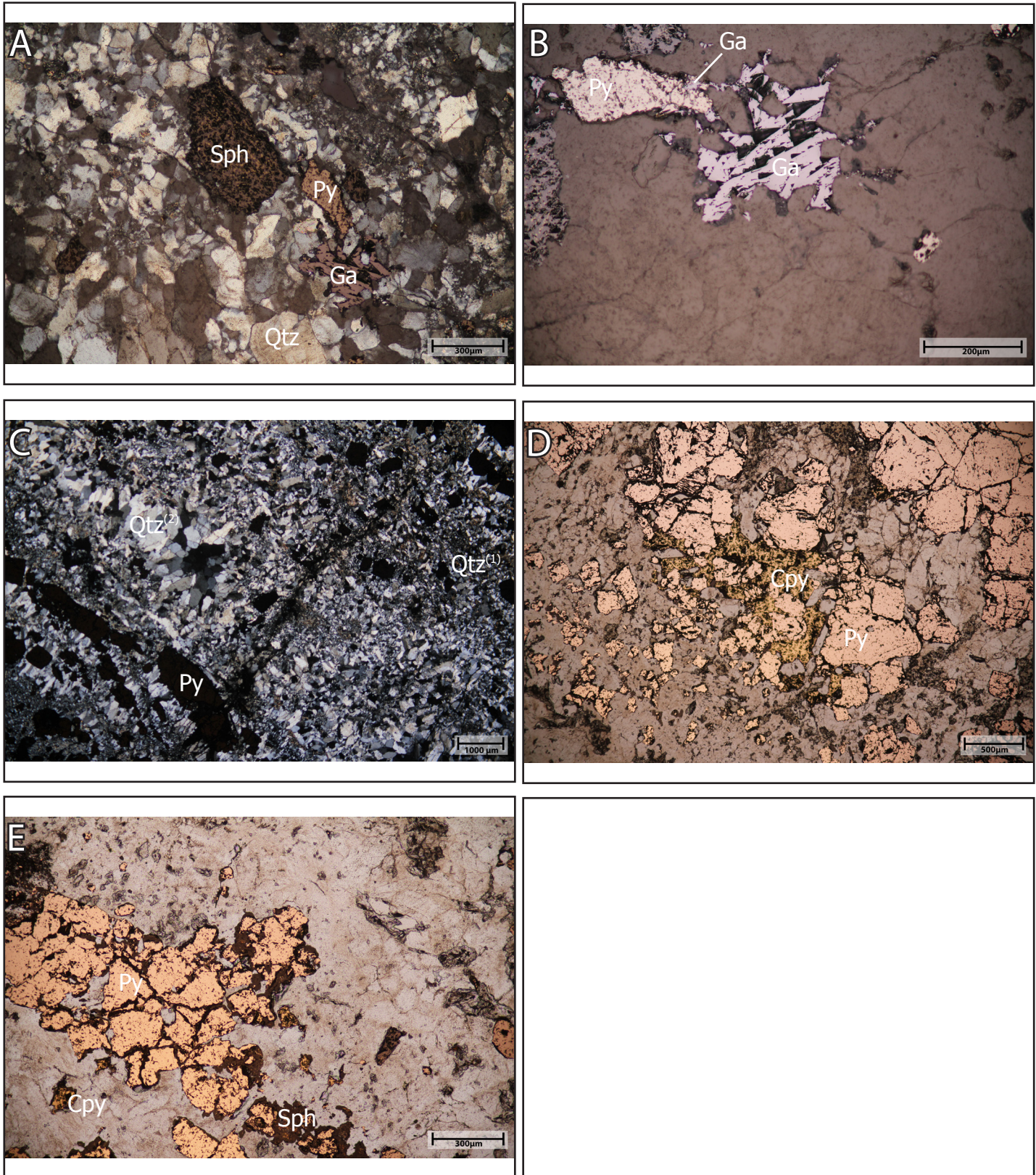


Fig 8A: Anhedra Sphalerite, Pyrite and Galena grains embayed in quartz-2 matrix, sphalerite shows moderately intense chalcopyrite disease. **Fig8B:** Magnified image of Fig8B, shows galena and pyrite intergrowth textures. **Fig8C:** Quartz-2 fills fractures in quartz-1 matrix. Disseminated subhedral pyrite present in quartz-1 vein matrix, higher concentrations of pyrite present in fractures filled with quartz-2. **Fig8D:** heavily fractured brecciated pyrite partially cemented by chalcopyrite. **Fig8E:** Heavily fractured pyrite intergrown with sphalerite. Chalcopyrite disease is moderate-intense in sphalerite.

Sample ID: UG S016

Sample was taken from vein-wallrock interface from exposed underground Vein 13 on level 703 at the Shahuayan mine.

Handsample Description:

Sampled from vein-wallrock interface. Wallrock is intensely sericite, pyrite altered. Apahnitic ground mass. Vein contains prismatic smoky-white quartz with a sulphide (pyrite, sphalerite) suture. Fluorite is also present locally. Late stage carbonate veining in wallrock resulted in brecciated wallrock.

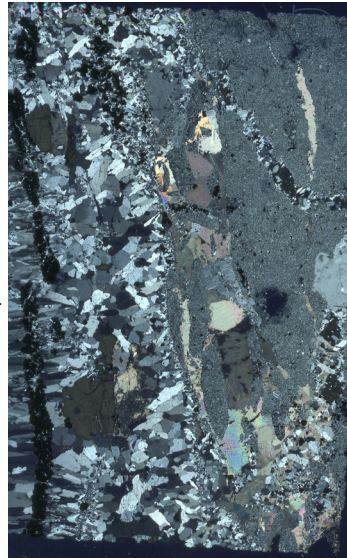


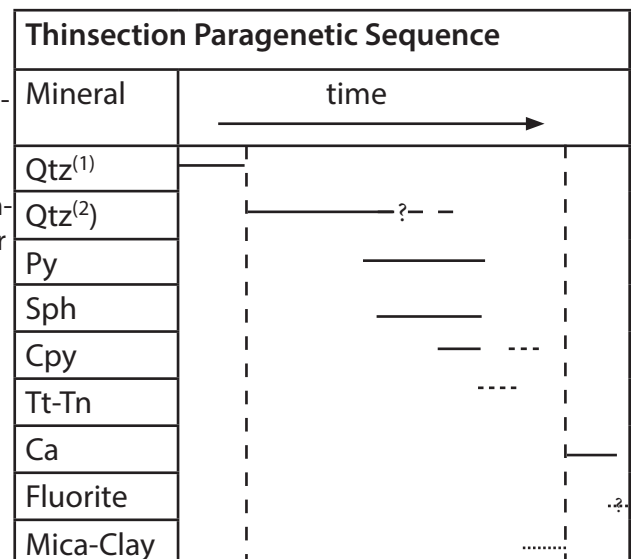
Fig 9: XPL scan of thin section

Mineralogy:

Mineral	Relative%	Textural Description
Sphalerite (Sph)	12%	Massive euhedral light brown in ppl-dark grey in xpl. Cpy as replacement/exsolution and intergrown
Pyrite (Py)	14%	Masisve anhedral blebbs- euhedral disseminated crystals. occurs as individual grains or interrown with sph, cpy, ga. Tt-tn and cpy sometimes shows replacement of py
Chalcopyrite	2%	Intergrown with Sph and as sub-micron anhedral blebbs in Sph (Cpy-disease).
Tetrahedrite-Tennantite (Tt-Tn)	tr	Unknown sulfosalt (Tetrahedrite-Tennantite?) partially replaces sphalerite
Quartz (1) (Qtz ⁽¹⁾)	4%	Very fine grained irregular anhedral quartz
Quartz (2) (Qtz ⁽²⁾)	30%	Prismatic/euhedral quartz associated with sph and cpy. Shows open space growing textures (comb-quartz)
Calcite (Ca)	10%	Interstitial with sulphide and qtz assemblages. Also late stage vein material. Coarse grained with distinct cleavage
Mica/clay (Cy)	6%	Very fine grained mica/clay, difficult to differentiate. Interstitial to sulphides and quartz assemblages
Fluorite (F)	tr	Interstitial to quartz and sulphide assemblage. Greenish tint in hand sample
Wallrock Assemblage:		
Quartz, relict plagioclase	20%	Intensely altered, alteration products are near indistinguishable

Summary and Interpretation

Sample is unique as it contains interstitial fluorite along with interstitial mica/clay and calcite. Euhedral-subhedral prismatic quartz crystals indicate growth towards empty space (comb-quartz texture) with pyrite in the suture. The sample shows typical crustiform and quartz-comb textures found in other samples. Tetrahedrite/Tennantite (?) are associated with sphalerite and chalcopyrite as with other samples. Wallrock is intensely altered relict plagioclase crystals completely altered into mica/clay?



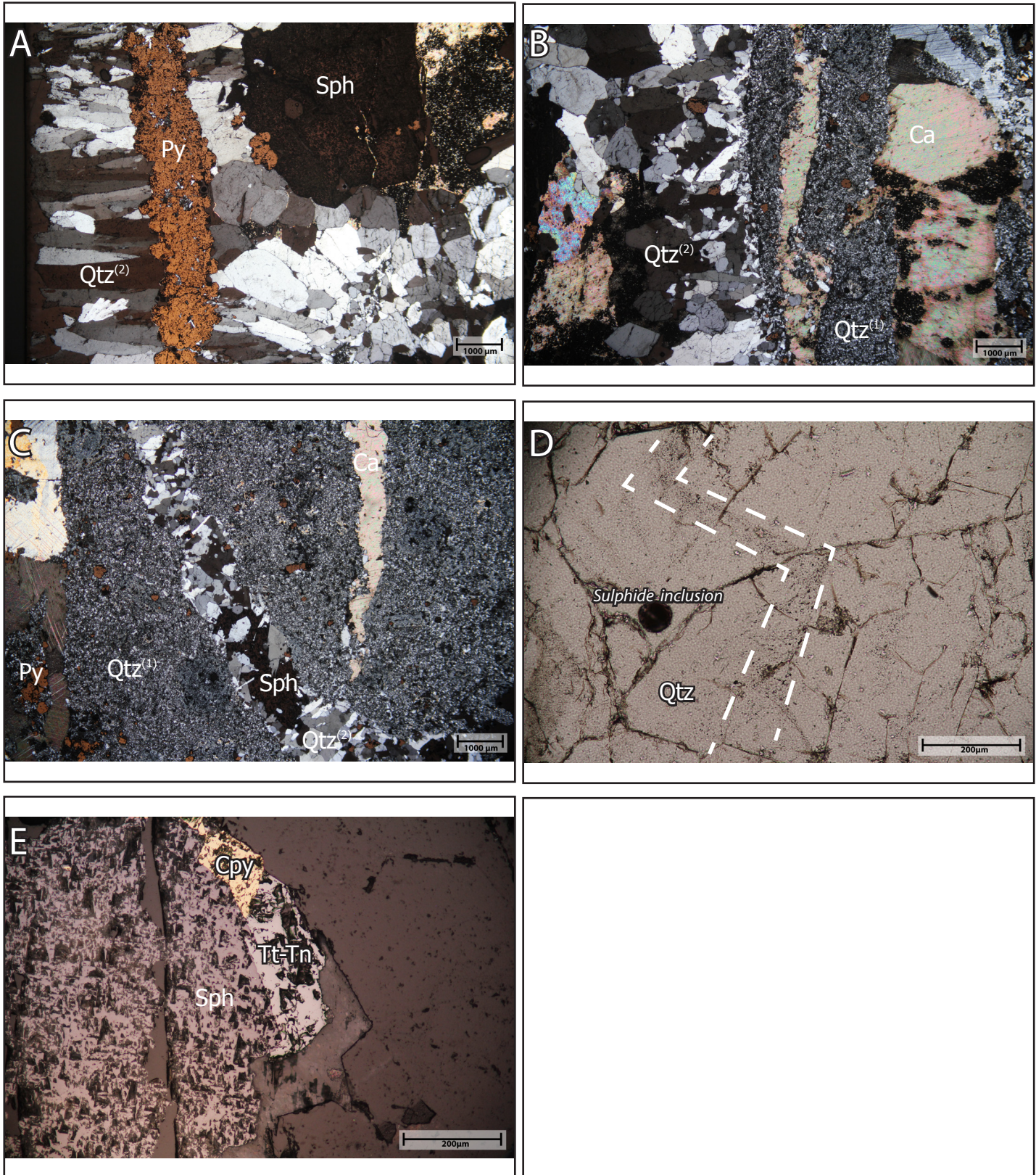


Fig 10A: Prismatic quartz (quartz-2) show openspace growth textures (Comb-quartz), pyrite is found in the suture. Sphalerite is also associated with this phase. Fig 10B: fine grained quartz phase precedes prismatic quartz growth towards open space. Quartz-1 zone is fractured and filled with subhedral calcite. Subhedral pyrite present in overprinting in quartz-1 zone. Fig 10C: Quartz-1 shows quartz-2+sphalerite+pyrite vein cutting it along with late stage calcite infilling a fracture. Fig 10D: Prismatic quartz with a sulphide inclusion (unknown) showing growth zoning and excellent zone zone of fluid inclusion analysis. Fig 10E: Sphalerite grain replaced by Cpy and Tt-Tn(?)

Sample ID: UGS S012B

Sample collected from an exposed underground vein, Vein 20a on Level 712 from the Shahumyan mine.

Hand Sample:

Massive honeybrown-grey sphalerite with interstitial carbonate. Intergrowth with cpy and pyrite. Massive sphalerite in contact with white-smokey prismatic quartz (comb quartz) and carbonate layer. Interstitial mica? anomalous in sample.

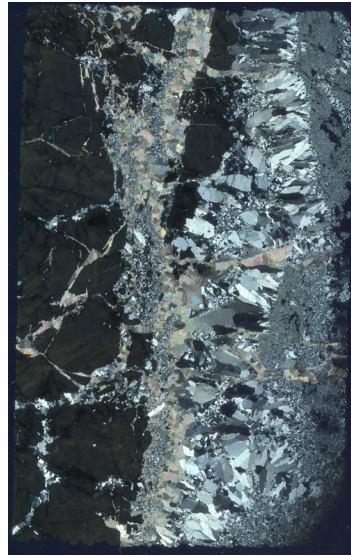


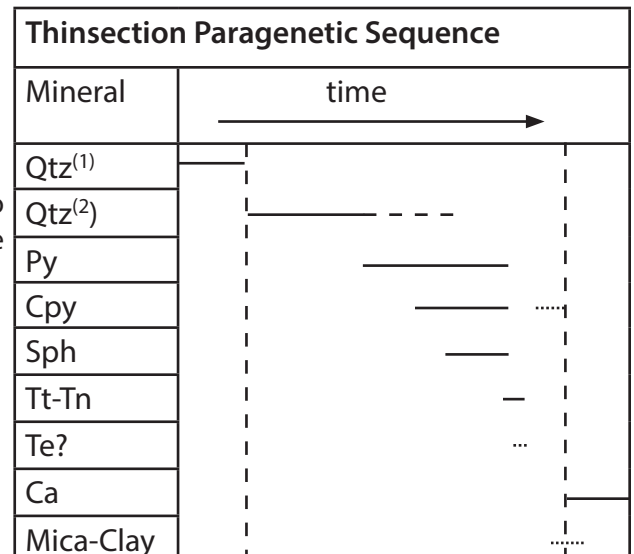
Fig 11: XPL scanned thinsection

Mineralogy:

Mineral	Relative %	Textural Description
Sphalerite (Sph)	30%	Massive zoned euhedral light brown in ppl-dark grey in xpl.. Cpy disease is present in sphalerite. Cpy filling fractures in sph. Zoning in sphalerite is strongly associated with cpy disease.
Pyrite (Py)	15%	Masive anhedral blebbs- euhedral disseminated crystals. occurs as individual grains or interrown with sph, cpy, ga. Tt-tn and cpy sometimes shows replacement of py. Pyrite along with cpy occurs in fractures present in sphalerite.
Chalcopyrite (Cpy)	10%	Anhedral heavily pitted blebbs intergrown with py-sph. Also present as replacement/exsolution in py and sph (cpy-disease)
Tetrahedrite-Tennantite(Tt-Tn)	1%	Present as anhedral-blebby replacement bodies in chalcopyrite and pyrite.
Unknown Telluride (Te?)	tr	Partial replacement of sphalerite (?)
Quartz (1) (Qtz ⁽¹⁾)	1%	Very fine grained irregular anhedral quartz
Quartz (2) (Qtz ⁽²⁾)	20%	Prismatic/euhedral quartz associated with sph and cpy. Shows open space growing textures (comb-quartz)
Calcite (Ca)	15%	Present as interstaial ,material in quartz or late stage veins cutting both sulphide and quartz assemblages. Fine grained to euhedral crystals showing perfect cleavage.
Mica/Clay	5%	Very fine grained mica/clay (indistinguishable). Present as interstitial material.

Summary and Interpretation

Unknown telluride (Te?) is replacing(?) a sphalerite grain within a pyrite grain. Late stage euhedral calcite with good cleavage infills veinlets or is interstitial to quartz-sulphide assemblage. Sphalerite is honey brown in color and shows growth zone bands similar to sphalerite in other veins. Pyrite is intergrown with sphalerite, it also occurs in fractures present in sphalerite (remobilized). Chalcopyrite is also present in fractures in sphalerite.



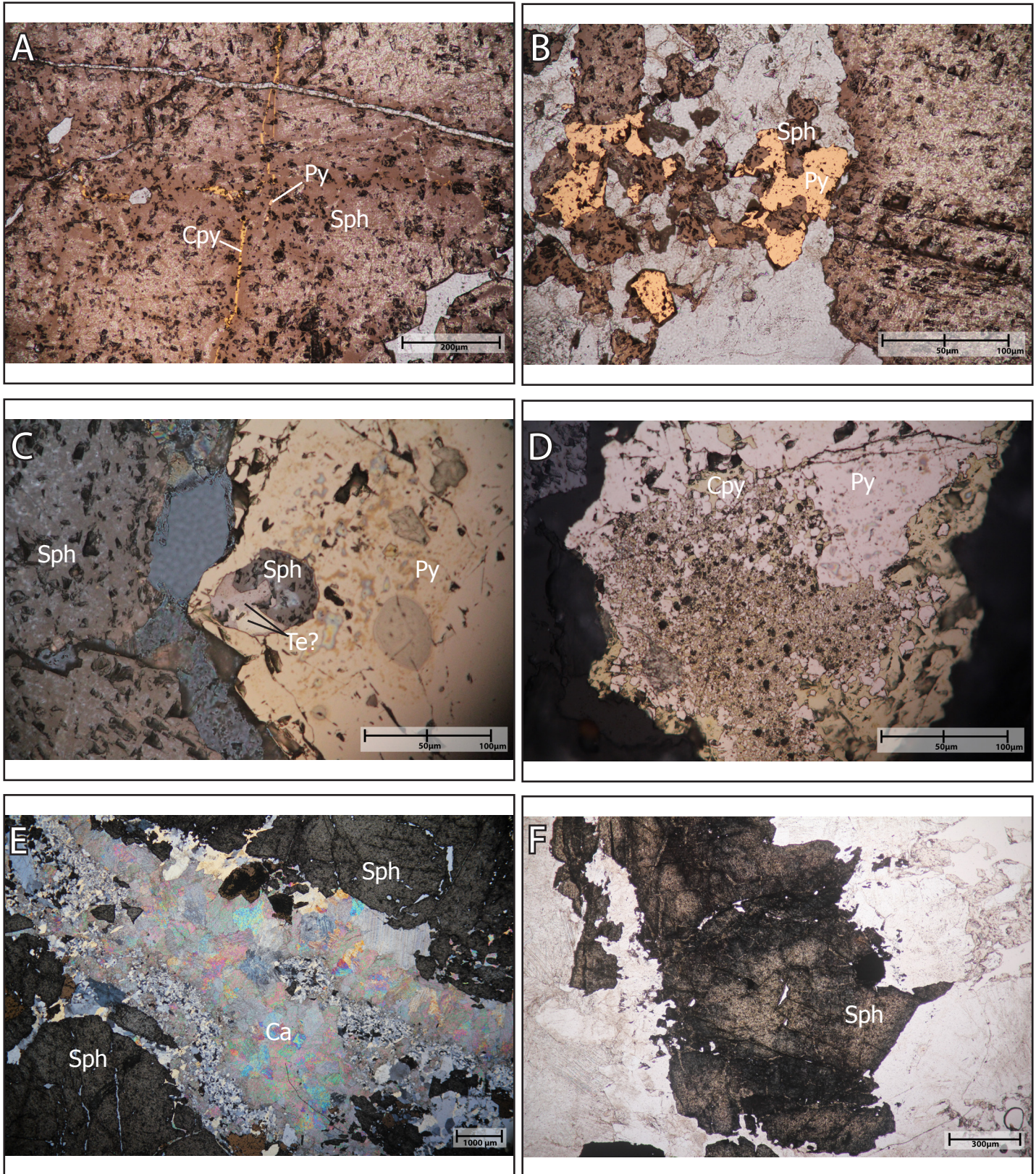


Fig 12A: Chalcopyrite and pyrite filling fracture in zoned sphalerite. Fig 12B: Pyrite intergrown with sphalerite Fig 10C: Quartz-1 shows quartz-2+sphalerite+pyrite vein cutting it along with late stage calcite infilling a fracture. Fig12C: Unknown tellurides along with sphalerite as inclusions in pyrite. Fig12D: Fractured/broken pyrite cemented by chalcopyrite. Fig12E: Late stage carbonate vein infilling vein. Late stage carbonate vein contains embayed floats of fractured sulphide and quartz-2. Fig12F: Zoned sphalerite.

Sample ID: SHDDR 247

Hole ID: SHDDR0247

Depth: 192.85

Assay: 0.0025%Cu, 0.0157%Zn, 0.1ppmAu, 4.5ppmAg

Handsample Description:

Intensely sericite-pyrite altered host rock with a quartz-pyrite vein. Host rock is a Plag-phyric dacite.

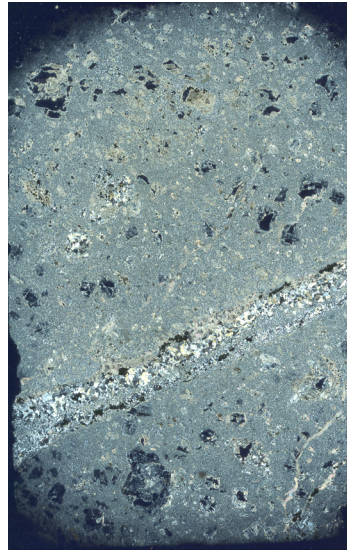


Fig 13: XPL scanned thinsection

Mineralogy:

Mineral	Relative%	Textural Description
Pyrite (Py)	7%	Massive anhedral blebbs- euhedral disseminated crystals. occurs as individual grains or interrown with sph, cpy, ga. Tt-tn and cpy sometimes shows replacement of py. Pyrite along with cpy occurs in fractures present in sphalerite.
Sphalerite (Sph)	tr	Massive zoned euhedral light brown in ppl-dark grey in xpl.. Cpy disease is present in sphalerite. Cpy filling fractures in sph. Zoning in sphalerite is strongly associated with cpy disease.
Quartz (2) (Qtz ⁽²⁾)	10%	Prismatic/euhedral quartz associated with sph and cpy. Shows open space growing textures (comb-quartz)
Calcite (Ca)	7%	Present as interstaial ,material in quartz or late stage veins cutting both sulphide and quartz assemblages. Fine grained to euhedral crystals showing perfect cleavage.
Mica/Clay	5%	Very fine grained mica/clay (indistinguishable). Present as interstitial material.
Wallrock Assemblage		
Plagioclase (Pg)	7%	Relict euhedral plagioclase phenocrysts completely replaced by mica/clay and minor carbonates. Partially altered plagioclase grains show numerous growth rims with core altered to mica/clay.
Quartz	4%	Embayed quartz with pyrite and mica/clay alteration lining fractures and rim.
Aphanitic Matrix	40%	altered plagioclase and quartz
Relict mafics	1%	Altered mafics (Hornblende) minor constituents.
Alteration		
Mica-Clay	15%	Replacing plagioclase. Very fine grained, undistinguishable between clay and muscovite. Biotite alteration may be present(dark and very fine grained)
Chlorite	3%	Present in matrix and often rimming plagioclase and hornblende grains
Pyrite	3%	euhedral pyrite present in altered hornblende grains

Summary and Interpretation

Intensely altered wallrock with a minor sulphide veinlet. Altered wallrock consists of chlorite, mica/clay, pyrite ± biotite(?) of hornblende and matrix; chlorite and mica/clay alteration of plagioclase. Late stage calcite veinlets cut through wallrock. Sulphosalts and tellurides were not observed in the vein.

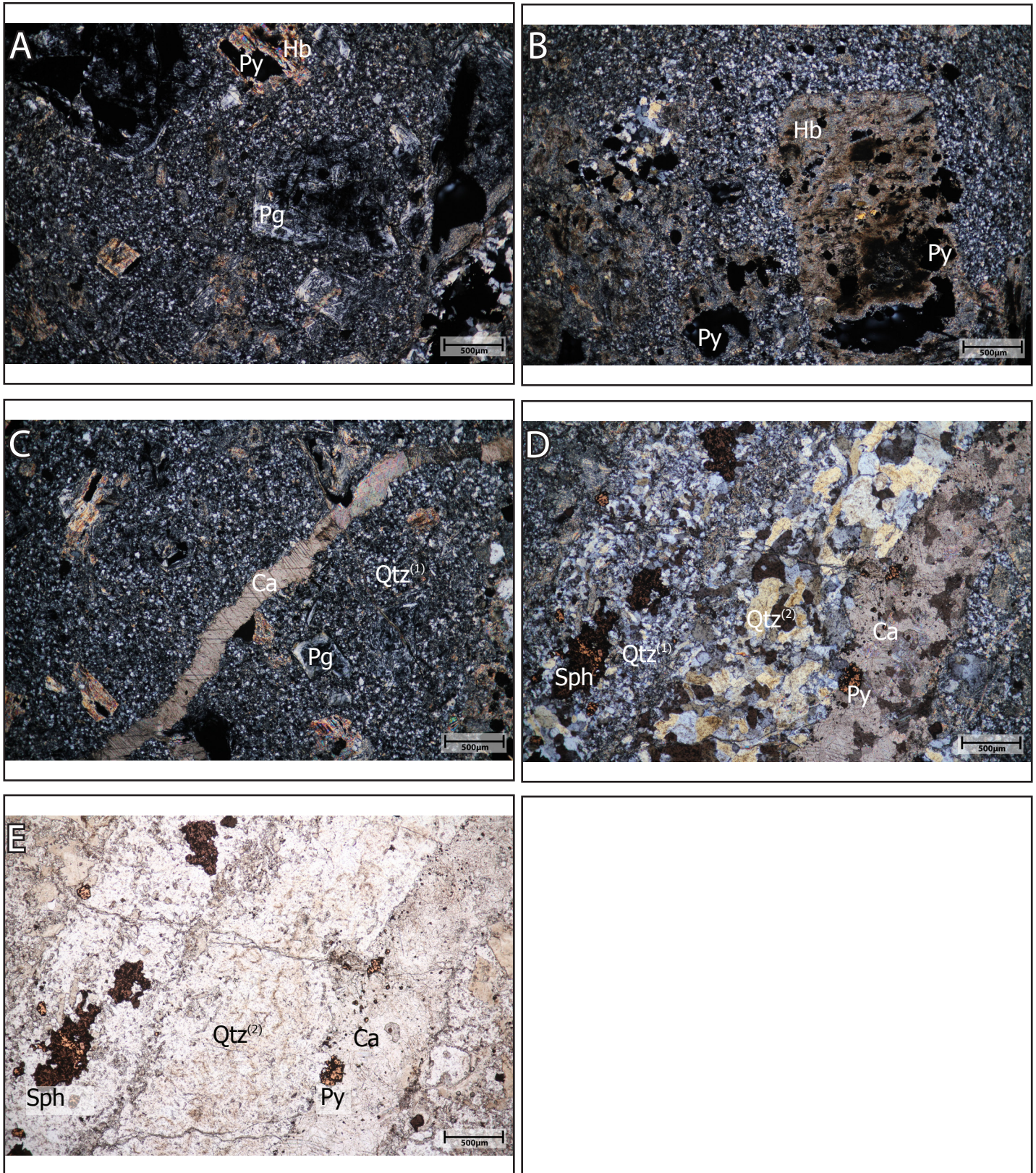


Fig 14A: Intensely altered matrix. Pyrite replacing core of hornblende, chlorite and mica/clay as a thin replacement rim around hornblende. Plagioclase is completely replaced by mica/clay at the rim and possibly albite(?) at its core, anomalous pyrite is present in Pg core. Plagioclase grains occasionally show growth zoning. Matrix is mainly composed of cryptocrystalline quartz and altered feldspar (plag). **Fig 14B:** Shows large hornblende phenocryst completely replaced by chlorite, clay, biotite and pyrite. **Fig 14C:** Late stage calcite vein cutting through host rock matrix. **Fig 14D(XPL), 14E(PPL):** Sphalerite present primarily in quartz rich zone, pyrite present at quartz-carbonate vein interface and in quartz rich part of the vein.

Sample ID: DCS S041

Hole ID: SHDDR0231

Depth: 382.4

Assay: 0.0047%Cu, 0.014%Zn, 0.02ppmAu, 0.5ppmAg

Handsample Description:

Intensely altered host rock, containing plagioclase phenocrysts, and embayed quartz eyes in an aphanitic groundmass. Quartz-Pyrite vein cutting through host rock.

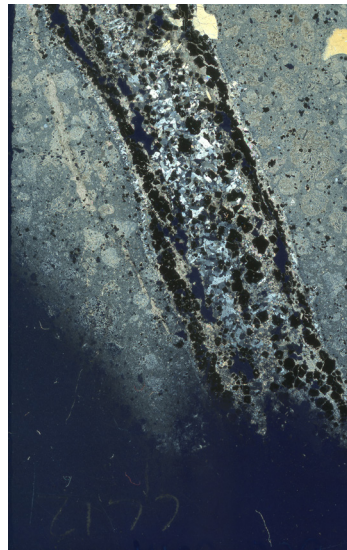


Fig 15: XPL scanned thinsection

Mineralogy:

Mineral	Relative%	Textural Description
Pyrite (Py)	25%	Masive anhedral blebbs- euhedral disseminated crystals. occurs as individual grains or interrown with sph, cpy, ga. Tt-tn and cpy sometimes shows replacement of py. Pyrite along with cpy occurs in fractures present in sphalerite.
Quartz (2) (Qtz ⁽²⁾)	13%	Prismatic/euhedral quartz associated with sph and cpy. Shows open space growing textures (comb-quartz)
Quartz (1) (Qtz ⁽¹⁾)	1%	Very fine grained anhedral quartz.
Calcite (Ca)	10%	Present as interstaial ,material in quartz or late stage veins cutting both sulphide and quartz assemblages. Fine grained to euhedral crystals showing perfect cleavage.
Wallrock Assemblage		
Plagioclase (Pg)	5%	Relict euhedral plagioclase phenocrysts completely replaced by mica/clay and minor cabronate.
Quartz	3%	Anhedral-rounded embayed quartz present in matrix. carbonate/clay alteration present in fractures and along the grain boundary.
Mica-Clay	10%	Replacing plagioclase. Very fine grained, ungingtusiabale between clay and muscovite.
Aphanitic Matrix	30%	altered plagioclase, quartz and mafic minerals
Relict Hornblende	tr	Altered hornblende (skeleton left)
Alteration		
Mica-Clay	15%	Replacing plagioclase. Very fine grained, undistingusiabale between clay and muscovite. Biotite alteration may be present(dark and very fine grained)
Chlorite	3%	Present in matrix and often rimming plagioclase and hornblende grains
Pyrite	3%	euhedral pyrite present in altered hornblende grains

Summary and Interpretation

Sample is very similar to SHDDR_247 in terms of vein and alteration. Plagioclase and hornblende and quartz phenocrysts are much large than in sample SHDDR_247. This sample is relatively more plagioclase rich compared to SHDDR_247. Intesely altered wallrock with a sulphide veinlet. Altered wallrock consists of chlorite, mica/clay, pyrite ± biotite(?) of hornblende and matrix; chlorite and mica/clay alteration of plagioclase. Sulphosalts and tellurides were not observed in vein.

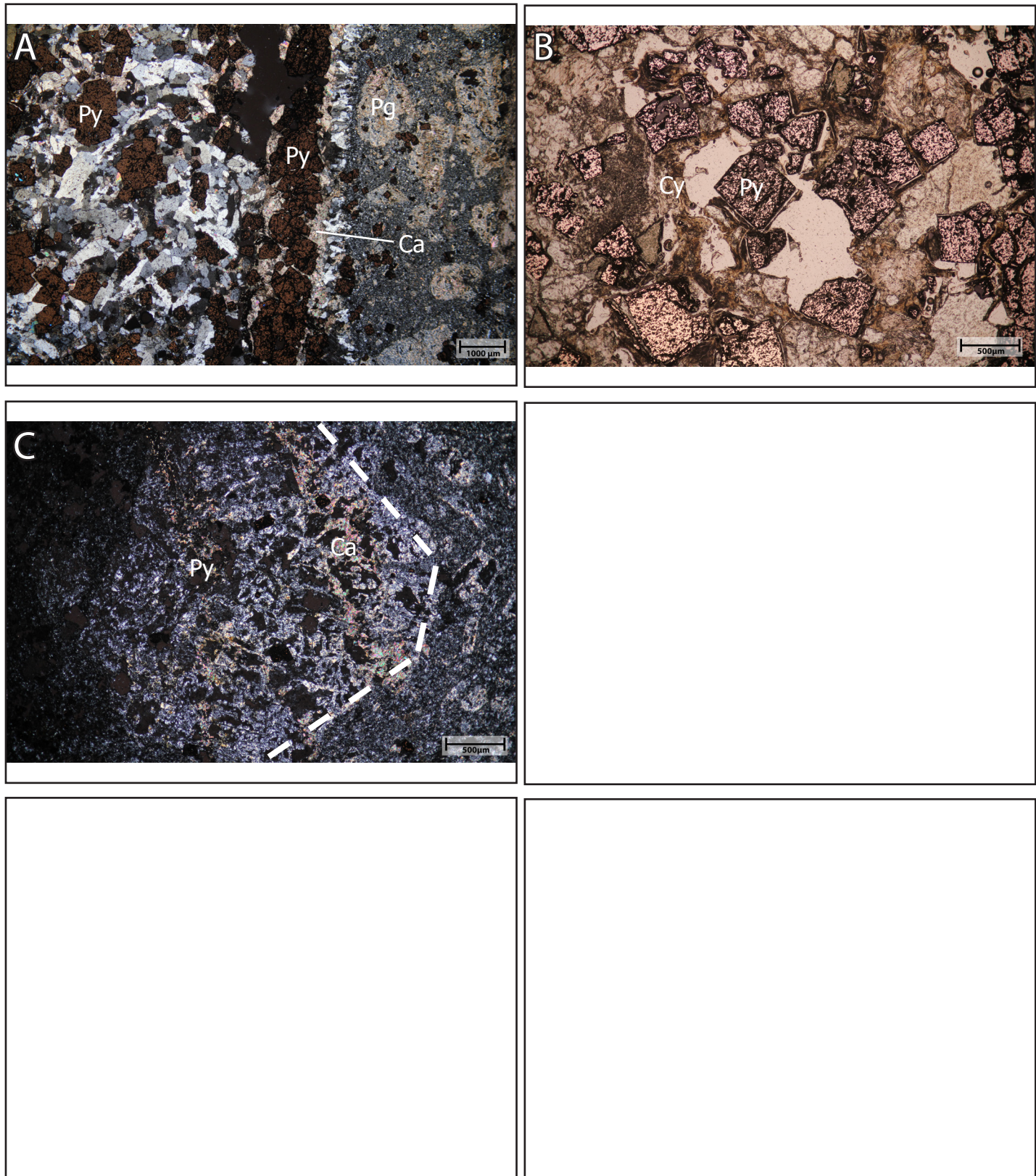


Fig 16A: Vein-wallrock interface, vein selvage shows prismatic quartz growing towards open space. Euhedral pyrite inclusions in both quartz-2 and calcite. Wallrock is intensely altered, plagioclase phenocrysts are completely replaced by mica/clay. **Fig 16B (PPL):** Euhedral pyrite with interstitial mica/clay. **Fig 16C (XPL):** Plagioclase phenocrysts in host rock replaced by albite (?) mica/clay and calcite and pyrite.

Sample ID: DCS S008

Hole ID: SHDDR0233

Depth: 324.35

Assay: 0.0063%Cu, 0.1094%Zn, 0.04ppmAu, 0.5ppmAg

Summary:

Brecciated host rock with chalcopyrite-pyrite vein, minor anomalous sphalerite.

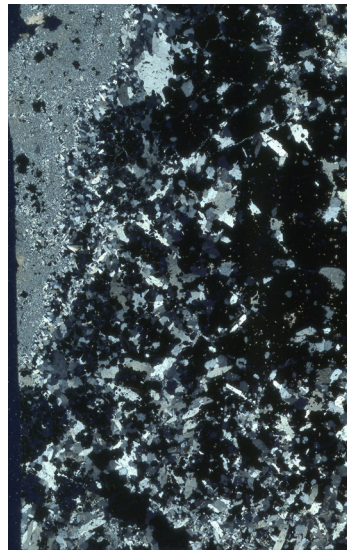


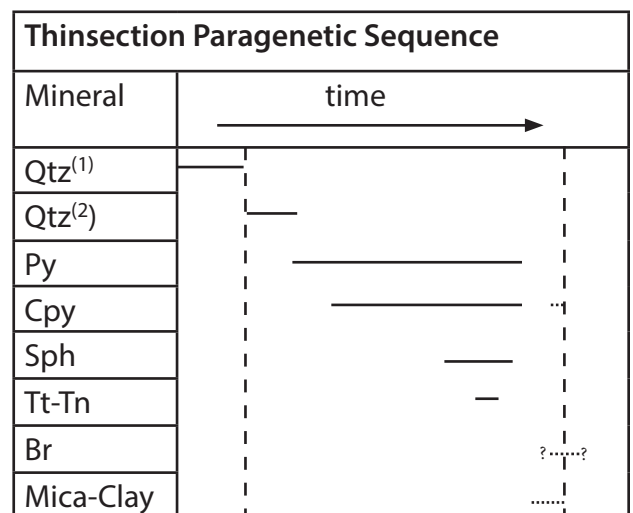
Fig 17: XPL scanned thinsection

Mineralogy:

Mineral	Relative%	Textural Description
Sphalerite (Sph)	1%	Fractured / subhedral light brown Sph intergrown with cpy and py. rare inclusions of tetrahedrite.
Chalcopyrite (Cpy)	38%	Anhedral heavily pitted blebbs intergrown with py.
Pyrite (Py)	33%	Cumulate anhedral-subhedral pyrite assemblages, intergrown with Sph. Tetrahedrite inclusion/replacement zones in pyrite
Tetrahedrite (Tt-Tn)	tr	Present primarily in pyrite and cpy grains as inclusions or replacement
Bornite(Bo)	tr	rarely replacing pyrite (?)
Quartz (1) (Qtz ⁽¹⁾)	1%	Very fine grained irregular anhedral quartz.
Quartz (2) (Qtz ⁽²⁾)	19%	Prismatic/euhedral quartz associated with Sph and Cpy. Shows open space growing textures (comb-quartz).
Mica/clay (Cy)	5%	Very fine grained mica/clay, difficult to differentiate. Interstitial to sulphides and quartz assemblages.

Summary and Interpretation

Massive chalcopyrite intergrown with pyrite and sphalerite. Despite the high amount of chalcopyrite, the bulk assay value for the meter of drill core associated with this sample shows very little Cu%. Bornite is interpreted to be replacing pyrite (?). Interstitial mica/clay infill between sulphide assemblages.



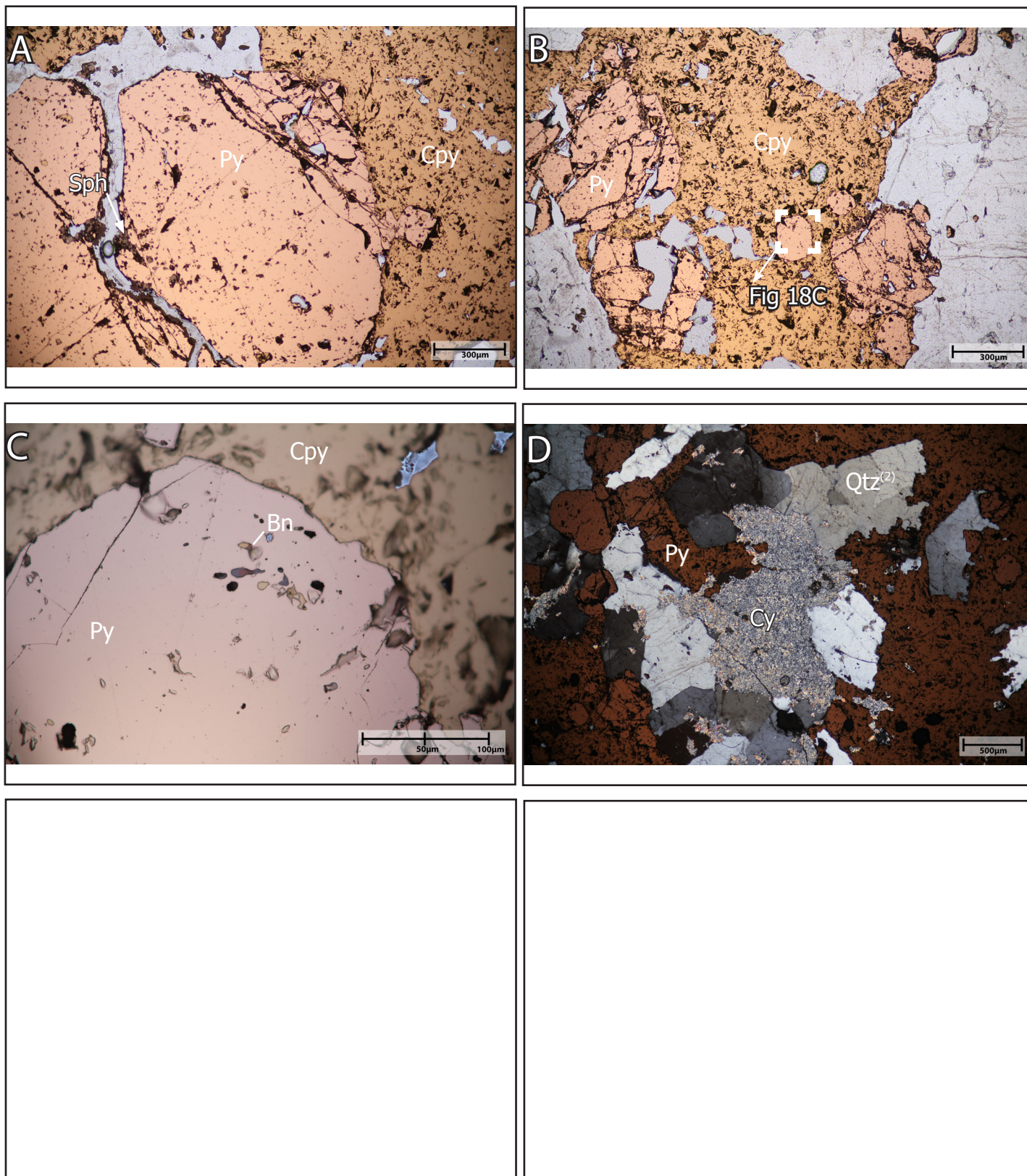


Fig 18A: Sphalerite pyrite and chalcopyrite are intergrown with each other, chalcopyrite fills fractures in pyrite. Fig 18B/C: Chalcopyrite and pyrite are intergrown, pyrite shows inclusions of Te? and bornite. Bornite appears to be replacing chalcopyrite inclusions in pyrite. Fig 18D: interstitial mica/clay in prismatic quartz-sulphide(pyrite) assemblage.

Sample ID: DCS S034

Hole ID: SHHDR0129

Depth: 194.9

Assay: 0.1604% Cu, 0.2341% Zn, 0.68ppm Au, 16.9ppm Ag

Handsample Description:

Euhedral-subhedral sphalerite, intergrown with anhedral-blebby chalcopyrite and pyrite. Interstitial quartz-carbonate. Anomalous mica/clay may be present

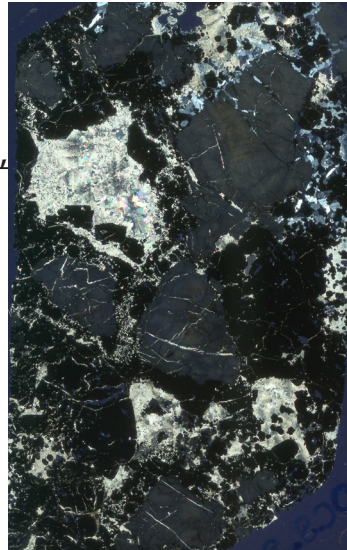


Fig 19: XPL scanned thinsection

Mineralogy:

Mineral	Relative %	Textural Description
Pyrite (Py)	30%	Cumulate anhedral-subhedral pyrite assemblages, intergrown with Sph. Tetrahedrite inclusion/replacement zones in pyrite
Sphalerite (Sph)	25%	Fractured / subhedral light brown Sph intergrown with cpy and py. rare inclusions of tetrahedrite. Growth zoning is present (dark brown-honey-brown).
Chalcopyrite (Cpy)	30%	Anhedral heavily pitted blebbs intergrown with py. Also present as sub-micron anhedral-blebbs in Sph. Also infills fractures in Sph
Tetrahedrite (Tt-Tn)	4%	Present primarily in pyrite and cpy grains as inclusions or replacement. Rarely occurs as replacement in sphalerite around rims or fractures.
Calcite(Ca)	5%	Fine -coarse grained, coarse grained crystals show cleavage.
Mica/clay (Cy)	3%	Very fine grained mica/clay, difficult to differentiate. Interstitial to sulphides and quartz assemblages. Associated with fine grained calcite.

Summary and Interpretation

Large sphalerite-chalcopyrite-pyrite vein with interstitial calcite and mica/clay. Sulfosalts are primarily present as partial-complete replacement of chalcopyrite or sphalerite. Fractures in sphalerite are infilled with chalcopyrite or calcite. Small variations seem to be present within the sulfosalt minerals observed, further analysis is required to differentiate between these phases.

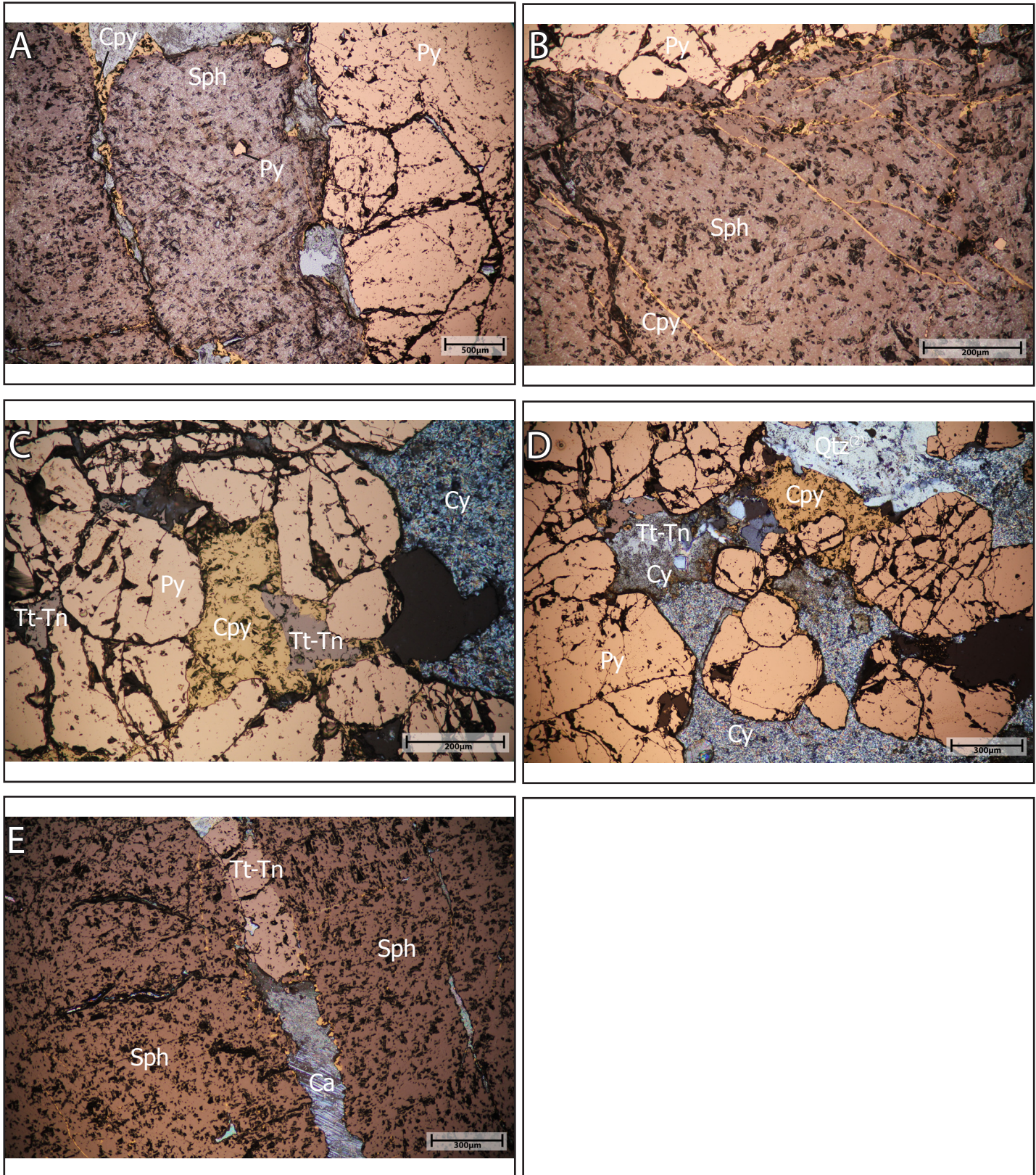


Fig 20A: Pyrite intergrown and as inclusions in sphalerite. Chalcopyrite present as replacement rims and as infill in sphalerite. Fig 20B: A higher magnification of Fig 2A, showing chalcopyrite filled fractures in sphalerite and pyrite inclusions in sphalerite. Fig 20C: Chalcopyrite as interstitial filling in heavily fractured pyrite, Tetrahedrite-Tennantite (?) partial- complete replacement of chalcopyrite. Fig 20D: Chalcopyrite intergrown with pyrite. Tt-Tn shows partial replacement of chalcopyrite. Mica/clay present interstitial to sulphides. Fig 20E: Sphalerite grains showing partial rim of chalcopyrite, Tt-Tn appears associated with sphalerite. Late stage calcite infilling/plugging veins and fractures in sphalerite.

Sample ID: DCS S037

Hole ID: SHDDR129

Depth: 308.5

Assay: 0.8574% Cu, 3.9947% Zn, 0.76ppm Au, 24ppm Ag

Handsample Description

Sulphides filling in brecciated wallrock near vein. cumulate blebby pyrite has high aspect ratios surrounded by relatively dark colored sphalerite. Wallrock intensely altered with mica and minor carbonate replacing plagioclase. Prismatic smokey quartz present similar to other vein samples (top right- Fig 21)

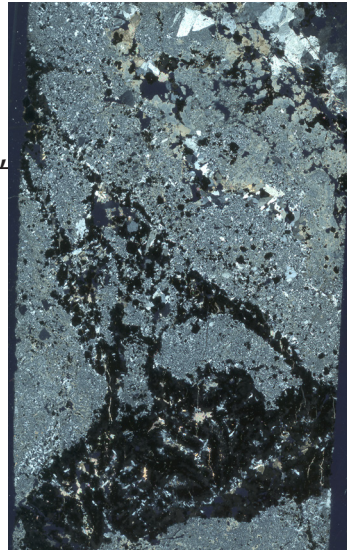


Fig 21: XPL scanned thinsection

Mineralogy:

Mineral	Relative %	Textural Description
Sphalerite (Sph)	22%	
Pyrite (Py)	18%	Large anhedral to cumulate blebby grains with high aspect ratios. Pyrite is intergrown but also as inclusions in Sph. Sph surrounding Py.
Chalcopyrite (Cpy)	3%	Present as anhedral blebbs intergrown with Py or as inclusions. A majority of Cpy in the sample is primarily present in Sph as replacement/exsolution in Sph (Cpy disease)
Tetrahedite (Tt-Tn)	3%	Primarily associated with Cpy. Partially-completely replacing Cpy,
Quartz (1) (Qtz ⁽¹⁾)	33%	Very fine grained irregular anhedral quartz, showing undulose extinction calcite and sulphide and Qtz ⁽²⁾ overprin or cut this stage
Quartz (2) (Qtz ⁽²⁾)	10%	Prismatic/euhedral quartz shows open space growth textures (comb-quartz).
Calcite (Ca)	6%	Fine grained, cleavage is not present.
Mica-Clay	4%	Very fine grained mica/clay, difficult to differentiate. Interstitial to sulphides and quartz assemblages. Associated with fine grained calcite.

Summary and Interpretation

The sample shows pyrite partially intergrown with sphalerite. The pyrite grains show a high aspect ratio architecture. The pyrite likely formed in veinlets/fractures which were then subsequently filled with Sph. Sphalerite is intensely replaced with chalcopyrite disease. Chalcopyrite -blebbs tend to be present along a preferential region in sphalerite. This preference may indicate the varying chemistry in hydrothermal fluids. Further analysing the sphalerite chemistry along these growth zones will allow us to approximate hydrothermal fluid chemistry. Tt-Tn as with other samples is associated with Cpy and Sph and are sub-micron in size.

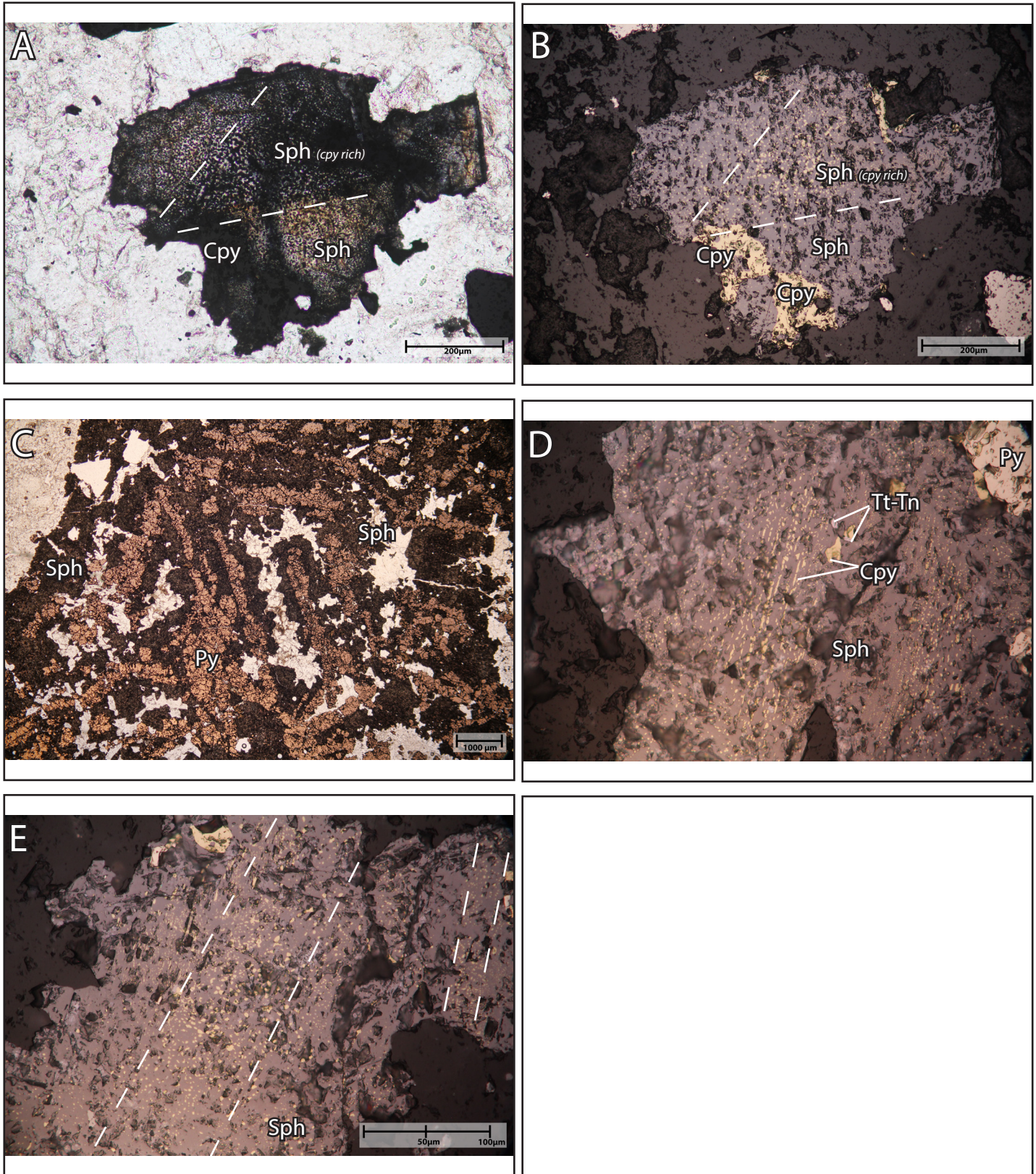


Fig 22A: PPL- Zoned sphalerite showing inclusions/replacement bodies of chalcopyrite along preferential planes. **Fig 22B- RL, PPL** same as Fig 22A. **Fig 22C:** Pyrite and sphalerite intergrown. Pyrite grains have a high aspect ratio, with sphalerite precipitating around pyrite. **Fig 22D:** An atypical texture of Cpy-disease (rods) in sphalerite, Tt-Tn? is replacing Cpy blebbs. **Fig 22E:** Both types of Cpy-disease textures, rounded blebbs and rods occur in this sphalerite grain which show zones of rich and poor Cpy-disease.

Sample ID: DCS 003A

Hole ID: SHDDR0403

Depth: 107.9

Assay: 0.174%Cu, 0.1087%Zn, 0.51ppmAu, 28.3ppm Ag

Handsample Description:

Disseminated- Blebby chalcopyrite, pyrite, and minor sphalerite with interstitial quartz and carbonate. Late stage vein cutting through sulphide assemblage

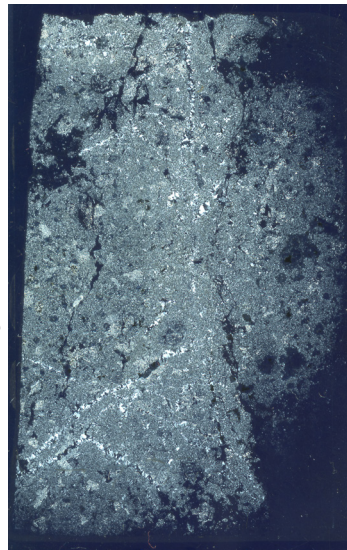


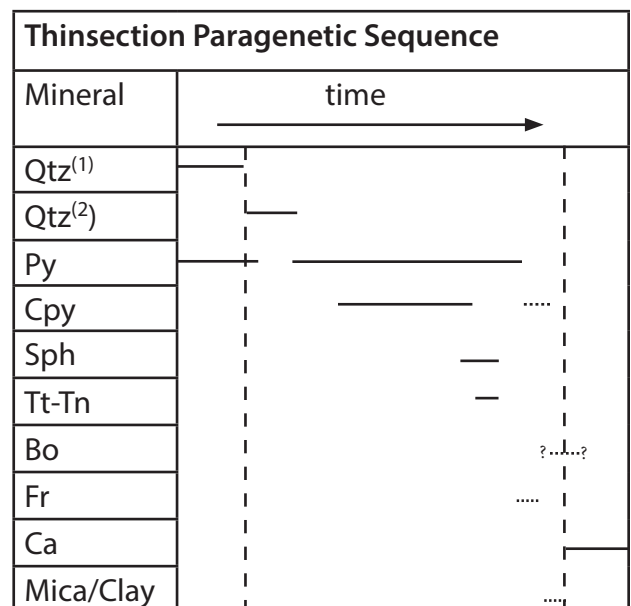
Fig 23: XPL scanned thinsection

Mineralogy:

Mineral	Relative %	Textural Description
Pyrite (Py)	20%	Disseminated euhedral to large anhedral-blebby grains. Bornite present in Py.
Chalcopyrite (Cpy)	10%	Present as anhedral blebbs intergrown with Py (also present as inclusions). Replaced by bornite and fribergite(?). Cpy partially replaces Sph in sample.
Sphalerite (Sph)	3%	Anhedral grains, replaced by Cpy and rarely Tt-Tn.
Tetrahedite (Tt-Tn)	1%	Primarily associated with Cpy. Partially-completely replacing Cpy, Uncertain of identification. SEM analysis required. Replaces Cpy
Fribergite ? (Fr)		
Bornite (Bo)	tr%	Partial- complete replacement of Cpy/Tetrahedrite-Tennantite
Quartz (2) (Qtz ⁽²⁾)	20%	Prismatic/euhedral quartz shows open space growth textures (comb-quartz).
Quartz (1) (Qtz ⁽¹⁾)	10%	Very fine grained irregular anhedral quartz, showing undulose extinction calcite and sulphide and Qtz ⁽²⁾ overprin or cut this stage
Calcite (Ca)	15%	Subhedral moderate clavage present.
Mica-Clay	10%	Very fine grained mica/clay, difficult to differentiate. Interstitial to sulphides and quartz assemblages. Associated with fine grained calcite.

Summary and Interpretation

Bornite appears to be replacing sulfosalts/ chalcopyrite inclusions in pyrite, unclear if it is a supergene processes. Sulfosalts appear to be replacing chalcopyrite present within pyrite. Several variations in sulfosalts seem to be present, fribergite is likely one of them, the others were left as Tt-Tn. Wall rock is intensely altered by carbonate, quartz, pyrite, chlorite ± mica/clay.



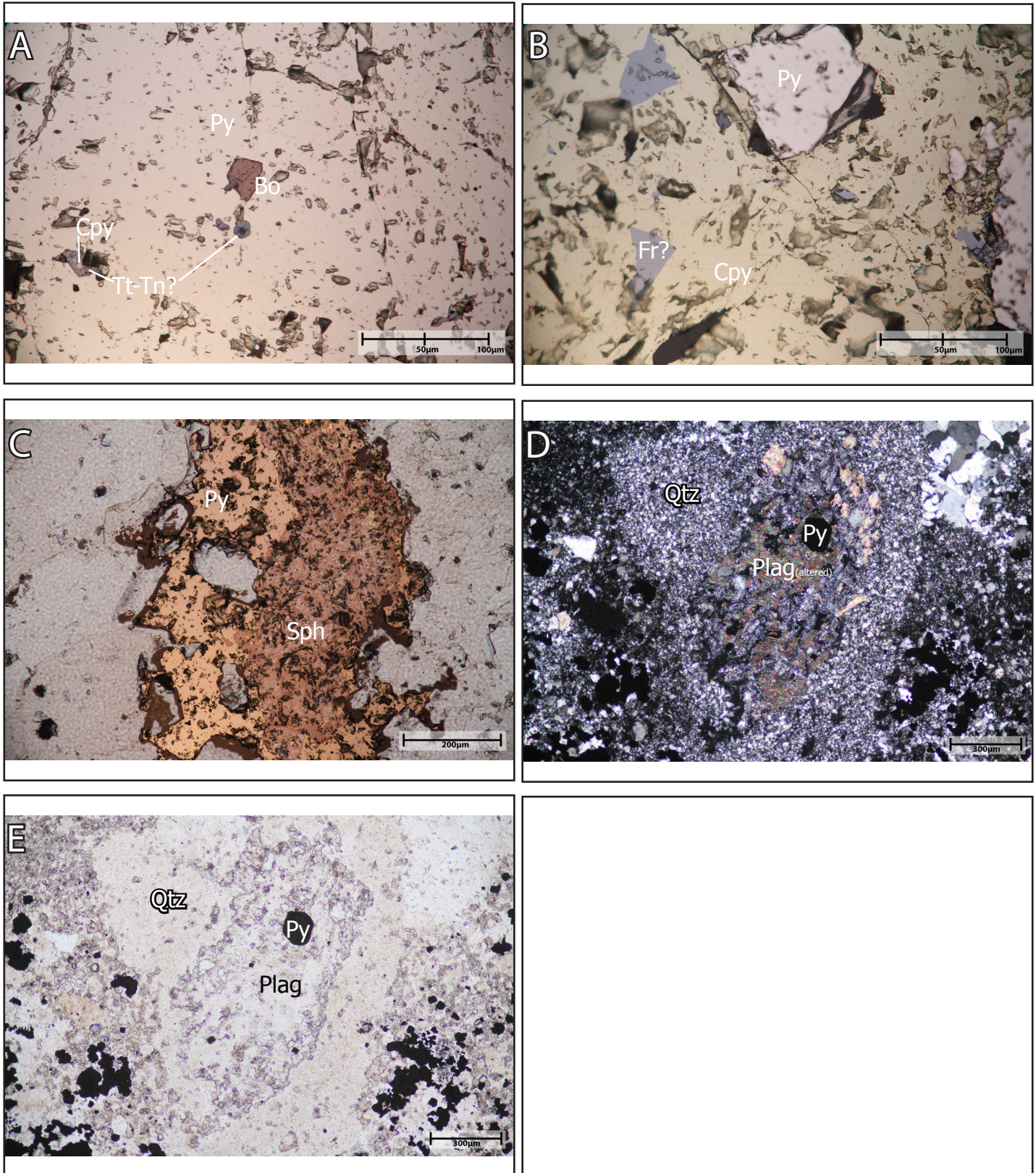


Fig 24A: Pyrite grain containing inclusions of Tt-Tn and Bo, Tt-Tn appears to replace chalcopyrite and in turn bornite replaces Tt-Tn. Fig 24B: Chalcopyrite vein with an inclusion of pyrite and unknown tellurides (likely freibergite). Fig 24C: Pyrite intergrown with sphalerite, chalcopyrite shows replacement rims and blebs in sphalerite. Fig 24D: XPL - Chlorite, Pyrite, Carbonate, Clay altered plagioclase phenocrysts. Weak pleochroism (light green-moderate green) within plagioclase crystal is interpreted to be a result of weak chlorite alteration. The phenocryst is surrounded by very fine grained quartz. Fig 24E: PPL of Fig 24D.

Sample ID: DCS S015B

Hole ID: SHDDR0016

Depth: 235.85m

Assay: 0.172%Cu, 5.74%Zn, 46.4ppmAu, 2200ppm Ag

Handsample Description:

Subhedral- blebby, sphalerite, pyrite, chalcopyrite with interstitial quartz carbonate gangue make up the vein. Wallrock is intensely altered (sericite/clay). Sulphides occur in the suture along with interstitial carbonate, vein selvage is primarily white cloudy quartz with pyrite.

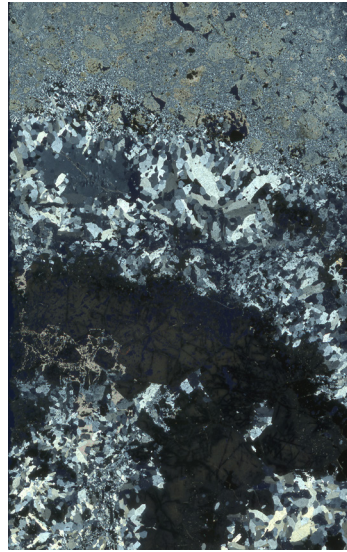


Fig 25: XPL scanned thinsection

Mineralogy:

Mineral	Relative %	Textural Description
Pyrite (Py)	12%	Disseminated euhedral to large anhedral-blebby grains. Intergrown with sph and py.
Chalcopyrite (Cpy)	10%	Present as anhedral blebbs intergrown with Py and Sph. Cpy partially replaces Sph in sample, occasionally fills fractures in Sph.
Sphalerite (Sph)	22%	Subhedral grains intergrown with pyrite and Cpy, Cpy also replaces Sph. Zones of Cpy disease present.
Tetrahedite (Tt-Tn)	1%	Found to be partially- completely replacing Cpy/Py and rarely found in Sph.
Unknown Telluride (Te?)	Tr	associated with chalcopyrite, sphalerite and pyrite found as inclusions in sphalerite, or as replacement bodies in pyrite and chalcopyrite along grain boundaries and fractures
Quartz (2) (Qtz ⁽²⁾)	15%	Prismatic/euhedral quartz shows open space growth textures (comb-quartz).
Quartz (1) (Qtz ⁽¹⁾)	5%	Very fine grained irregular anhedral quartz, showing undulose extinction calcite and sulphide and Qtz ⁽²⁾ overprint or cut this stage
Calcite (Ca)	5%	Fine grained, cleavage is not present.
Mica-Clay	2%	Very fine grained mica/clay, difficult to differentiate. Interstitial to sulphides and quartz assemblages. Associated with fine grained calcite.
Wallrock		
Plagioclase + Mafics (Matrix)	~14%	Very fine grained, completely altered? (mica/calcite)
Plagioclase (Phenocryst)	~2%	relict plagioclase replaced by mica/clay and minor carbonate.
Quartz (Embayed)	~1%	embayed quartz in matrix, altered in fractures and rim
Alteration		
Mica/Clay	~2%	partial to complete replacement of matrix and phenocrysts in wallrock
Calcite	~2%	partial replacement in matrix and phenocrysts.
Pyrite	~1%	euhedral cubic-subhedral pyrite grains present in altered plagioclase grains in the wallrock.

Summary and Interpretation

Chalcopyrite found as large anhedral grains intergrown with pyrite and sphalerite. It is also found as replacement/inclusion blebbs in sphalerite (chalcopyrite disease), or as veins in sphalerite. Tellurides are present in pyrite, sphalerite and chalcopyrite as replacement bodies along grain boundaries or along fractures. Calcite occurs as late stage infill

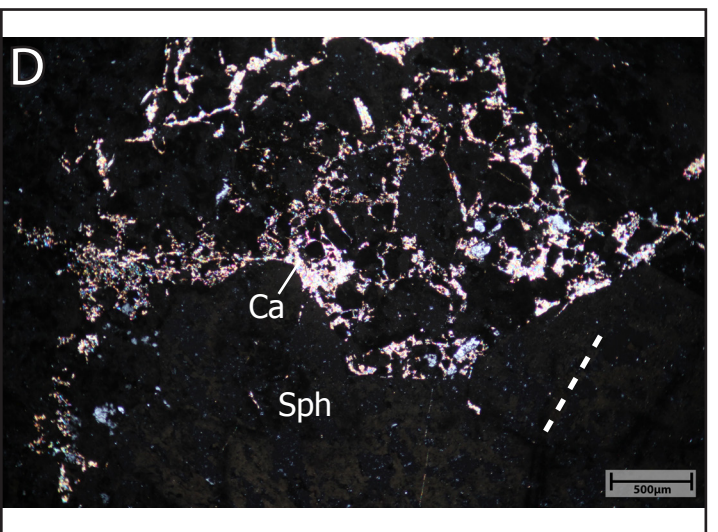
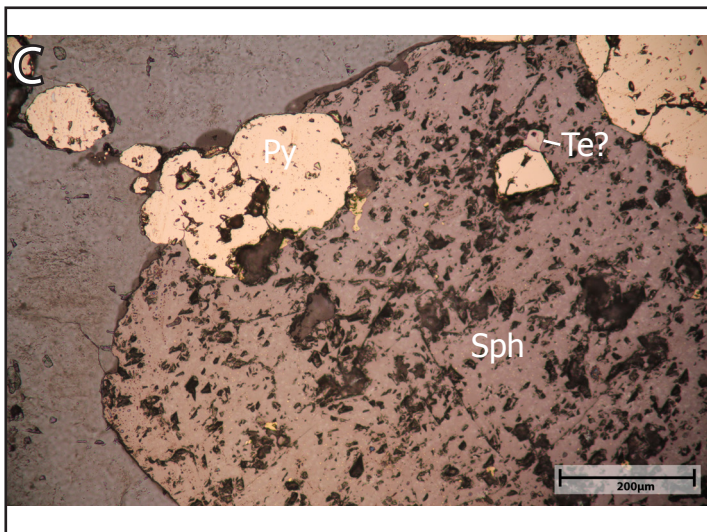
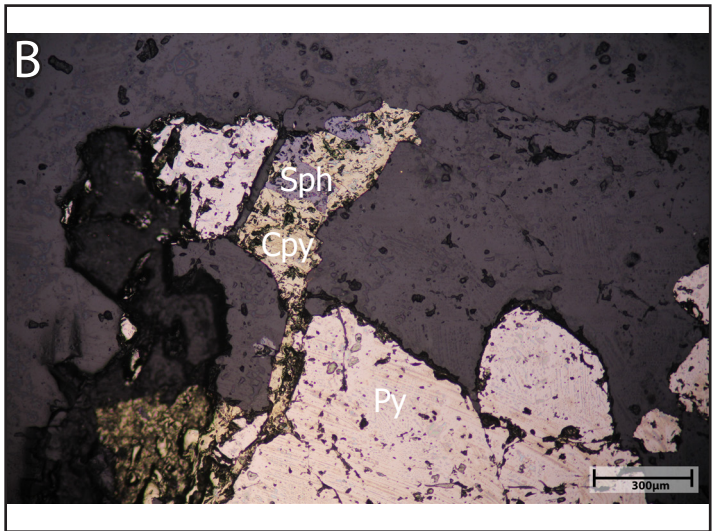
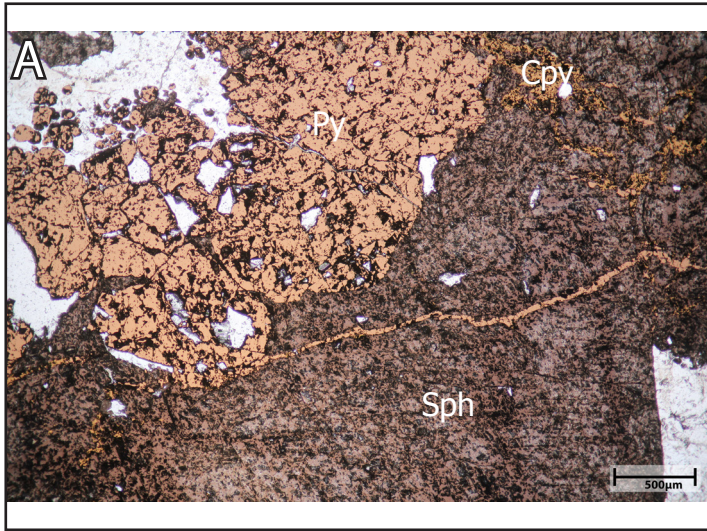


Fig 26A: Pyrite filled fracture in sphalerite, pyrite and chalcopyrite intergrown with sphalerite. **Fig 26B:** Chalcopyrite intergrown with chalcopyrite. Pyrite and chalcopyrite intergrown with each other. **Fig 26C:** Pyrite intergrown with sphalerite, unknown Telluride (Te?) associated with pyrite. Chalcopyrite replacement in sphalerite (cpy-disease). **Fig 26D:** SXPL- Calcite infilling brecciated sphalerite grain.

Sample ID: DCS S054

Hole ID: SHHDR0190

Depth: 150.25

Assay: 0.183% Cu, 2.308% Zn, 376.5ppm Au, 100ppm Ag

Handsample Description:

Blebbly and fracture filled hessite, sphalerite, chalcopyrite and pyrite. Interstitial quartz-carbonate. late stage calcite filled fractures. Highest observed grade of all examined drillcore.

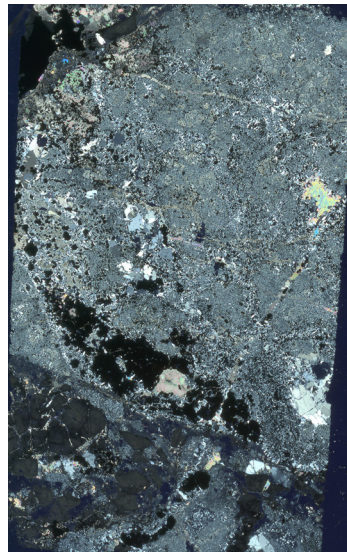


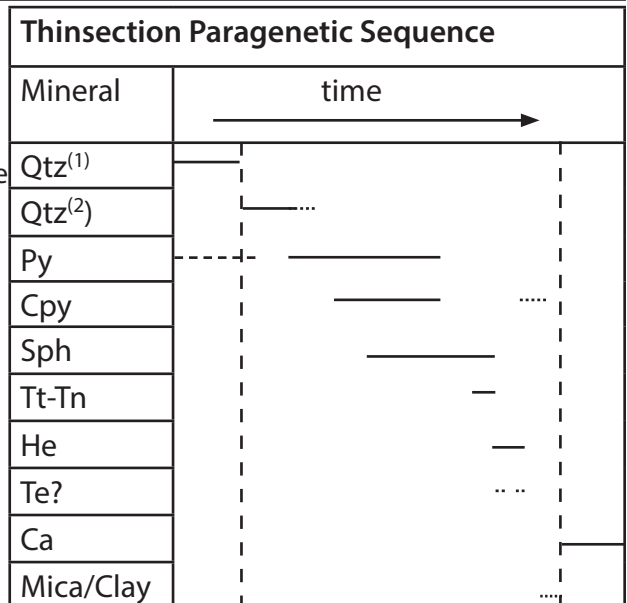
Fig 27: XPL scanned thinsection

Mineralogy:

Mineral	Relative %	Textural Description
Sphalerite (Sph)	15%	Subhedral grains intergrown with pyrite and Cpy, Cpy also replaces Sph. Zones of Cpy disease present.
Pyrite (Py)	12%	Disseminated euhedral to large anhedral-blebby grains. Intergrown with sph and py.
Chalcopyrite (Cpy)	10%	Present as anhedral blebbs intergrown with Py and Sph. Cpy partially replaces Sph in sample, occasionally fills fractures in Sph.
Hessite	7%	Large grain of hessite with inclusions of Py, Sph and unknown telluride mineral. Hessite present in fractures.
Tetrahedite (Tt-Tn)	3%	Found to be partially- completely replacing Cpy/Py and rarely found in Sph.
Unknown Telluride (Te?)	tr	Sylvanite? Coloradoite? SEM work is necessary to identify Telluride
Quartz (2) (Qtz ⁽²⁾)	10%	Prismatic/euhedral quartz shows open space growth textures (comb-quartz).
Quartz (1) (Qtz ⁽¹⁾)	35%	Very fine grained irregular anhedral quartz, showing undulose extinction calcite and sulphide and Qtz ⁽²⁾ overprin or cut this stage
Calcite (Ca)	5%	Fine grained, cleavage is not present.
Mica-Clay	2%	Very fine grained mica/clay, difficult to differentiate. Interstitial to sulphides and quartz assemblages. Associated with fine grained calcite.

Summary and Interpretation

Tellurides in section are large enough to be identified as large anhedral bodies of hessite with inclusions of altaite (?) coloradoite (?), and replacement by petzite (?). The very high Au and relatively high Ag-values likely correspond with petzite(?) and hessite. Hessite grains contain inclusions of sphalerite, chalcopyrite and pyrite. This relationship between hessite and sph,cpy,py indicates that hessite likely precipitated at a later stage.



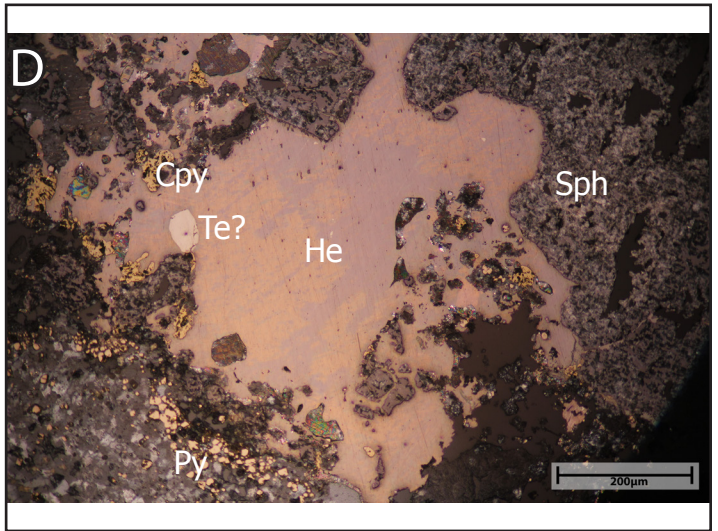
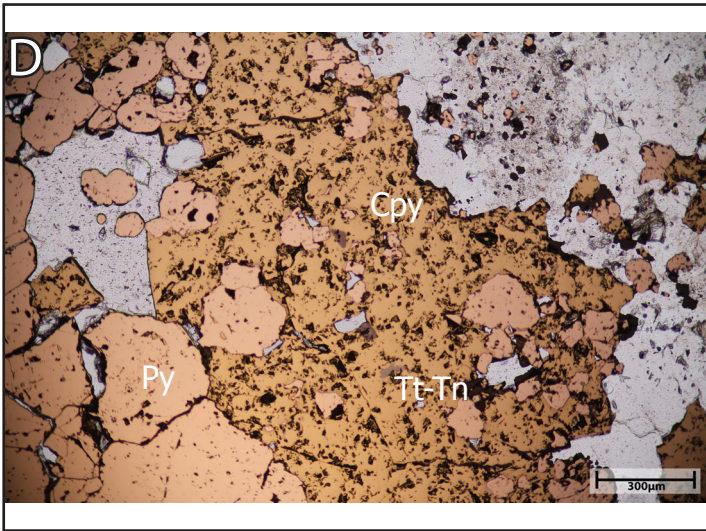
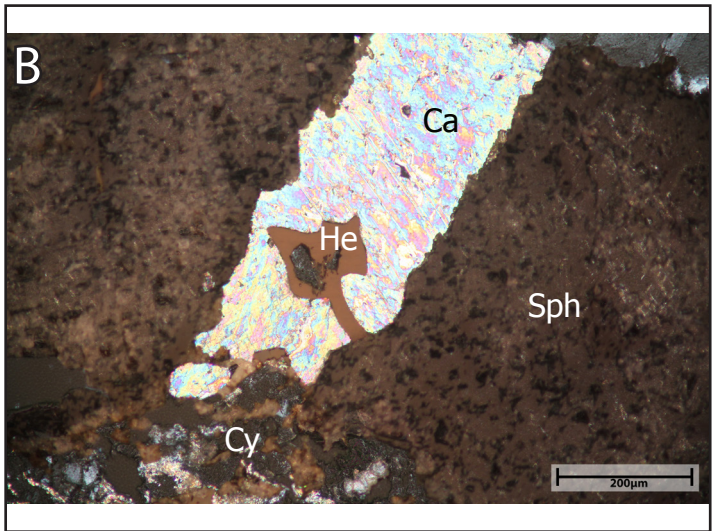
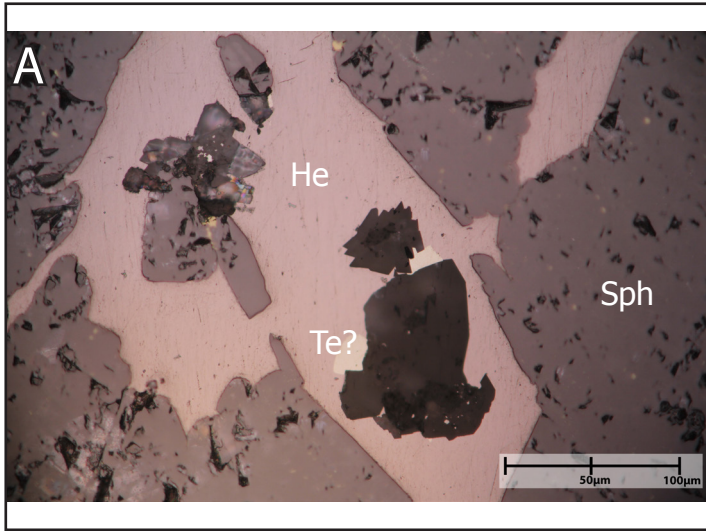


Fig 28A: PPL-Hessite interstitial with brecciated sphalerite vein, unknown telluride (Te?) replacing hessite. Sphalerite showing chalcocopyrite disease. **Fig 28B:** XPL- sphalerite inclusion in hessite, interstitial calcite present between the two sphalerite grains. **Fig 28C:** Fractured and brecciated pyrite cemented by chalcopyrite, Tt-Tn partially replacing chalcopyrite. **Fig 28D:** XPL- Large anhedral hessite grain interstitial to/ inclusions of sphalerite, unknown telluride mineral replacing hessite, anhedral disseminated pyrite present in quartz gangue.

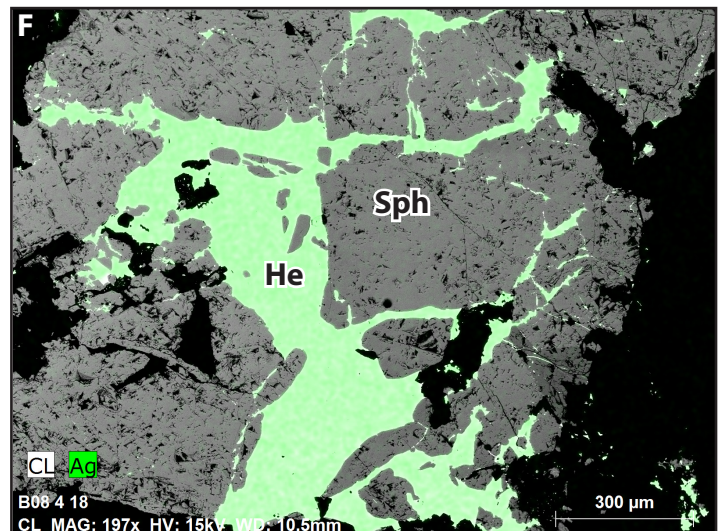
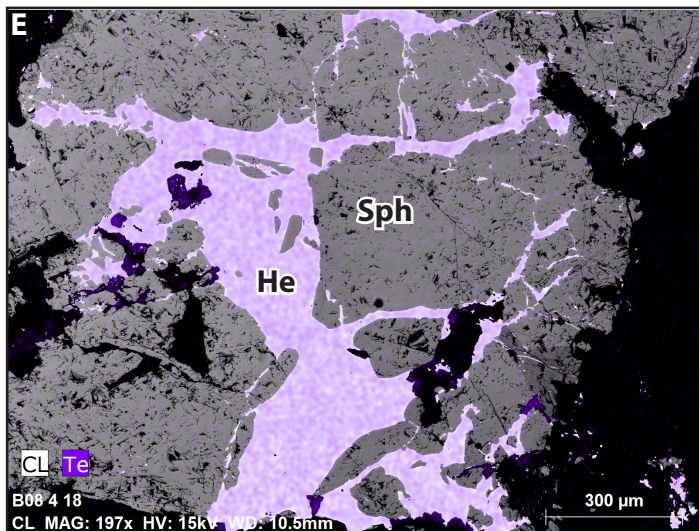
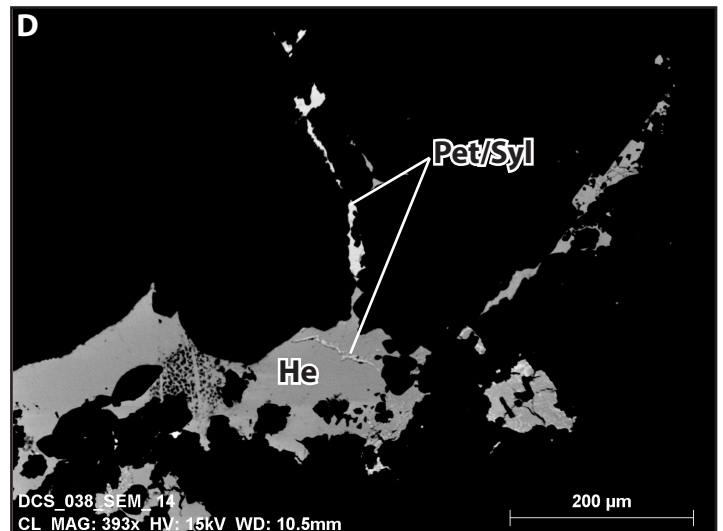
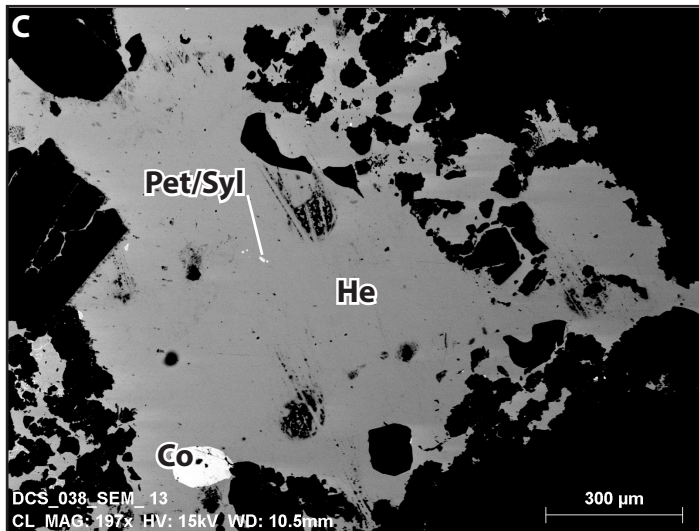
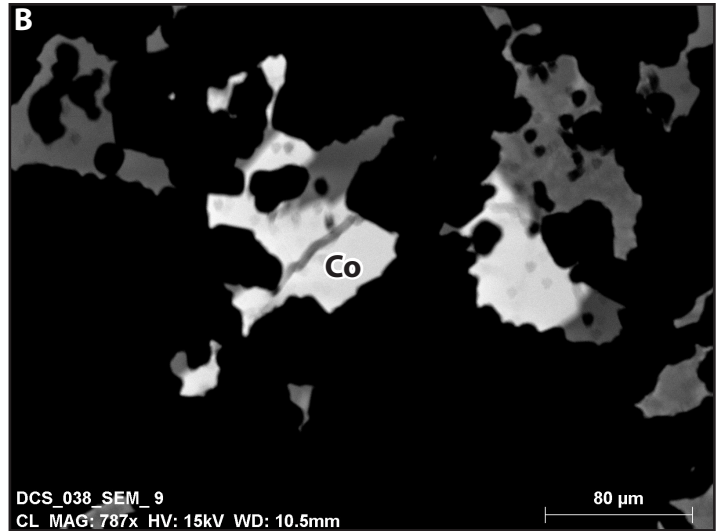
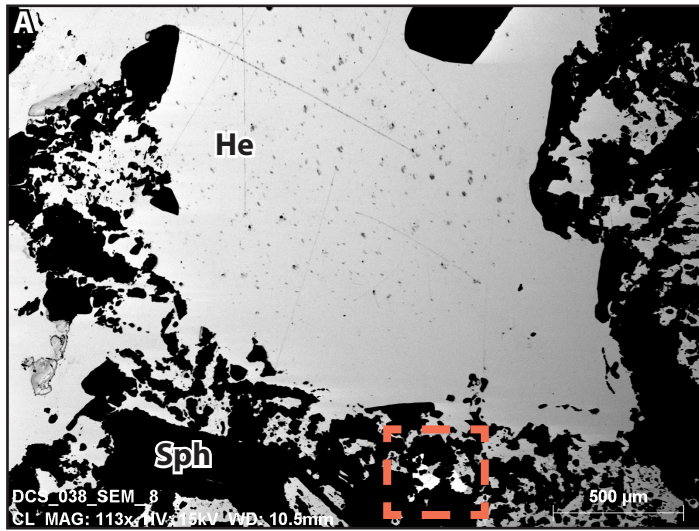


Fig 29A: Large grain of Hessite observed under reflected light, shows slight chemical variations, Fig 29B is an enlarged version of the red box in Fig 29A showing coloradoite (HgTe); Fig 29C hessite with inclusions/ replacement bodies of Pb and Au tellurides; Fig 29D shows Au telluride minerals along fractures and boundaries replacing hessite. Fig 29E and Fig 29F are elemental maps showing the distribution of Te and Ag in the FOV, native Te is observed in Fig 29E

Sample ID: DCS S038A

Hole ID: SHDDR0231

Depth: 99.2-99.4m

Assay: 1.81%Cu, 6.58%Zn, 0.72ppmAu, 42.6ppmAg

Handsample Description:

Sulphide selvage (pyrite) in contact with moderately altered wallrock. Sphalerite intergrown with pyrite. Quartz-carbonate infill at vein suture.

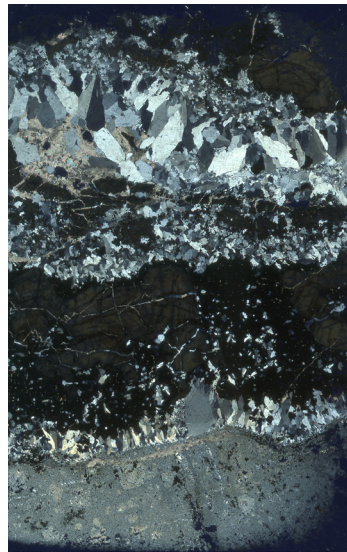


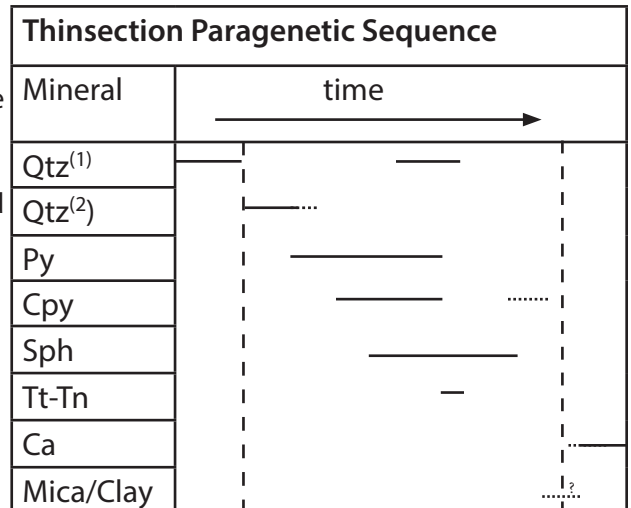
Fig 30: XPL scanned thinsection

Mineralogy:

Mineral	Relative %	Textural Descriptions
Sphalerite (Sph)	20%	Subhedral-blebby grains partial replacement by Cpy (disease) and rarely Tt-Tn. Shows growth zoning represented by varying colorations (honey-brown to greyish-brown) .
Pyrite (Py)	16%	Disseminated euhedral grains to large anhedral-blebby cumulates intergrown with Cpy, Sph. Pyrite also present in fractures. Tt-Tn replaces py occasionally.
Chalcopyrite (Cpy)	12%	Intergrown with Py, replaced by Tt-Tn, replaces/exsolution from Sph
Tetrahedrite (Tt-Tn)	4%	replaces Py and Cpy, rarely sph at rims.
Quartz (2) (Qtz ⁽²⁾)	12%	Prismatic/euhedral quartz shows open space growth textures (comb-quartz).
Quartz (1) (Qtz ⁽¹⁾)	20%	Very fine grained irregular anhedral quartz, showing undulose extinction calcite and sulphide and Qtz ⁽²⁾ overprin or cut this stage
Mica/Clay	2%	Interstitial infill, fine grained difficult to distingush between clay/mica
Calcite (Ca)	6%	Finegrained to euhedral grains with good cleavage. Present in veins cutting sulphide and Qtz ⁽¹⁾ assemblage.
Wallrock		
Plagioclase (phenocryst) (Pg)	3%	Pg phenocrysts observed with moderate to strong replacement (mica/clay)
Matrix (Plag+Hb+Qtz)	13%	Moderate alteration some are partially preserved (Fig A)
Alteration		
Mica/Clay	5%	Complete replacement to dusting of plagioclase.

Summary and Interpretation

Vein selvage contains prismatic quartz with distinct growth zones, with great fluid inclusion assemblages in addition to massive pyrite intergrown with sphalerite. Quartz contains small inclusions of sulphide indicating it likely percipitated at similar times to sphalerite. Wallrock is moderately altered plagioclase grains show fine grained clay alteration (dusting). Tetrahedrite (?) replaces chalcopyrite beginning at grain boundaries.



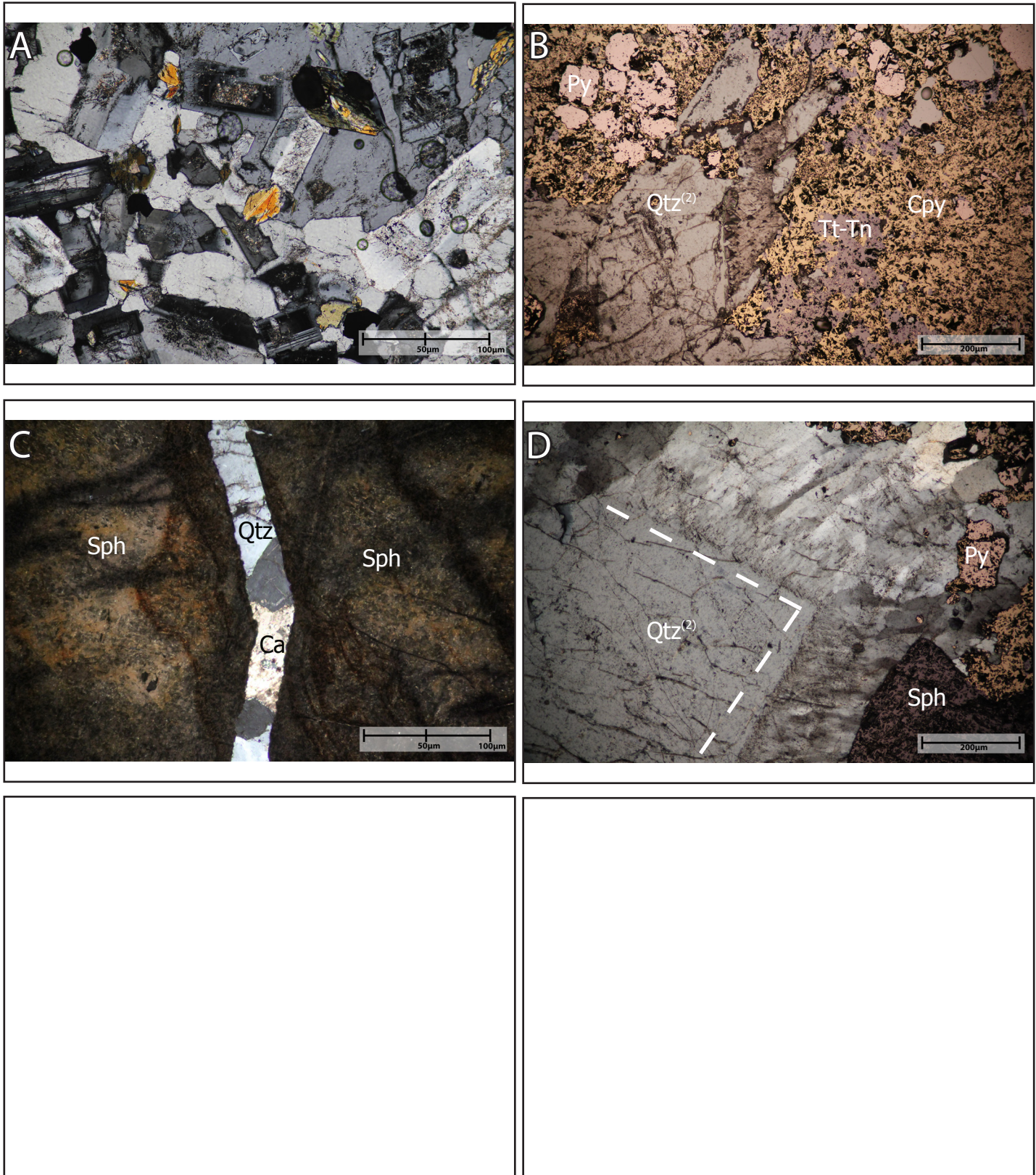


Fig 31A: Plagioclase grains partially-completely altered, mica/clay alteration. **Fig31B:** Pyrite intergrown with chalcopyrite, Tt-Tn replacing chalcopyrite. **Fig31C:** Vein filled with quartz and calcite cutting through a zoned sphaerite grain. **Fig 31D:** Prismatic quartz showing growth zones (outlined) and associated with pyrite, sphaerite and chalcopyrite.

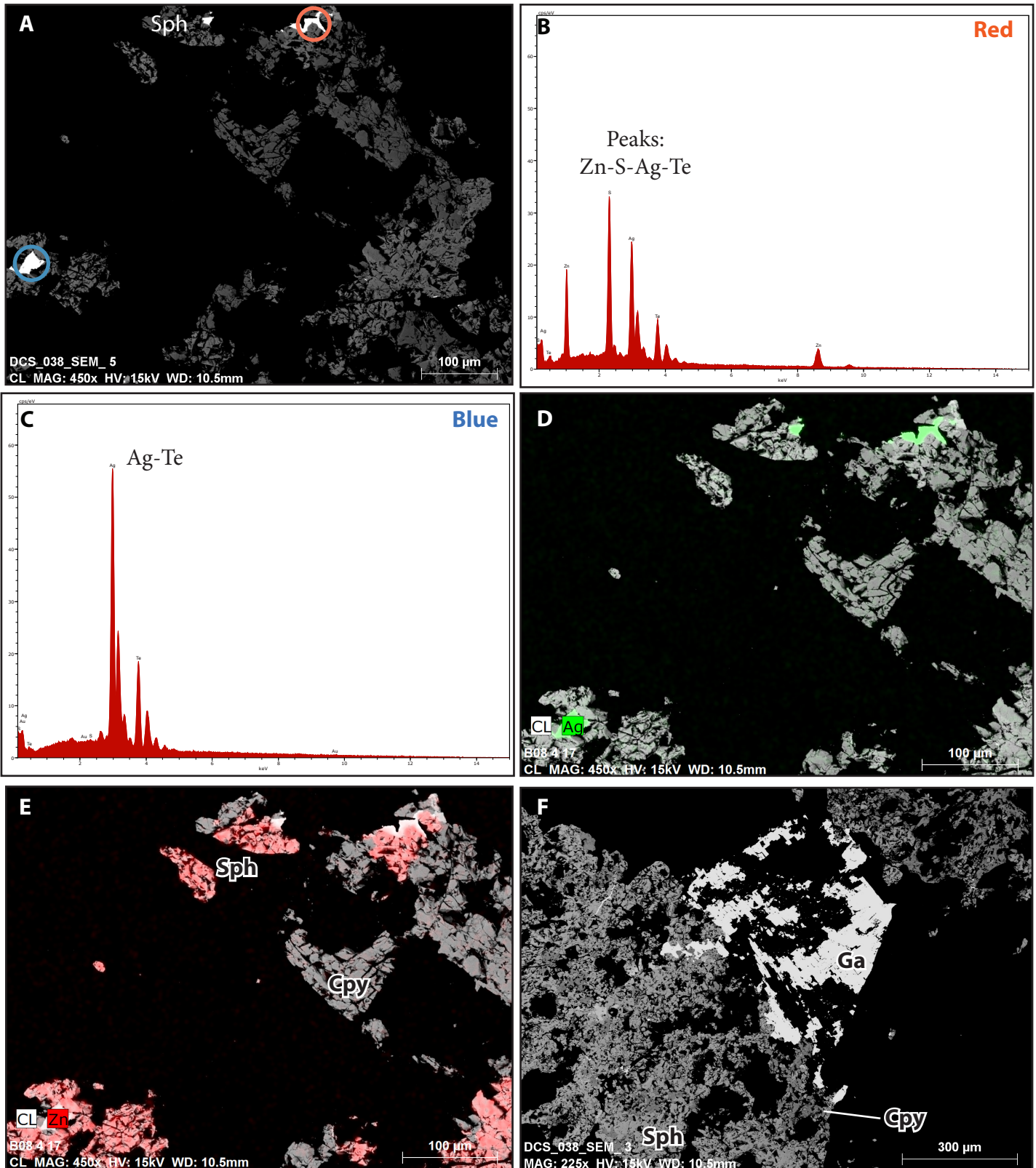


Fig 32A: Spot analysis locations shown, spectra are shown in Fig 32B and Fig 32C. **Fig 32B:** AgTe mineral (Hessite) also contains Zn and S contaminants from the sphalerite surrounding it; **Fig 32C:** Hessite (AgTe) grain with no contaminants; **Fig 32D:** elemental map showing the distribution of Ag in the FOV; **Fig 32E:** elemental map showing distribution of Zn (sphalerite) in the FOV. It shows the partial replacement of sphalerite by silver tellurides; **Fig 32F** is a grain of galena surrounded by sphalerite and chalcocopyrite.

Sample ID: DCS S095A

Hole ID: SHDDR0177

Depth: 321.9

Assay: 0.0363%Cu, 1.93%Zn, 0.14ppmAu, 3ppmAg

Handsample Description:

Intergrown anhedral-blebby sph, and minor cpy. Interstitial infill of quartz and carbonate, Minor mica/clay may be present.

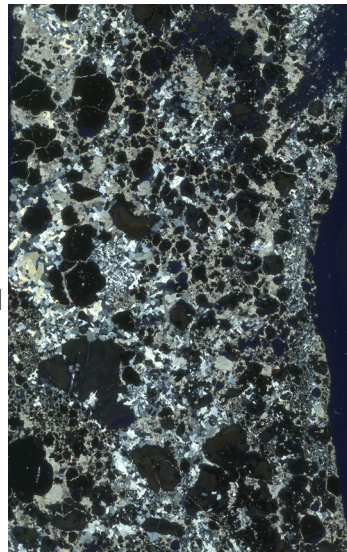


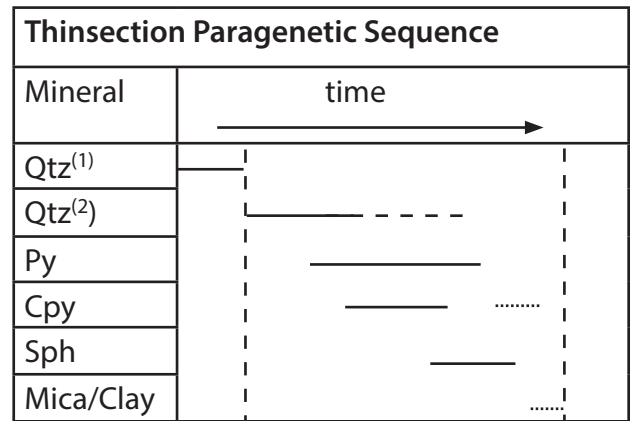
Fig 33: XPL scanned thinsection

Mineralogy:

Mineral	Relative %	Textural Description
Pyrite (Py)	25%	Cumulate anhedral-subhedral pyrite assemblages, intergrown with Sph. Tetrahedrite inclusion/replacement zones in pyrite
Sphalerite (Sph)	20%	Fractured / subhedral light brown Sph intergrown with cpy and py. rare inclusions of tetrahedrite. Growth zoning is present (dark brown-honey-brown).
Chalcopyrite (Cpy)	5%	Anhedral heavily pitted blebbs intergrown with py. Also present as inclusions/replacement in Py and Sph.
Quartz (1) (Qtz ⁽¹⁾)	30%	Very fine grained irregular anhedral quartz, showing undulose extinction calcite and sulphide and Qtz ⁽²⁾ assemblages often cut this stage.
Quartz (2) (Qtz ⁽²⁾)	5%	Coarse grained quartz intergrown with Sph and Cpy.
Calcite(Ca)	5%	Fine grained, cleavage is not present.
Mica/clay (Cy)	5%	Very fine grained mica/clay, difficult to differentiate. Interstitial to sulphides and quartz assemblages. Associated with fine grained calcite.

Summary and Interpretation

Pyrite present as both large subhedral blebbs and as disseminated anhedral- grains. Mica/clay is interstitial to quartz-sulphide assemblages. Sphalerite-chalcopyrite and pyrite show similar relationships to other thinsections observed already (e.g. DCS_S034, DCS_S008).



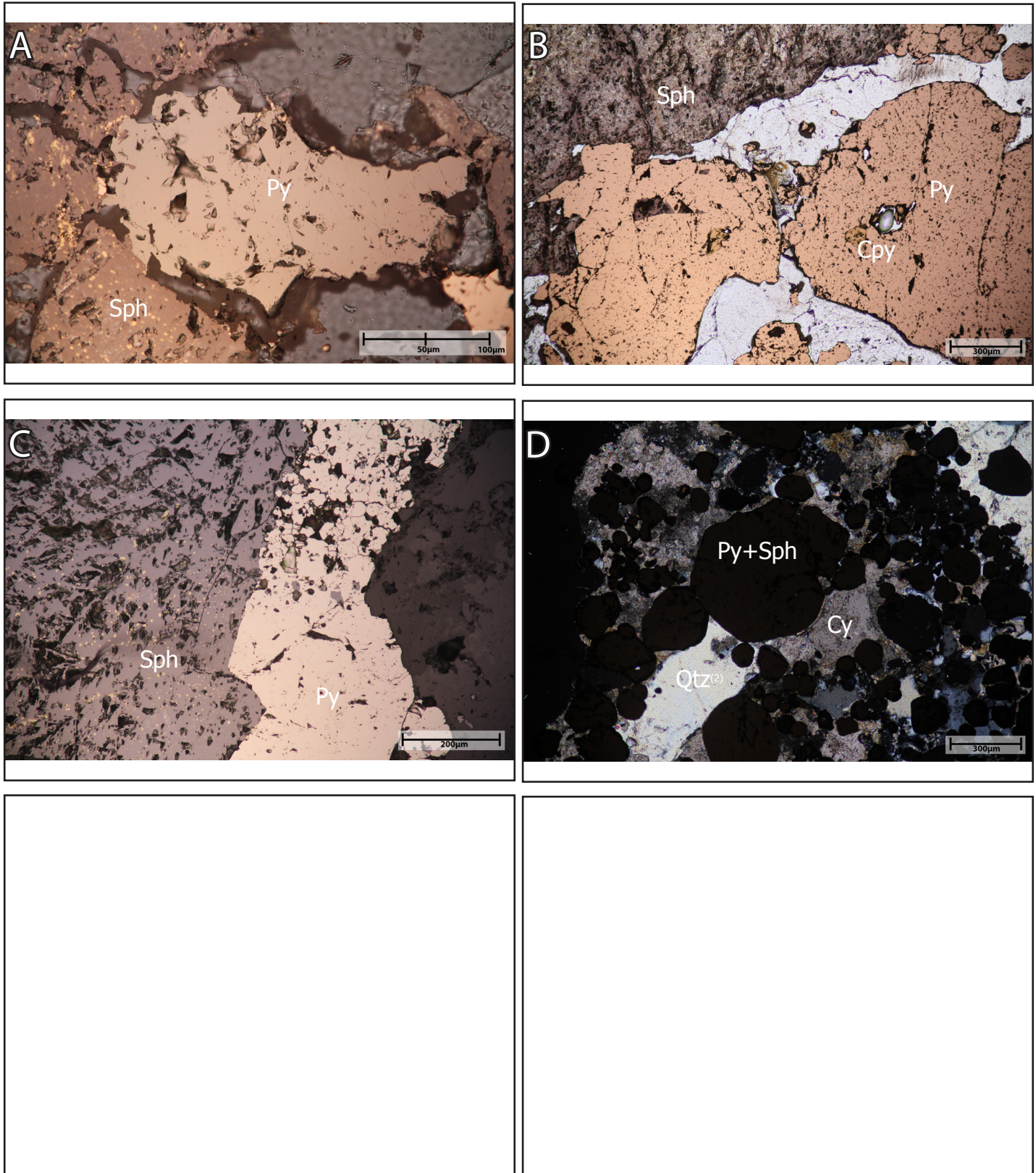


Fig 34A: Sphalerite intergrown with pyrite. Sphalerite shows chalcopyrite disease. **Fig34B:** Sphalerite intergrown with pyrite, chalcopyrite present as inclusion in pyrite and as Cpy disease in sphalerite. **Fig34C:** Sphalerite intergrown with pyrite. Sphalerite shows chalcopyrite disease. **Fig 34D (XPL):** Interstitial mica/clay (Cy) infill between sulphide and quartz assemblages.

Sample ID: DCS S095B

Hole ID: SHDDR0177

Depth: 321.8

Assay: 0.0363%Cu, 1.93%Zn, 0.14ppmAu, 3ppmAg

Handsample Description

Smokey white quartz vein cutting through brecciated sulphide assemblage. Sulphide assemblage consists of pyrite, chalcopyrite and sphalerite cemented by carbonate

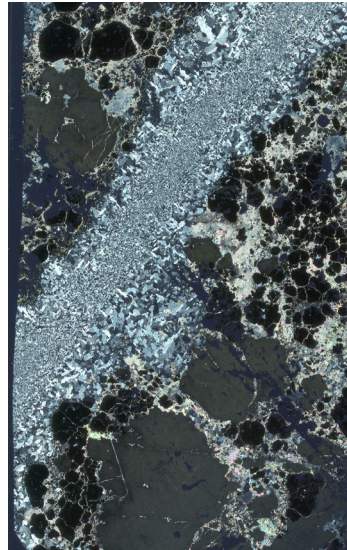


Fig 35: XPL scanned thinsection

Mineralogy:

Mineral	Relative %	Textural Description
Sphalerite (Sph)	20%	Euhedral-subhedral light brown Sph intergrown with py. Growth zoning is present (dark brown-honeybrown).
Pyrite (Py)	25%	Anhedral blebby pyrite assemblages, intergrown with Sph.
Chalcopyrite (Cpy)	tr	Present as inclusions/replacement in Py and Sph.
Quartz (1) (Qtz ⁽¹⁾)	30%	Very fine grained irregular anhedral quartz, showing undulose extinction calcite and sulphide and Qtz ⁽²⁾ assemblages often cut this stage.
Quartz (2) (Qtz ⁽²⁾)	5%	Coarse grained quartz associated with disseminated pyrite blebbs. random orientation as opposed to open space growth observed in other samples.
Calcite(Ca)	5%	Fine grained, cleavage is not present.
Mica/Clay(1) (Cl ¹)	5%	Whitish very fine grained, cut/overprinted by (Cl ²) alteration. Interstitial to sulphides and quartz assemblages.
Mica/Clay (2)(Cl ²)	5%	Yellowish very fine grained mica alteration interstitial to sulphides and quartz assemblages. Primary pathway through fractures and hydrothermal flow zones.

Summary and Interpretation

DCS_S095B is taken from same interval as DCS_S095A, and shows similar sulphide textures however, the sample shows a quartz vein crosscutting sulphide assemblage. Quartz present in the vein shows two stages of quartz (fine-grained and coarse grained). Coarse grained quartz in this section does not show prismatic growth, and is randomly oriented.

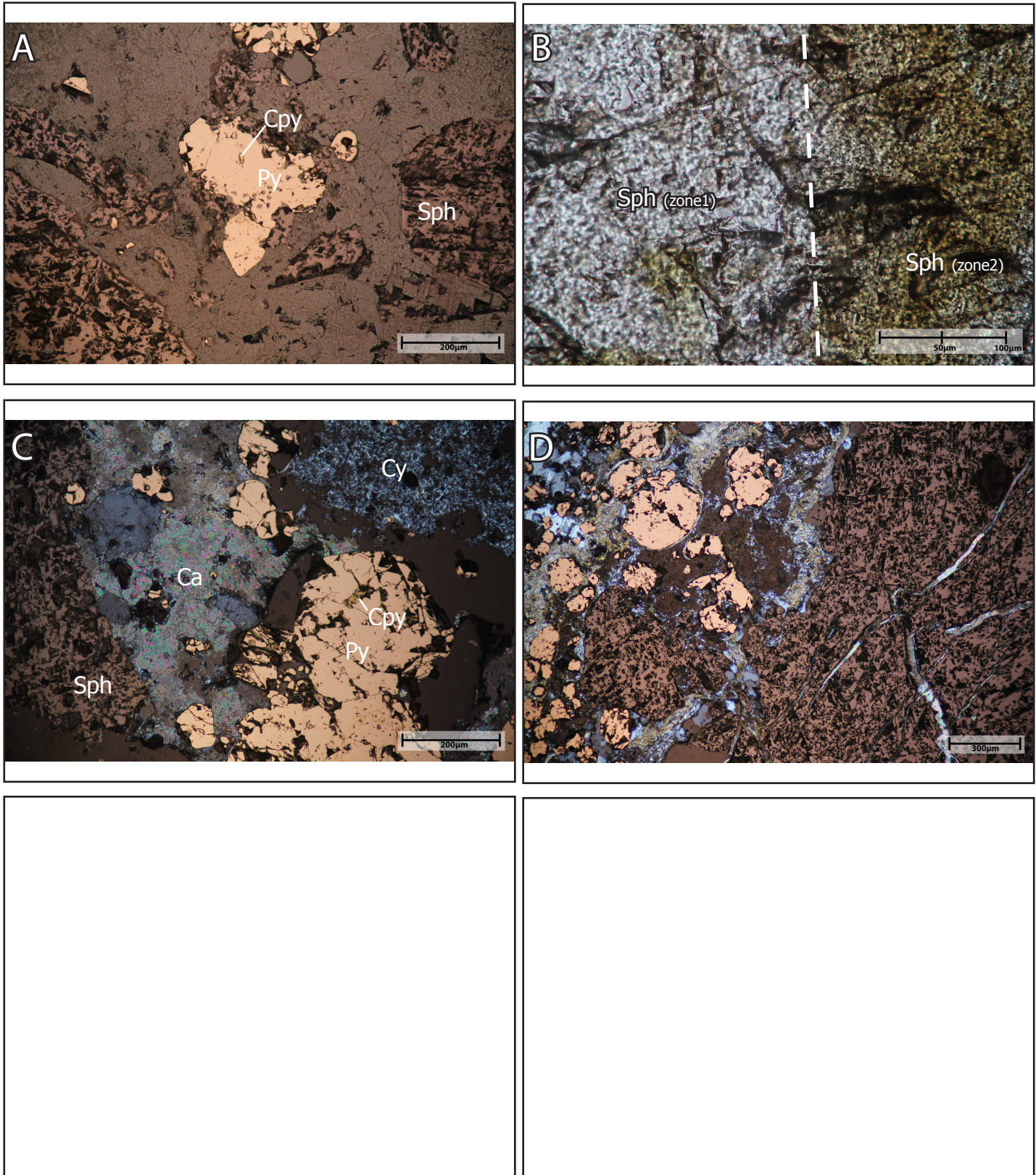


Fig 36A: Sphalerite intergrown with pyrite. Chalcopyrite present as replacement blebbs in sphalerite and as inclusions in pyrite. Fig 36B: Zoned sphalerite showing submicron inclusions/replacement of chalcopyrite in the honey brown zone with none present in zone 1 of sphalerite. Fig 36C: Chalcopyrite inclusions in pyrite, calcite and clay present as interstitial infill between sulphide assemblages. Fig 36D: fractured sphalerite and rounded pyrite grains present in an interstitial mi-ca/clay rich matrix. Fractures in sphalerite in-filled with calcite.

Sample ID: DCC S009

Hole ID: CEED07

Depth: 225.55

Assay: N/A

Handsample Description:

Quartz-sulphide chlorite vein hosted in andesite. Host rock contains porphyritic 0.5-1.5mm hornblende and altered plagioclase grains in a aphinitic matrix. Plagioclase grains are altered to clay and chlorite. Hornblende show pyritic alteration. Vein contains large grains of pyrite and chalcopyrite in a quartz-chlorite gangue. Minor interstitial calcite is also present

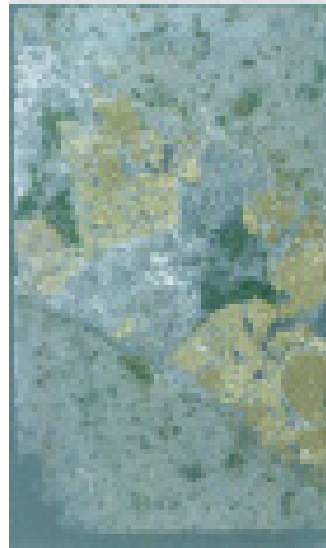


Fig 37: Scanned thinsection

Mineralogy:

Mineral	Relative %	Textural Descriptions
Pyrite (Py)	11	Anhedral blebbs. Pyrite is also present infilling fractures
Chalcopyrite (Cpy)	20	Replacing hornblende?
Quartz (2) (Qtz ⁽²⁾)	14	Prismatic coarse grained quartz associated with sulphides. show open-space growing (comb quartz)
Mica/Clay	7	Fine grained, replacing plagioclase grains and rimming hornblende grains
Calcite (Ca)	3	Interstitial material between quartz, and sulphide grains
Chlorite (Chl)	8	Present as radial fibrous grains in vein
Wallrock		
Amphibole (phenocryst) (Hb)	tr	minor relict amphiboles, a majority is completely altered to chlorite and dessiminated pyrite.
Plagioclase	tr	minor relict plagioclase present, a majority of primary plagioclase is completely altered to mica/clay.
Quartz	5	very fine grained, present in matrix. overprinted/ altered with mica/clay
Alteration		
Chlorite (Chl)	15	complete-partial replacement of mafics
Epidote (Ep)	tr	Complete-partial replacement of mafic minerals.
Mica/Clay	15	Complete to partial replacement of plagioclase and mafic grains.

Description and Interpretation

This sample has been taken from Centralni West along with two other samples: DCC_S026A and DCC_S017. All three samples show Cu mineralization, as opposed to the polymetallic type mineralization observed in samples thus far. Alteration assemblages are very similar to samples from Shahumyan, showing a sericite/illite, quartz assemblage overprinting the initial chlorite rich assemblage. This sample shows hydrothermal chlorite within the quartz-sulphide vein which may indicate higher temperature fluids. The hydrothermal chlorite within the vein shows a radiating crystal morphology and has a blueish-purple interference color which may indicate higher Fe- content. Chlorite in the host rock completely replaces mafic minerals (hornblende) and is considerably has a more bluish interference color compared to the vein chlorite. Pyrite grains are brecciated, and also present along minor veinlets/ fractures.

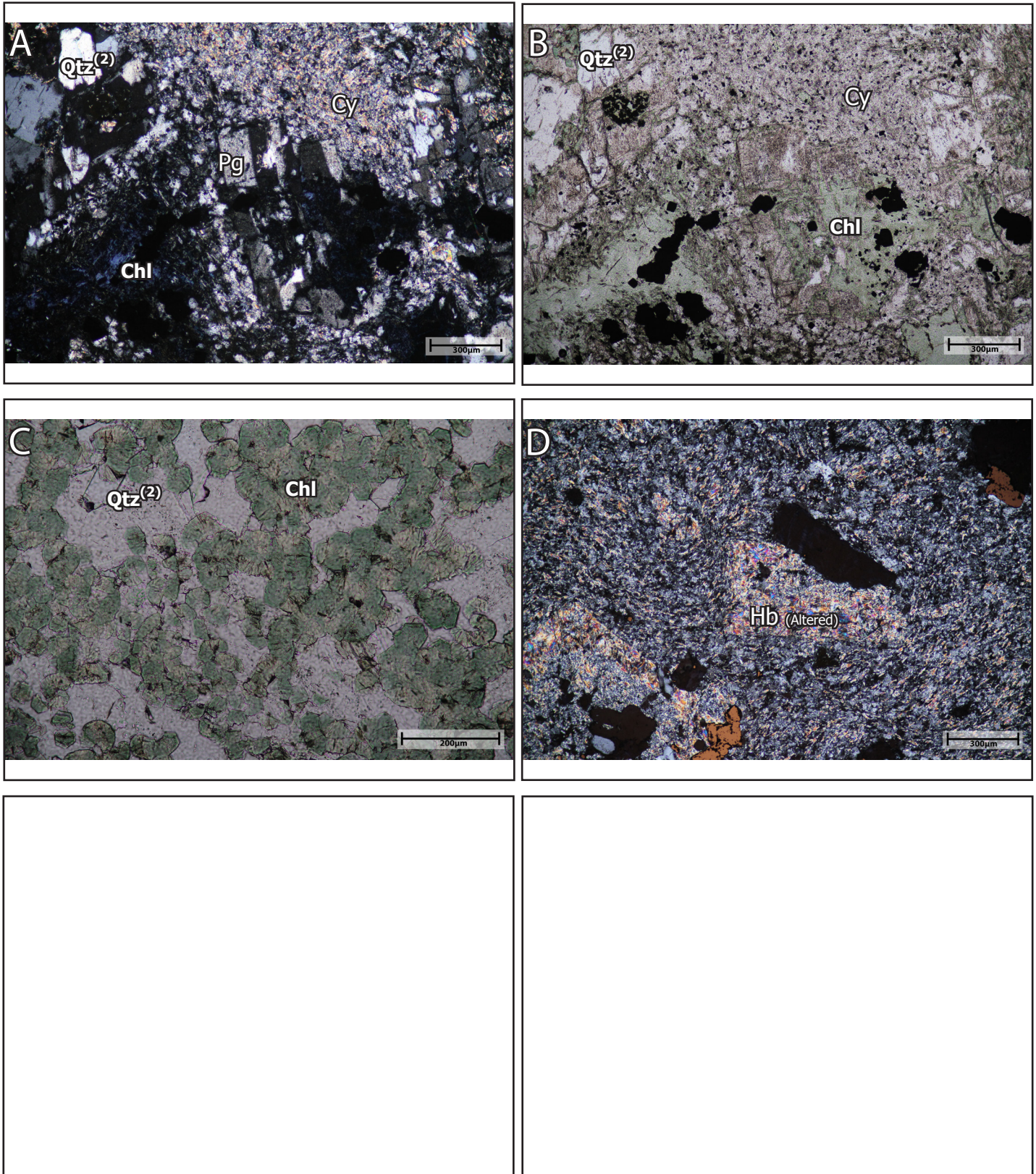


Fig 37A: XPL- Plagioclase altered to mica-clay, amphiboles completely replaced by Fe-rich chlorite. Fe-rich chlorite also rims plagioclase grains. Fig 36B: PPL view of Fig 36A. Fig 36C: Radial Fe-rich hydrothermal chlorite is present within vein material and is interstitial to prismatic quartz. Fig 36D: Hornblende altered to epidote and chlorite.

Sample ID: DCC S026A

Hole ID: CEDDE05

Depth: 222.35

Assay: N/A

Hand Sample Description:

Quartz sulphide vein, hosted in andesite. Host rock is strongly fractured and subsequently mineralized. Chalcopyrite is anhedral and very coarse grained, whereas pyrite is subhedral to anhedral and medium to coarse grained. Hostrock fragments within the vein appear to be initially chlorite altered and subsequently strongly silicified.

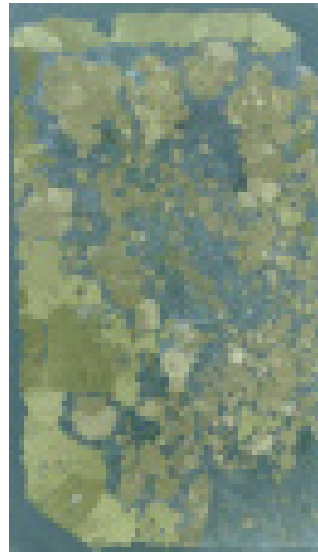


Fig38: Scanned thinsection

Mineralogy:

Mineral	Relative %	Textural Descriptions
Pyrite (Py)	20	Subhedral-euhedral crystals, heavily fractured and slightly higher reflectance than Py ² and occurs as inclusions or is intergrown with Cpy
Chalcopyrite (Cpy)	23	Disseminated to large anhedral grains heavily pitted with a slightly lower reflectance than Py. Associated with Py grains which are either intergrown or occur as inclusions.
Quartz (Qtz)	40	Medium to coarse grained crystals showing undulose extinction
Calcite (Ca)	2	Medium sized interstitial grains between sulphide and quartz grains.
Mica/Clay (Cl)	8	Fine to medium grained crystals showing radial textures
Chlorite (Chl)	7	Accumulation of radial aggregates of chlorite, likely Fe rich

Description and Interpretation

Sulphide vein within an andesite hostrock, the hostrock is not observed in this sample. Chlorite is interpreted to be part of vein material which likely precipitated from hydrothermal fluids. The bluish-purple interference color suggests the chlorite has a higher Fe-content. Hydrothermal sericite/clay is found to be interstitial between quartz and sulphide grains.

Thinsection Paragenetic Sequence	
Mineral	time →
Qtz	_____
Py	----- _____ -----
Cpy	_____
Ca	_____
Chl	—?— _____
Mica/Cl	—?— _____

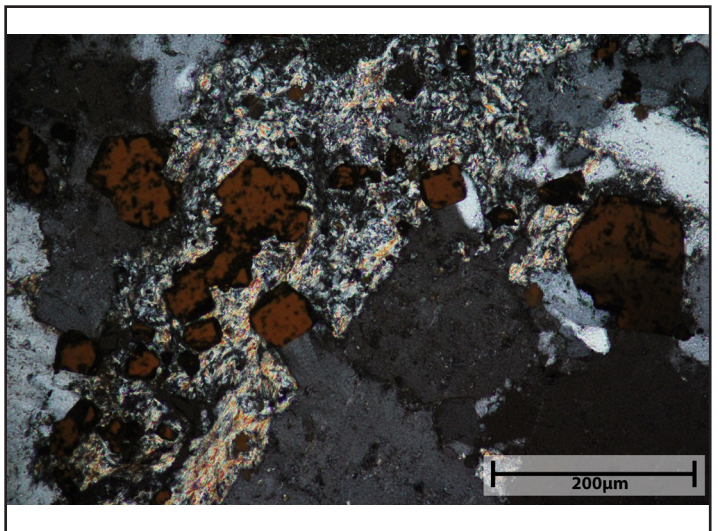
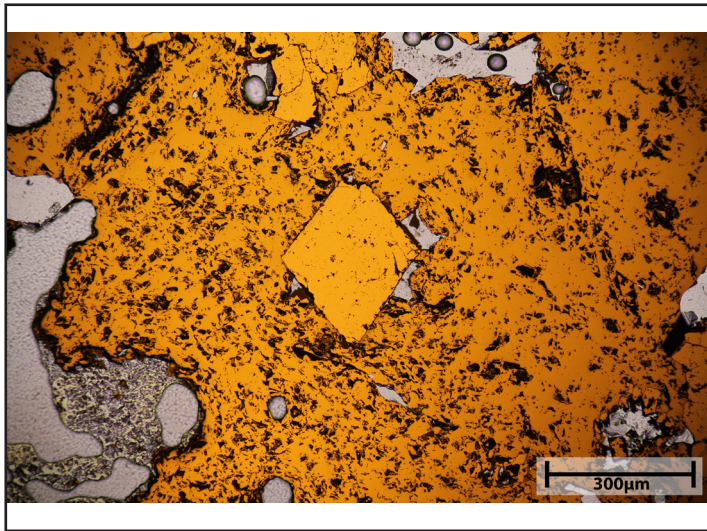
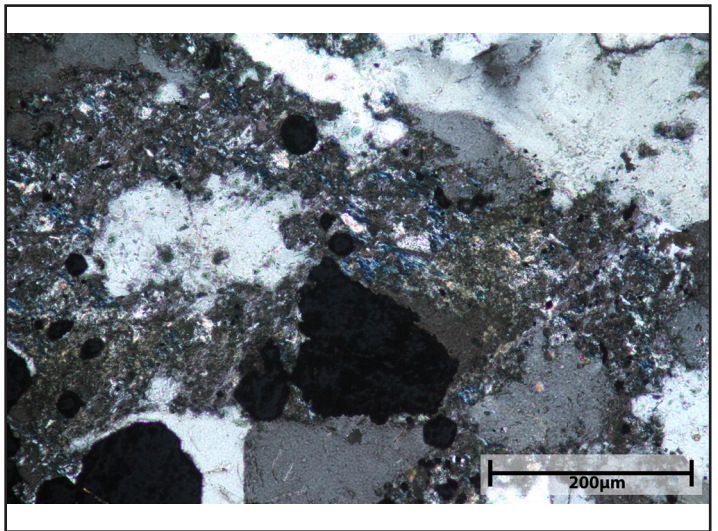
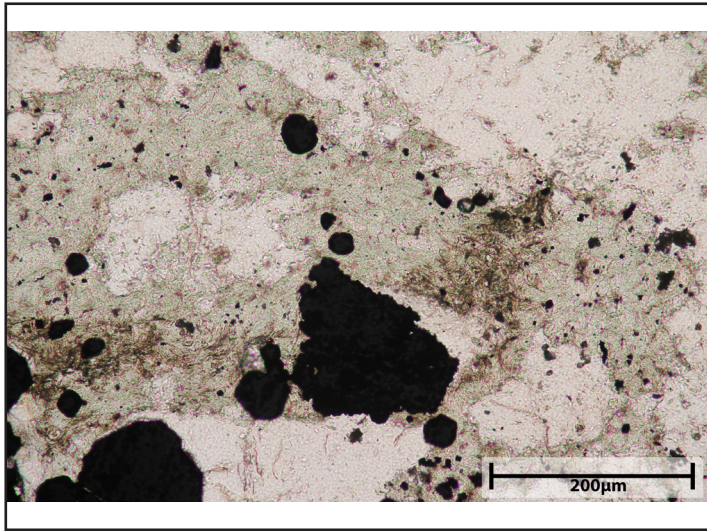


Fig 39A: (PPL) Chlorite and mica/clay alteration overprinting quartz grains. Fig 37B: XPL-microphotograph of Fig 37A, second order blue- purple interference color indicates Fe-rich chlorite. Fig 37C: Two stages of pyrite present, Cpy is interpreted to be the later stage with inclusions of sub- euhedral Py grains. Fig 37D: Medium to coarse grained muscovite.

Sample ID: DCC S017

Hole ID: CEDDE06

Depth: 146.9

Assay: N/A

Handsample Description:

A sulphide vein within an andesite hostrock. Andesite is strongly silicified with minor sericite/clay alteration. Chalcopyrite is anhedral and coarse grained whereas pyrite is subhedral and medium grained. Pyrite and chalcopyrite appear to be interstitial.

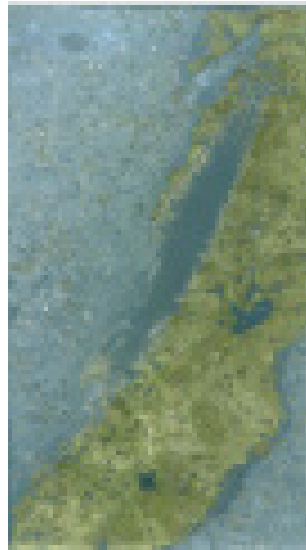


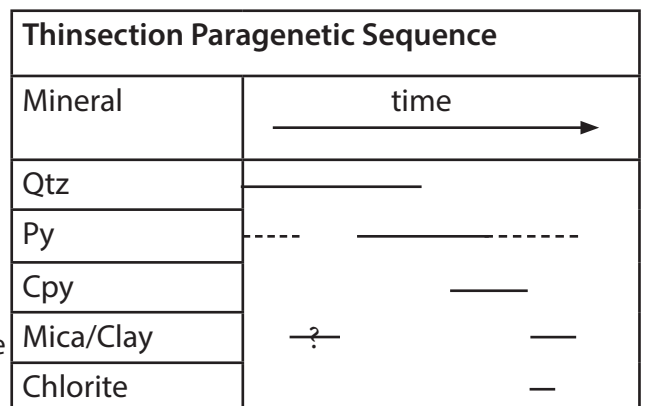
Fig40: Scanned thinsection

Mineralogy:

Mineral	Relative %	Textural Descriptions
Pyrite (Py)	8	Euhedral-subhedral pyrite as inclusions in Cpy. Pyrite also occurs as disseminated grains in host rock, often present in relict plagioclase and amphibole grains.
Chalcopyrite (Cpy)	25	Replacing hornblende?
Quartz (2) (Qtz ⁽²⁾)	8	Prismatic coarse grained quartz associated with sulphides. show open-space growing (comb quartz)
Calcite (Ca)	2	Present as interstitial infill between grains and as veins cutting pyrite grains.
Wallrock		
Plagioclase	12	Relict plagioclase, completely altered to mica/clay
Quartz	25	Ubiquitous fine anhedral grains present in matrix.
Alteration		
Mica/Clay	18	Very fine grained muscovite and illite intermixed replacing primary plagioclase grains. Muscovite also present as medium-coarse grains
Chlorite	tr	present along fractures within relict plagioclase and weakly replacing plagioclase grains

Description and Interpretation

Sulphide vein within an andesite hostrock. Hostrock adjacent to vein strongly altered into a quartz, sericite/illite assemblage. Sulphide assemblage includes primarily pyrite and chalcopyrite. Two different assemblages of pyrite may be present, distinguished by their morphology and relationship with chalcopyrite. Early stage pyrite tends to be cubic euhedral-subhedral grains and occur as inclusions within chalcopyrite. Chlorite is found in trace amounts as fracture infill. Sericite/clay is ubiquitous within matrix as an alteration mineral. It is often found to be replacing relict plagioclase grains, as fracture fill and interstitial material



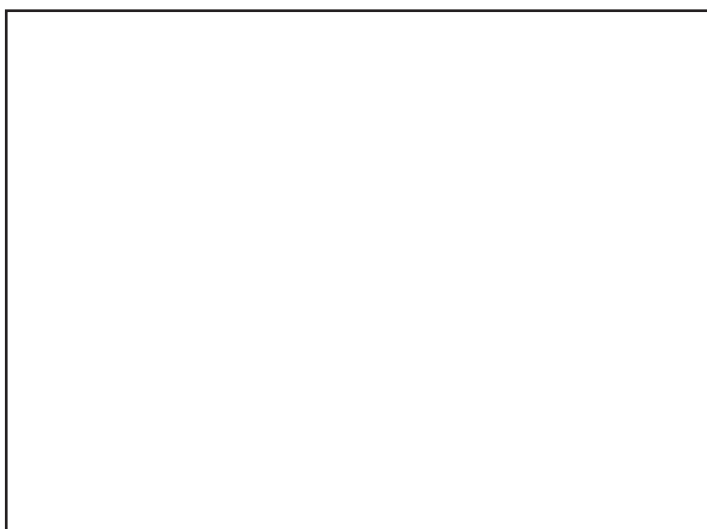
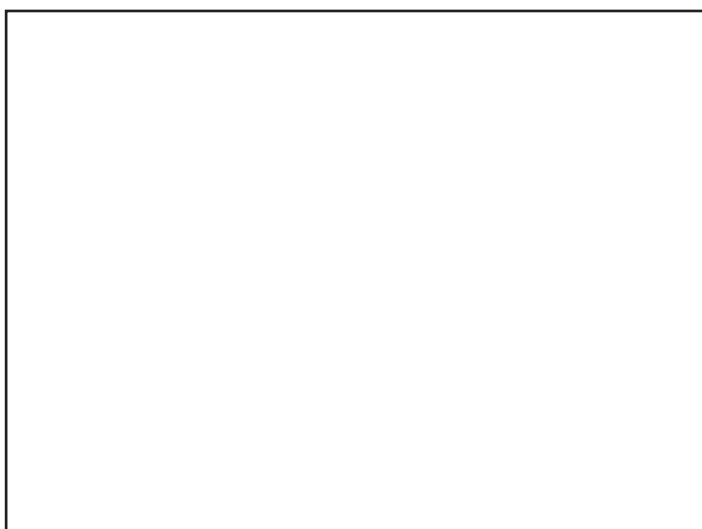
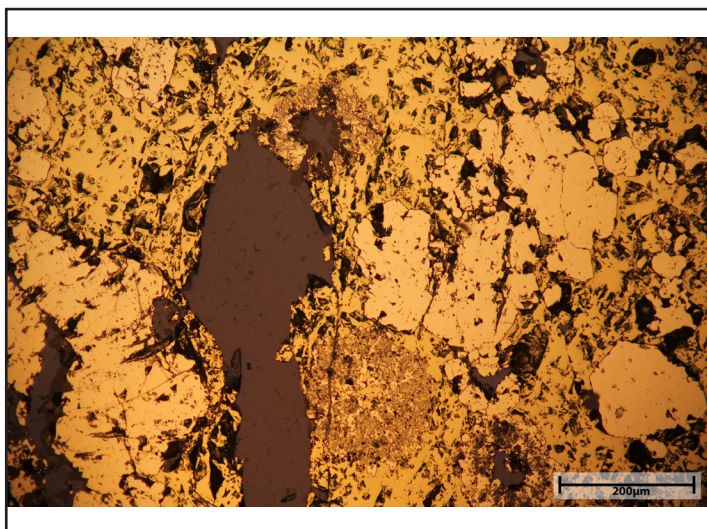
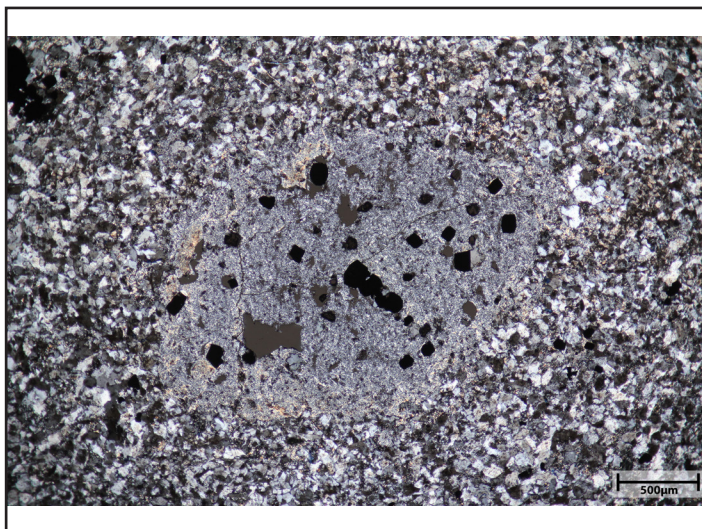
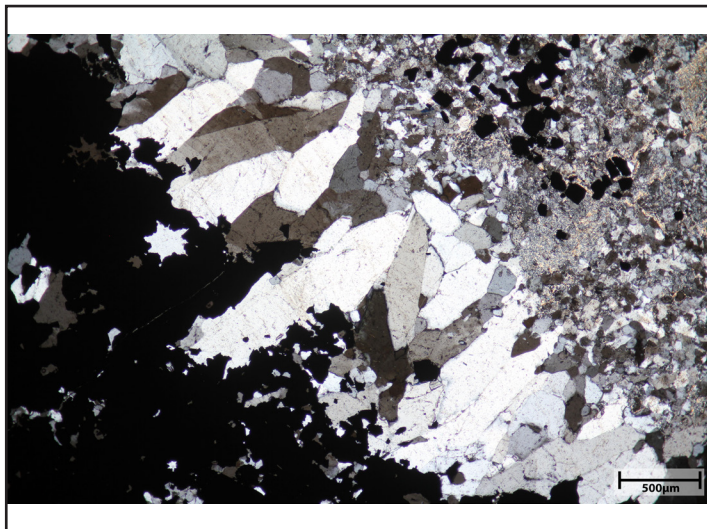


Fig 41A: (XPL-TRS) Chalcopyrite-pyrite vein, with fine grained quartz as gangue. Vein selvage contains euhedral coarse crystalline quartz (comb quartz), wallrock present shows intense alteration. Plagioclase in wallrock is completely replaced by mica/clay, unclear whether finegrained muscovite (sericite) or illite or both . Disseminated pyrite is also present in the wallrock. Fig 38B: Fine- medium grained muscovite alteration